VIBRATION-BASED MONITORING OF TALL BUILDINGS

by

Emre Aytulun

B.S., Civil Engineering, Boğaziçi University, 2014

M.S., Civil Engineering, Boğaziçi University, 2017

Submitted to the Institute for Graduate Studies in
Science and Engineering in partial fulfillment of
the requirements for the degree of
Doctor of Philosophy

Graduate Program in Civil Engineering

Boğaziçi University

2023

ACKNOWLEDGEMENTS

I owe Prof. Serdar Soyöz a debt of gratitude for accepting me to his research team and giving the responsibility of many different projects to me. I am also grateful to him for his endless trust and good communication. His valuable guidance and support in every field are absolutely precious. My sincere thanks to him because, my thinking and research skill improved thanks to his knowledge and experience. In addition, he always encouraged me to be unique, which helped me to develop my engineering skill and to stimulate to do my best. Actually, there is no words to thank to him.

I would like to thank to Prof. Kutay Orakçal and Prof. Ufuk Yazgan for their valuable comments and suggestions improved my thesis. Also, I thank to Prof. Cem Yalçın and Prof. Ercan Yüksel for accepting to be my thesis juries. Besides, I would like to thank Prof. Hilmi Luş for his valuable contributions to my thesis.

I thank my colleagues Oğuz Şenkardeşler, Hüseyin Çolak, Cem Tura and Enes Çukacı for all the fun and friendship. I sincerely thank to Oğuz and Hüseyin for increasing my awareness to my project with their suggestions and for promoting to continue my project in most proper way with discussions. I thank to Cem and Enes for their valuable suggestions and contributions to increase the value of my thesis.

Also, I take this opportunity to express the profoundest gratitude from my deep heart to my family for their sacrifices, love, and support. Without their extreme supports and the carefree environment that they provided, it would not be possible for me to follow a PhD degree. Last but not the least, I am very thankful to my wife, Ceren, without her, this thesis would not have been possible. Her unending love, valuable support and incredible tolerance were indescribable. Actually, there is actually no words to thanks to her. Actually, I have to mention a person who is more important to me than anything else. My son Emir Uraz was born in the middle of this study and he was my fundamental motivation by strengthening me every day to finish this study.

ABSTRACT

VIBRATION-BASED MONITORING OF TALL BUILDINGS

Tall buildings are indispensable solutions in cities where economy and population grow rapidly. Parallel to advancements in technology, number of tall buildings in regions with high seismicity increased dramatically in recent years. On the other hand, it is crucial to conduct condition assessment of such structures after an earthquake due to public safety and owner-need reasons. Structural Health Monitoring systems enable condition assessment of structures before, during and after earthquake rapidly, remotely and objectively. Structural Health Monitoring systems are mandatory to be installed on tall buildings in Turkey since 2019 because of their significant contribution to our understanding of dynamic behavior of tall buildings and our capability of condition monitoring. However, limited number of sensors are instrumented for tall buildings due to economic reasons. With the motivations and reasons mentioned above, three unique methodologies on development and updating of simplified models of tall buildings based on system identification results are presented. These methodologies are able to estimate responses of non-instrumented floors from instrumented floors; therefore, condition assessment of tall buildings after an earthquake can be precisely performed by computing inter-story drift ratios and tracking changes in modal parameters. In addition, proposed methodologies are validated with recorded responses of real structures under different earthquakes. Lastly, in-house developed software platform for real - time monitoring of tall buildings is presented.

ÖZET

YÜKSEK YAPILARDA TİTREŞİM BAZLI İZLEME

Yüksek yapılar ekonominin ve nüfusun hızla arttığı şehirlerde vazgeçilmez çözümlerdir. Teknolojideki gelişmelere paralel olarak, depremselliği yüksek olan bölgelerde yüksek yapı sayısı son yıllarda önemli ölçüde artmıştır. Öte yandan, bu tür yapıların deprem sonrası durum değerlendirmesinin yapılması kamu güvenliği ve bina sahibinin ihtiyacı nedeniyle çok önemlidir. Yapı Sağlığı İzleme sistemleri, deprem öncesi, sırası ve sonrasında yapıların durum değerlendirilmesinin hızlı, uzaktan ve objektif şekilde yapılmasını sağlamaktadır. Yapı Sağlığı İzleme sistemlerinin yüksek yapıların dinamik davranışını anlamamıza ve durum izleme kabiliyetimize önemli katkıları nedeniyle Türkiye'de 2019'dan beri yüksek yapılara kurulması zorunludur. Ancak ekonomik nedenlerleden dolayı yüksek yapılara sınırlı sayıda sensörler yerleştirilmektedir. Yukarıda belirtilen motivasyon ve nedenlerle, bu tezde sistem tanımlama sonuçlarına dayalı basitleştirilmiş yüksek yapı modellerinin geliştirilmesi ve güncellenmesi için üç yeni metodoloji sunulmuştur. Bu metodolojiler, sensor bulunmayan katların tepkilerini sensor bulunan katların tepkilerinden tahmin edebilmektedir; bu nedenle, olası bir deprem sonrasında yüksek yapıların durum değerlendirilmesi, katlar arası öteleme oranlarının hesaplanması ve modal değerlerdeki değişikliklerin izlenmesi ile hassas bir şekilde gerçekleştirilebilmektedir. Ayrıca önerilen metodolojilerin, gerçek yapıların farklı depremler altındaki titreşim kayıtları kullanılarak doğrulaması yapılmıştır. Son olarak, yüksek yapıların gerçek zamanlı izlenmesi için geliştirilen yazılım platformu sunulmuştur.

TABLE OF CONTENTS

ACKNOWLEDGEMENTS iii
ABSTRACT iv
ÖZET v
LIST OF FIGURES viii
LIST OF TABLES xxvii
LIST OF SYMBOLS xxviii
LIST OF ACRONYMS/ABBREVIATIONS xxx
1. INTRODUCTION 1
1.1. Overview and Research Objective 1
1.2. Thesis Outline 2
1.3. Literature Review 3
2. FINITE ELEMENT MODEL OF TALL BUILDING 10
2.1. Modelling of Frame Elements 15
2.2. Modelling of Coupling Beams 18
2.3. Modelling of Structural Walls 18
2.4. Modelling of Basement Walls 21
2.5. Modelling of Slabs and Floor Diaphragm Consideration 21
2.6. Modelling of P-Δ Columns and Geometric Non-linearity 22
3. NONLINEAR TIME HISTORY ANALYSIS OF TALL BUILDING 23
3.1. Ground Motion Selection 23
3.2. Results of Nonlinear Time History Analysis 25
4. ESTIMATION OF NON-INSTRUMENTED FLOOR RESPONSES 40
4.1. Stepped Timoshenko Beam Model (STBM) 41
4.2. Discrete Timoshenko Beam Model (DTBM) 62
4.3. Nonlinear Simplified Model (NLSM) 81
4.4. Comparison of Three Different Estimation Approaches 119
5. DAMAGE EVALUATION 123
6. REAL WORLD APPLICATIONS 140

6.1. Non-Damaged Tall Building 140
6.2. Damaged RC Building 158
7. SOFTWARE DEVELOPMENT 170
8. SUMMARY AND CONCLUSION 174
REFERENCES 178
APPENDIX A: PERMISSIONS FOR THE FIGURES 193

LIST OF FIGURES

Figure 2.1. Elastic spectra. 13

Figure 2.2. Dimension of structural members and 3D geometry of the tall building. 13

Figure 2.3. Nonlinear modelling methods of structural members [49]. 14

Figure 2.4. Modelling principles of displacement-based element and force-based element. 16

Figure 2.5. Concrete material model in finite element model. 17

Figure 2.6. Reinforcement steel material model in finite element model. 17

Figure 2.7. Two-node link element and mechanical properties for coupling beams in finite element model. 19

Figure 2.8. Mechanism of multi-layer shell element [69]. 20

Figure 3.1. Target spectrum defined in TBSC, spectral acceleration values for different return periods and location of structure and North Anatolian Fault. 24

Figure 3.2. Response spectra of earthquakes, mean spectra and target spectra. 26

Figure 3.3. Time history graphs of ground motion records. 26

Figure 3.4. Labels and points for nonlinear time history analysis results. . . . 29

Figure 3.5. P1-X inter-story drift ratios. 29

Figure 3.6. P1-Y inter-story drift ratios. 30

Figure 3.7. P2-X inter-story drift ratios. 30

Figure 3.8. P2-Y inter-story drift ratios. 31

Figure 3.9. P01 shear forces. 31

Figure 3.10. P02 shear forces. 32

Figure 3.11. P03 shear forces. 32

Figure 3.12. P04 shear forces. 33

Figure 3.13. P05 shear forces. 33

Figure 3.14. P06 shear forces. 34

Figure 3.15. P07 shear forces. 34

Figure 3.16. P08 shear forces. 35

Figure 3.17. P09 shear forces. 35

Figure 3.18. P10 shear forces. 36

Figure 3.19. Chord rotation of coupling beams - down. 36

Figure 3.20. Chord rotation of coupling beams - up. 37

Figure 3.21. Strain-gauge results. 37

Figure 3.22. Demand/Capacity ratio for beam rotations. 38

Figure 3.23. Demand/Capacity ratio for beam shear forces. 38

Figure 3.24. Demand/Capacity ratio for column rotations. 39

Figure 3.25. Demand/Capacity ratio for column shear forces. 39

Figure 4.1. Mathematical models of tall building with different approaches. . . 42

Figure 4.2. Relation between effective bending rigidity and effective shear rigidity. 44

Figure 4.3. STBM-X: updated and identified modal properties. 46

Figure 4.4. STBM-Y: updated and identified modal properties. 46

Figure 4.5. STBM-X: recorded (black solid line) and estimated (red dashed line) floor displacements, eq id: 178. 48

Figure 4.6. STBM-X: recorded (black solid line) and estimated (red dashed line) floor displacements, eq id: 549. 49

Figure 4.7. STBM-X: recorded (black solid line) and estimated (red dashed line) floor displacements, eq id: 879. 49

Figure 4.8. STBM-X: recorded (black solid line) and estimated (red dashed line) floor displacements, eq id: 1115. 50

Figure 4.9. STBM-X: recorded (black solid line) and estimated (red dashed line) floor displacements, eq id: 1165. 50

Figure 4.10. STBM-X: recorded (black solid line) and estimated (red dashed line) floor displacements, eq id: 1615. 51

Figure 4.11. STBM-X: recorded (black solid line) and estimated (red dashed line) floor displacements, eq id: 1633. 51

Figure 4.12. STBM-X: recorded (black solid line) and estimated (red dashed line) floor displacements, eq id: 1794. 52

Figure 4.13. STBM-X: recorded (black solid line) and estimated (red dashed line) floor displacements, eq id: 3954. 52

Figure 4.14. STBM-X: recorded (black solid line) and estimated (red dashed line) floor displacements, eq id: 5836. 53

Figure 4.15. STBM-X: recorded (black solid line) and estimated (red dashed line) floor displacements, eq id: 6980. 53

Figure 4.16. STBM-Y: recorded (black solid line) and estimated (red dashed line) floor displacements, eq id: 178. 54

Figure 4.17. STBM-Y: recorded (black solid line) and estimated (red dashed line) floor displacements, eq id: 549. 54

Figure 4.18. STBM-Y: recorded (black solid line) and estimated (red dashed line) floor displacements, eq id: 879. 55

Figure 4.19. STBM-Y: recorded (black solid line) and estimated (red dashed line) floor displacements, eq id: 1115. 55

Figure 4.20. STBM-Y: recorded (black solid line) and estimated (red dashed line) floor displacements, eq id: 1165. 56

Figure 4.21. STBM-Y: recorded (black solid line) and estimated (red dashed line) floor displacements, eq id: 1615. 56

Figure 4.22. STBM-Y: recorded (black solid line) and estimated (red dashed line) floor displacements, eq id: 1633. 57

Figure 4.23. STBM-Y: recorded (black solid line) and estimated (red dashed line) floor displacements, eq id: 1794. 57

Figure 4.24. STBM-Y: recorded (black solid line) and estimated (red dashed line) floor displacements, eq id: 3954. 58

Figure 4.25. STBM-Y: recorded (black solid line) and estimated (red dashed line) floor displacements, eq id: 5836. 58

Figure 4.26. STBM-Y: recorded (black solid line) and estimated (red dashed line) floor displacements, eq id: 6980. 59

Figure 4.27. STBM: error values between recorded and estimated floor displacements. 60

Figure 4.28. STBM-X: estimated inter-story drift ratios. 61

Figure 4.29. STBM-Y: estimated inter-story drift ratios. 61

Figure 4.30. DTBM: General overview and equilibrium equations of non-uniform simplified mathematical model of structure. 62

Figure 4.31. DTBM-X: updated and identified modal properties. 67

Figure 4.32. DTBM-Y: updated and identified modal properties. 68

Figure 4.33. DTBM-X: recorded (black solid line) and estimated (red dashed line) floor displacements, eq id: 178. 68

Figure 4.34. DTBM-X: recorded (black solid line) and estimated (red dashed line) floor displacements, eq id: 549. 69

Figure 4.35. DTBM-X: recorded (black solid line) and estimated (red dashed line) floor displacements, eq id: 879. 69

Figure 4.36. DTBM-X: recorded (black solid line) and estimated (red dashed line) floor displacements, eq id: 1115. 70

Figure 4.37. DTBM-X: recorded (black solid line) and estimated (red dashed line) floor displacements, eq id: 1165. 70

Figure 4.38. DTBM-X: recorded (black solid line) and estimated (red dashed line) floor displacements, eq id: 1615. 71

Figure 4.39. DTBM-X: recorded (black solid line) and estimated (red dashed line) floor displacements, eq id: 1633. 71

Figure 4.40. DTBM-X: recorded (black solid line) and estimated (red dashed line) floor displacements, eq id: 1794. 72

Figure 4.41. DTBM-X: recorded (black solid line) and estimated (red dashed line) floor displacements, eq id: 3954. 72

Figure 4.42. DTBM-X: recorded (black solid line) and estimated (red dashed line) floor displacements, eq id: 5836. 73

Figure 4.43. DTBM-X: recorded (black solid line) and estimated (red dashed line) floor displacements, eq id: 6980. 73

Figure 4.44. DTBM-Y: recorded (black solid line) and estimated (red dashed line) floor displacements, eq id: 178. 74

Figure 4.45. DTBM-Y: recorded (black solid line) and estimated (red dashed line) floor displacements, eq id: 549. 74

Figure 4.46. DTBM-Y: recorded (black solid line) and estimated (red dashed line) floor displacements, eq id: 879. 75

Figure 4.47. DTBM-Y: recorded (black solid line) and estimated (red dashed line) floor displacements, eq id: 1115. 75

Figure 4.48. DTBM-Y: recorded (black solid line) and estimated (red dashed line) floor displacements, eq id: 1165. 76

Figure 4.49. DTBM-Y: recorded (black solid line) and estimated (red dashed line) floor displacements, eq id: 1615. 76

Figure 4.50. DTBM-Y: recorded (black solid line) and estimated (red dashed line) floor displacements, eq id: 1633. 77

Figure 4.51. DTBM-Y: recorded (black solid line) and estimated (red dashed line) floor displacements, eq id: 1794. 77

Figure 4.52. DTBM-Y: recorded (black solid line) and estimated (red dashed line) floor displacements, eq id: 3954. 78

Figure 4.53. DTBM-Y: recorded (black solid line) and estimated (red dashed line) floor displacements, eq id: 5836. 78

Figure 4.54. DTBM-Y: recorded (black solid line) and estimated (red dashed line) floor displacements, eq id: 6980. 79

Figure 4.55. DTBM: error values between recorded and estimated floor displacements. 79

Figure 4.56. DTBM-X: estimated inter-story drift ratios. 80

Figure 4.57. DTBM-Y: estimated inter-story drift ratios. 81

Figure 4.58. NLSM: detailed information about procedure to determine mass and elastic stiffness of springs. 83

Figure 4.59. NLSM: changes in error values during updating. 84

Figure 4.60. NLSM: changes in mass distribution of structure during updating. 84

Figure 4.61. NLSM: changes in elastic stiffness distribution of structure during updating. 85

Figure 4.62. NLSM-X: updated and identified modal properties. 86

Figure 4.63. NLSM-Y: updated and identified modal properties. 86

Figure 4.64. Steps of unscented kalman filter. 87

Figure 4.65. Steps of simulated annealing. 88

Figure 4.66. Information about nonlinear curve of springs and nonlinear updating procedure. 89

Figure 4.67. NLSM: comparison of displacements. 90

Figure 4.68. NLSM: comparison of inter-story drift ratios. 90

Figure 4.69. NLSM-X: recorded (black solid line) and estimated (red dashed line) floor displacements, eq id: 178. 91

Figure 4.70. NLSM-X: recorded (black solid line) and estimated (red dashed line) floor displacements, eq id: 549. 92

Figure 4.71. NLSM-X: recorded (black solid line) and estimated (red dashed line) floor displacements, eq id: 879. 92

Figure 4.72. NLSM-X: recorded (black solid line) and estimated (red dashed line) floor displacements, eq id: 1115. 93

Figure 4.73. NLSM-X: recorded (black solid line) and estimated (red dashed line) floor displacements, eq id: 1165. 93

Figure 4.74. NLSM-X: recorded (black solid line) and estimated (red dashed line) floor displacements, eq id: 1615. 94

Figure 4.75. NLSM-X: recorded (black solid line) and estimated (red dashed line) floor displacements, eq id: 1633. 94

Figure 4.76. NLSM-X: recorded (black solid line) and estimated (red dashed line) floor displacements, eq id: 1794. 95

Figure 4.77. NLSM-X: recorded (black solid line) and estimated (red dashed line) floor displacements, eq id: 3954. 95

Figure 4.78. NLSM-X: recorded (black solid line) and estimated (red dashed line) floor displacements, eq id: 5836. 96

Figure 4.79. NLSM-X: recorded (black solid line) and estimated (red dashed line) floor displacements, eq id: 6980. 96

Figure 4.80. NLSM-Y: recorded (black solid line) and estimated (red dashed line) floor displacements, eq id: 178. 97

Figure 4.81. NLSM-Y: recorded (black solid line) and estimated (red dashed line) floor displacements, eq id: 549. 97

Figure 4.82. NLSM-Y: recorded (black solid line) and estimated (red dashed line) floor displacements, eq id: 879. 98

Figure 4.83. NLSM-Y: recorded (black solid line) and estimated (red dashed line) floor displacements, eq id: 1115. 98

Figure 4.84. NLSM-Y: recorded (black solid line) and estimated (red dashed line) floor displacements, eq id: 1165. 99

Figure 4.85. NLSM-Y: recorded (black solid line) and estimated (red dashed line) floor displacements, eq id: 1615. 99

Figure 4.86. NLSM-Y: recorded (black solid line) and estimated (red dashed line) floor displacements, eq id: 1633. 100

Figure 4.87. NLSM-Y: recorded (black solid line) and estimated (red dashed line) floor displacements, eq id: 1794. 100

Figure 4.88. NLSM-Y: recorded (black solid line) and estimated (red dashed line) floor displacements, eq id: 3954. 101

Figure 4.89. NLSM-Y: recorded (black solid line) and estimated (red dashed line) floor displacements, eq id: 5836. 101

Figure 4.90. NLSM-Y: recorded (black solid line) and estimated (red dashed line) floor displacements, eq id: 6980. 102

Figure 4.91. NLSM: error values between recorded and estimated floor displacements. 102

Figure 4.92. NLSM-X: estimated inter-story drift ratios. 103

Figure 4.93. NLSM-Y: estimated inter-story drift ratios. 104

Figure 4.94. NLSM-X: nonlinear curves of flexural springs (initial curves: solid line, estimated curves: dashed line). 105

Figure 4.95. NLSM-X: distribution of estimated M_d. 105

Figure 4.96. NLSM-X: distribution of estimated M_y. 106

Figure 4.97. NLSM-X: distribution of estimated M_u. 106

Figure 4.98. NLSM-X: distribution of estimated θ_d. 107

Figure 4.99. NLSM-X: distribution of estimated θ_y. 107

Figure 4.100. NLSM-X: distribution of estimated θ_u. 108

Figure 4.101. NLSM-X: nonlinear curves of shear springs (initial curves: solid line, estimated curves: dashed line). 108

Figure 4.102. NLSM-X: distribution of estimated V_d. 109

Figure 4.103. NLSM-X: distribution of estimated V_y. 109

Figure 4.104. NLSM-X: distribution of estimated V_u. 110

Figure 4.105. NLSM-X: distribution of estimated D_d. 110

Figure 4.106. NLSM-X: distribution of estimated D_y. 111

Figure 4.107. NLSM-X: distribution of estimated D_u. 111

Figure 4.108. NLSM-Y: nonlinear curves of flexural springs (initial curves: solid line, estimated curves: dashed line). 112

Figure 4.109. NLSM-Y: distribution of estimated M_d. 112

Figure 4.110. NLSM-Y: distribution of estimated M_y. 113

Figure 4.111. NLSM-Y: distribution of estimated M_u. 113

Figure 4.112. NLSM-Y: distribution of estimated θ_d. 114

Figure 4.113. NLSM-Y: distribution of estimated θ_y. 114

Figure 4.114. NLSM-Y: distribution of estimated θ_u. 115

Figure 4.115. NLSM-Y: nonlinear curves of shear springs (initial curves: solid line, estimated curves: dashed line). 115

Figure 4.116. NLSM-Y: distribution of estimated V_d. 116

Figure 4.117. NLSM-Y: distribution of estimated V_y. 116

Figure 4.118. NLSM-Y: distribution of estimated V_u. 117

Figure 4.119. NLSM-Y: distribution of estimated D_d. 117

Figure 4.120. NLSM-Y: distribution of estimated D_y. 118

Figure 4.121. NLSM-Y: distribution of estimated D_u. 118

Figure 4.122. Comparison of error values between recorded and estimated floor displacements for x direction. 120

Figure 4.123. Comparison of error values between recorded and estimated floor displacements for y direction. 120

Figure 4.124. Comparison of inter-story drift ratios for x direction. 121

Figure 4.125. Comparison of inter-story drift ratios for y direction. 121

Figure 5.1. Changes in modal frequencies for x direction, eq id: 178. 124

Figure 5.2. Changes in modal frequencies for x direction, eq id: 549. 124

Figure 5.3. Changes in modal frequencies for x direction, eq id: 879. 125

Figure 5.4. Changes in modal frequencies for x direction, eq id: 1115. 125

Figure 5.5. Changes in modal frequencies for x direction, eq id: 1165. 126

Figure 5.6. Changes in modal frequencies for x direction, eq id: 1655. 126

Figure 5.7. Changes in modal frequencies for x direction, eq id: 1633. 127

Figure 5.8. Changes in modal frequencies for x direction, eq id: 1794. 127

Figure 5.9. Changes in modal frequencies for x direction, eq id: 3954. 128

Figure 5.10. Changes in modal frequencies for x direction, eq id: 5836. 128

Figure 5.11. Changes in modal frequencies for x direction, eq id: 6980. 129

Figure 5.12. Changes in modal frequencies for y direction, eq id: 178. 129

Figure 5.13. Changes in modal frequencies for y direction, eq id: 549. 130

Figure 5.14. Changes in modal frequencies for y direction, eq id: 879. 130

Figure 5.15. Changes in modal frequencies for y direction, eq id: 1115. 131

Figure 5.16. Changes in modal frequencies for y direction, eq id: 1165. 131

Figure 5.17. Changes in modal frequencies for y direction, eq id: 1655. 132

Figure 5.18. Changes in modal frequencies for y direction, eq id: 1633. 132

Figure 5.19. Changes in modal frequencies for y direction, eq id: 1794. 133

Figure 5.20. Changes in modal frequencies for y direction, eq id: 3954. 133

Figure 5.21. Changes in modal frequencies for y direction, eq id: 5836. 134

Figure 5.22. Changes in modal frequencies for y direction, eq id: 6980. 134

Figure 5.23. Damage index vs. maximum drift ratio graphs (blue points for sf: 2475*0.33, red points for sf: 2475*0.67, black points for sf: 2475). . 136

Figure 5.24. Damage distribution based on maximum drift ratio (blue bars for sf: 2475*0.33, red bars for sf: 2475*0.67, yellow bars for sf: 2475). 137

Figure 5.25. Damage index vs. maximum chord rotation/yield chord rotation ratio graphs for coupling beams (blue points for sf: 2475*0.33, red points for sf: 2475*0.67, black points for sf: 2475). 138

Figure 5.26. Damage distribution based on maximum chord rotation/yield chord rotation ratio for coupling beams (blue bars for sf: 2475*0.33, red bars for sf: 2475*0.67, yellow bars for sf: 2475). 138

Figure 5.27. Summary of damage index vs. maximum inter-story drift ratio. . . 139

Figure 6.1. SHM system and sensor layout of tall building. 140

Figure 6.2. Scattering of modal frequencies. 142

Figure 6.3. Scattering of modal damping ratios. 142

Figure 6.4. Changes in mode shapes. 143

Figure 6.5. Distribution of identified modal frequencies. 144

Figure 6.6. Distribution of identified modal damping ratios. 145

Figure 6.7. (a) Location of the building and the earthquake. (b) Vibration records from the building. (c) FAS of input motion – basement floor x direction. (d) FAS of input motion – basement floor y direction. 145

Figure 6.8. Singular values of Hankel matrices. 146

Figure 6.9. Stabilization diagrams for N4SID method - from up to bottom: before, during and after earthquake. 147

Figure 6.10. Identified mode shapes with N4SID method. 148

Figure 6.11. Relation between the effective bending rigidity and the effective shear rigidity. 150

Figure 6.12. Updated and identified modal properties of STBM for x direction. 150

Figure 6.13. Updated and identified modal properties of STBM for y direction. 151

Figure 6.14. Updated and identified modal properties of DTBM for x direction. 151

Figure 6.15. Updated and identified modal properties of DTBM for y direction. 152

Figure 6.16. Recorded and estimated floor accelerations for whole duration for x direction (STBM). 152

Figure 6.17. Recorded and estimated floor accelerations for two seconds for x direction (STBM). 153

Figure 6.18. Recorded and estimated floor accelerations for whole duration for y direction (STBM). 153

Figure 6.19. Recorded and estimated floor accelerations for two seconds for y direction (STBM). 154

Figure 6.20. Recorded and estimated floor accelerations for whole duration for x direction (DTBM). 154

Figure 6.21. Recorded and estimated floor accelerations for two seconds for x direction (DTBM). 155

Figure 6.22. Recorded and estimated floor accelerations for whole duration for y direction (DTBM). 155

Figure 6.23. Recorded and estimated floor accelerations for two seconds for y direction (DTBM). 156

Figure 6.24. Estimated inter-story drift ratios for STBM and DTBM. 156

Figure 6.25. Damage index vs. maximum inter-story drift ratio graphs for STBM and DTBM. 157

Figure 6.26. General overview of the building [48]. 158

Figure 6.27. SHM system and sensor layout of the building. 159

Figure 6.28. Time history graphs for Northridge Earthquake. 160

Figure 6.29. Observed structural damages on building after Northridge Earthquake – north view [120]. 160

Figure 6.30. Observed structural damages on building after Northridge Earthquake – south view [120]. 161

Figure 6.31. Changes in modal frequencies under Northridge Earthquake. . . . 161

Figure 6.32. Identified mode shapes before and after Northridge Earthquake. . 162

Figure 6.33. Relation between the effective bending rigidity and the effective shear rigidity. 163

Figure 6.34. Changes in error values during updating. 164

Figure 6.35. Changes in mass distribution of building in Van Nuys during updating. 164

Figure 6.36. Changes in elastic stiffness distribution of building in Van Nuys during updating. 164

Figure 6.37. Updated and identified modal properties. 165

Figure 6.38. Recorded and estimated floor accelerations for north-south. 166

Figure 6.39. Recorded and estimated floor accelerations for east-west. 166

Figure 6.40. Nonlinear behavior of springs after updating for north-south. . . . 167

Figure 6.41. Nonlinear behavior of springs after updating for east-west. 167

Figure 6.42. Estimated inter-story drift ratios. 168

Figure 6.43. Damage index vs. maximum inter-story drift ratio graph for damage assessment of building. 169

Figure 7.1. Graphical user interface of real time monitoring module. 170

Figure 7.2. Graphical user interface of system identification (freq domain) module. 171

Figure 7.3. Graphical user interface of system identification (time domain) module. 171

Figure 7.4. Graphical user interface of signal processing module. 172

Figure 7.5. Automatically created report by in-house developed software. . . . 173

Figure A.1. Usage permission for Figure 2.3. 193

Figure A.2. Usage permission for Figure 2.8. 194

Figure A.3. Usage permission for Figure 6.29 and Figure 6.30. 195

LIST OF TABLES

Table 2.1. Modelling stages of tall building 10

Table 2.2. Material properties 11

Table 2.3. Gravity loads 11

Table 2.4. Effective stiffness multipliers for design stages 12

Table 3.1. Selected ground motion records and scale factors 25

Table 3.2. Modal analysis results 28

Table 5.1. Summary of frequency changes 135

Table 5.2. Performance levels and suggested threshold values 136

Table 6.1. System identification results of tall building in Istanbul under ambient condition 141

Table 6.2. Identified natural frequencies and damping ratios of tall building in Istanbul with N4SID method 148

Table 6.3. Comparison of identified modal frequencies with results of other studies in literature 162

LIST OF SYMBOLS

A	Cross-sectional Area
C	Ratio Between Flexural Rigidity and Shear Rigidity
E	Young Modulus
$E(\alpha)$	Error Value
E^*	Effective Young Modulus
E_{init}	Initial Young Modulus
E_{secant}	Secant Young Modulus
E_e^H	Horizontal Earthquake Load
E_e^Z	Vertical Earthquake Load
f	Frequency
f_{cd}	Design Compressive Strength of Concrete
f_{ce}	Expected Compressive Strength of Concrete
f_{ck}	Characteristic Compressive Strength of Concrete
f_{yd}	Design Yield Strength of Steel
f_{ye}	Expected Yield Strength of Steel
f_{yk}	Characteristic Yield Strength of Steel
F_{a}	Short-period Site Factor
F_{v}	Long-period Site Factor
G	Dead Load
G	Shear Modulus
G^*	Effective Shear Modulus
$G_{initial}$	Initial Shear Modulus
h	Weighting coefficient for MAC value
H	Lateral Soil Pressure
H	Transfer Matrix
Hz	Hertz
I	Moment of Inertia
k	Weighting Coefficient for Modal Frequency

k_e	Elastic Spring Stiffness
k'	Shear Coefficient
K	Stiffness Matrix
M	Mass Matrix
M	Bending Moment
Q	Live Load
Q	Shear Force
S	Snow Load
S_1	Horizontal Response Spectral Acceleration Coefficient at 1.0s
S_a	Elastic Spectral Acceleration
S_d	Elastic Spectral Displacement
S_D1	Horizontal Response Spectral Acceleration at 1.0s
S_DS	Horizontal Response Spectral Acceleration at 0.2s
S_S	Horizontal Response Spectral Acceleration Coefficient at 0.2s
T	Natural Period of Structure
V	Shear Force
Y	Transverse Displacement
$W(\xi)$	Transverse Deflection of Timoshenko Beam
α	Rayleigh Damping Mass Coefficient
β	Rayleigh Damping Stiffness Coefficient
ε	Error Value
ω	Natural Frequency
Γ	Modal Participation Factor
ϕ	Mode Shape
$\phi(\xi)$	Rotational Deflection of Timoshenko Beam
ψ	Slope
ρ	Mass Density
θ	Rotation
ξ	Modal Damping Ratio

LIST OF ACRONYMS/ABBREVIATIONS

2D	Two Dimensional
3D	Three Dimensional
CB	Coupling Beam
CL	Critical Level
CP	Collapse Prevention
CV	Coefficient Vector
DI	Damage Index
DTBM	Discrete Timoshenko Beam Model
EFDD	Enhanced Frequency Domain Decomposition
EW	East-West Direction
FEM	Finite Element Model
FEMA	Federal Emergency Management Agency
GPa	Giga-Pascal
IO	Immediate Occupancy
kN	Kilo-Newton
LS	Life Safety
MAC	Modal Assurance Criteria
MPa	Mega-Pascal
N4SID	Subspace State Space System Identification
NIF	Number of Instrumented Floors
NIM	Number of Identified Modes
NLSM	Nonlinear Simplified Model
NLTH	Nonlinear Time History
NPT	Time Length of Data
NS	North-South Direction
PEER	Pacific Earthquake Engineering Research
PIDR	Peak Inter-story Drift Ratio
PGA	Peak Ground Acceleration

PSD	Power Spectral Density
SA	Simulated Annealing
SF	Scale Factor
SHM	Structural Health Monitoring
STBM	Stepped Timoshenko Beam Model
TBSC	Turkish Building Seismic Code
TMM	Transfer Matrix Method
UKF	Unscented Kalman Filter
UU	Uninterrupted Use

1. INTRODUCTION

1.1. Overview and Research Objective

Number of tall buildings in earthquake prone areas increased dramatically in recent years. Since Structural Health Monitoring (SHM) systems provide significant benefit to assess condition of structures after earthquakes, installation of these systems in many tall buildings is required by owners. However, limited number of sensors are used to identify and control dynamic properties of structures due to economic reasons.

Tracking only the changes in dynamic properties may not always be sufficient to assess condition of structures after an earthquake. Although changes in dynamic properties of structure are generally caused by structural stiffness change, some external mechanisms such as soil-structure interaction may change dynamic properties of structures. Therefore, in this study, a method using both fundamental frequency changes and maximum inter-story drift ratios was proposed for damage assessment of structures.

On the other hand limited number of sensors are not enough to accurately calculate inter-story drift ratios throughout entire structure. Linear and polynomial interpolation techniques are preferred to estimate responses of non-instrumented floors from instrumented floors and to predict inter-story drift ratios along structures. However, these techniques are not appropriate to detect abnormalities of non-instrumented floors.

In this study, linear and nonlinear simplified models of modelled tall building in OpenSess according to seismic code were created to predict dynamic responses of non-instrumented floors from instrumented floors. However, it is clear that since there is limited information about structures with Structural Health Monitoring systems, assumptions of simplified models due to uncertainties in structural parameters were

updated based on recorded responses and system identification results by using advanced optimization algorithms.

The main motivation in this study is to use changes in dynamic properties of structures and inter-story drift ratio as damage indicators because they can be estimated by SHM systems. Therefore, detailed finite element model (FEM) of a representative tall building was created to perform necessary simulations and to create correlation between changes in dynamic properties, inter-story drift ratios and structural deformations. Finally, reliable threshold values for different performance levels were proposed for condition assessment of structures.

Proposed methodologies were validated with recorded dynamic responses of real structures under different earthquakes causing different damage levels. OpenSees [1, 2] was used to create finite element model (FEM) of structures. On the other and, simplified mathematical models of structures was created in Matlab [3]. Also, Matlab [3] was utilized in order to develop updating and optimization algorithms.

1.2. Thesis Outline

The thesis consists of 7 main chapters. In the first chapter, a comprehensive summary of previous studies in literature is presented.

In the second and third chapters, linear and nonlinear finite element models of a tall building are created. This finite element model is a representative model for a real structure in order to perform necessary simulations and validate proposed methodologies.

In the forth chapter, proposed methodologies to create linear and nonlinear simplified mathematical models of tall buildings are presented in details. Besides, a methodology for optimization of simplified mathematical models of tall buildings based on vibration data recorded by Structural Health Monitoring system is presented.

These simplified models provide estimation of non-instrumented floor responses from responses of instrumented floors.

In the fifth chapter, a unique approach are proposed for condition assessment and functionality of tall buildings after earthquake. This method is capable of performing reliable condition assessment of structures by tracking changes in dynamic properties and maximum inter-story drift ratios.

In the sixth chapter, proposed methodologies are validated through analysis of vibration data recorded by Structural Health Monitoring systems of two different structures. One of these structures remained in elastic range and suffered no damage under earthquake. However, the other structure was severely damaged after strong seismic event.

In the seventh chapter, in house-developed software for real-time monitoring of structures is introduced. The main goal of developed software is to determine condition and functionality of structures remotely, rapidly and objectively by analyzing of vibration records in real time after earthquakes and send automatically created analysis report to responsible authorities.

In the final section, a comprehensive summary of the study is provided. Additionally, detailed recommendations for future researches are presented.

1.3. Literature Review

Today, condition assessment of structures is performed by visual inspections; however, this method is often time-consuming, person-dependent and sometimes not possible. On the contrary, SHM systems can help us to assess condition of structures in rapid, remote and objective fashion. By analyzing vibration records and controlling the changes in dynamic properties of structures, condition of structures can be reliably determined. Therefore, SHM systems are preferred for structures that are costly and

important for economy and human life such as tall buildings, bridges, energy and industrial structures. For instance, SHM systems are utilized in order to observe effects of temperature, wind speed and traffic loading on structural members of suspension bridges [4, 5]. In addition, vibration-based monitoring studies on reinforced concrete bridges in literature showed that damage on structural members can be detected by controlling not only the dynamic properties but also the structural parameters [6, 7]. With the developments in technology, the installation of SHM systems increases on infrastructures due to their economic importance. Oliveira *et al.* [8, 9] identified dynamic properties of wind turbine from one year vibration data and researchers attributed changes in dynamic properties of the structure to change in foundation stiffness and small damages on blades by using regression analysis. Pereira *et al.* [10] analyzed the vibration data of a dam for six months. The uniqueness of this study, changes in dynamic properties of dam was controlled during first filling of reservoir. The numerical model of the structure was validated with the results of system identification and forced vibration test.

Some researchers have focused to identify the dynamic properties of tall buildings using ambient vibration records. In many studies, effects of soil-structure interaction and environmental factors on dynamic properties of monitored structures were investigated with experimental modal analysis and analytical models. Brownjohn [11] identified dynamic properties of the two different office buildings by using output only system identification techniques from ambient vibration data. Celebi [12] examined the response of a 20-storey steel building under low amplitude vibrations and concluded that closeness between the dominant frequency of soil and second translational-torsional mode frequency of structure causes resonance. Nayeri *et al.* [13] identified dynamic properties of 17-story building under ambient conditions by using two different system identification techniques and identified results were analyzed in statistical approach. In addition, environmental effects on dynamic properties of structure were considered and a correlation between temperature and modal frequencies was obtained. Yuen and Kuok [14] collected ambient vibration data from 18-story building during one year and determine dynamic properties of structure to identify, evaluate and eliminate the

effects of ambient interference such as temperature and relative humidity on dynamic properties during vibration data processing. Celebi *et al.* [15] inferred the dynamic properties of a tall building from recorded data under ambient condition. Researchers asserted that response of structure will be different under a seismic action due to outrigger columns and water tanks on the roof. Celebi *et al.* [16] analyzed low-amplitude ambient data in order to determine dynamic properties of building located on the MIT campus. It was observed that structure had significant torsional behavior because of asymmetric placement of both shear walls and heavy equipment at the roof. Zhang *et al.* [17] investigated change in dynamic properties of super tall building during its construction. It was found that modal frequencies were affected by number of floors and changes in temperature and humidity. Mordret *et al.* [18] identified dynamic properties of tall building by using continuous ambient vibration records with the seismic interferometry method. It was observed that variations in velocities calculated by filtering vibration records in certain frequency range are consistent with changes in modal properties for corresponding frequency range. Also, it was observed that shear wave velocity is proportionally related with temperature and inversely related with humidity.

In addition to these studies, many researchers have analyzed behavior of tall buildings under earthquakes. These studies significantly increased after Tohoku earthquake in Japan. Some of studies in literature used vibration data from real structures, while others were conducted by using large-scale experimental setups and analytical models. Celebi and Safak [19, 20] analyzed response of buildings during 1989 Loma Prieta earthquake. Analysis results showed that rocking behavior and soil-structure interaction are significant in identifying behavior of structures during an earthquake. Kohler *et al.* [21] investigated the changes in dynamic properties of 17-story building in the University of California campus before and after earthquakes. It was shown that modal frequencies of structure decreased about 7% to 12% during the earthquake and reverted to pre-earthquake level in several minutes. Snieder and Safak [22] analyzed response of building under earthquake by deconvolution method. Deconvolution method clearly estimate wave propagation profile when top response of building as-

sumed as reference. On the other hand, fundamental modes of building were clearly identified by deconvolution method when basement response of building is assumed as reference. In addition, this study emphasized that shear wave velocity estimated by seismic interferometry approach is useful to evaluate current situation of building. Rodgers and Celebi [23] investigated the response of the 13-story steel building in Los Angeles under the earthquakes that have been recorded since 1971. Changes in modal frequencies of structure have been checked and wave analysis has been performed to control the damage that may occur after earthquakes. Todorovska and Trifunac [24-27] detected damages on six-story reinforced building exposed to the 1979 Imperial Valley earthquake by using different methods. Moaveni *et al.* [28] created finite element model of seven-story structure tested on shake table and updated the model by altering elasticity modulus of shear wall to identify numerically designated damage. Bodin *et al.* [29] investigated effects of three earthquakes to the eight-story steel structure. Dynamic response analysis of the structure presented that frequencies of fundamental modes reduced approximately 45% after earthquakes. However, analysis of ambient vibration records collected after earthquakes indicated that there was a recovery period for E-W direction. On the other hand, natural frequencies of N-S direction remained below those before earthquakes due to permanent damage. Saito *et al.* [30] examined effects of earthquakes in Japan on high-rise buildings located in different cities. According to identification results, first mode frequencies of reinforced concrete structures decreased by 20% and the first mode damping ratio increased by 3% due to the cracks in structural elements. Ebrahimian *et al.* [31] modelled Millikan Library with Timoshenko Beam and validated model by analyzing vibration records of building under Yorba Linda earthquake with seismic interferometry. Results showed that simulated shear wave velocity for Timoshenko Beam model is greater than measured shear wave velocity. Therefore, it was concluded that Timoshenko Beam approach is more appropriate for structures with low fundamental frequencies such as reinforced concrete buildings with shear walls. Celebi *et al.* [32] analyzed dynamic properties of tall buildings before, during and after severe earthquakes. Identification results clearly showed that modal frequencies decreased during main shock event compared to those computed before earthquake. Researchers asserted that permanent non-linearity resulted

in higher fundamental modal period and damping ratio after events than expected for some tall buildings. In addition to that, soil-structure interaction, rocking motion and low damping ratio are significant effects causing prolonged shaking for some tall buildings according to researchers. Abazarsa *et al.* [33] proposed new system identification technique to reliably determine mode shapes of structures from non-stationary vibration response during earthquakes. After verification and validation of proposed model, results obtained from shake table test and finite element model updated based on identification results were compared. Astorga *et al.* [34] proposed robust correlation between variation of natural frequencies and inter-story drift ratios. It provides useful and unique way to quantify structural damages after severe ground motions. For this purpose, researchers analyzed dynamic responses of 24 buildings in Japan under strong earthquakes. Gharari *et al.* [35] improved blind modal identification technique to identify dynamic properties of the structure during seismic excitation. In order to reliably identify complex mode shape, improved technique combines generalized eigen-decomposition and rough–fuzzy c-means clustering techniques. Kashima [36] investigated dynamic properties of four high-rise steel structures suffered from Tohoku Earthquake in Japan to understand effects of severe earthquakes on the structures as well as to observe which effects change dynamic properties of the structures with time. For this purpose, correlation between response amplitude and natural periods were established by using regression analysis in order to effectively evaluate variation in natural periods of structures. Taciroglu *et al.* [37] proposed new method to predict soil-foundation stiffness of structure under ground motion. In this method, Timoshenko beam considering soil properties with springs is updated based on identified results. The proposed method is validated by using vibration record of Millikan Library under 2002 Yorba Linda earthquake. Shirzad *et al.* [38] developed new method to identify soil-foundation stiffness from recorded seismic response. For this method, mathematical Timoshenko beam model considering soil properties with springs is created and Baseyian method is utilized to identify dynamic properties of model.

Recently, important studies about estimation of non-instrumented floor responses from instrumented floors have increased. Miranda and Taghavi [39] developed simpli-

fied mathematical model with combination of shear and flexural beams to predict dynamic response of structures under earthquakes. Also, it was concluded that effect of non-uniform stiffness distribution is limited on response of buildings that behave like flexural beam. Taghavi and Miranda [40] quantified accuracy of developed method by comparing exact and approximate results. Goel [41] compared piece-wise cubic interpolation technique and mode-based interpolation technique for estimation of non-instrumented floor responses by using recorded dynamic responses of two buildings under Northridge Earthquake. It was concluded that accelerometers should be located at points where mechanical properties of structures change to obtain more reliable results from piece-wise cubic interpolation technique. On the other hand, mode-based method gives more accurate results than piece-wise cubic interpolation technique and effects of senor location were limited. The most important disadvantage of mode-based method is that modal parameters must be obtained from previously created computer model or mathematical model. Kaya *et al.* [42] developed mode shape-based method to estimate responses of non-instrumented floors from instrumented floors for buildings. This method uses linear combination of shear and flexural beams with least square algorithm. Also, mode shape-based method is compared with linear and cubic interpolation approaches and predicted responses of non-instrumented floors better than other two methods. Limongelli [43] used cubic interpolation method to estimate responses of non-instrumented floors from instrumented floors for three different buildings. In addition, parametric studies were conducted to determine the most accurate sensor locations for buildings. Limongelli suggested that if a single sensor is used to monitor responses of structures, it would be appropriate to place it at intermediate floor. Besides, Limongelli [44, 45] used cubic interpolation method to detect structural damages with probabilistic approach by calculating frequency response functions of instrumented floors. Acunzo *et al.* [46] proposed new approach for mathematical models of structures by using virtual sensors to predict responses of non-instrumented floor from instrumented floors. Mathematical models created by this method were validated with vibration records of real building under various earthquake records. Hoult [47] developed simple mathematical model of structures based on modal parameters to estimate inter-story drift ratio along the entire structure with minimal instrumentation.

Proposed method was used for damage assessment of 20-story building. Differences between simulated and measured responses were encountered due to assumed damping ratio. Also, it was concluded that suggested method may be insufficient to estimate responses of non-instrumented floors for buildings show nonlinear behavior under severe earthquake and have geometric irregularity.

Considering relevant studies in literature, important studies have been carried out on vibration-based structural health monitoring of tall buildings and understanding dynamic behavior of tall buildings under severe earthquakes. In addition, some researchers focused on determination of building functionality by using different damage indicators such as changes in dynamic properties, maximum inter-story drift ratios and wave propagation speeds. However, limited number of sensors is generally preferred for monitoring of structures which is not appropriate to estimate inter-story drift ratios and wave propagation profiles accurately. This study proposes a new approach for condition assessment of structures which uses changes in dynamic properties and maximum inter-story drift ratio as damage indicators together. In addition, correlation between these parameters and structural deformations was created for reliable assessment. For this purpose, detailed FEM of a representative tall building was created to perform necessary simulations. Afterwards, relation between damage indicators and deformation of coupling beams was created to determine threshold values for reliable condition assessment. The main reason of using deformation of coupling beams is that changes in stiffness and integrity of coupling beams due to damage directly influence dynamic properties and inter-story drift ratios of structures.

2. FINITE ELEMENT MODEL OF TALL BUILDING

In this study, it was aimed to create a robust correlation between deformations of structural elements and inter-story drift ratios and also changes in dynamic properties of structures because inter-story drift ratios during an earthquake and dynamic properties of structures can be obtained by SHM systems. Therefore, a tall building was modelled in OpenSees in order to perform necessary simulations according to Turkish Building Seismic Code (TBSC) [48].

Modelling of the tall building was performed in three stages with different approaches and performance levels. Detailed information about modelling stages of the tall building is presented in Table 2.1.

Table 2.1. Modelling stages of tall building.

Stage	**Approach**	**Ground Motion Level**	**Performance Level**
I	Strength-Based	Design Level Earthquake	Life Safety
II	Strength-Based	Service Level Earthquake	Operational
III	Deformation-Based	Maximum Considered Earthquake	Collapse Prevention

Firstly, the tall building was analyzed in OpenSees [1, 2] under Design Level Earthquake and Service Level Earthquake and modelled with Strength-Based Approach in order to satisfy Life Safety and Operational performance levels, respectively. Structure was divided into six different sections and all structural members were modelled with elastic frame and shell elements in OpenSees. Boundary condition of FEM was assumed as fixed and foundation model was neglected for the sake of simplicity. Material properties used in modelling process are given in Table 2.2. Also, gravity loads defined according to the seismic code are shown in Table 2.3.

Table 2.2. Material properties.

Material	**Type**	**Mechanical Properties**
Concrete	C50	$\mathrm{E}_{init} = 5000\sqrt{f_{ck}} = 35355.34$ MPa $\mathrm{E}_{secant} = 22(f_{ck}/10)^{0.3} = 35654.40$ MPa $\mathrm{f}_{cd} = f_{ck}/1.5, f_{ce} = 1.3f_{ck}$
Steel	S420	E=200 GPa $\mathrm{f}_{yk} = 420$ MPa $\mathrm{f}_{yd} = f_{yk}/1.15, f_{ye} = 1.2f_{yk}$

Table 2.3. Gravity loads.

Dead Loads		**Live Loads**	
Self-weight of concrete	25.0 kN/m^3	Residential floors	2.0 kN/m^2
Celling plaster+Floor finishing+Installments	2.0kN/m^2	Basement floors	5.0 kN/m^2
Infill walls for residential floors	1.0kN/m^2	Snow load (roof)	1.0 kN/m^2
Landscape (ground floor)	5.0kN/m^2	Garden (ground) floor	3.5 kN/m^2

Load combinations were determined according to the seismic code and the standards. Load combinations considering both horizontal and vertical components of ground motions are expressed as

$$G + Q + 0.2S + E_e^H + 0.3E_e^Z, \tag{2.1}$$

$$0.9G + H + E_e^H - 0.3E_e^Z, \tag{2.2}$$

where horizontal seismic loads are defined as

$$E_e^H = \pm E_e^X \pm 0.3E_e^Y, \tag{2.3}$$

$$E_e^H = \pm 0.3E_e^X \pm E_e^Y, \tag{2.4}$$

and vertical component of ground motion is included with simplified approach as

$$E_e^Z = (2/3)(S_{DS})G, \tag{2.5}$$

where G is dead load of the structure. Additionally, S is snow load and H is lateral soil pressure on basement walls. For the sake of simplicity, H was assumed 0.

Effective stiffness multipliers for stage I and stage II were defined according to TBSC and represented in Table 2.4. Also, total mass during earthquake was defined according to the seismic code. While no coefficient was used for dead loads, live loads were scaled by 0.3.

Table 2.4. Effective stiffness multipliers for design stages.

	Modelling Stages			
	I	**II**	**I**	**II**
Walls-Slab (In-Plane)	**Axial**		**Shear**	
Structural Walls	0.50	0.75	0.50	1.00
Basement Walls	0.80	1.00	0.50	1.00
Slabs	0.25	0.50	0.25	0.80
Walls - Slab (Out of Plane)	**Bending**		**Shear**	
Structural Walls	0.25	1.00	1.00	1.00
Basement Walls	0.50	1.00	1.00	1.00
Slabs	0.25	0.50	1.00	1.00
Frame Elements	**Bending**		**Shear**	
Coupling Beams	0.15	0.30	1.00	1.00
Moment Frame Beams	0.35	0.70	1.00	1.00
Moment Frame Columns	0.70	0.90	1.00	1.00
Structural Walls (Equivalent frame)	0.50	0.80	0.50	1.00

Dynamic loads were defined for Design Level Earthquake and Service Level Earthquake according to the seismic code and were represented in Figure 2.1. Detailed information about definition of elastic spectra is given in Ground Motion Selection section. Structural system behavior factors (R) in X and Y directions were determined 8 and 7, respectively according to the seismic code. Dynamic loads were reduced based on these values for stage I. On the other hand, R was assumed as 1 for stage II for each direction.

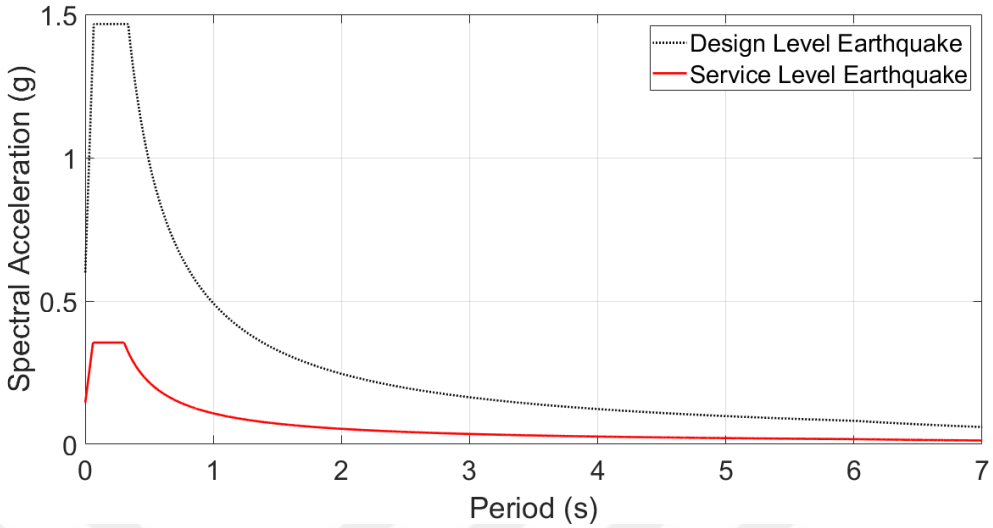

Figure 2.1. Elastic spectra.

After linear seismic analyses, dimensions of structural elements were determined according to inter-story drift ratios and demand/capacity ratios of ductile and brittle structural members. Dimensions and reinforcement details of insufficient members were updated to satisfy limits in the seismic code. Figure 2.2 represents dimension of structural members and 3D geometry of tall building.

Dimension of Structural Members

	Grp A	Grp B	Grp C	Grp D	Grp E	Grp F
Basement Columns	100	N/A				
Perimeter Columns	160	140	120	100	80	70
Interior Columns	180	170	150	130	110	90
Basement Walls	50	N/A				
Perimeter Beams	N/A	50X70				
Secondary Beams	40X60					
Coupling Beams	50X80					
Structural Walls	100	100	90	80	70	60
Tower Slab	N/A	30				
Transfer Slab	50	N/A				
Basement Slab	35	N/A				
Core Wall Slab	15					
Story Height	320					

All columns are square.

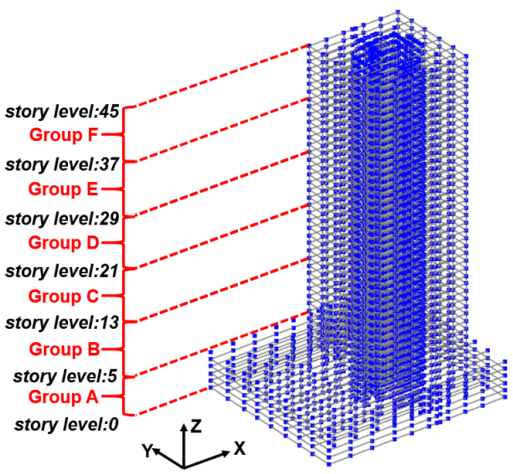

Figure 2.2. Dimension of structural members and 3D geometry of the tall building.

Nonlinear analysis has started to be used more widely thanks to development of computer technology and many studies improved modelling methods of structures. Nonlinear analysis more accurately estimates demand of external loads under dynamic loads because there are limited assumptions compared to linear modelling. In literature, many techniques have been developed for nonlinear modelling of structural members. Figure 2.3 shows the most significant nonlinear modelling methods of structural members. These modelling techniques generally aimed to consider material-induced nonlinear behavior of structural members. Concentrated plasticity modelling methods is preferred to simply reflect nonlinear behavior of structural elements. The main advantage of this modelling technique is short analysis time. On the other hand, distributed plasticity modelling methods need more detail study on structural members. Nonlinear concrete and steel reinforcement material models must be precisely defined to estimate realistic global nonlinear behavior of structure. The main disadvantage of this modelling technique is long analysis time.

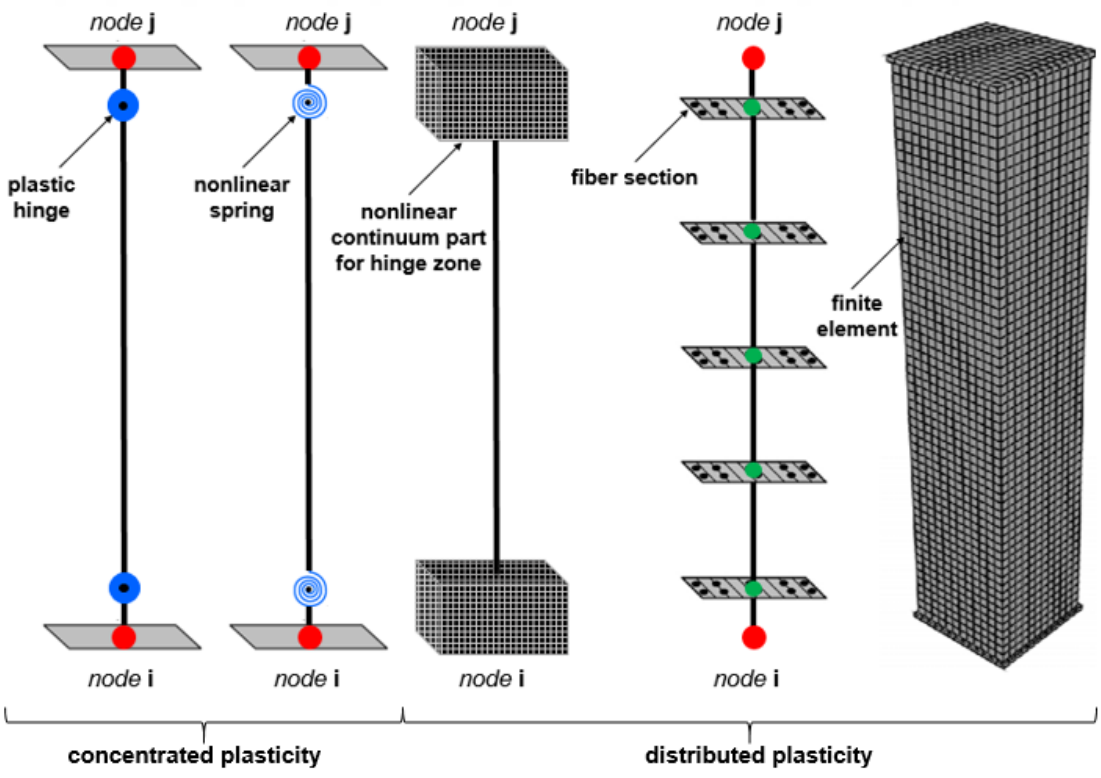

Figure 2.3. Nonlinear modelling methods of structural members [49].

Finally, nonlinear FEM of tall building was modelled to conduct time history analyses under Maximum Considered Earthquake ground motion level in OpenSees. Since some of commercial earthquake engineering programs do not provide stiffness matrix during and after analysis, it is not possible to control changes in dynamic properties of structural model. On the other hand, since OpenSees enables to control mass, damping and stiffness matrices after each analysis step, dynamic properties of structure can be followed.

In the following sections, modelling approaches of structural elements in FEM is explained in detail.

2.1. Modelling of Frame Elements

Frame elements (columns and beams) of the tall building were modelled with fiber sections. Displacement-based element and force-based element are two different modelling types of fiber elements in OpenSees. There are important studies comparing nonlinear behavior of structural models created by using these two different element types [50-52].

Displacement-based element assumes linear curvature distribution and constant axial strain along element. Therefore, multiple elements per story are needed for each element in order to accurately calculate inelastic behavior of sections. On the other hand, force-based element assumes constant axial and shear force between nodes of element. Also, moments of integration sections between nodes are estimated with linear distribution. Therefore, it is possible to accurately capture inelastic behavior of sections satisfying compatibility equations by using single element with appropriate number of integration section. Figure 2.4 shows fundamental modelling principles of displacement-based element and force-based element. In this study, displacement-based element was utilized to create fiber sections of frame elements.

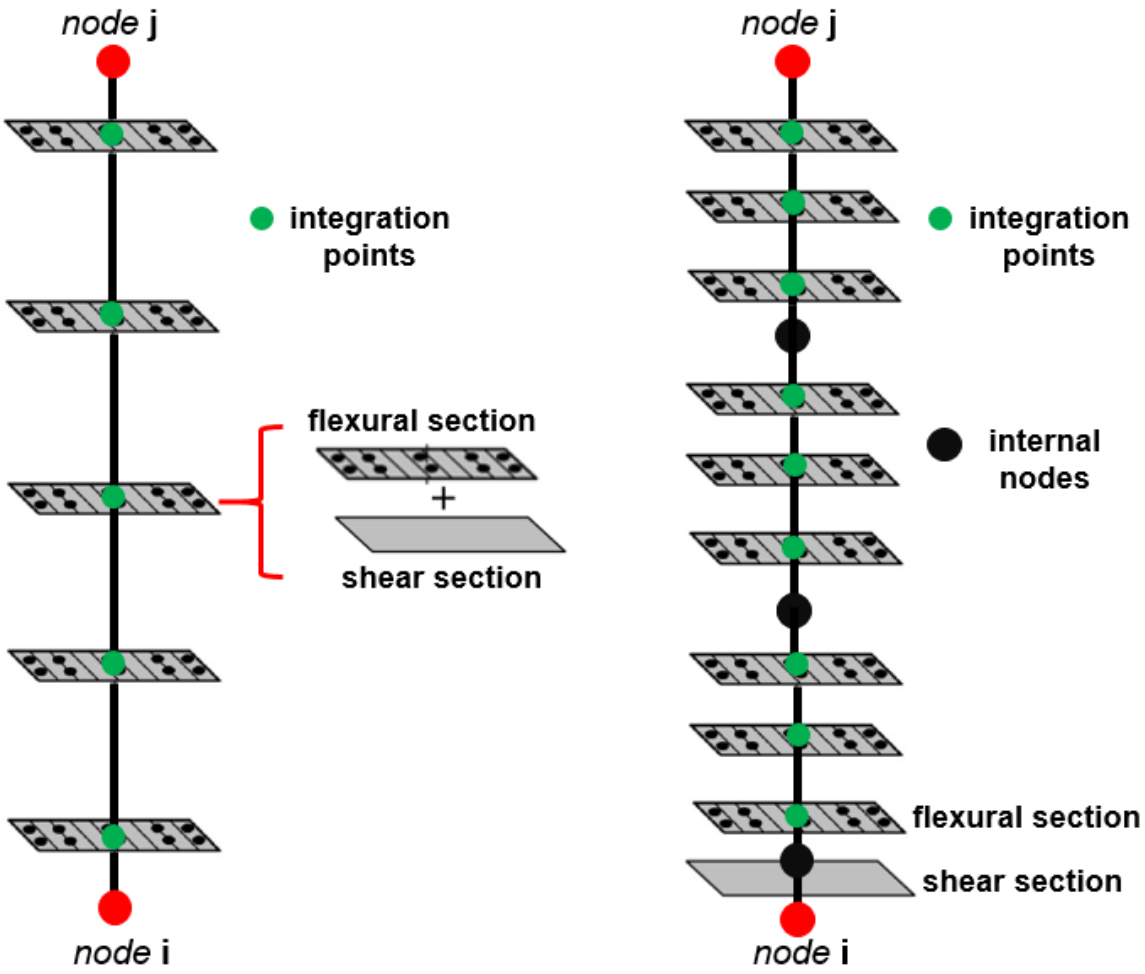

Figure 2.4. Modelling principles of displacement-based element and force-based element.

Fiber sections for displacement-based frame elements were constructed by a four-node quad element object. This element uses a bilinear isoperimetric formulation to create fiber sections. Confined and unconfined concrete material models were defined with uniaxial Kent-Scott-Park concrete material model (Concrete01). This material type uses cyclic degradation parameters based on Karsan-Jirsa loading-unloading procedure. Reinforcement steel material was modelled by uniaxial Giuffre-Menegotto-Pinto steel material object (Steel02) [53, 54]. This material type considers kinematic hardening and isotropic hardening for nonlinear behavior. Figure 2.5 and Figure 2.6 represent concrete and reinforcement steel material models used in FEM, respectively.

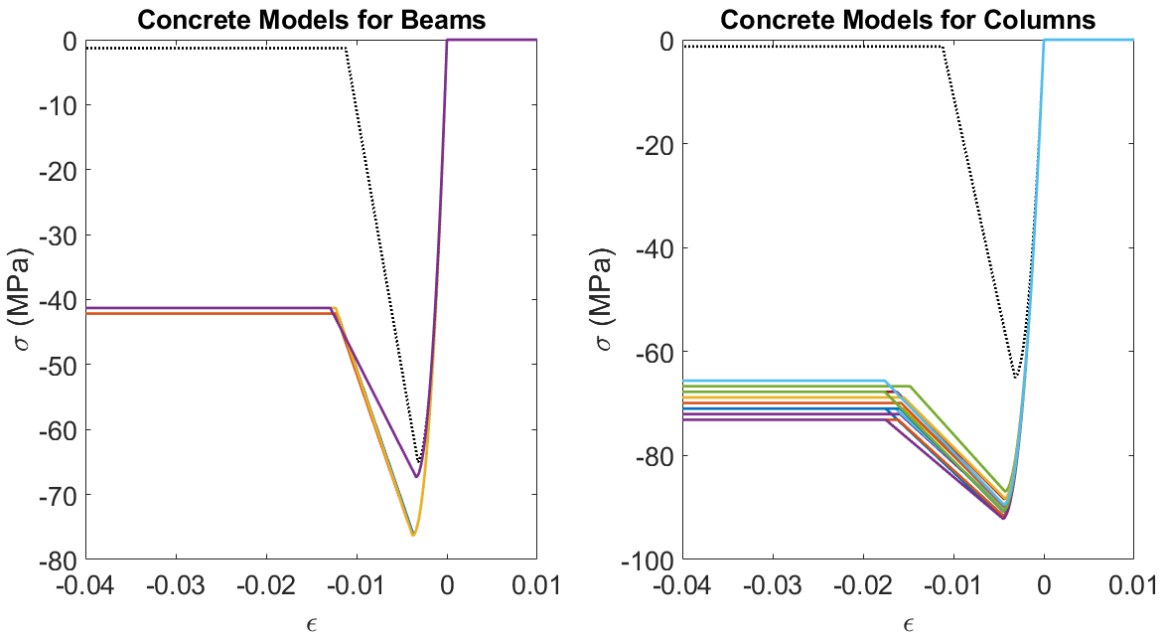

Figure 2.5. Concrete material model in finite element model.

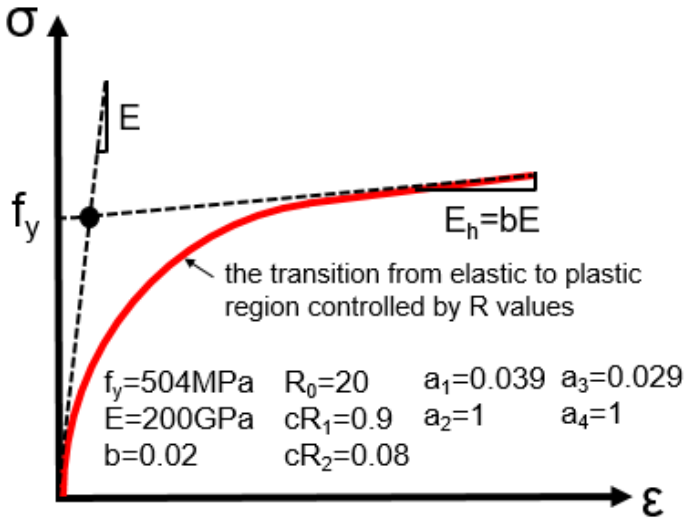

Figure 2.6. Reinforcement steel material model in finite element model.

2.2. Modelling of Coupling Beams

Coupling beams are the most critical structural members for tall buildings due to fact that significant portion of inelastic energy is dissipated by them during earthquakes. Therefore, proper modelling of coupling beams increases reliability of analysis results. There are two different options for modelling of coupling beams in literature. While one of them uses moment-rotation hinges at the end zones of beams, other one uses shear force-displacement hinge at the mid-span of beam.

In this study, coupling beams were modelled by using two-node link element option in OpenSees with nonlinear shear force-displacement spring at mid-span of section [55]. In addition, elastic behaviors were assumed with constant stiffness for axial force-displacement and flexural moment-rotation springs.

There are many options for modelling nonlinear behavior of shear force-displacement springs in literature [56, 57]. In this study, hysteretic behavior of nonlinear shear force-displacement springs was defined by uniaxial Giuffre-Menegotto-Pinto material model (Steel02) [53, 54]. With this material model, it is aimed to define nonlinear behavior that is very close to elastic perfectly behavior and takes into account cyclic degradation [58, 59]. Therefore, parameter values used in material model of coupling beams to define cyclic degradation were assumed from studies in literature [57]. Figure 7 represents simple visualization and mechanical properties of two-node link element used for coupling beams.

2.3. Modelling of Structural Walls

In tall buildings, it is mandatory to use structural walls in order to reduce inter-story drifts. The combination of structural walls and frames (beams and columns) creates more ductile systems to withstand external loads. Structural walls are forced to deform under bending moments at generally upper floors. On the other hand, lateral displacements in frames are observed at lower floors due to high shear force. Therefore,

large amount of load due to bending is resisted by frames at upper part of building and large amount of shear forces is resisted by structural walls at lower part of building.

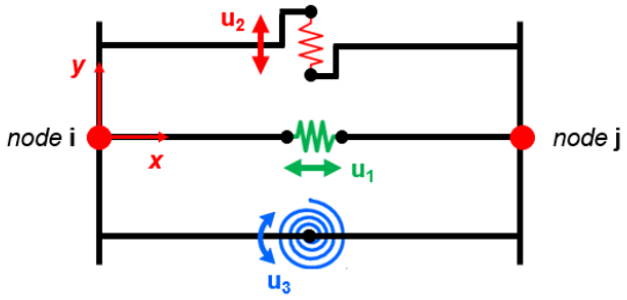

u_1:axial u_2:shear u_3:flexural

Elastic axial spring stiffness (K_a)	EA/L
Elastic flexural spring stiffness (K_f)	EI/L
Nonlinear shear spring elastic stiffness (K_s)	$(12EI/L^3)+(GA/L)$
Nonlinear shear spring yield force (V_y)	$2A_{sd}f_{ye}\sin\gamma$
Parameters to control the transition from elastic to plastic branches	R_0=18.5, cR_1=0.9, cR_2=0.1
Ratio between post-yield tangent and initial elastic tangent	b=0.003
Isotropic hardening parameter	$a_1=a_1$=0.14, $a_2=a_4$=1.0
E is modulus of elasticity, A is area of cross section, I is moment of inertia of cracked section, L is length of beam, A_{sd} is reinforcement area, f_{ye} is reinforcement yield strength, γ is angle between beam and diagonal reinforcement.	

Figure 2.7. Two-node link element and mechanical properties for coupling beams in finite element model.

There are several methods to create finite element model of structural walls in OpenSees. One of them is to create fiber sections by using displacement-based element or force-based element between nodes. Appropriate geometry of FEM can be obtained by connecting structural walls modelled by fiber sections to frames with rigid elements such as rigid beams or rigid bars. However, main disadvantages of models developed in this way are long analysis time and convergence problems. [56], [60-62]. Second option is to use multiple-vertical-line-element-model (MVLEM) [63, 64]. This element model is calibrated and validated by experiments and reasonably estimates axial-flexural behavior of structural walls. However, this model does not consider contribution of shear behavior to flexural behavior. On the other hand, subsequently developed element model

which is shear-flexure interaction multiple-vertical-line-element-model (SFI-MVLEM) is capable to take into account interaction between shear and axial-flexural for non-linear behavior of structural walls [65-67]. The disadvantage of these two wall models is that they can be utilized only for 2D finite element models. The most preferred element model to create nonlinear structural walls for FEM in OpenSees is multi-layer shell element because it does not increase analysis time and does not cause significant convergence problems [57], [68]. This element model consists of nonlinear concrete layer and nonlinear smeared rebar layers (Figure 2.8). This element model was preferred to simulate response of nonlinear structural walls in different tall building FEMs [69-71]. In this study, multi-layer shell element was preferred to create nonlinear structural walls for FEM. The main reasons is that it provides fast convergence during analysis of FEM by considering nonlinear behavior of concrete under cracking and crushing and nonlinear behavior of steel reinforcement by taking into account Bauschinger effect. Five internal nodes were used at each story for modelling of multi-layer shell elements in order to properly simulate nonlinear response of structural walls.

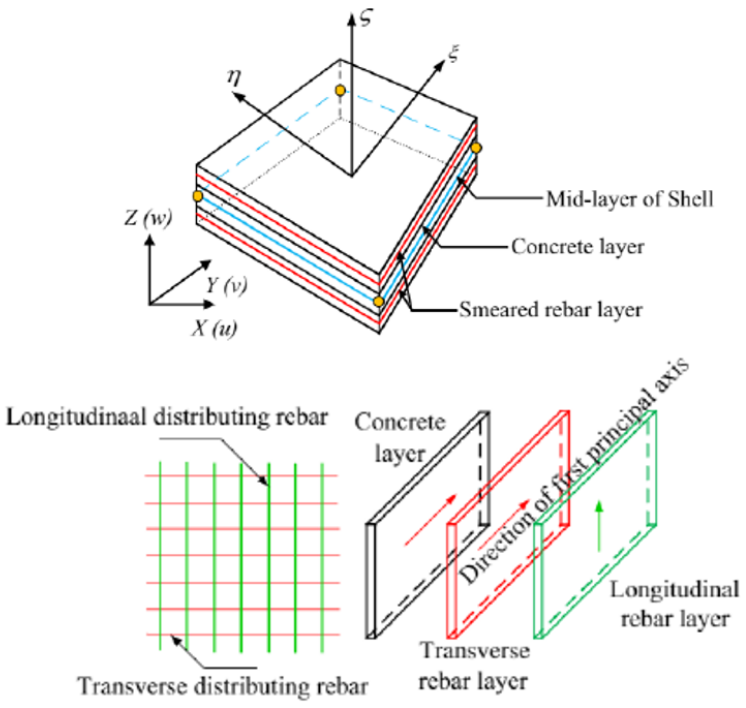

Figure 2.8. Mechanism of multi-layer shell element [69].

2.4. Modelling of Basement Walls

Basement walls around structures are load-bearing structural elements that transfer most of inertial forces formed in upper floors onto foundation and also resist forces and moments created by ground motions. Therefore, it is assumed that perimeter basement walls show completely elastic behavior under ground motions and does not pass into plastic range. In this study, perimeter basement walls were modelled by using elastic shell elements (ShellMITC4).

2.5. Modelling of Slabs and Floor Diaphragm Consideration

In nonlinear analyses, realistic representation of in-plane behavior of floor diaphragms is important since transfer of inertial forces at story levels is controlled by diaphragm behavior. Due to limitations on available modeling options in current software for nonlinear modeling of slab behavior, floor diaphragms are modeled with either elastic shell elements or employing rigid diaphragm assumptions.

In most cases, rigid diaphragm assumption is preferred since including elastic slab elements in nonlinear model increases both modeling and computational effort. However, rigid diaphragm assumption is not appropriate and may lead to unreasonable lateral load distribution among vertical members in structures with torsional irregularities and diaphragm discontinuities. Also, rigid diaphragm assumption is not appropriate at transfer floors due to backstay effects that may develop where shear forces are transferred from vertical elements in tower to rigid basement walls around perimeter of basement. Modeling in-plane diaphragm behavior as rigid diaphragm overestimates backstay effects and may result in unrealistically high shear force demands on tower walls in basement, due to reversal in direction of shear force of walls.

Even though force transfer due to backstay effects mainly develop at first transfer floor, diaphragms under first transfer floor may also contribute to transfer mechanism. Due to this reason, first two basement floor diaphragms were modeled with elastic

shell elements (ShellMITC4) in nonlinear FEM to consider possible redistribution of in-plane forces between diaphragms. Also, tower floors of structure were also modelled with elastic shell elements (ShellMITC4) to consider out-of-plane behavior of slabs.

2.6. Modelling of P-Δ Columns and Geometric Non-linearity

Geometric non-linearity (second order effects) due to combination of lateral displacement and vertical load must be considered to evaluate behavior of tall buildings under ground motions. It is a fact that second-order moments are so critical in tall buildings because these structures are more flexible and their structural elements carry more vertical load when compared to shorter structures. These effects amplify base shear force, story moments and axial loads on vertical structural members, so it is clear that contribution of geometric non-linearity must be considered in seismic analysis of tall buildings.

Therefore, P-Δ leaning column was modelled in order to consider second order effect during nonlinear time history analysis. In P-Δ leaning column method, elastic bar elements that can only resist axial loads are included in nonlinear model and story weight of each story is additionally loaded on these P-Δ columns. Story masses of elastic bars were calculated from $(G + nQ + (0.3(2/3)S_{DS}G)$. Young's modulus of elastic bars was assumed as initial stiffness value of expected concrete. Also, area of elastic bars was calculated from total cross-sectional area of columns and structural walls obtained from plan view of certain floor.

3. NONLINEAR TIME HISTORY ANALYSIS OF TALL BUILDING

Nonlinear time history analysis (NLTHA) of tall buildings is important to simulate and understand dynamic response of these structures under extreme ground motions. In order to perform NLTHA, ground motion records are selected and scaled according to target spectrum. In this chapter, ground motion selection and assessment of structural element deformations after NLTHA are explained in detail.

3.1. Ground Motion Selection

Ground motions are selected according to target spectrum which can be uniform hazard spectrum obtained from probabilistic or deterministic seismic hazard analysis. Deterministic seismic hazard analysis calculates level of ground motion created by the largest earthquake for specific region independent of time dimension. On the other hand, probabilistic seismic hazard analysis investigates probability of earthquake occurring for different return periods. Theoretically, seismic hazard curve obtained from deterministic or probabilistic seismic hazard analysis represents seismicity of specific region and gives valuable information about seismic demand resisted by structures. Alternatively, target spectrum can be design spectrum which is defined by seismic codes.

In this study, target spectrum was determined according to equations in TBSC. These equations use spectral acceleration values at short period and 1.0s period. Also, local soil conditions are considered with F_s and F_1 coefficients. The target spectrum was scaled with 1.3. This coefficient is intended to replace the spectral acceleration values obtained from the hazard map (which is the geometric mean of the two components) with the maximum resultant of the two components (maximum spectral acceleration in any horizontal direction). Figure 3.1 represents target spectrum, spectral acceleration values for different return periods and location of structure and North Anatolian Fault.

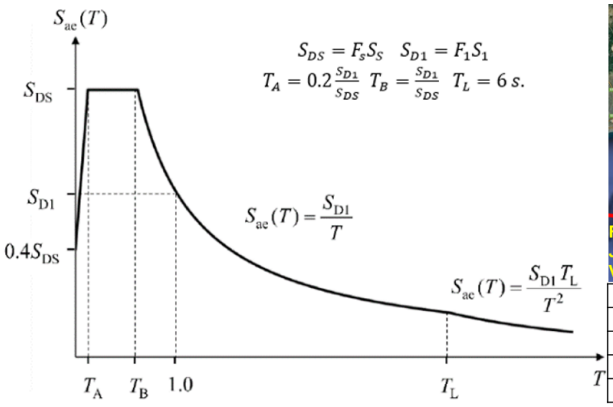

Definition of target spectrum according to TBSC

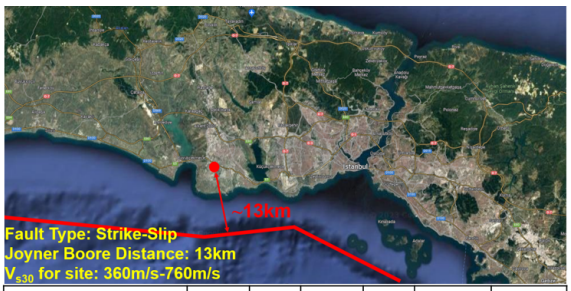

Return Period (Year)	S_s (g)	F_s	S_1 (g)	F_1	S_{DS} (g)	S_{D1} (g)
43	0.273	1.30	0.072	1.50	0.355	0.108
72	0.443	1.30	0.117	1.50	0.576	0.176
475	1.222	1.20	0.328	1.50	1.466	0.492
2475	2.122	1.20	0.584	1.42	2.546	0.827

Spectral acceleration values and site amplification factors

Figure 3.1. Target spectrum defined in TBSC, spectral acceleration values for different return periods and location of structure and North Anatolian Fault.

Ground motion records were selected from PEER NGA-WEST2 ground motion database. Magnitude and distance of selected ground motions should be reasonable for the structure and the fault location. For this, the most appropriate method is to choose magnitude and distance pair estimated from dis-aggregation analysis. In dis-aggregation analysis, magnitude and distance pair which has large amount of contribution to seismic risk of specific region is obtained after seismic hazard analysis.

Selected ground motion records were scaled by using amplitude scaling method. In this method, firstly square root of sum of squares (SRSS) of response spectra (X and Y directions) of each ground motion record was calculated in order to determine average resultant response spectrum. Finally, scale factor of each ground motion record were determined so that geometric mean of average resultant response spectra stays above target spectrum between 0.2T and 1.5T (T: fundamental period of structure).

In selection and scaling of ground motion records, it is aimed to limit scale factors of ground motion records to 5, but it is difficult to find ground motion records for determined fault properties, magnitude, distance and V_{s30} ranges. Therefore, some scale factors turned out to be greater than 5. In addition, lowest usable frequencies of selected ground motion records are compatible with fundamental period of structure.

Due to nature of ground motion selection, there is scattering between response spectra of selected ground motions. Therefore, it is aimed that response spectra of selected ground motions stay between mean$\pm 1\sigma$. Table 3.1 represents selected ground motion records. Response spectrum of each earthquake, average response spectrum of all earthquakes and target spectrum were also shown in Figure 3.2. Also, unscaled ground motion records were represented in Figure 3.3.

Table 3.1. Selected ground motion records and scale factors.

ID	**Ground Motion**	**Magnitude**	**Rjb (km)**	**Vs30 (m/s)**	**Lowest Usable Frequency (Hz)**	**Sampling Rate (s)**	**Scale Factor (2475 Year Return Period)**
178	Imperial Valley	6.53	10.79	162.94	0.063	0.005	2.54
549	Chalfant Valley	6.19	14.38	303.47	0.125	0.005	4.73
879	Landers	7.28	2.19	1369.00	0.000	0.005	1.51
1115	Kobe	6.90	28.08	256.00	0.125	0.010	4.12
1165	Kocaeli	7.51	3.62	811.00	0.125	0.005	3.20
1615	Duzce	7.14	9.14	338.00	0.063	0.010	7.64
1633	Manjil	7.37	12.55	723.95	0.130	0.020	1.94
1794	Hector Mine	7.13	31.06	379.32	0.017	0.005	5.27
3954	Tottori	6.61	15.58	967.27	0.038	0.005	5.98
5836	El Mayor	7.20	28.53	264.57	0.100	0.005	2.77
6980	Darfield	7.00	72.50	484.49	0.038	0.005	5.38

3.2. Results of Nonlinear Time History Analysis

In this section, results of NLTHA performed under selected 11 ground motion records were presented. Scale factors of ground motion records were determined according to target spectrum for 2475 return period. However, analyses were performed for two additional coefficients to observe different damage levels. For this purpose, scale factors determined based on 2475 return period target spectrum were multiplied by 0.33 and 0.67 in order to simulate minor and moderate damage levels.

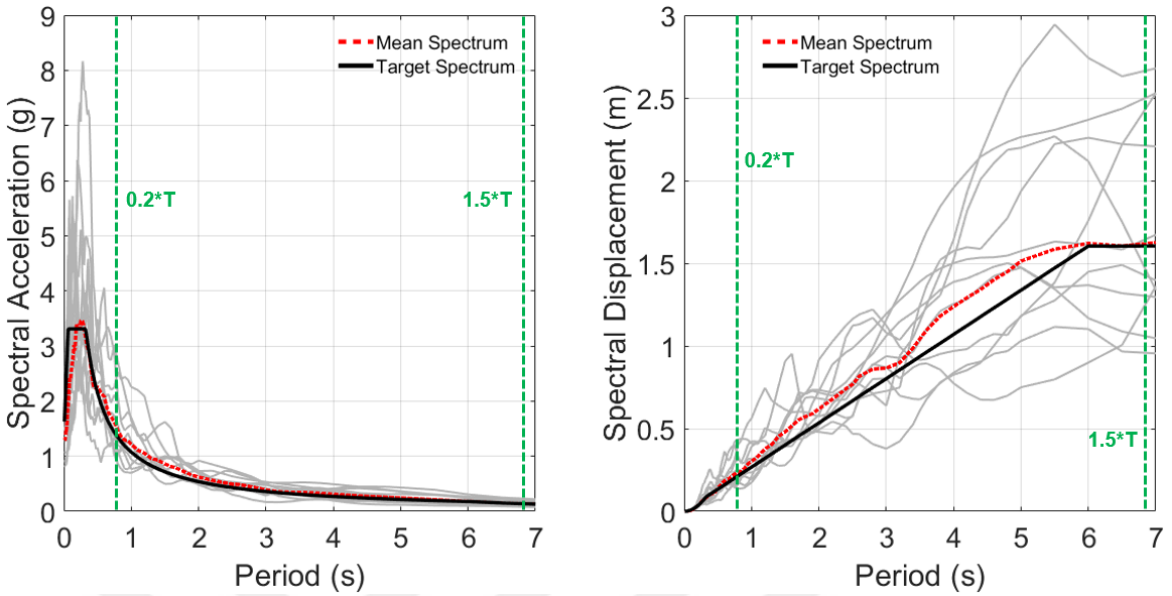

Figure 3.2. Response spectra of earthquakes, mean spectra and target spectra.

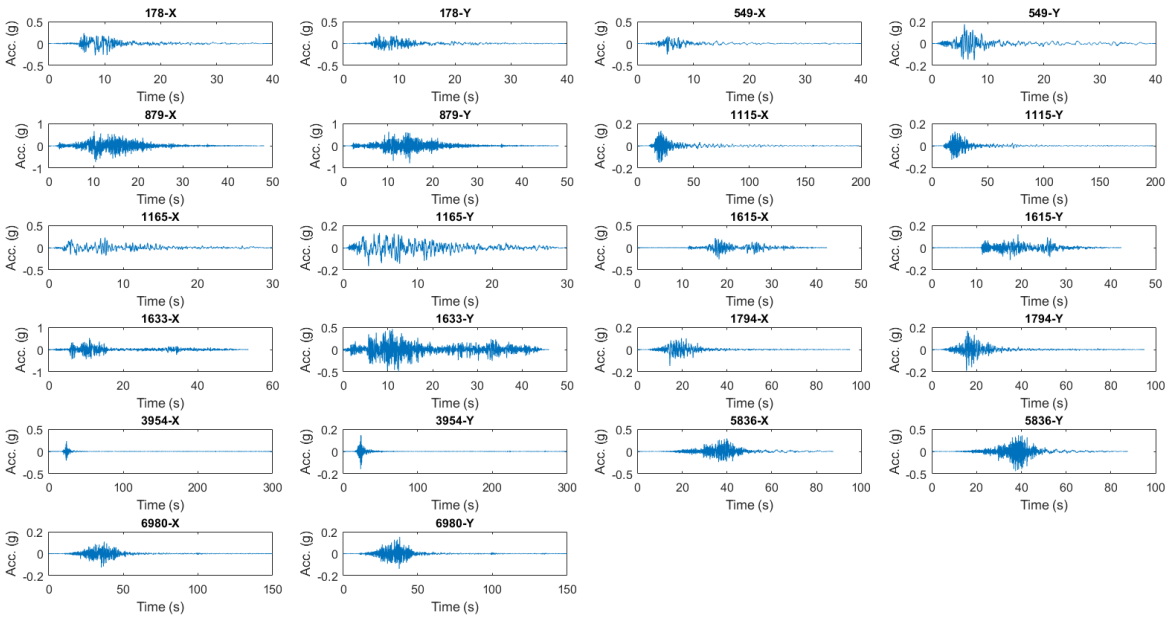

Figure 3.3. Time history graphs of ground motion records.

FEM of tall building does not have geometric irregularities. Also, structural members are positioned in symmetrical order. Therefore, it was not necessary to rotate

ground motions 90 degree and reanalyze them. In this study, ground motion records were applied in the horizontal direction and vertical ground motion records were not used in analyzes.

Work Station that has Intel(R) Xeon(R) W-2133 CPU @3.60 GHz processor with six cores and 128 GB RAM was used to complete 33 analyses. Six different analyses were performed simultaneously. Analysis time was long when compared to analysis time of standard tall building model. One of the most important reasons is that changes in dynamic properties of structure such as modal frequencies and mode shapes were controlled after each analysis step. Another important reason is that rigid diaphragms were not used in FEM, slabs were modelled by shell elements with appropriate meshing approaches. Also, zero-path (duration: $2[(T_x + T_y)/2]$) was added to end of ground motion records to observe damping effect to dynamic response of structure during free vibration.

Modal analysis results after nonlinear gravity load analysis were represented in Table 3.2. Accumulated mass factor up to 50th mode were obtained 0.968 for X direction and 0.972 for Y direction.

Rayleigh Damping was used to describe damping behavior of structure during analyses [72]. In this method, damping matrix is generated from mass and stiffness matrix with α and β coefficients ($\zeta = \alpha K + \beta M$). OpenSees introduces various options for stiffness matrix to define Rayleigh Damping based on studies in literature [73-75]. In this study, initial stiffness matrix was used to define Rayleigh Damping ratio and 2.5% damping ratio was assumed for all modes. In addition, nonlinear behavior of structural elements contribute to total damping ratio of structure during nonlinear analysis.

Analyses results showed that beams and columns remained in elastic region for Maximum Considered Earthquake (2475 return period) according to thresholds in the seismic code. Also, axial deformations of structural walls are below limits. Therefore,

there will be no additional discussions about structural parameters remaining in elastic region. Figure 3.4 shows labels and points for nonlinear analysis results presented in between Figure 3.5 - Figure 3.25. These figures show NLTHA results for:

- Shear forces and rotations of beams
- Shear forces and rotations of columns
- Inter-story drift ratios
- Shear forces of structural walls
- Chord rotations of coupling beams

Table 3.2. Modal analysis results.

Mode Number	**Period (s)**	**Mass X**	**Mass Y**	**$\sum$ Mass X**	**$\sum$ Mass Y**
1	4.60	1.42e-6	0.46	1.42e-6	0.46
2	4.15	0.48	1.13e-6	0.48	0.46
3	3.34	1.15e-6	8.41e-6	0.48	0.46
4	1.07	0.009	3.49e-4	0.48	0.46
5	1.01	0.127	6.37e-6	0.61	0.46
6	1.00	3.93e-6	0.149	0.61	0.61
7	0.49	2.31e-5	1.60e-5	0.61	0.61
8	0.47	0.057	4.64-7	0.67	0.61
9	0.41	2.71e-7	0.070	0.67	0.68
10	0.29	2.36e-5	1.48-5	0.67	0.68
11	0.27	0.046	2.59e-7	0.72	0.68
12	0.23	5.22e-8	0.057	0.72	0.74
.....	.....	.....	.....	.....	.....
49	0.05	0.006	9.56e-4	0.97	0.97
50	0.05	3.32e-4	3.36e-8	0.97	0.97

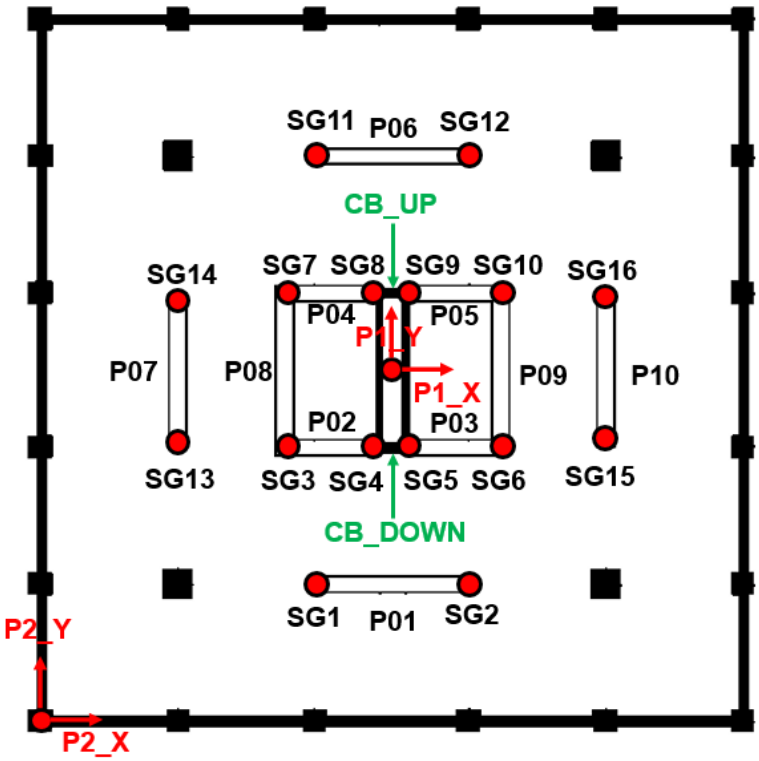

Figure 3.4. Labels and points for nonlinear time history analysis results.

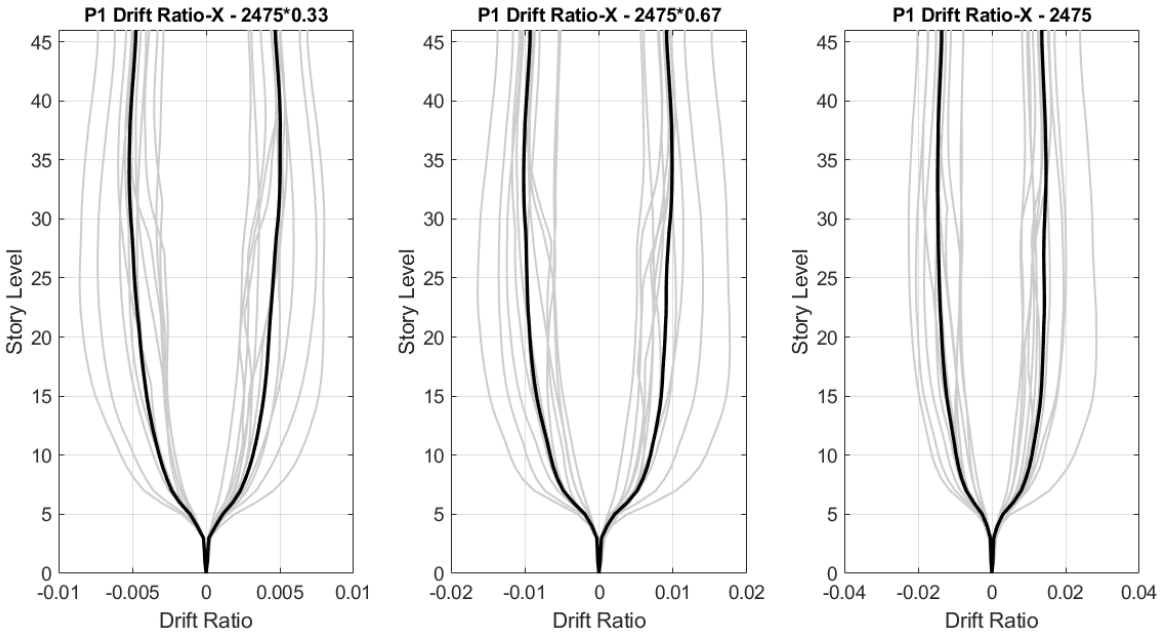

Figure 3.5. P1-X inter-story drift ratios.

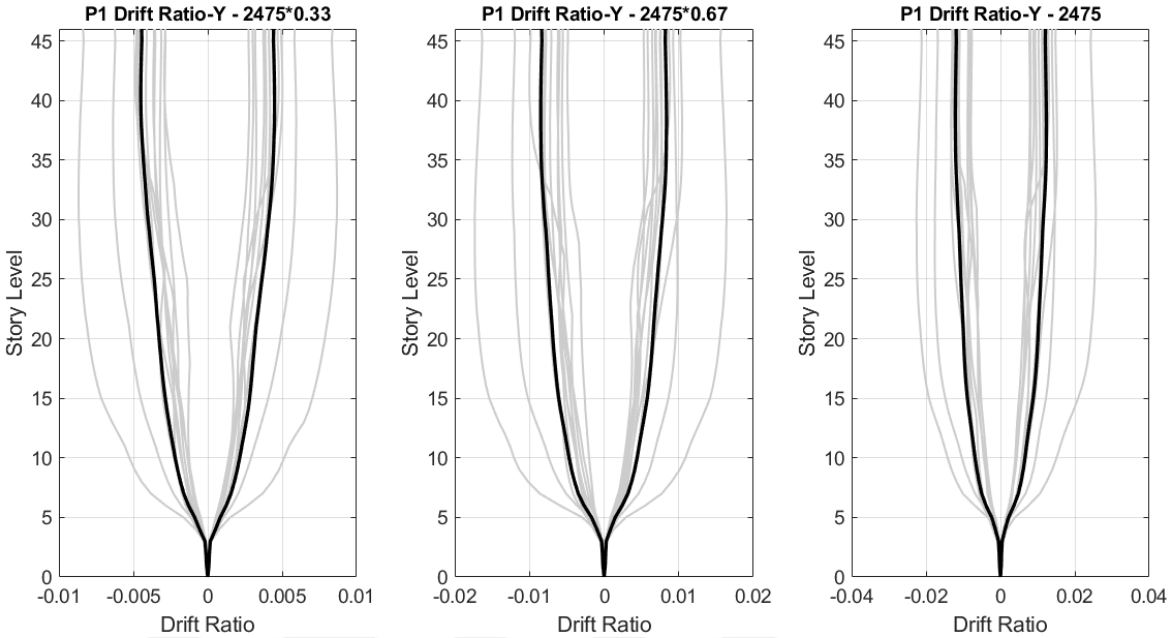

Figure 3.6. P1-Y inter-story drift ratios.

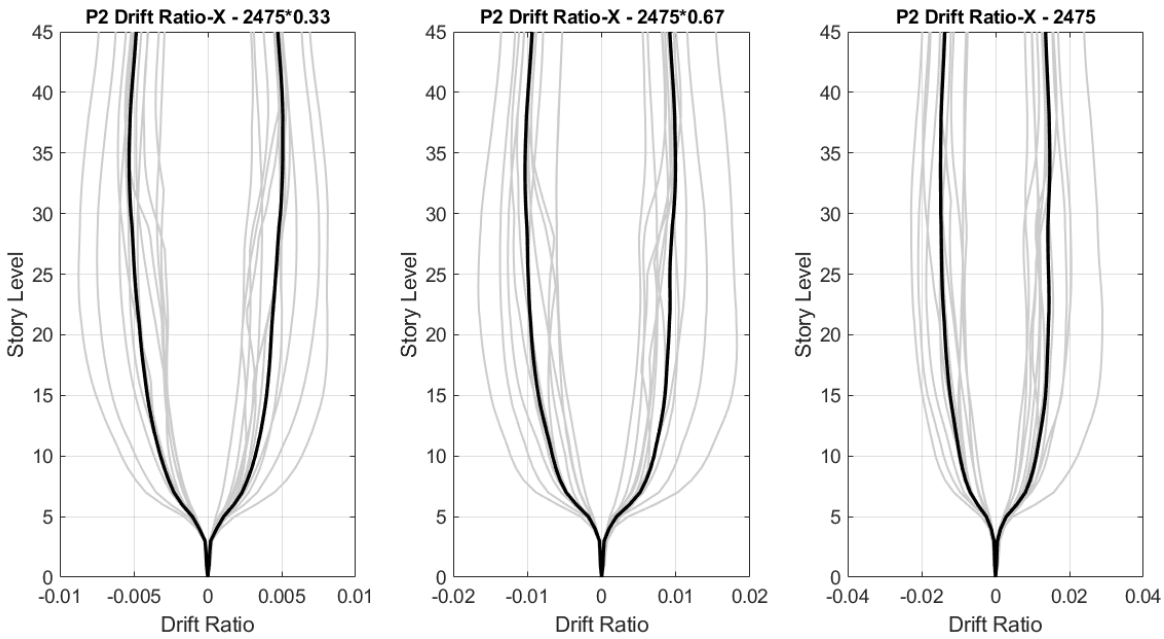

Figure 3.7. P2-X inter-story drift ratios.

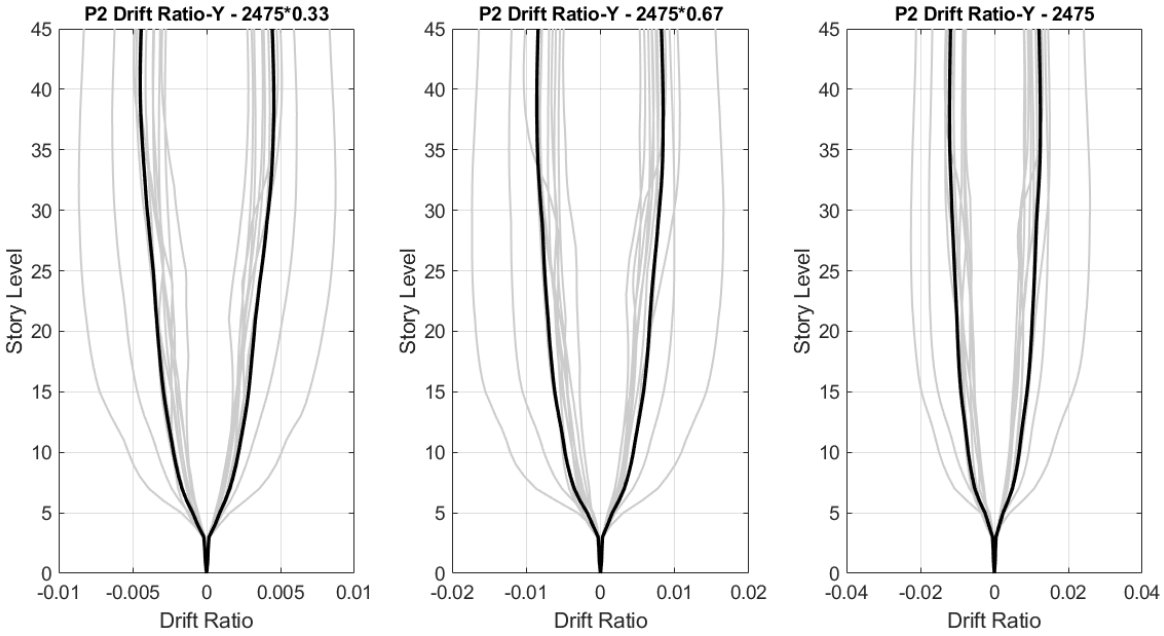

Figure 3.8. P2-Y inter-story drift ratios.

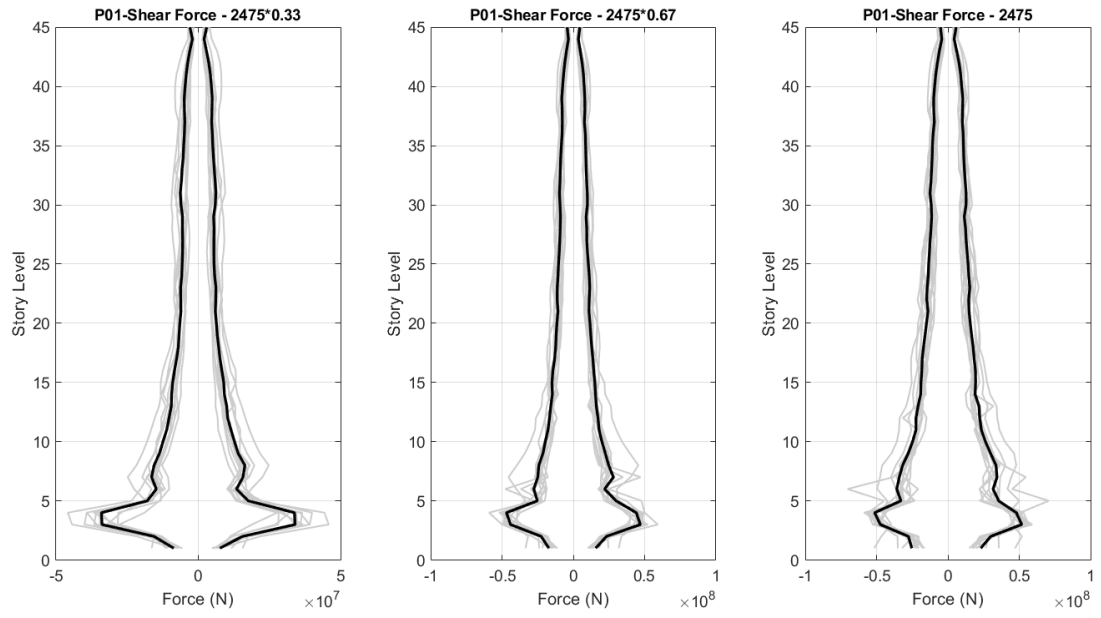

Figure 3.9. P01 shear forces.

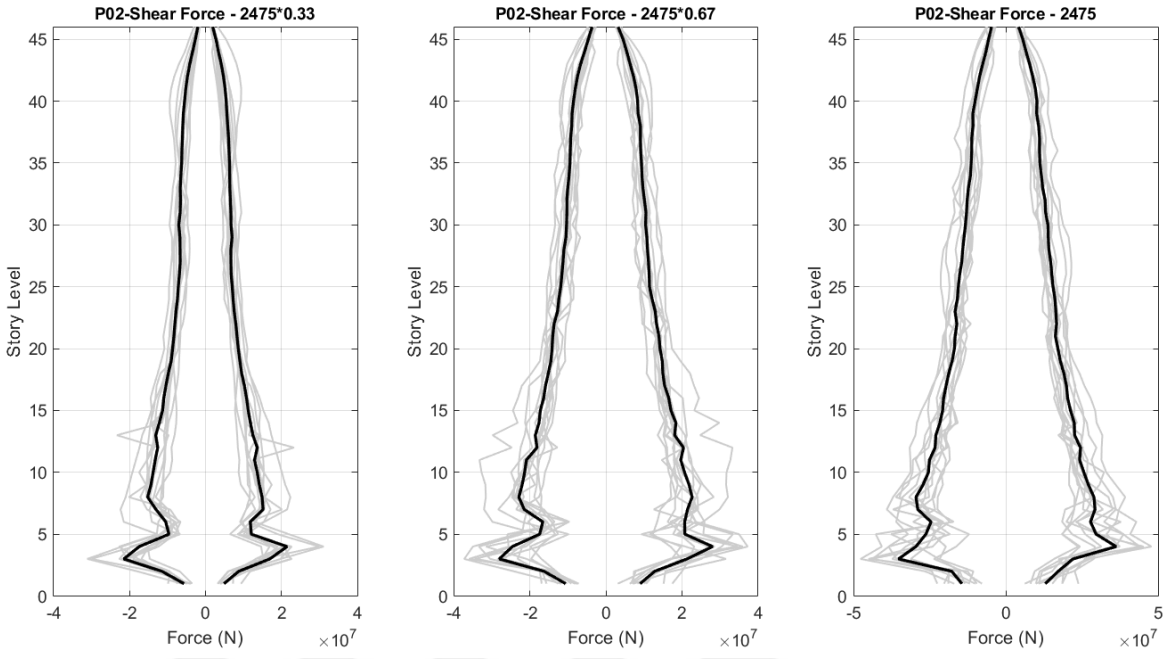

Figure 3.10. P02 shear forces.

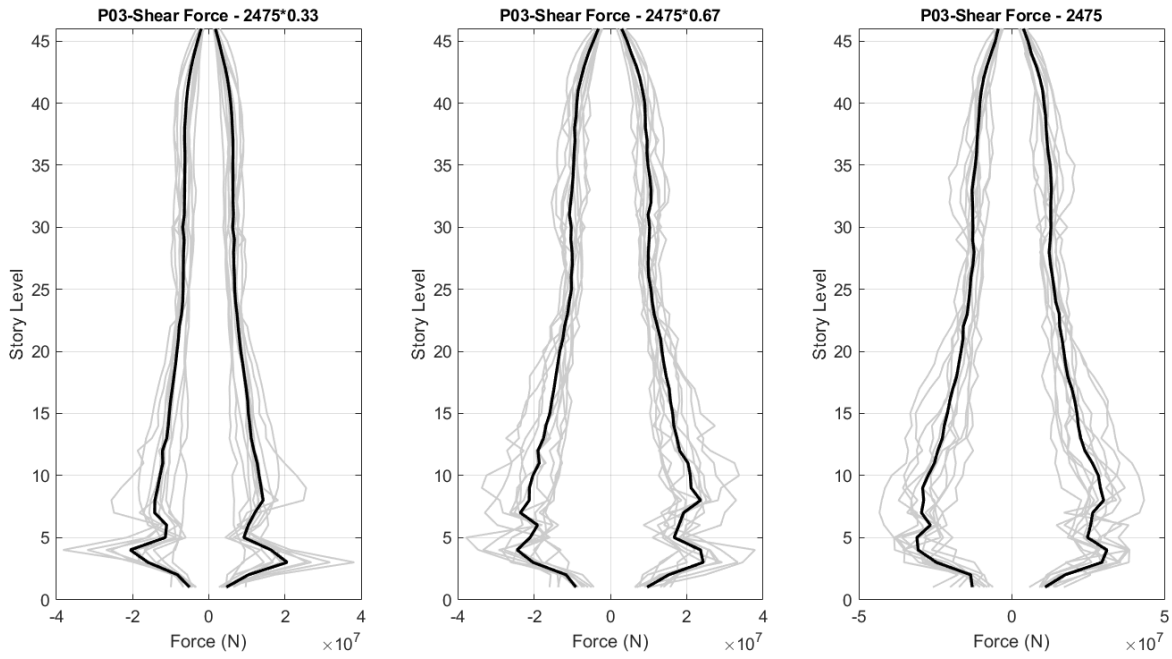

Figure 3.11. P03 shear forces.

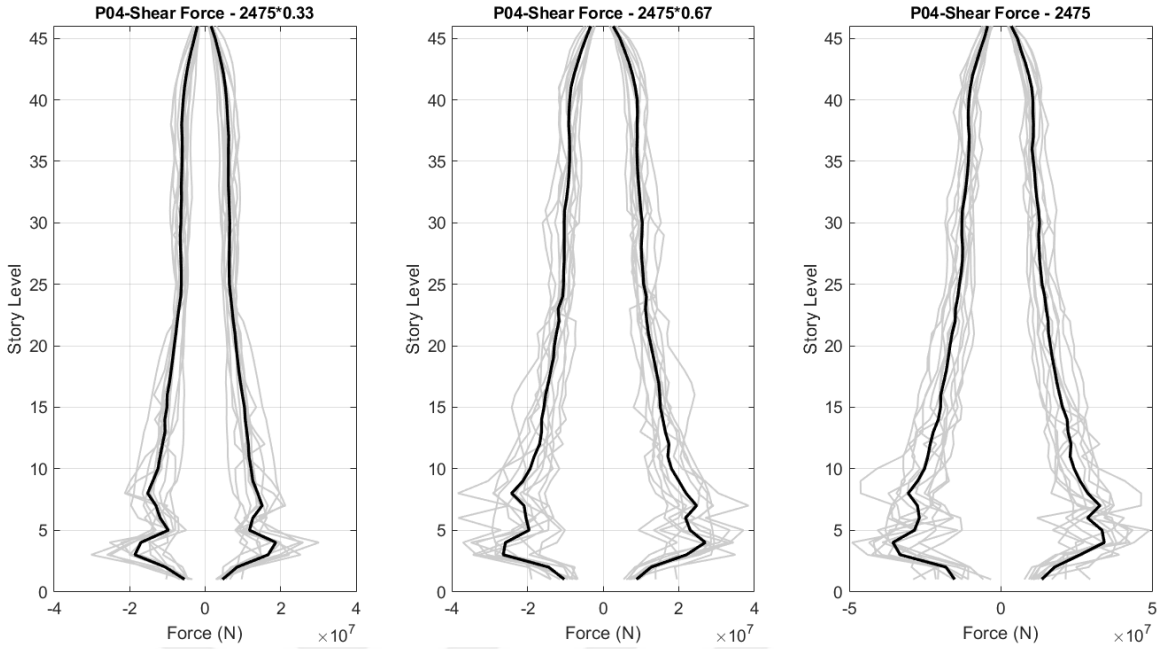

Figure 3.12. P04 shear forces.

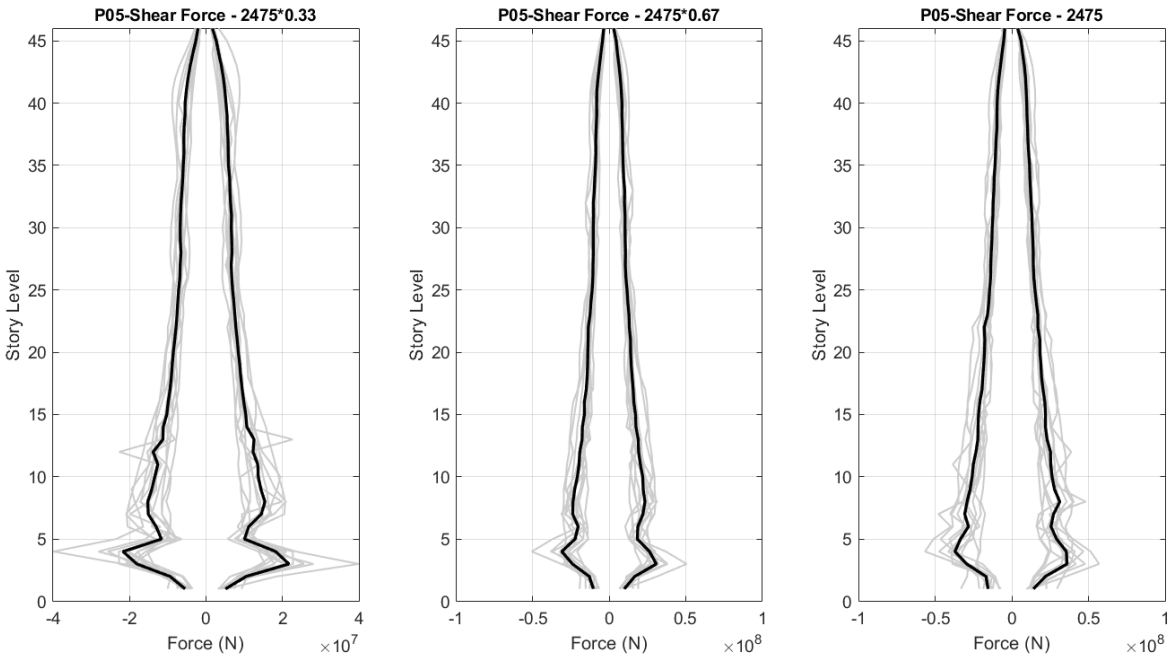

Figure 3.13. P05 shear forces.

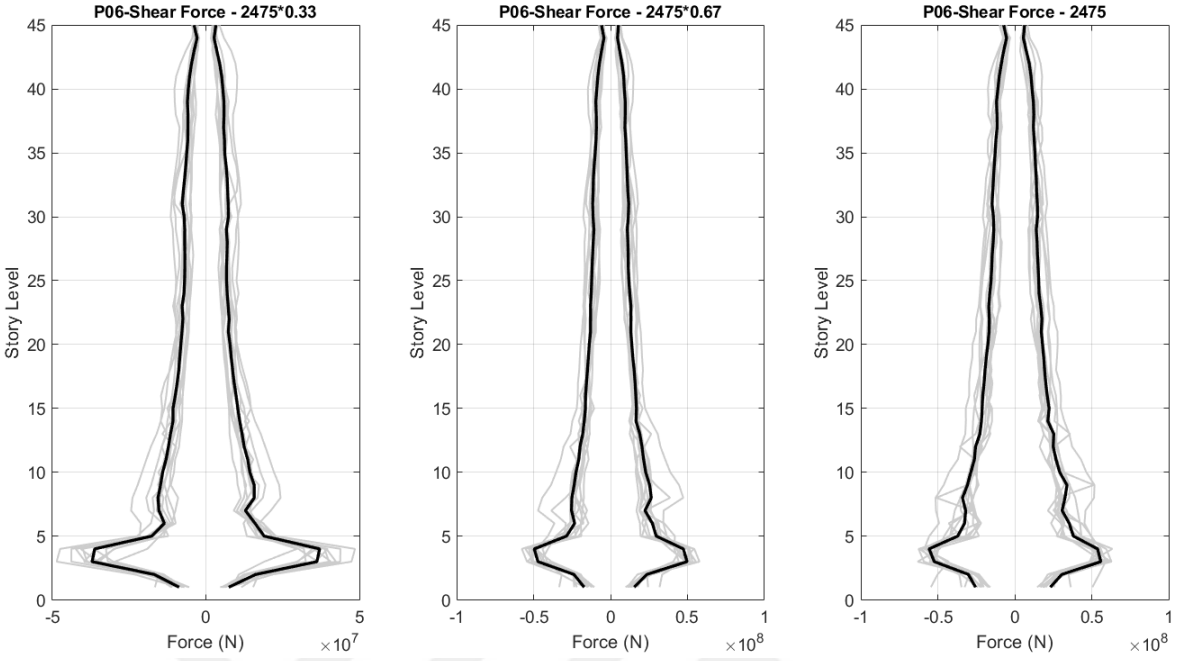

Figure 3.14. P06 shear forces.

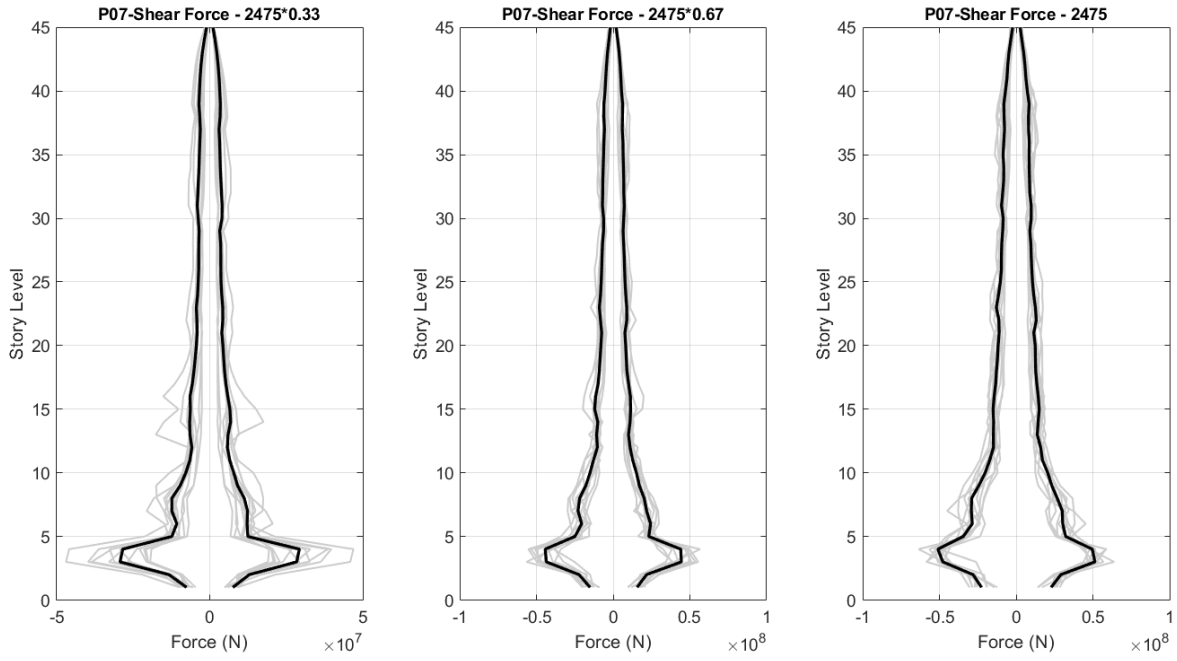

Figure 3.15. P07 shear forces.

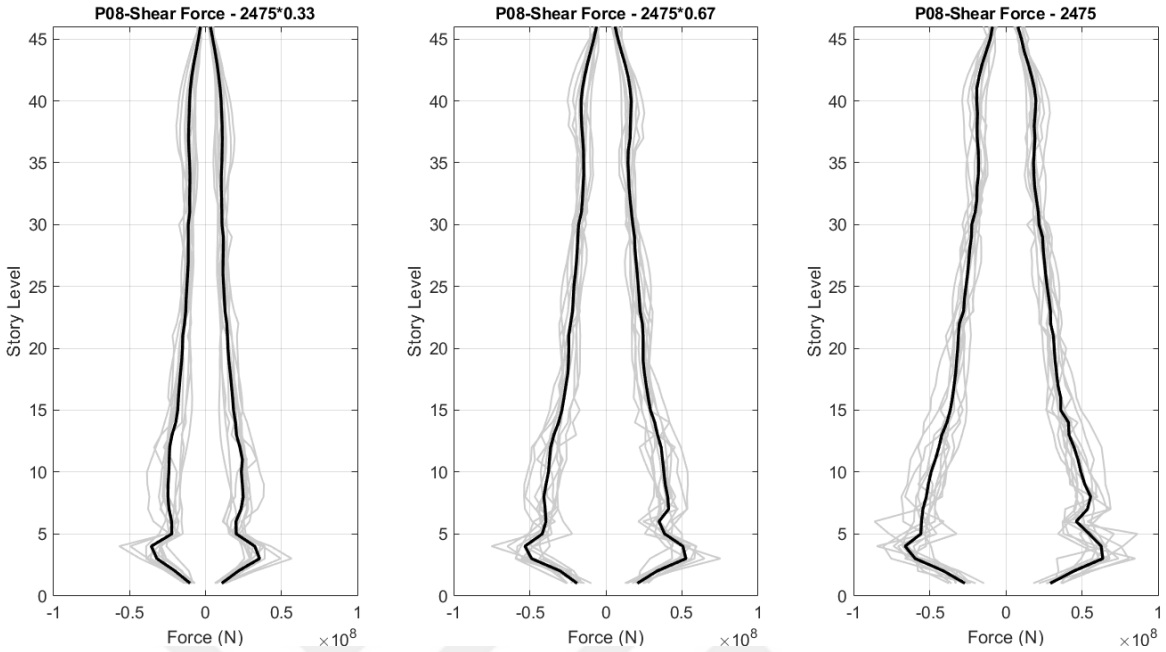

Figure 3.16. P08 shear forces.

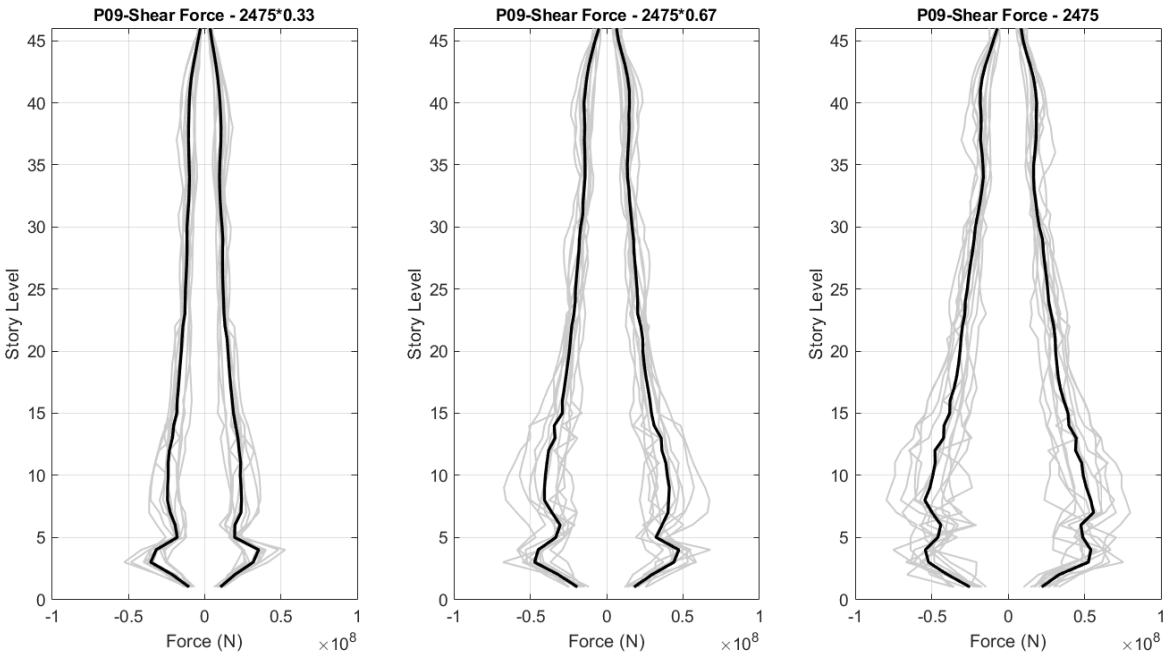

Figure 3.17. P09 shear forces.

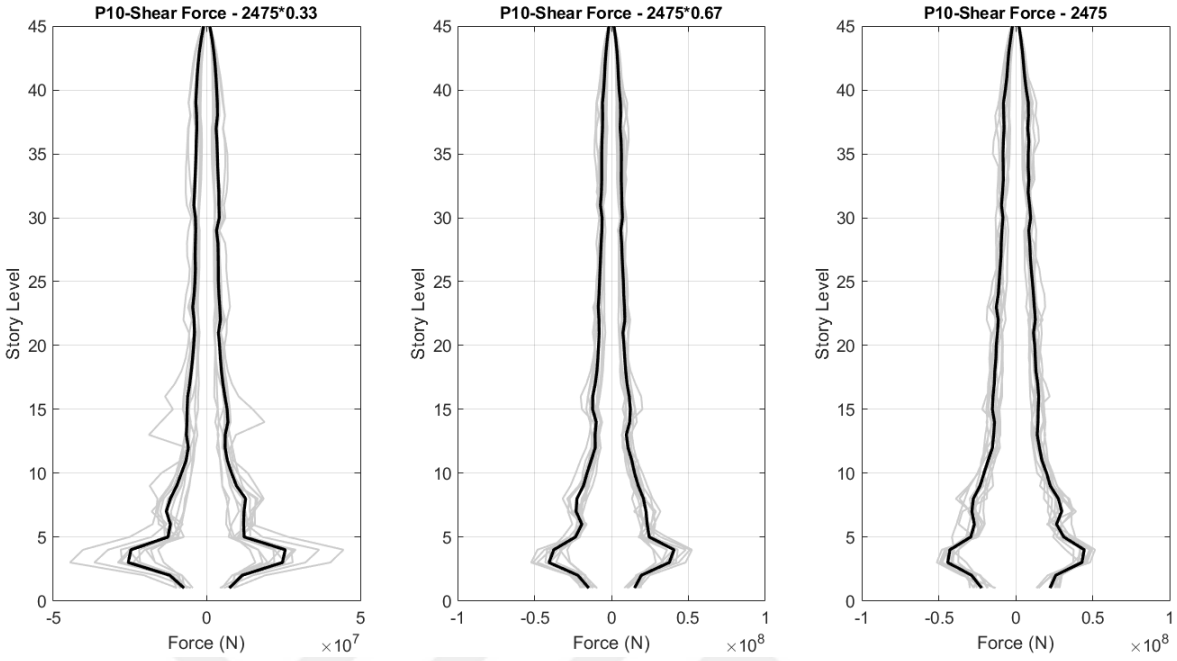

Figure 3.18. P10 shear forces.

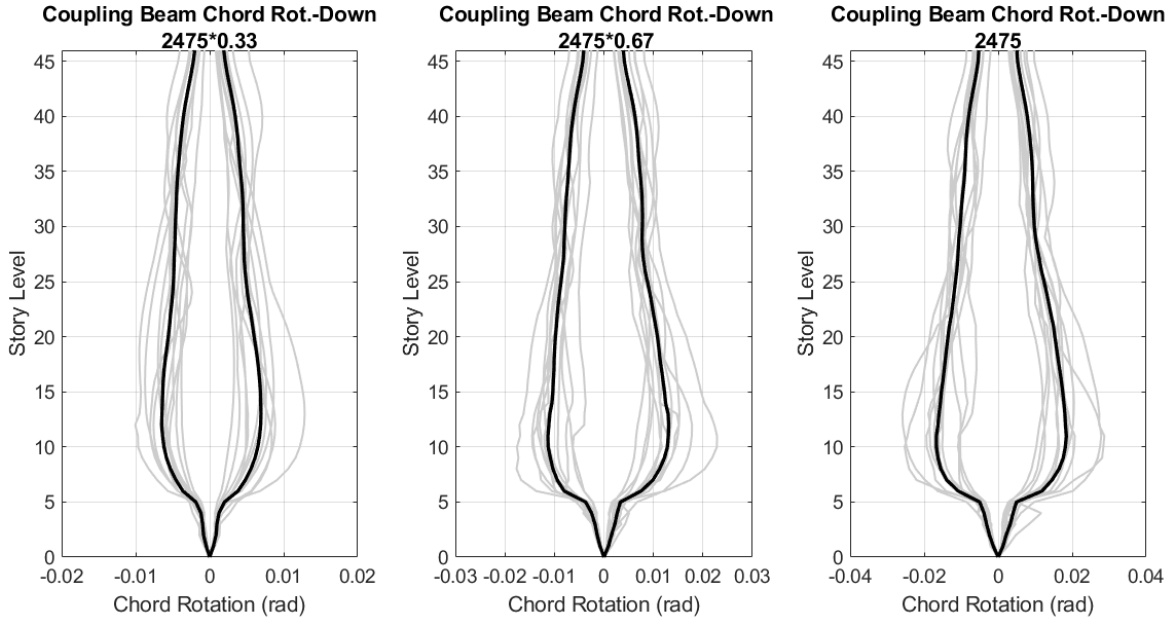

Figure 3.19. Chord rotation of coupling beams - down.

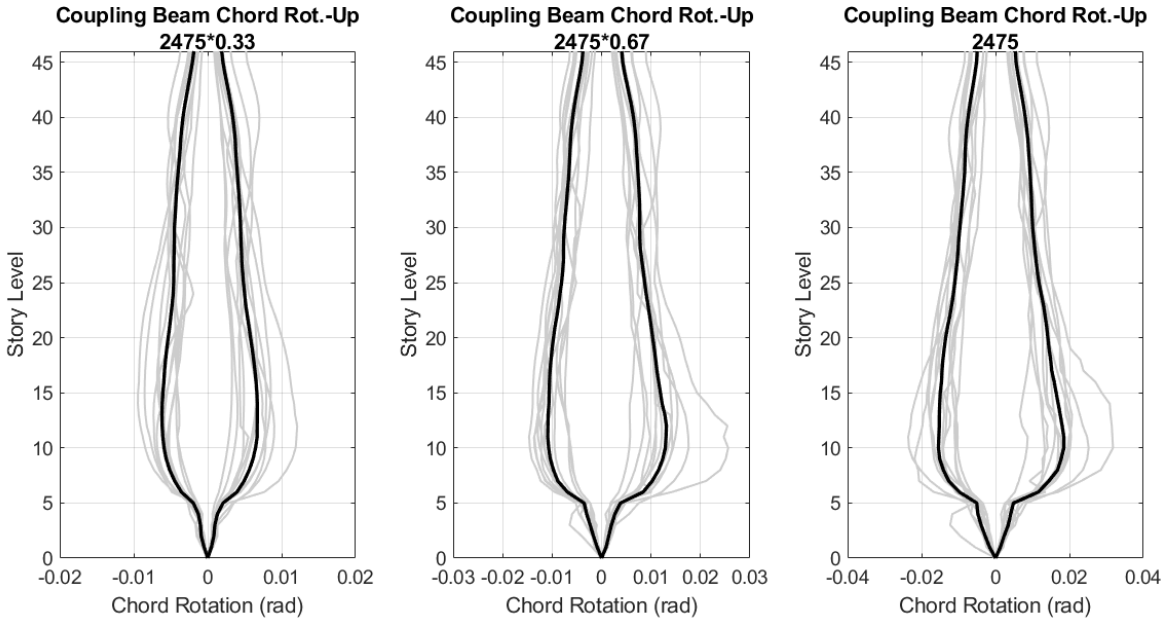

Figure 3.20. Chord rotation of coupling beams - up.

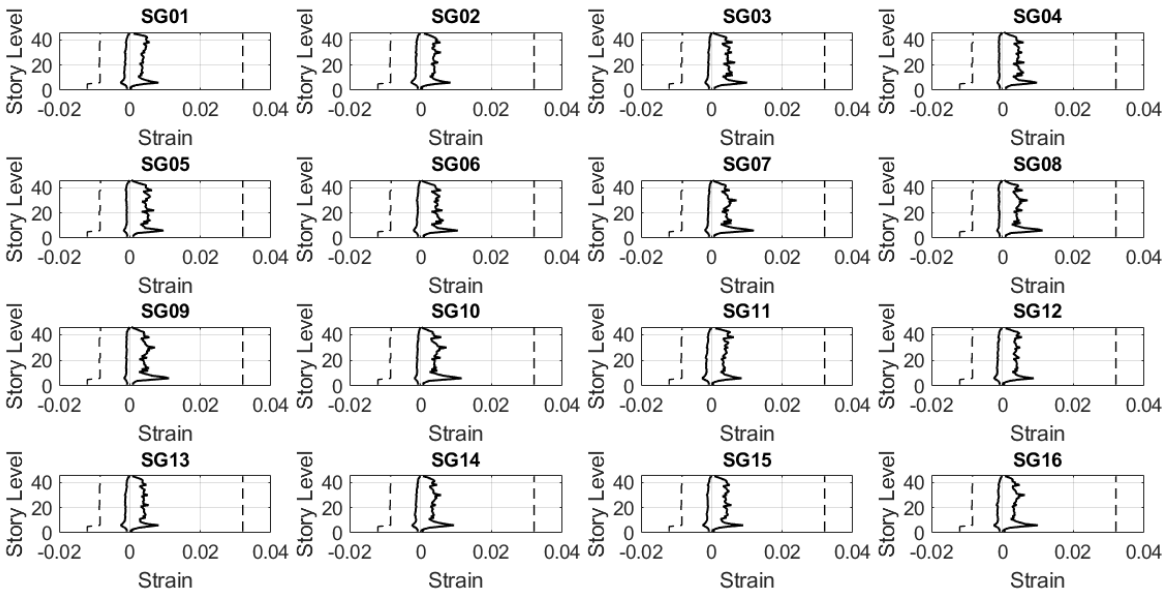

Figure 3.21. Strain-gauge results.

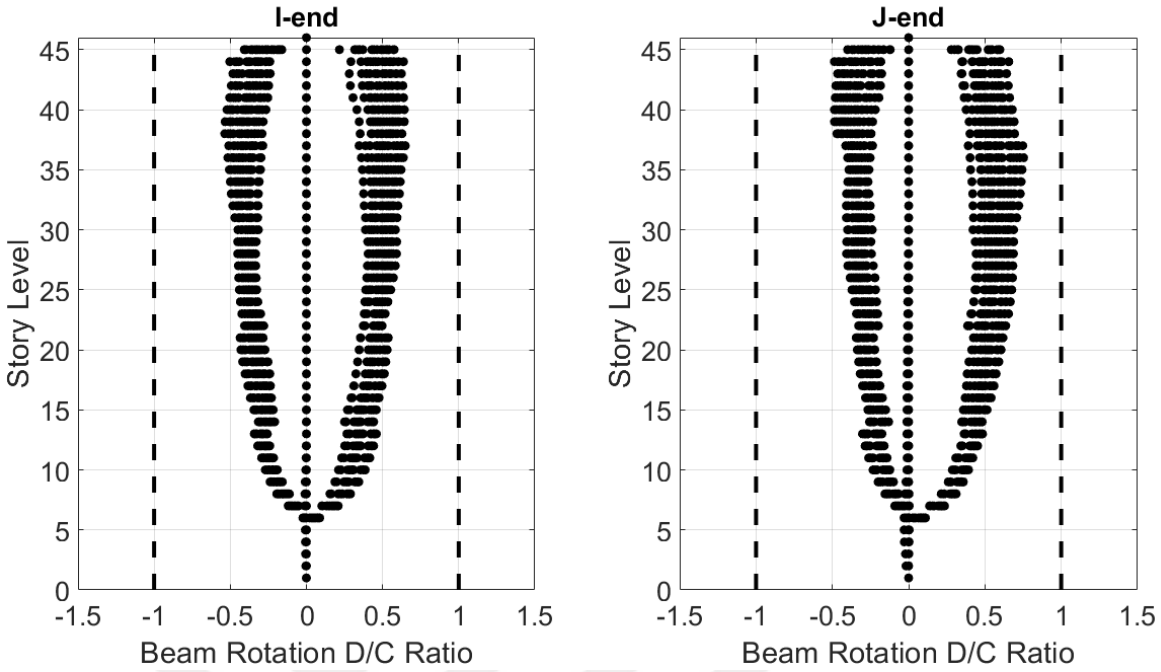

Figure 3.22. Demand/Capacity ratio for beam rotations.

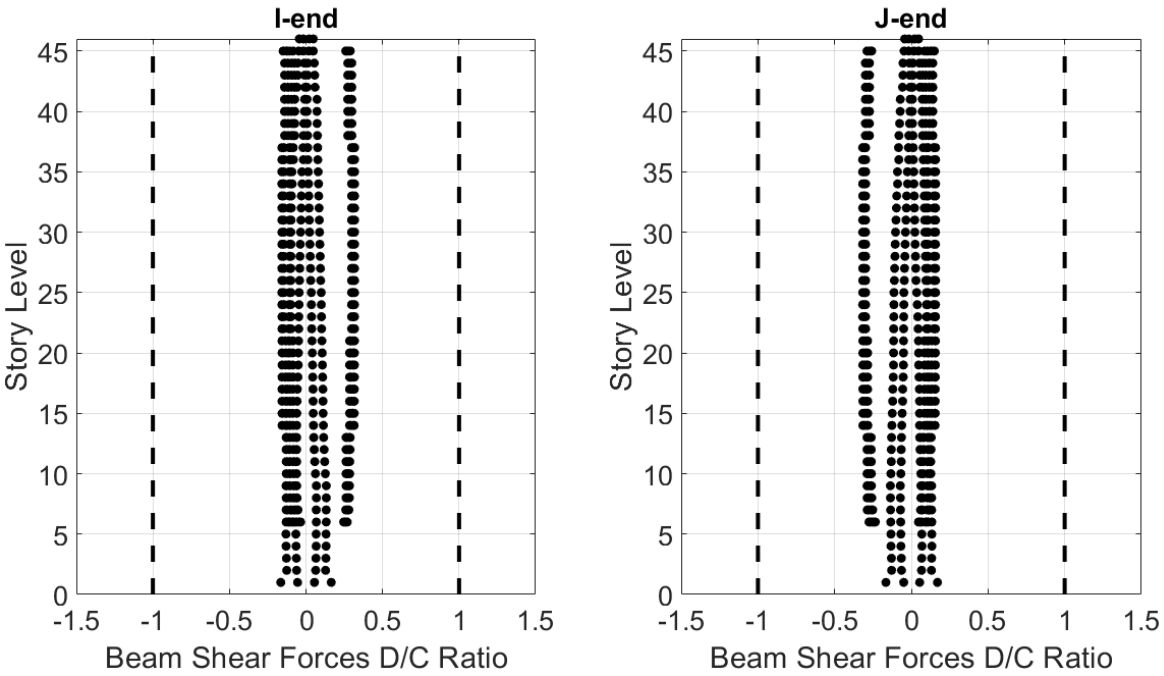

Figure 3.23. Demand/Capacity ratio for beam shear forces.

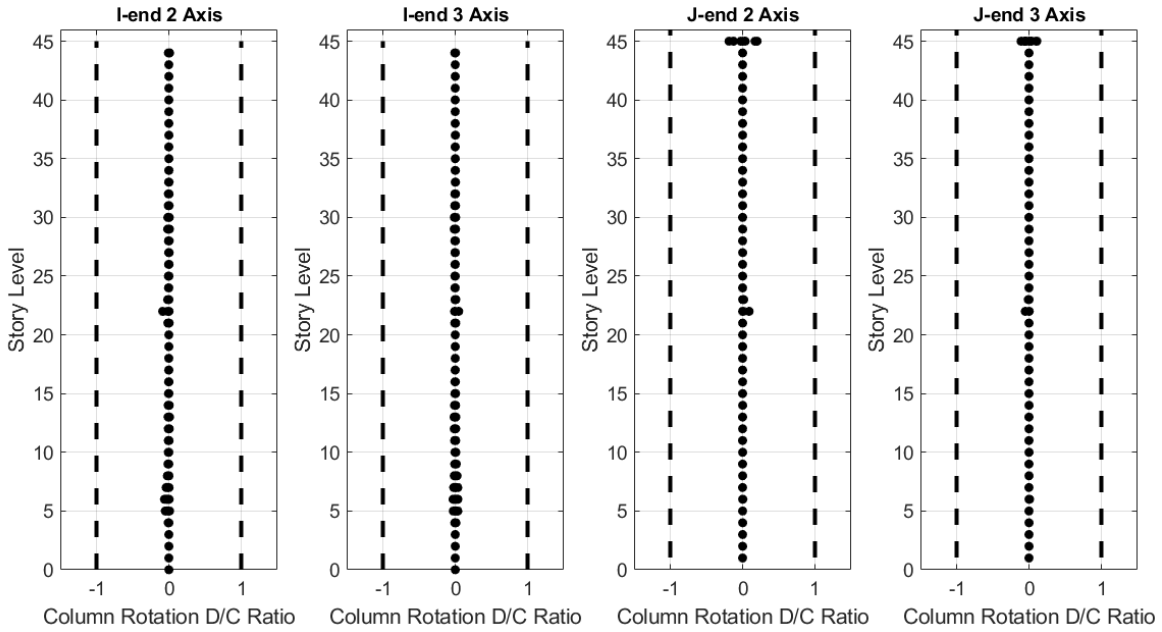

Figure 3.24. Demand/Capacity ratio for column rotations.

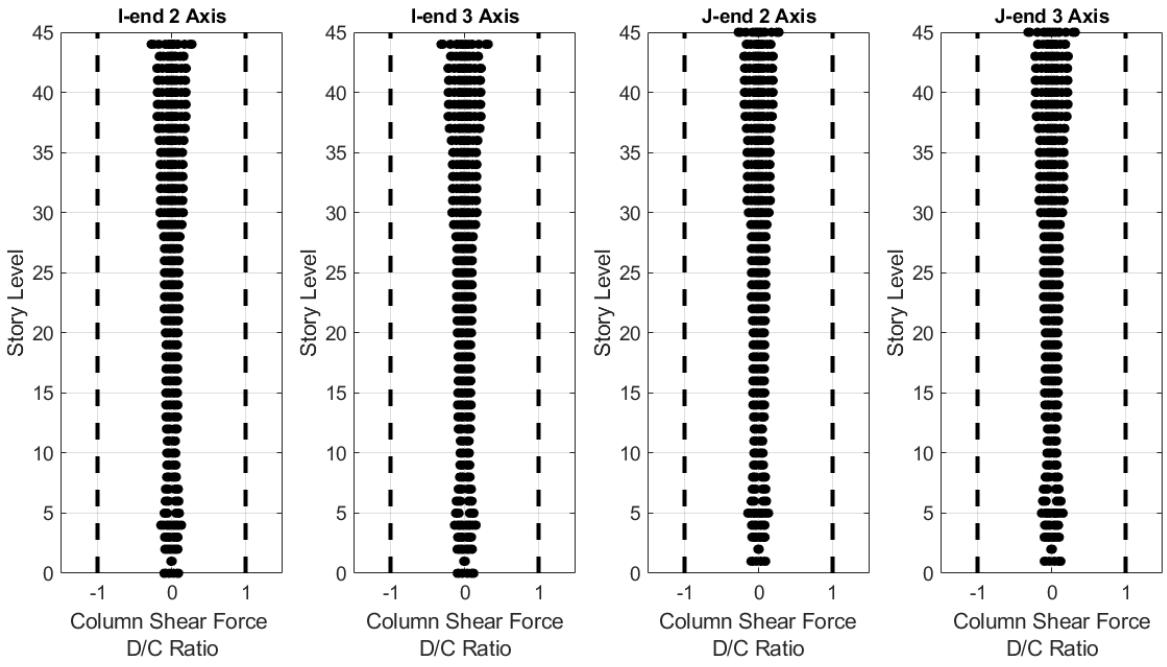

Figure 3.25. Demand/Capacity ratio for column shear forces.

4. ESTIMATION OF NON-INSTRUMENTED FLOOR RESPONSES

Tracking changes in modal parameters is one way of condition assessment. However, different mechanism occurring during earthquakes such as soil-structure interaction can also change modal values of structures. Therefore, alternative approaches such as controlling inter-story drift ratios can be used for condition assessment of tall buildings. On the other hand, using accelerometers on each story is not preferred to monitor tall buildings due to practical and economical reasons. Therefore, estimation of non-instrumented floor responses from instrumented floor responses has always been an important research topic.

It is very difficult to create detailed FEM of each tall building instrumented with SHM systems. Therefore, different methods were utilized to estimate response of non-instrumented floors from instrumented floors in literature. Linear interpolation and cubic interpolation methods are most preferred approaches due to their fast calculation times and simple algorithms [41], [43], [76, 77]. These methods need identification of dynamic properties and recorded displacements at instrumented floors to predict modal displacement of non-instrumented floors. Although linear and cubic interpolation methods estimate similar responses of non-instrumented floors for the first mode, capability of cubic interpolation method to estimate responses of non-instrumented floors for higher modes is better due to its high degree polynomial function. In addition, there are significant studies in literature that create correlation between frequency response function of instrument floors by cubic interpolation technique to estimate response of non-instrumented floors and to detect damage locations [44, 45]. It is a fact that sensors should be located at regular intervals along structure in accordance with stiffness change locations to increase accuracy of these methods. The main disadvantage of these methods is to use mode shapes before and/or after earthquake and not considering nonlinear effects for estimation of non-instrumented floor responses during earthquakes. Therefore, these methods are capable to accurately predict responses

of non-instrumented floors in cases that structures show elastic behavior under weak earthquakes.

On the other hand, estimation of non-instrumented floor responses under strong earthquake causing high non-linearity is a challenging topic because dynamic properties and responses of structure significantly change. Therefore, simplified mathematical models of structures created based on basic geometric and mechanical properties of structures provide great advantage to understand behavior of structures. In addition, response of non-instrumented floors can be obtained from instrumented floor responses by optimizing simplified mathematical models based on vibration data recorded by SHM systems.

In this study, simplified analytical models of tall building were created with different methods as alternative approaches. The most important advantage of these models is that they can be updated and optimized by vibration data recorded by SHM systems. In these models, combination of shear and flexural behaviors of tall buildings were considered to estimate responses of non-instrumented floors from instrumented floors. Also, nonlinear behavior of structural elements in analytical model can be considered with nonlinear springs. Simple visualization of created simplified mathematical models is shown in Figure 4.1.

4.1. Stepped Timoshenko Beam Model (STBM)

In early studies, Euler-Bernoulli beam equations were used to estimate elastic response of tall buildings under external effects such as wind and earthquake. Although flexural behavior dominates response of tall buildings due to their slenderness, structural walls increase their shear rigidity. Therefore, Timoshenko beam model [78], which takes into account contributions of both flexural and shear behaviors in differential equation of a beam vibration, provides great advantage for simplified mathematical model of tall buildings.

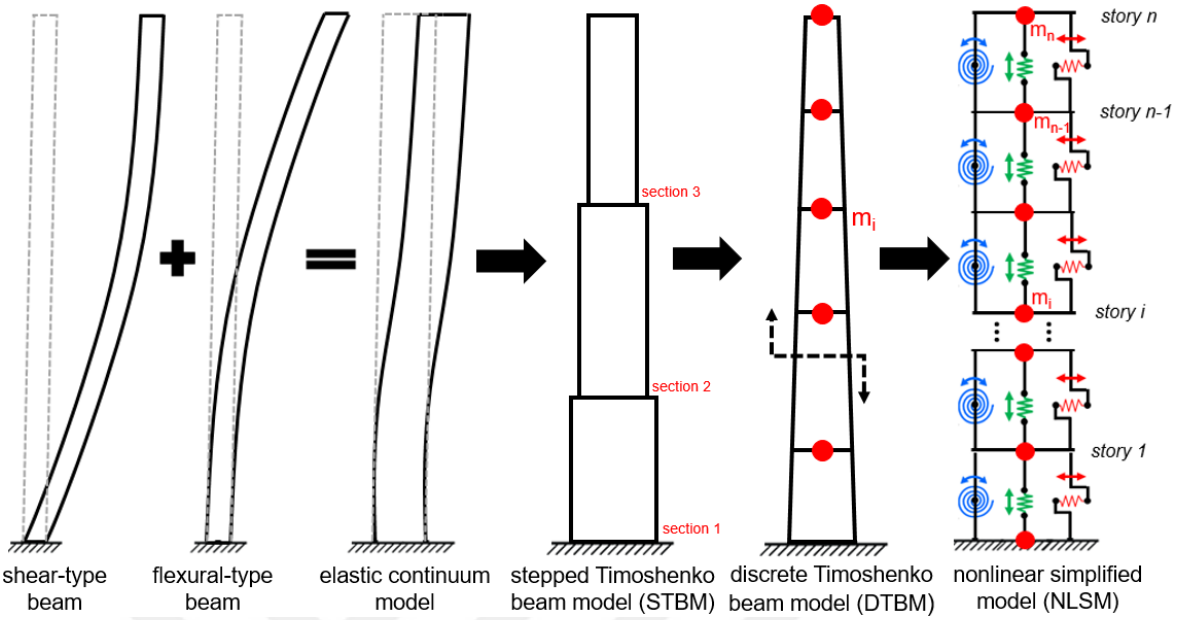

Figure 4.1. Mathematical models of tall building with different approaches.

Closed-form equations of Timoshenko beam model [79, 80] were developed for tall buildings whose mass and stiffness distribution are uniform or close to uniform along their height. Therefore, the equations were rearranged for non-uniform tall building model to properly estimate dynamic responses with mathematical beam model because the structure has five wide basement floors surrounded by rigid walls and so, rigidity of the structure abruptly changes at transfer floor. In order to consider this non-uniformity, the beam model was divided into three sub-steps and normal functions of transverse deflection, $W_i(\xi)$, and rotational angle due to bending, $\phi_i(\xi)$, for each step can be written as

$$\begin{aligned} W_i(\xi) = A_i cosh(\lambda_{i,1}\xi) + B_i sinh(\lambda_{i,1}\xi) \\ +C_i cos(\lambda_{i,2}\xi) + D_i sin(\lambda_{i,2}\xi), \end{aligned} \tag{4.1}$$

$$\begin{aligned} \phi_i(\xi) = A_i m_{i,1} sinh(\lambda_{i,1}\xi) + B_i m_{i,1} cosh(\lambda_{i,1}\xi) \\ +C_i m_{i,2} sin(\lambda_{i,2}\xi) + D_i m_{i,2} cos(\lambda_{i,2}\xi), \end{aligned} \tag{4.2}$$

where $l_i < \xi < l_{i+1}$, $\xi = x/L$, $\nu_i = E_i/(k_i G_i)$, $r_i = 1/(A_i L^2)$, $s_i = \nu_i r_i$, $\tau_i = (\rho_i A_i L^4 \omega^2)/(E_i I_i)$, $\alpha_i = (\tau_i(r_i + s_i))/2$, $\beta_i = \tau_i(\tau_i r_i s_i - 1)$, $\lambda_{i,1} = ((\alpha_i^2 - \beta_i)^{0.5} - \alpha_i)^{0.5}$, $\lambda_{i,2} = ((\alpha_i^2 - \beta_i)^{0.5} + \alpha_i)^{0.5}$, $m_{i,1} = (\tau_i s_i + \lambda_{i,1}^2)/\lambda_{i,1}$, $m_{i,1} = (\tau_i s_i - \lambda_{i,2}^2)/\lambda_{i,2}$. Arbitrary

constants in equations (A_i, B_i, C_i, D_i) are calculated from continuity equations and boundary conditions. These relations can be expressed as

$$W_1(\xi) = W_2(\xi) \text{ at } \xi = l_1, \tag{4.3}$$

$$W_1{}'(\xi) = W_2{}'(\xi) \text{ at } \xi = l_1, \tag{4.4}$$

$$E_1 I_1 \phi_1'(\xi) = E_2 I_2 \phi_2'(\xi) \text{ at } \xi = l_1, \tag{4.5}$$

$$k_1 G_1 A_1 (W_1{}'(\xi) - \phi_1(\xi)) = k_2 G_2 A_2 (W_2{}'(\xi) - \phi_2(\xi)) \text{ at } \xi = l_1, \tag{4.6}$$

$$W_2(\xi) = W_3(\xi) \text{ at } \xi = l_2, \tag{4.7}$$

$$W_2{}'(\xi) = W_3{}'(\xi) \text{ at } \xi = l_2, \tag{4.8}$$

$$E_2 I_2 \phi_2'(\xi) = E_3 I_3 \phi_3'(\xi) \text{ at } \xi = l_2, \tag{4.9}$$

$$k_2 G_2 A_2 (W_2{}'(\xi) - \phi_2(\xi)) = k_3 G_3 A_3 (W_3{}'(\xi) - \phi_3(\xi)) \text{ at } \xi = l_2, \tag{4.10}$$

$$W_1(\xi) = 0 \text{ at } \xi = 0, \tag{4.11}$$

$$\phi_1(\xi) = 0 \text{ at } \xi = 0, \tag{4.12}$$

$$\phi_2'(\xi) = 0 \text{ at } \xi = 1, \tag{4.13}$$

$$W_2{}'(\xi) - \phi_2(\xi) = 0 \text{ at } \xi = 1. \tag{4.14}$$

When these equations are reorganized in matrix form, $X(\omega)$, the values equalizing determinant of the matrix to zero give modal frequencies of the structure in that direction. Solution of the equation in these frequency values gives the arbitrary constants, CV, for corresponding frequency value. Relation between $X(\omega)$ and CV is defined as

$$X(\omega)CV = 0, \tag{4.15}$$

where CV is coefficient vector of A_i-D_i i=1,2,3 and $X(\omega)$ is 12x12 characteristic matrix. Although basic geometrical properties of tall building is known, effective elastic modulus and effective shear modulus of the structure, E^* and G^*, which are needed to create the most appropriate Timoshenko beam model, must be properly estimated. Although there are many methods to estimate E^* and G^* from geometrical properties of structural elements, recommended method in literature [81] was used to estimate relation between effective elastic modulus and effective shear modulus of the structure. Based on this method, relation between the effective bending rigidity and the effective

shear rigidity was created by using modal frequency ratios obtained from modal analysis of FEM as shown in Figure 4.2.

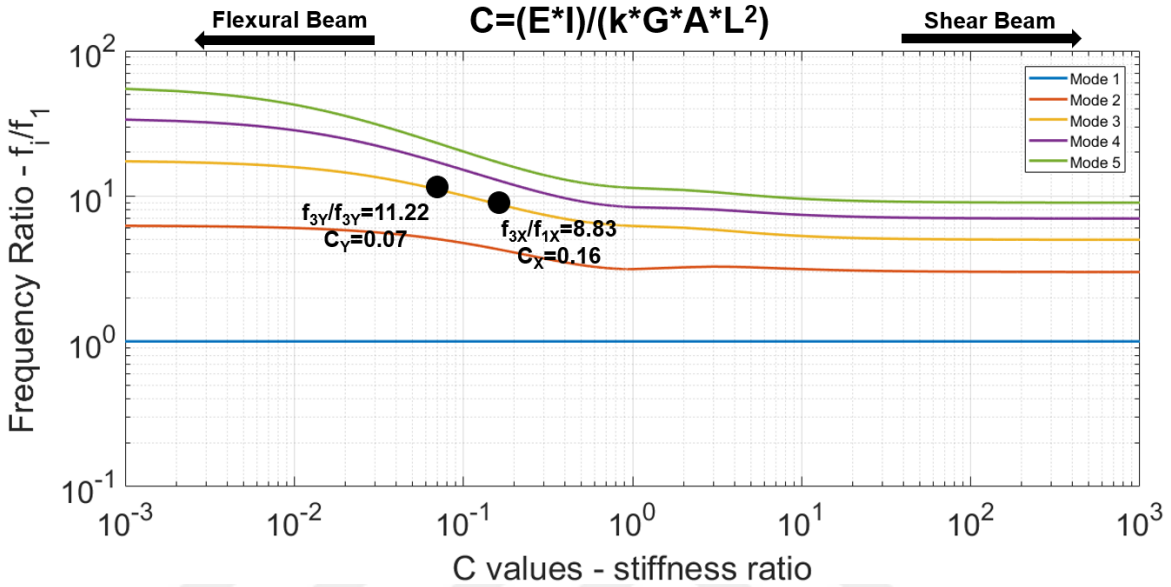

Figure 4.2. Relation between effective bending rigidity and effective shear rigidity.

In order to obtain the most suitable mathematical beam model for the structure, an algorithm was developed by using error function. The error function is expressed as

$$E(\alpha) = \sum (k_i[(f_i^* - f_i)/f_i^*]^2 + h_i[1 - MAC_i]^2), \tag{4.16}$$

where α is correction coefficient, i is mode number, k_i is weighting coefficient for i^{th} modal frequency, h_i is weighing coefficient for i^{th} modal assurance criteria, f_i^* is modal frequency of ith mode for FEM, f_i is estimated modal frequency of ith mode for mathematical model, MAC_i is modal assurance criteria for i^{th} mode shape.

In the algorithm, initial values of G^* are separately calculated from shear beam formula ($G^*_{initial} = \rho(4Lf_1)^2$) for each direction and correlation between E^* and G^* are provided by using C values calculated based on modal frequency ratios of FEM for both directions [82]. Algorithm updates mass and G^* value in each step until it finds minimum error value between results of FEM and stepped Timoshenko beam model.

In the analyses, it was assumed that there were sensors at only five points of modelled tall building (Story 0, Story 5, Story 18, Story 31 and Story 45). Updated modal frequencies and mode shapes were represented for both directions in Figure 4.3 and Figure 4.4.

In algorithm, non-updated models are stepped beam models of the structure whose geometry, mass and stiffness distribution is uniform. On the other hand, updated models represent mathematical beam models of the structure consisting of three different sections with different mass and stiffness values.

According to mathematical representation of Timoshenko beam, dynamic properties of uniform numerical beam model are highly dependent on ratio between the flexural rigidity and shear rigidity (C value).

In addition to C value, proper definition of mass and stiffness distribution in mathematical model is critical to estimate consistent modal frequencies and mode shapes with identification results for non-uniform stepped models.

It is obvious from modal frequencies and MAC values that updating algorithm creates the most suitable mathematical model by calibrating mass, E^* and G^* values for three different sections to obtain minimum error value between results of FEM and stepped Timoshenko beam model.

Although contribution of MAC values to error value is limited, obtaining consistent mode shapes with identification results is essential to estimate more reliable acceleration values of non-instrumented floors.

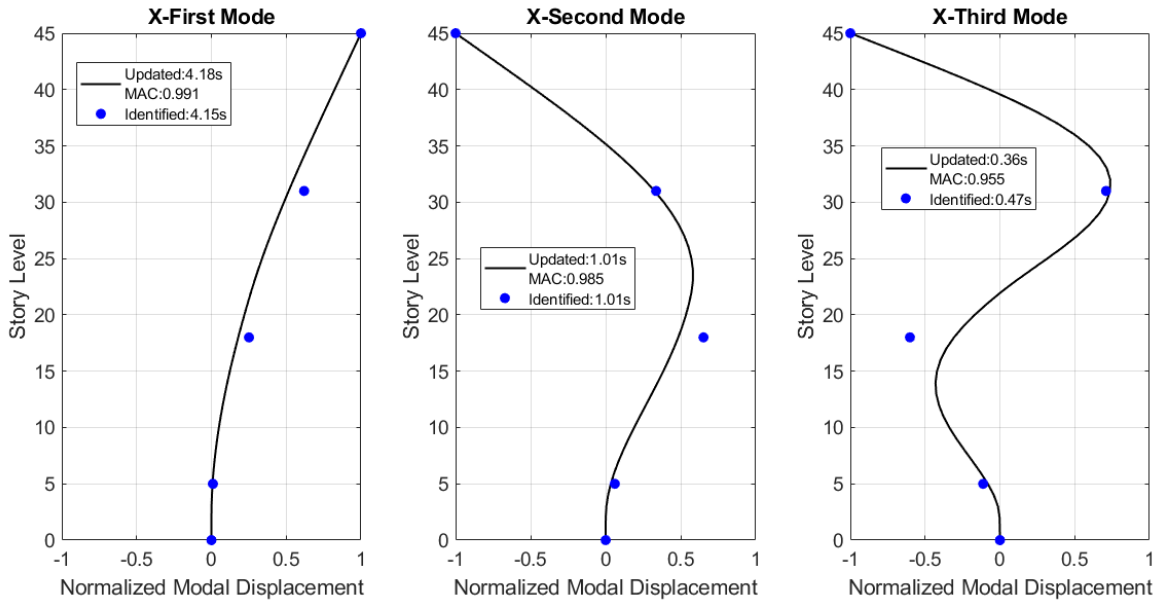

Figure 4.3. STBM-X: updated and identified modal properties.

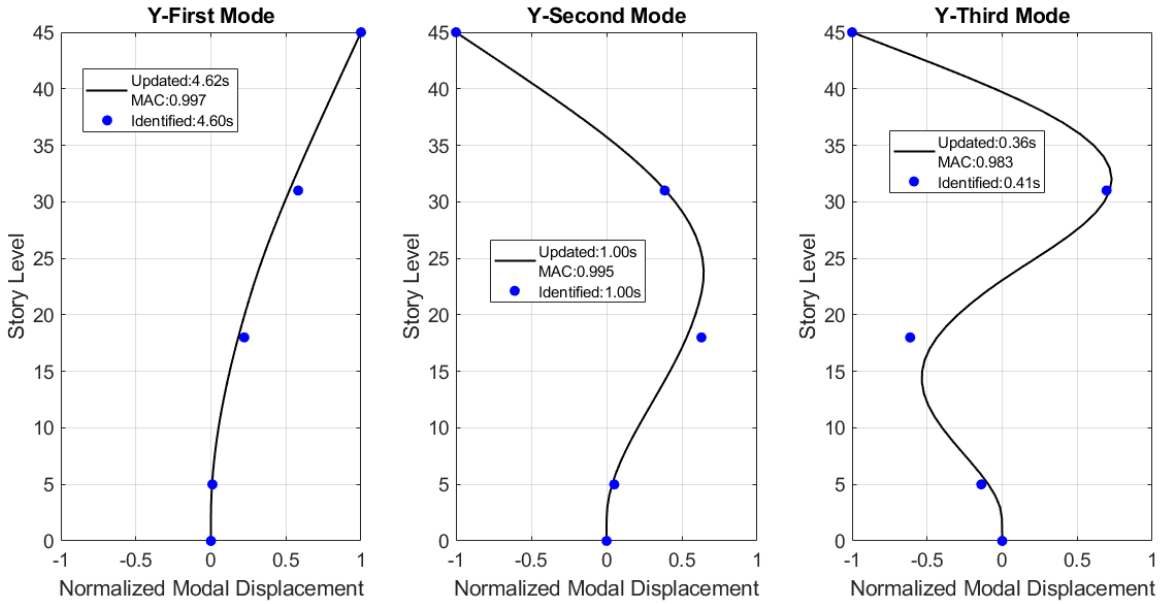

Figure 4.4. STBM-Y: updated and identified modal properties.

Recorded modal accelerations at each instrumented story, $\ddot{z}_{j,k}(t)$, were calculated by band-pass filtering of recorded accelerations around each identified modal frequency. On the other hand, modal acceleration of jth mode for multi-story buildings can be calculated by linear transformation and orthogonality of modes [72]. Therefore, time-variation of modal acceleration for k^{th} floor of beam model can be defined as

$$\ddot{y}_{j,k} = \Gamma_j c_j \phi_{j,k} \ddot{q}_j(t) = c_j \phi_{j,k} \ddot{D}_j(t), \tag{4.17}$$

where Γ_j is j^{th} modal participation factor, c_j is j^{th} mode unknown weighting coefficient, ϕ_j is j^{th} normalized mode shape of Timoshenko beam and $\ddot{q}_j(t)$ is j^{th} mode acceleration of single-degree-of-freedom system. In this study, error function represented in Equation 4.18 is utilized to estimate time-variation of modal acceleration for k^{th} floor of mathematical model, $\ddot{y}_{j,k}$. Error values can be calculated as

$$\varepsilon_j(t) = \sum_{k=1}^{NIF} [\ddot{z}_{j,k}(t) - \ddot{y}_{j,k}(t)]^2, \tag{4.18}$$

in which $\varepsilon_j(t)$ is error function for the jth mode, $\ddot{z}_{j,k}(t)$ is recorded modal acceleration for the jth mode, $\ddot{y}_{j,k}(t)$ is estimated modal acceleration for the jth mode. Minimizing $\varepsilon_j(t)$ with respect to c_j in Equation 4.19, $\frac{\partial \varepsilon_j(t)}{\partial c_j}$ gives the most appropriate time-variation of modal acceleration for k^{th} floor of mathematical model [83]. The equality can be written as

$$(\sum_{k=1}^{NIF} \phi_{j,k}^2)(C_j \ddot{D}_j(t)) = \sum_{k=1}^{NIF} \phi_{j,k} \ddot{z}_{j,k}(t), \tag{4.19}$$

where NIF is number of instrumented floors. Floor accelerations of the beam model can be calculated by superposition of modal accelerations. Floor accelerations can be written as

$$\ddot{y}_j(t) = \sum_{k=1}^{NIM} \ddot{y}_{j,k}(t), \tag{4.20}$$

where NIM is number of identified modes. Total acceleration, $\ddot{y}_j^T(t)$, at any floor can be computed from

$$\ddot{y}_j^T(t) = \ddot{y}_j(t) + \ddot{y}_g(t), \tag{4.21}$$

where $\ddot{y}_j(t)$ and $\ddot{y}_g(t)$ are j^{th} floor acceleration and ground acceleration, respectively.

Floor displacements were calculated by double integration of estimated floor accelerations. In order to obtain velocity and displacement values from acceleration data, best straight-fit line was removed from acceleration data. Before integration, zero-phase digital filtering by using Butterworth filter was applied to recorded acceleration data in order to prevent significant phase delay.

In general, superposition of modal displacements for three modes are adequate to properly obtain floor displacements of multi-story buildings [84]. Therefore, first three modal displacements for each direction were combined to estimate total floor responses of tall building. Figure 4.5 – Figure 4.26 represent recorded and estimated floor displacements for X and Y directions.

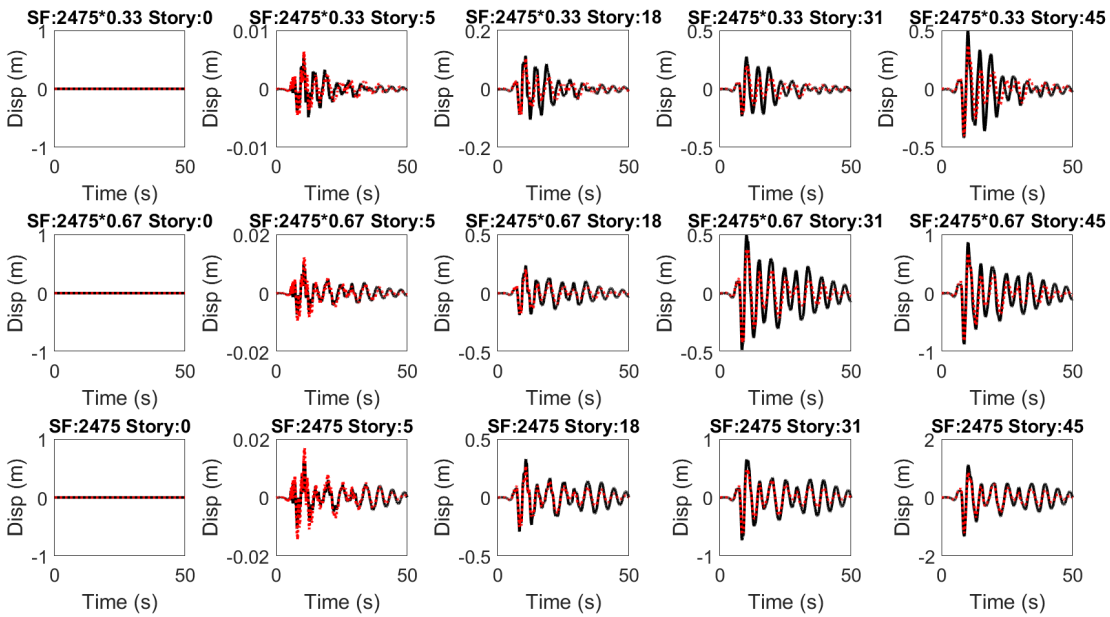

Figure 4.5. STBM-X: recorded (black solid line) and estimated (red dashed line) floor displacements, eq id: 178.

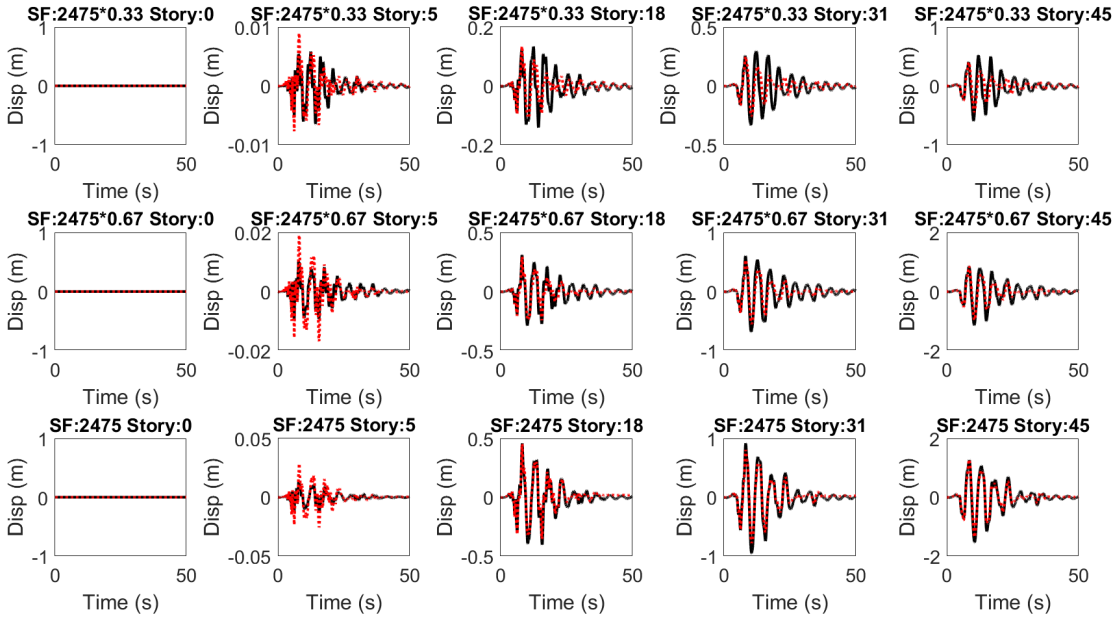

Figure 4.6. STBM-X: recorded (black solid line) and estimated (red dashed line) floor displacements, eq id: 549.

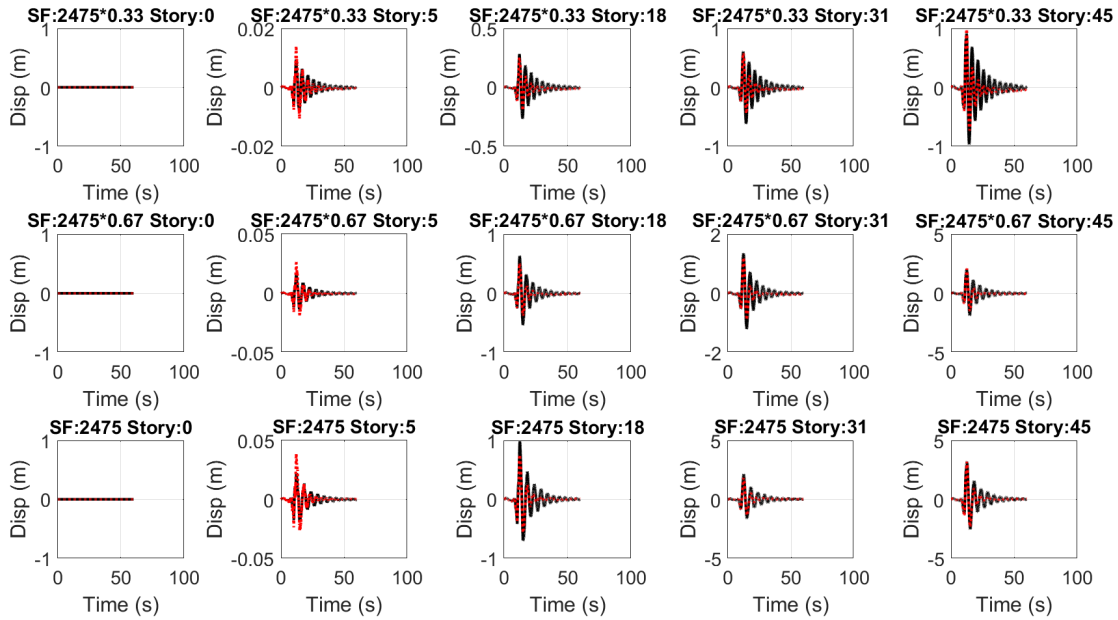

Figure 4.7. STBM-X: recorded (black solid line) and estimated (red dashed line) floor displacements, eq id: 879.

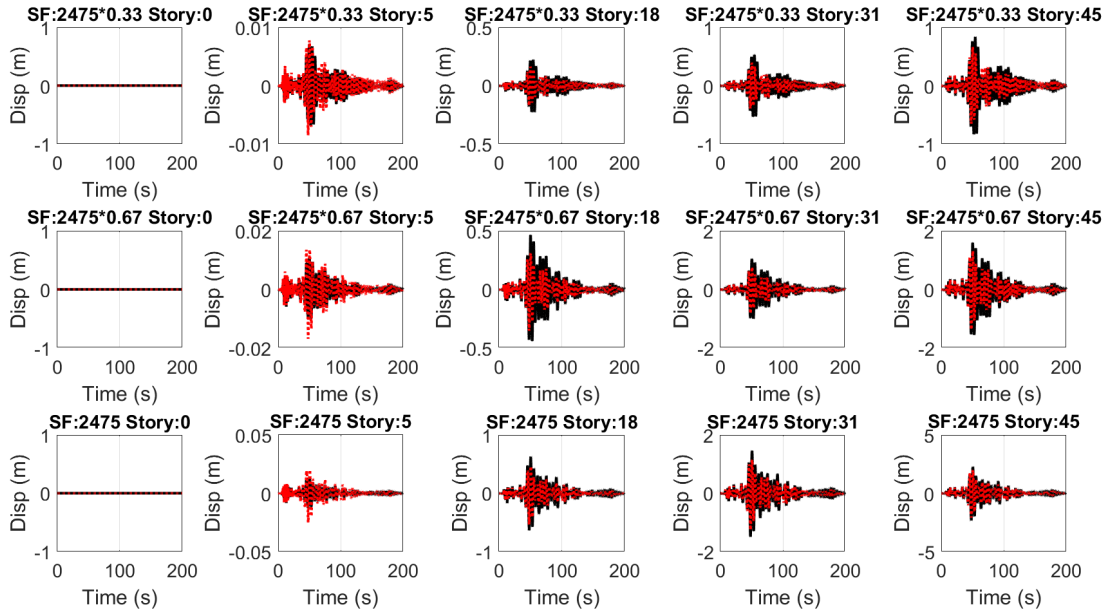

Figure 4.8. STBM-X: recorded (black solid line) and estimated (red dashed line) floor displacements, eq id: 1115.

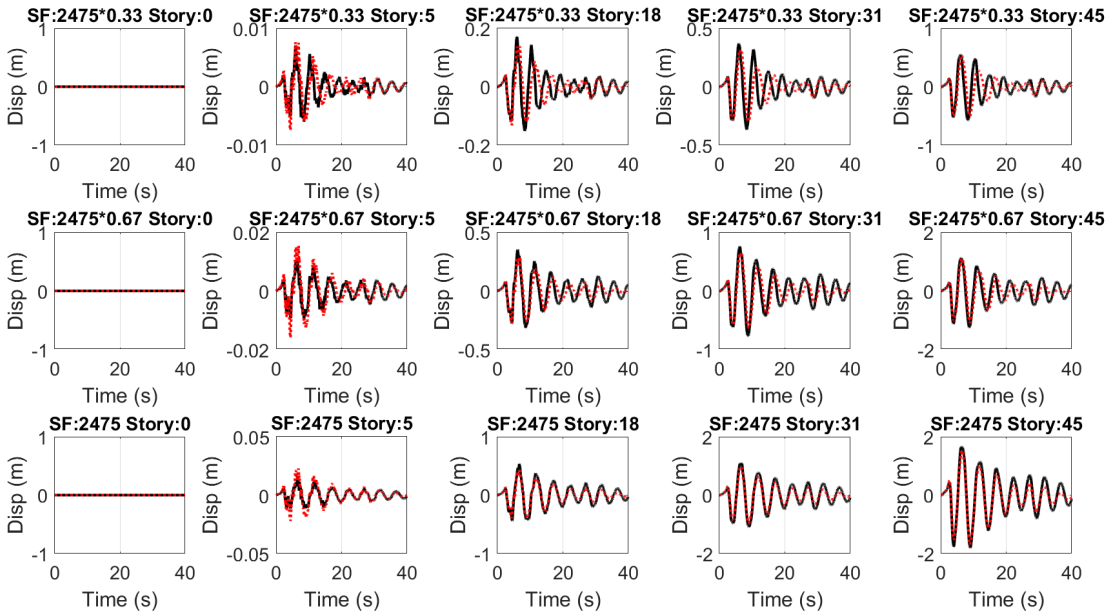

Figure 4.9. STBM-X: recorded (black solid line) and estimated (red dashed line) floor displacements, eq id: 1165.

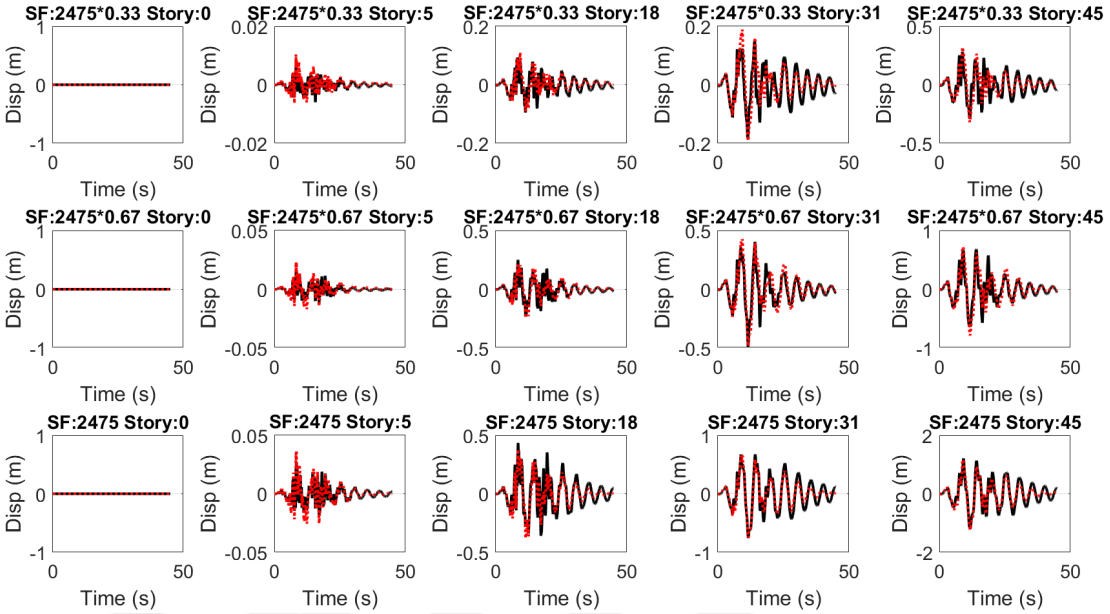

Figure 4.10. STBM-X: recorded (black solid line) and estimated (red dashed line) floor displacements, eq id: 1615.

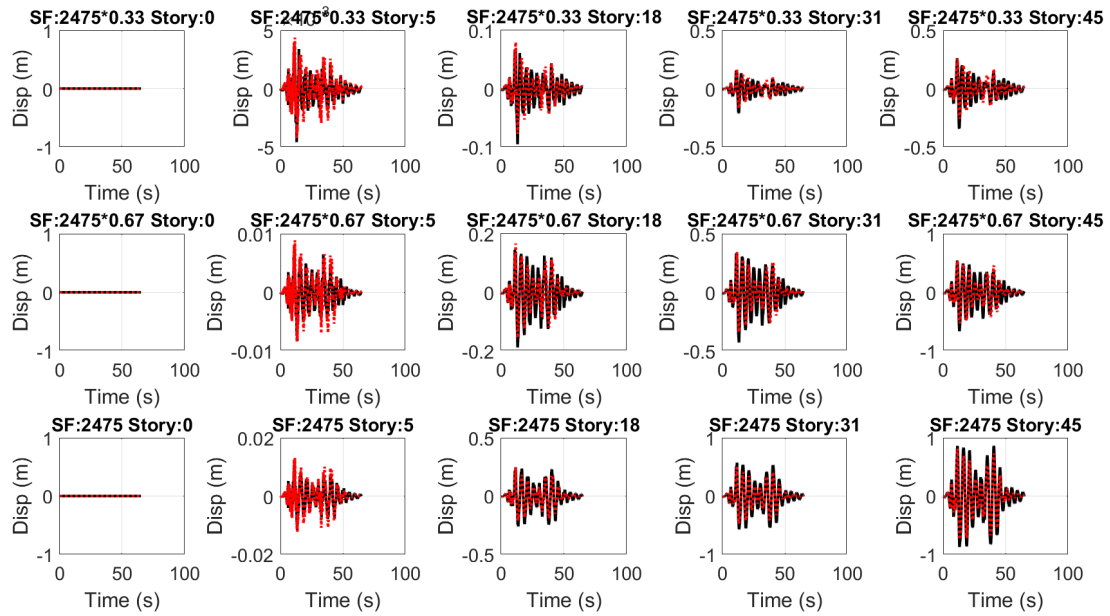

Figure 4.11. STBM-X: recorded (black solid line) and estimated (red dashed line) floor displacements, eq id: 1633.

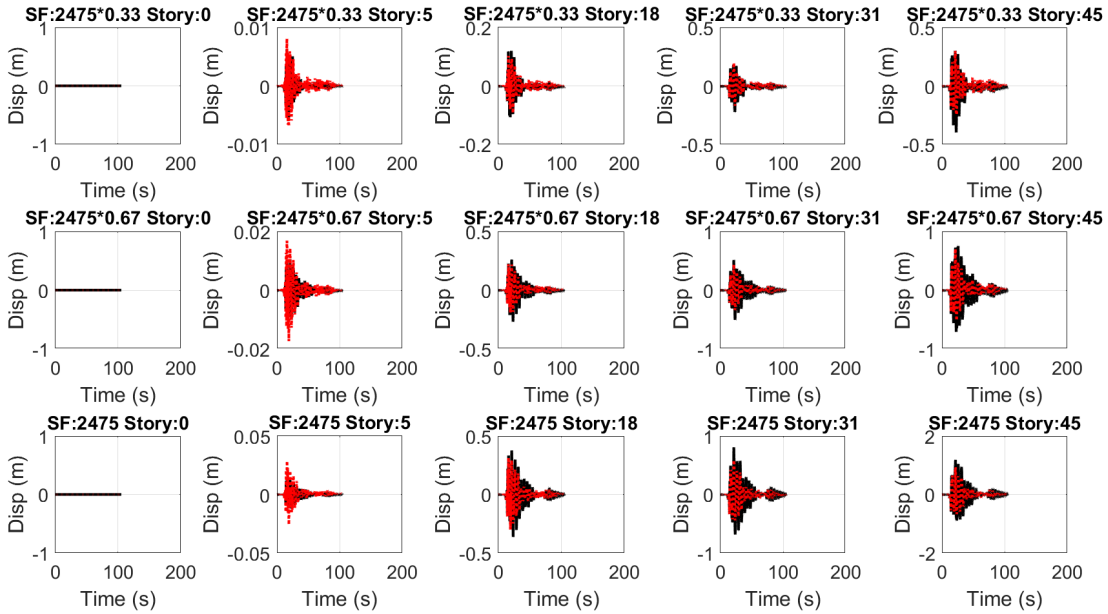

Figure 4.12. STBM-X: recorded (black solid line) and estimated (red dashed line) floor displacements, eq id: 1794.

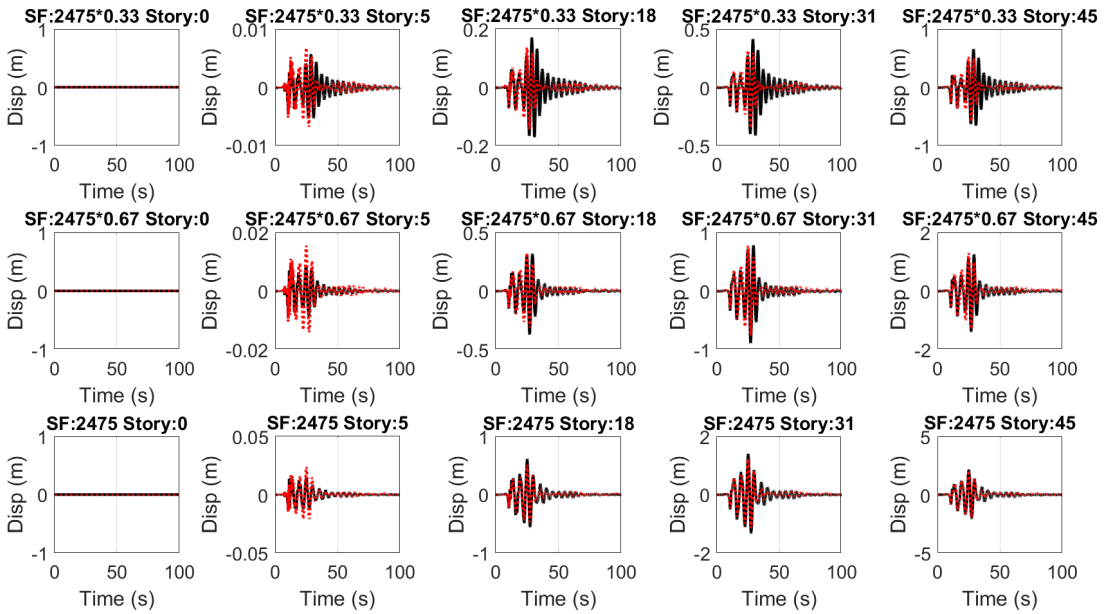

Figure 4.13. STBM-X: recorded (black solid line) and estimated (red dashed line) floor displacements, eq id: 3954.

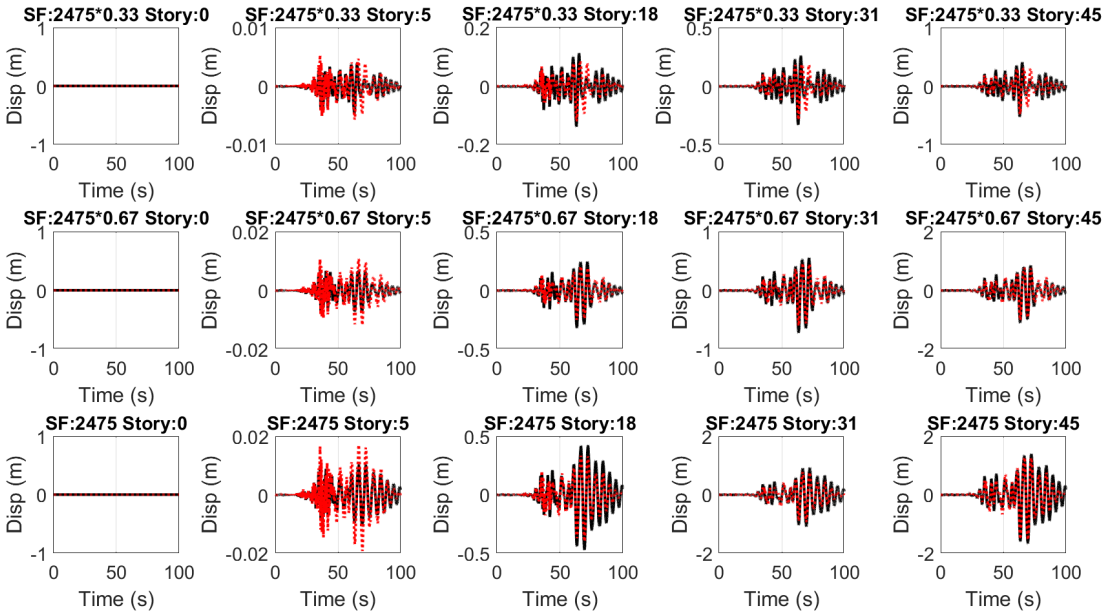

Figure 4.14. STBM-X: recorded (black solid line) and estimated (red dashed line) floor displacements, eq id: 5836.

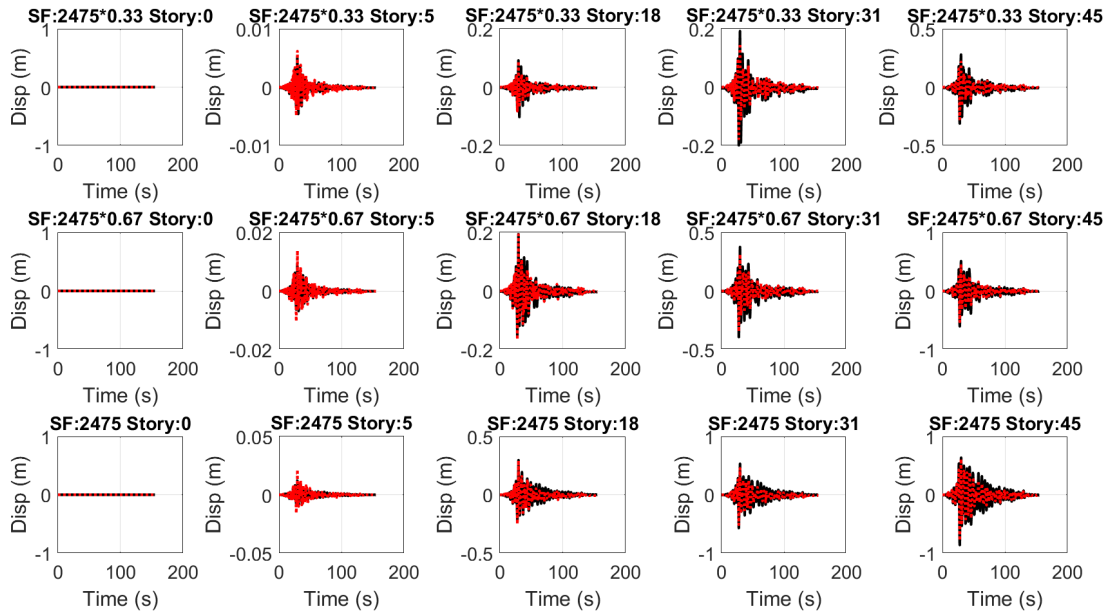

Figure 4.15. STBM-X: recorded (black solid line) and estimated (red dashed line) floor displacements, eq id: 6980.

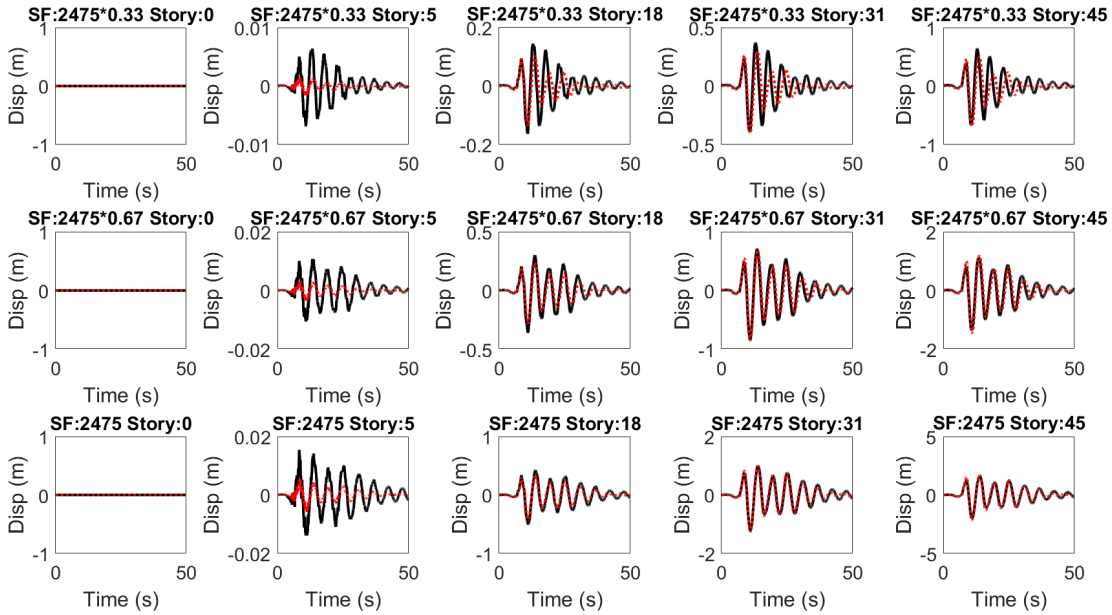

Figure 4.16. STBM-Y: recorded (black solid line) and estimated (red dashed line) floor displacements, eq id: 178.

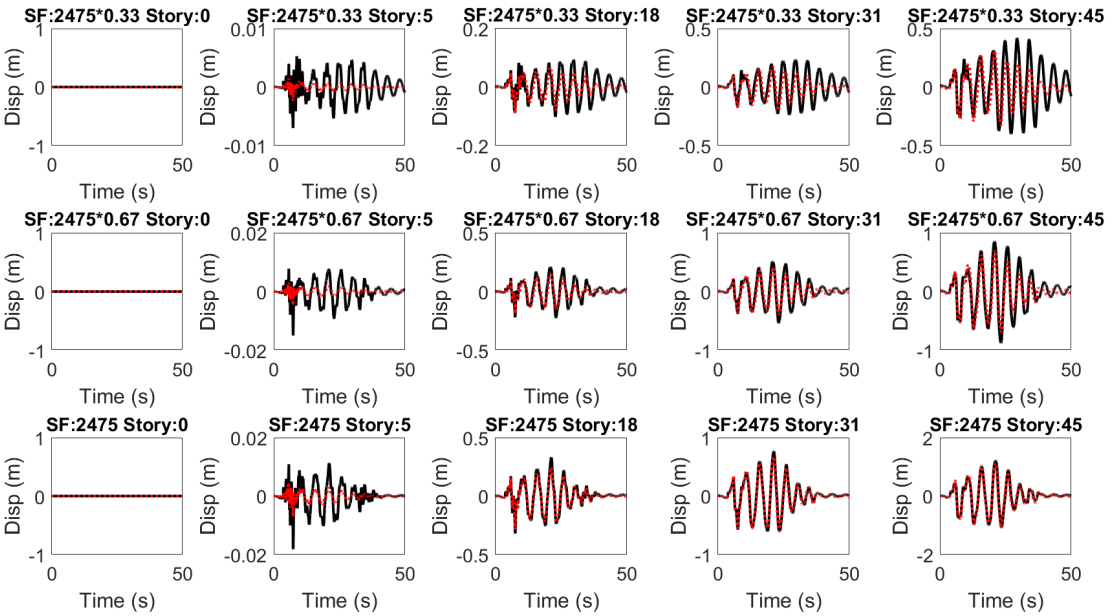

Figure 4.17. STBM-Y: recorded (black solid line) and estimated (red dashed line) floor displacements, eq id: 549.

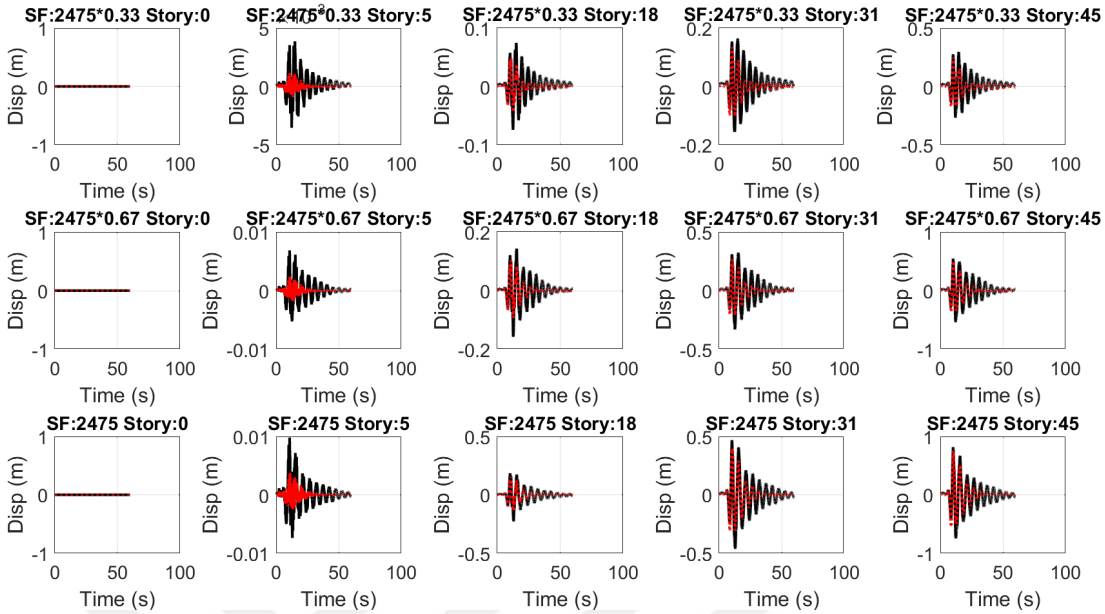

Figure 4.18. STBM-Y: recorded (black solid line) and estimated (red dashed line) floor displacements, eq id: 879.

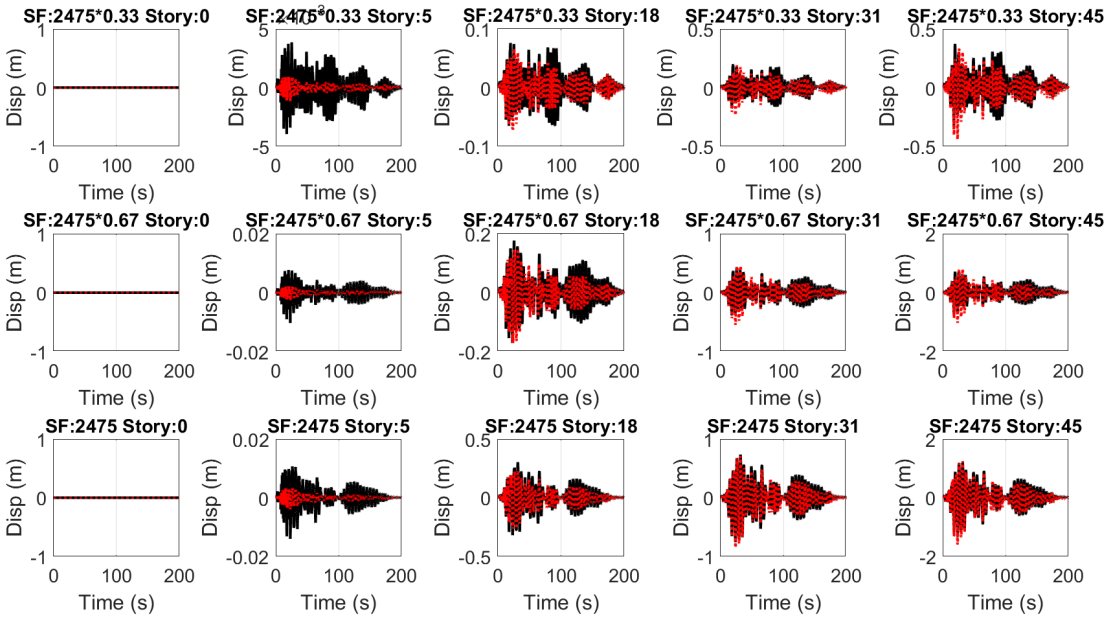

Figure 4.19. STBM-Y: recorded (black solid line) and estimated (red dashed line) floor displacements, eq id: 1115.

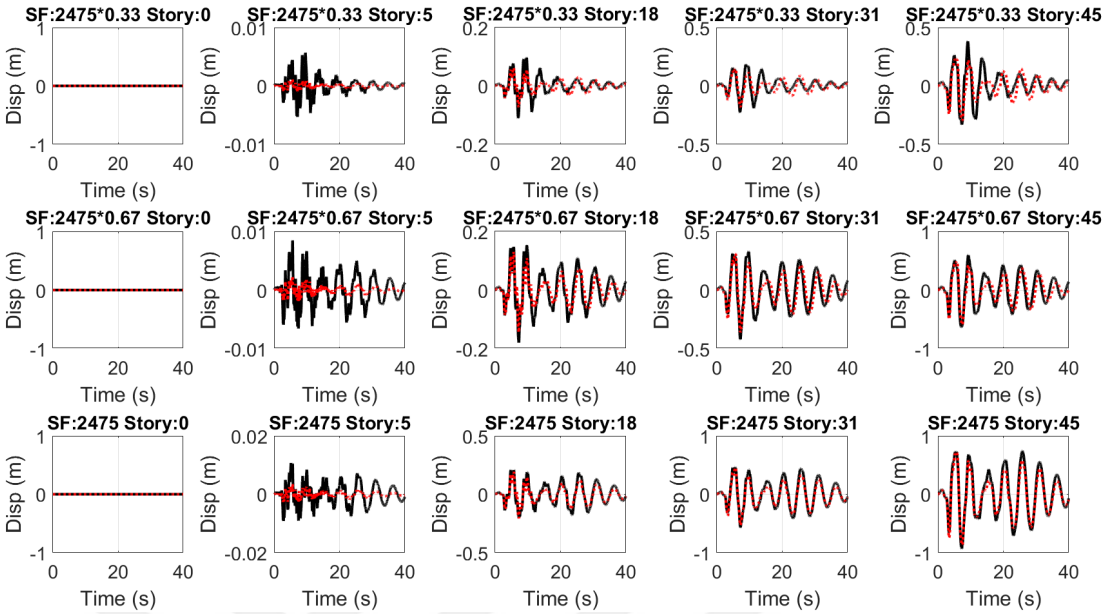

Figure 4.20. STBM-Y: recorded (black solid line) and estimated (red dashed line) floor displacements, eq id: 1165.

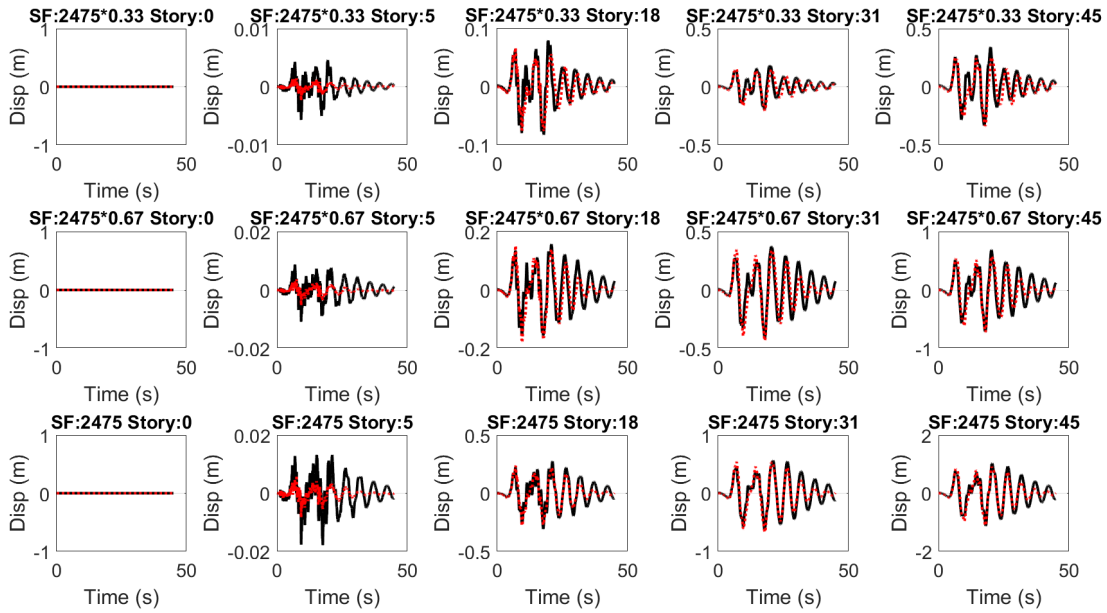

Figure 4.21. STBM-Y: recorded (black solid line) and estimated (red dashed line) floor displacements, eq id: 1615.

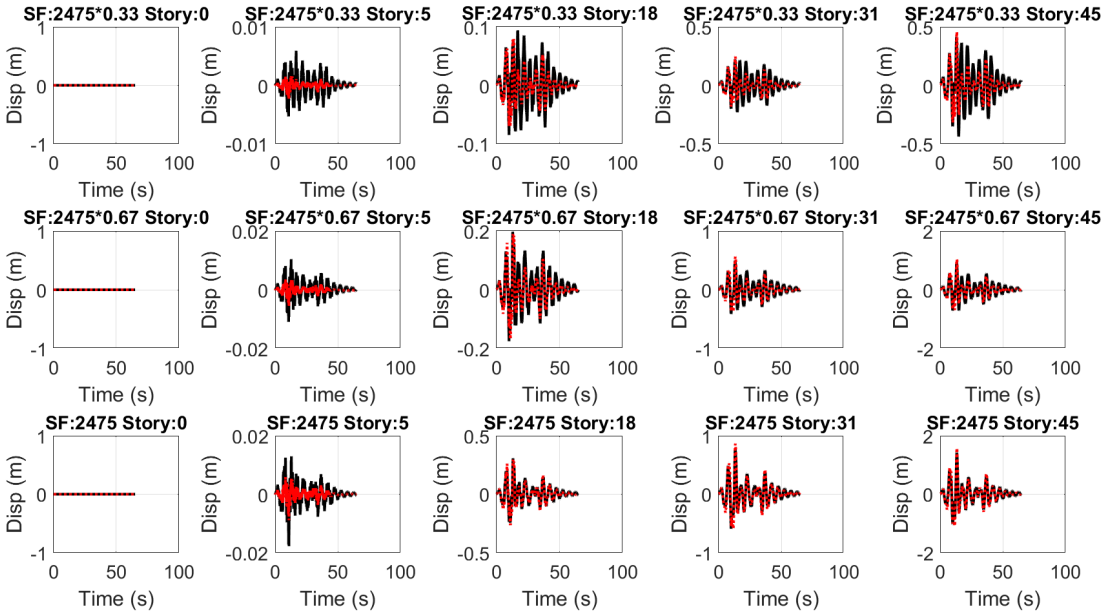

Figure 4.22. STBM-Y: recorded (black solid line) and estimated (red dashed line) floor displacements, eq id: 1633.

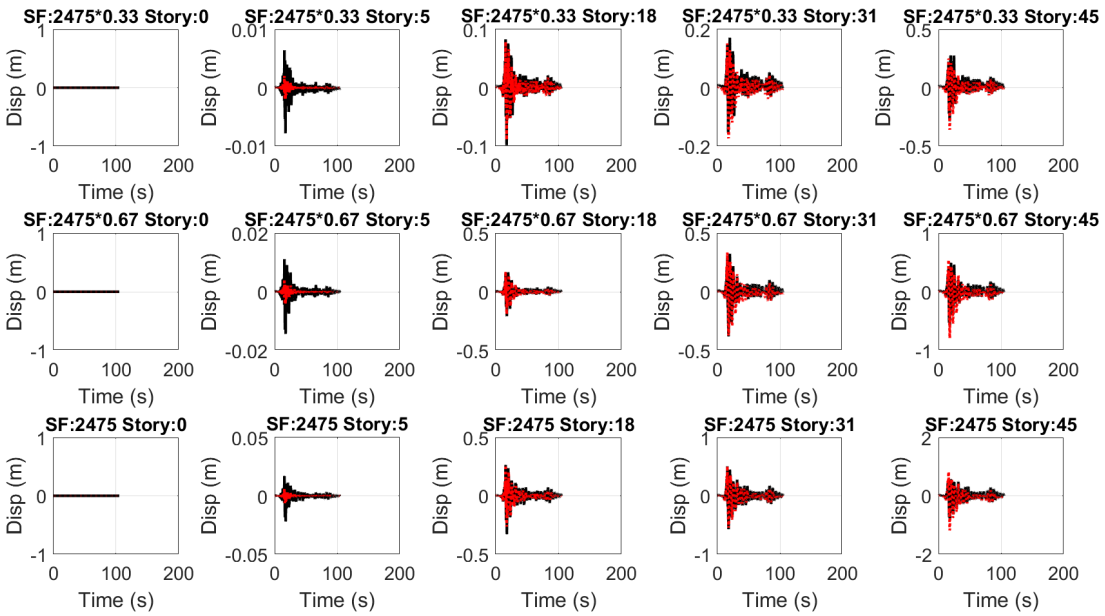

Figure 4.23. STBM-Y: recorded (black solid line) and estimated (red dashed line) floor displacements, eq id: 1794.

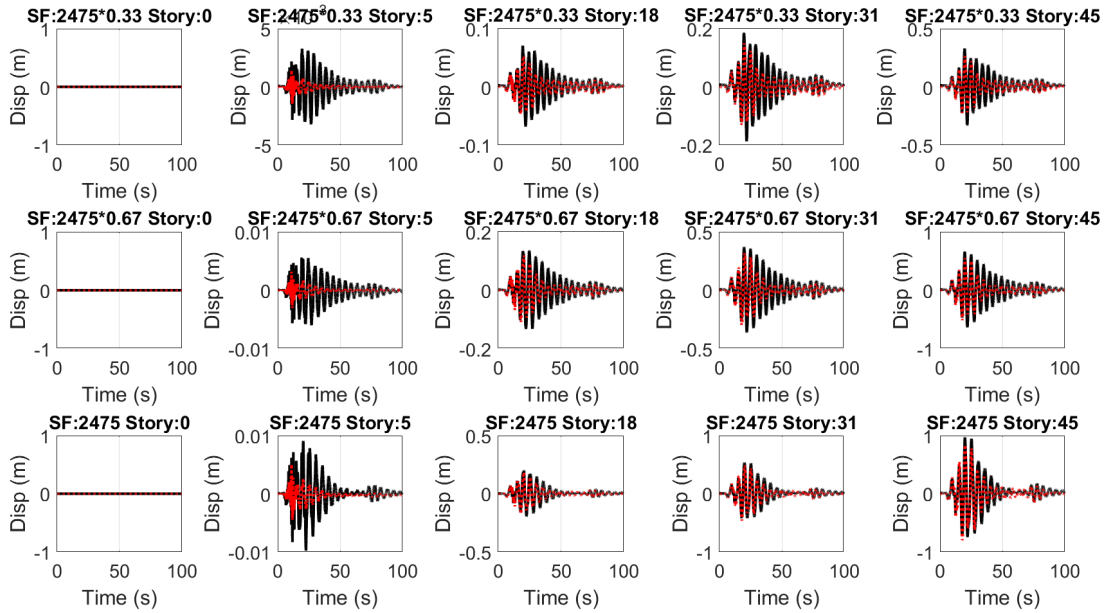

Figure 4.24. STBM-Y: recorded (black solid line) and estimated (red dashed line) floor displacements, eq id: 3954.

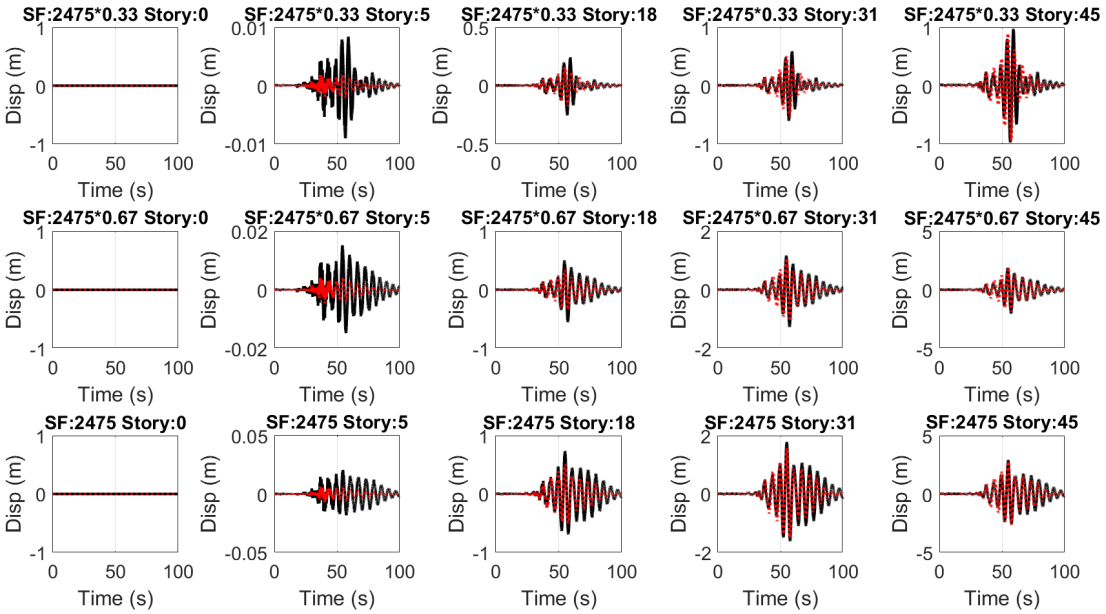

Figure 4.25. STBM-Y: recorded (black solid line) and estimated (red dashed line) floor displacements, eq id: 5836.

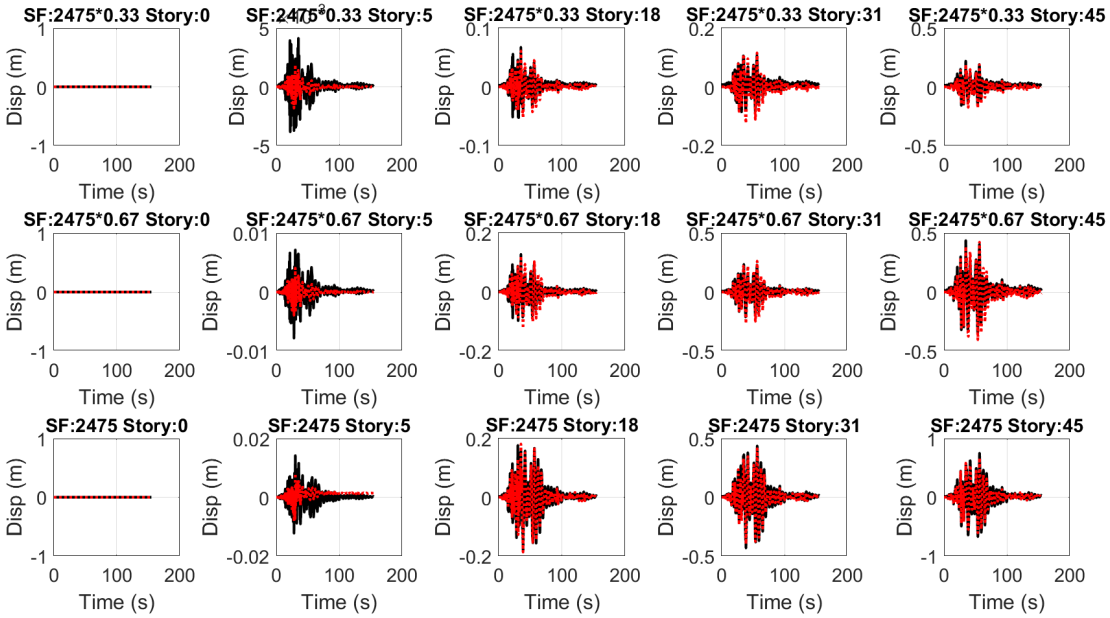

Figure 4.26. STBM-Y: recorded (black solid line) and estimated (red dashed line) floor displacements, eq id: 6980.

There are equations to calculate difference between recorded and estimated responses in literature [43], [83]. Accuracy of the method proposed in this study were examined by computing difference between recorded and estimated floor displacements with Equation 4.22 and calculated error values are represented for X and Y directions in Figure 4.27.

The difference between recorded floor responses and estimated floor responses can be calculated from

$$Error_k = \sqrt{\frac{\sum_{t=0}^{NPT}[z_k(t) - y_k(t)]^2}{\sum_{t=0}^{NPT}[z_k(t)]^2}}, \tag{4.22}$$

where $z_k(t)$ is the simulated floor displacements, $y_k(t)$ is estimated floor displacements and NPT is time length of data. Although there is no reference range to compare the obtained error values, this error function is to enable an objective evaluation for the proposed method.

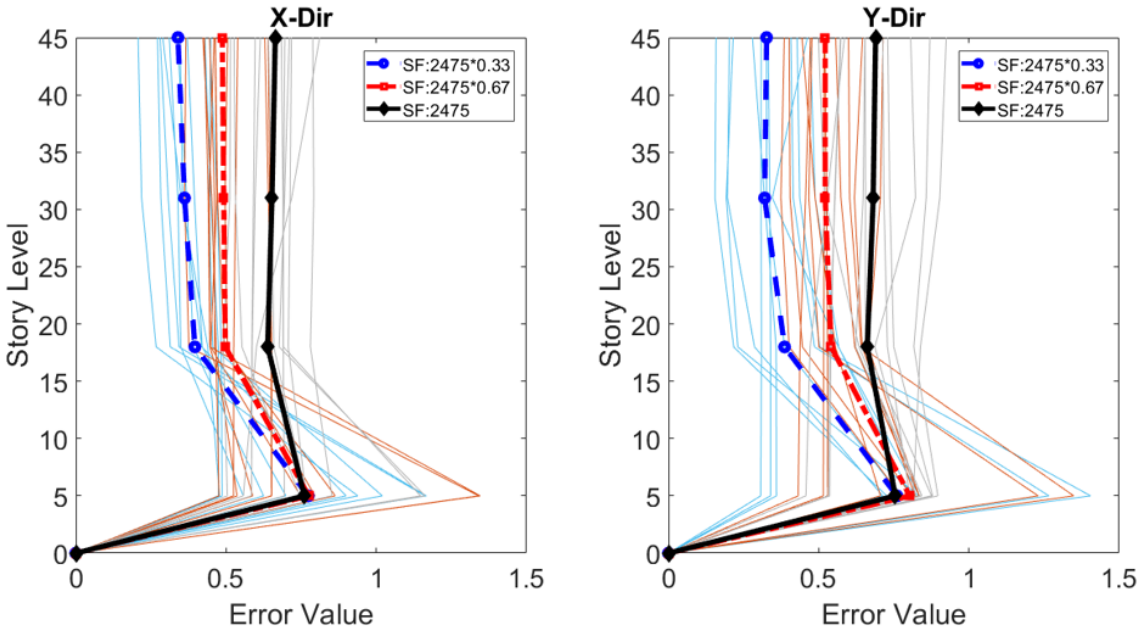

Figure 4.27. STBM: error values between recorded and estimated floor displacements.

It can be clearly observed that recorded and estimated floor displacements show good agreement for instrumented floors. Since structural elements start to pass from elastic region to plastic region with increasing scale factors, error values of instrumented floors increase. Also, maximum error value was obtained at 5th floor because stiffness of structure changes abruptly at that floor with finished basement walls.

After updating simplified mathematical model of the structure, dynamic responses at all floors were estimated and inter-story drift ratios were calculated at each floor along the entire structure. Figure 4.28 and Figure 4.29 represent inter-story drift ratios of the structure for both directions under earthquakes with different scale factors.

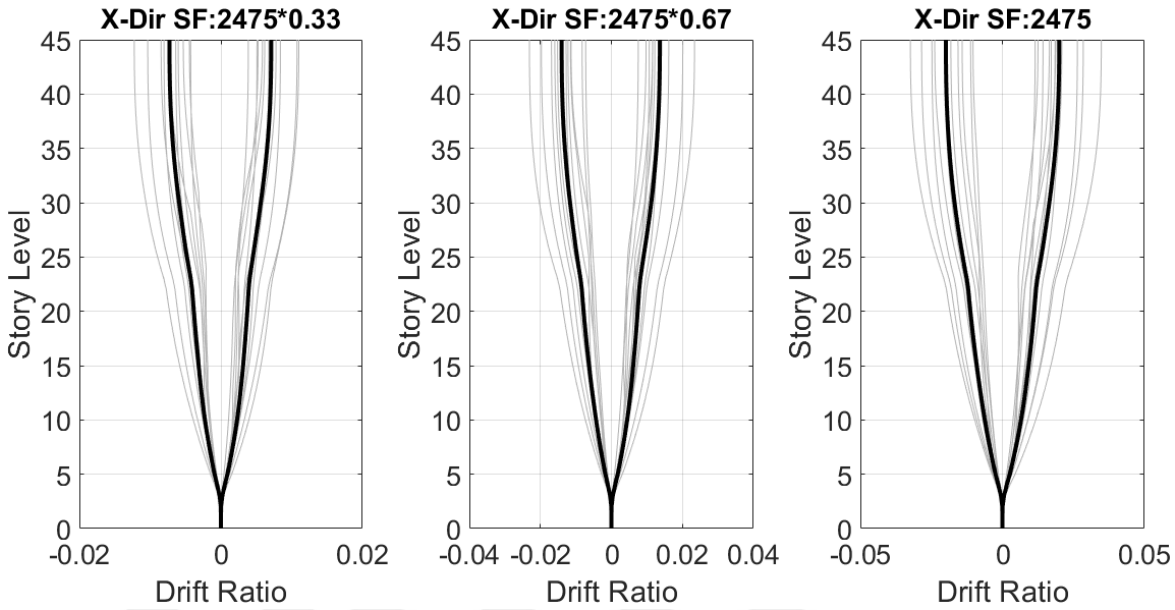

Figure 4.28. STBM-X: estimated inter-story drift ratios.

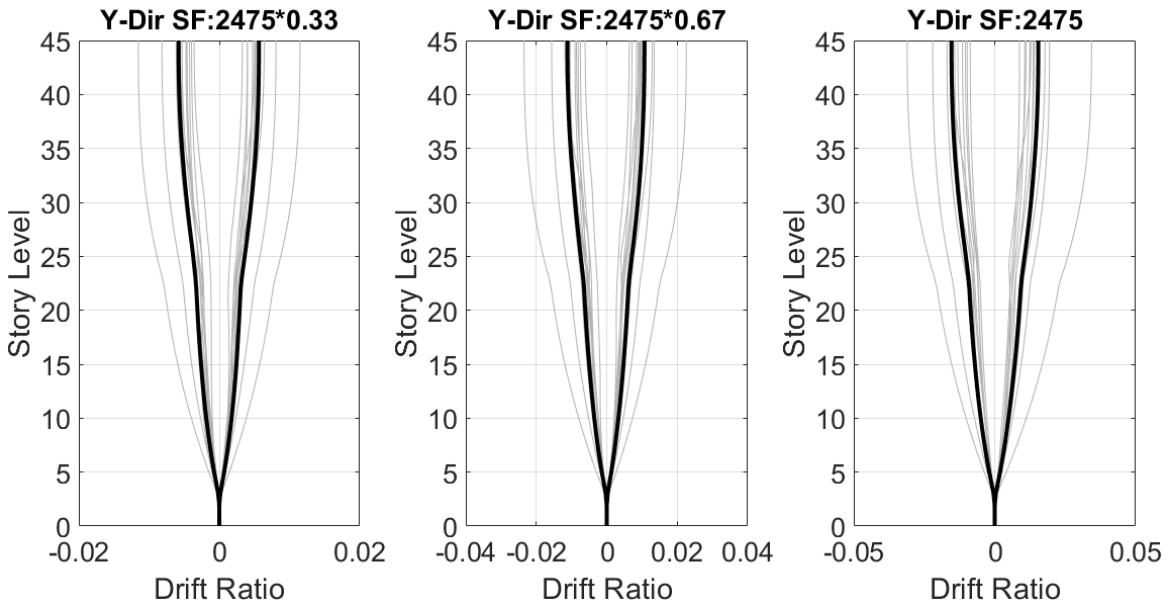

Figure 4.29. STBM-Y: estimated inter-story drift ratios.

4.2. Discrete Timoshenko Beam Model (DTBM)

In this part, continuous Timoshenko beam model was divided into multiple discrete sections with different mechanical properties in order to create simplified mathematical model of structure. Dynamic response of mathematical model was estimated by Transfer Matrix Method (TMM) [85]. This method enables better dynamic response estimation of mathematical model by modelling each story of structure with different mechanical properties. Figure 4.30 represents equilibrium equations for non-uniform mathematical model of structure.

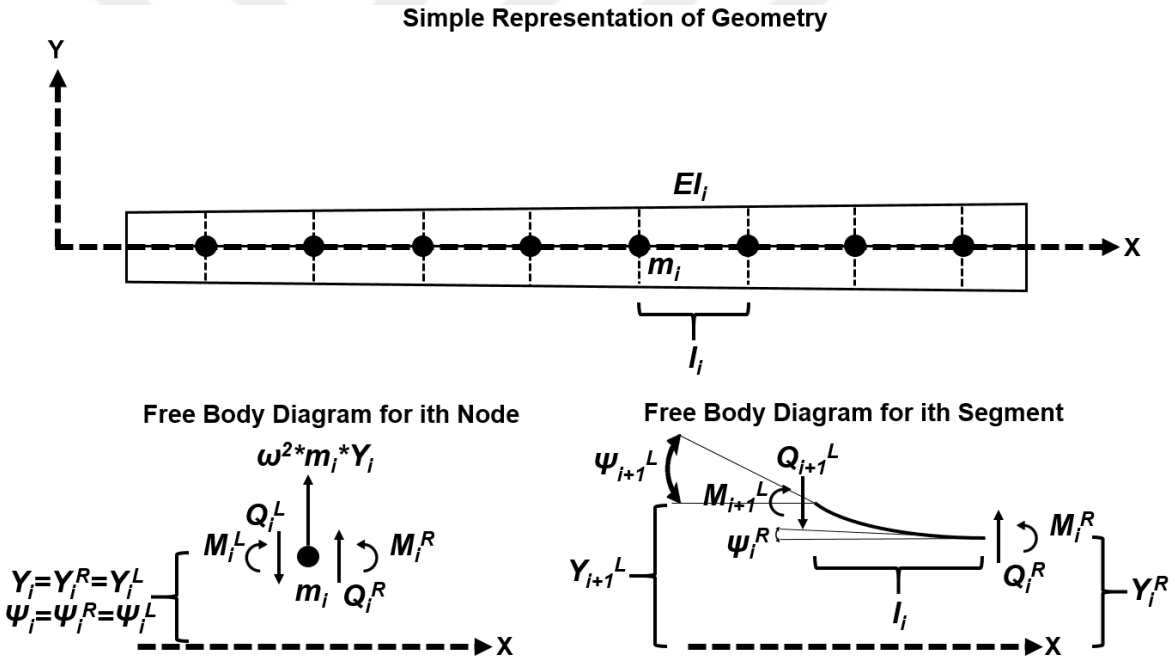

Figure 4.30. DTBM: General overview and equilibrium equations of non-uniform simplified mathematical model of structure.

In this figure, m_i represents lumped mass of ith story, l_i defines height of ith story and I_i shows moment of inertia of cross-sectional area of ith floor. Also, Young's modulus ofi^{th} floor is represented by E_i.

It is clear that total force in Y direction and moment with respect to Z axis must be equal to 0 to provide equilibrium conditions at i^{th} node. Therefore, force equilibrium and moment equilibrium can be provided as

$$\sum F_y = Q_i^R + \omega^2 m_i Y_i - Q_i^L = 0, \tag{4.23}$$

$$\sum M_z = M_i^R - M_i^L = 0. \tag{4.24}$$

In addition, equilibrium conditions must provide deformation continuity at i^{th} node. Therefore, equations can be created as

$$\psi_i = \psi_i^R = \psi_i^L, \tag{4.25}$$

$$Y_i = Y_i^R = Y_i^L. \tag{4.26}$$

In the equations, the symbols Q, M, Y and ψ define shear force, bending moment, transverse displacement and slope at i^{th} story, respectively. Frequency of simplified mathematical beam model is represented by ω. Matrix form of equations providing equilibrium conditions for i^{th} node can be presented as

$$\begin{bmatrix} Y_i^R \\ \psi_i^R \\ M_i^R \\ Q_i^R \end{bmatrix} = \begin{bmatrix} 1 & 0 & 0 & 0 \\ 0 & 1 & 0 & 0 \\ 0 & 0 & 1 & 0 \\ -m_i\omega^2 & 0 & 0 & 1 \end{bmatrix} \begin{bmatrix} Y_i^L \\ \psi_i^L \\ M_i^L \\ Q_i^L \end{bmatrix} = \begin{bmatrix} H_{Si} \end{bmatrix} \begin{bmatrix} Y_i^L \\ \psi_i^L \\ M_i^L \\ Q_i^L \end{bmatrix}. \tag{4.27}$$

In addition, total force in Y direction and moment with respect to Z axis must be equal to 0 to provide equilibrium conditions at i^{th} segment. Therefore, force equilibrium and moment equilibrium can be provided as

$$\sum F_y = Q_{i+1}^L - Q_i^R = 0, \tag{4.28}$$

$$\sum M_z = M_{i+1}^L + Q_{i+1}^L l_i - M_i^R = 0. \tag{4.29}$$

Equilibrium conditions must provide deformation continuity at i^{th} segment. Therefore, equations can be created as

$$\psi_{i+1}^L = \psi_i^R + \alpha_i^{\psi M} M_{i+1}^L + \alpha_i^{\psi Q} Q_{i+1}^L, \tag{4.30}$$

$$Y_{i+1}^L = Y_i^R + l_i \psi_i^R + \alpha_i^{YM} M_{i+1}^L + \alpha_i^{YQ} Q_{i+1}^L, \tag{4.31}$$

where α_i^{YM} and $\alpha_i^{\psi M}$ are coefficients for linear and angular displacements, respectively. They are needed in order to define unit linear and angular deformations for $(i+1)^{th}$ segment relative to i^{th} segment when unit bending moment is applied at $(i+1)^{th}$ segment. On the other hand, α_i^{YQ} and $\alpha_i^{\psi Q}$ are coefficients for linear and angular displacements, respectively. They are needed in order to define unit linear and angular deformations for $(i+1)^{th}$ segment relative to i^{th} segment when unit shear force is applied at $(i+1)^{th}$ segment. These coefficients are defined in terms of length of segment, modulus of elasticity and moment of inertia [85]. These coefficients are expressed as

$$\alpha_i^{YM} = \frac{l_i^2}{2EI_i}, \tag{4.32}$$

$$\alpha_i^{\psi M} = \frac{l_i}{EI_i}, \tag{4.33}$$

$$\alpha_i^{YQ} = \frac{l_i^3}{3EI_i}, \tag{4.34}$$

$$\alpha_i^{\psi Q} = \frac{l_i^2}{2EI_i}. \tag{4.35}$$

Matrix form of equations providing equilibrium conditions for i^{th} segment can be represented as

$$\begin{bmatrix} Y_{i+1}^L \\ \psi_{i+1}^L \\ M_{i+1}^L \\ Q_{i+1}^L \end{bmatrix} = \begin{bmatrix} 1 & l_i & \frac{l_i^2}{2EI_i} & \frac{l_i^3}{-6EI_i} \\ 0 & 1 & \frac{l_i}{EI_i} & \frac{-l_i^2}{-2EI_i} \\ 0 & 0 & 1 & -l_i \\ 0 & 0 & 0 & 1 \end{bmatrix} \begin{bmatrix} Y_i^R \\ \psi_i^R \\ M_i^R \\ Q_i^R \end{bmatrix} = \begin{bmatrix} H_{Fi} \end{bmatrix} \begin{bmatrix} Y_i^R \\ \psi_i^R \\ M_i^R \\ Q_i^R \end{bmatrix}. \tag{4.36}$$

However, these equations are valid for only flexural beams. Shear deformation and inertia effects due to lumped mass must be considered in order to reorganize these equations for Timoshenko beams. Shear deformation and inertia effects due to lumped mass can be calculated as

$$|M_{Ri}| = J_i \omega^2 \psi_i, \tag{4.37}$$

$$|Y_{Si}| = l_i \frac{Q_i}{k' G A_i}. \tag{4.38}$$

In these equations, J_i is moment of inertia of lumped mass m_i, G is shear modulus, k' represents shear coefficient and A_i is defined to represent cross-sectional area of ith segment. Based on new updates for Timoshenko beam, H_{Si} and H_{Fi} matrices can be

clearly obtained. Transfer matrix is equal to multiplication of H_{Si} and H_{Fi} matrices. H_{Si} and H_{Fi} matrices can be computed by

$$\left[H_{Si}\right] = \begin{bmatrix} 1 & 0 & 0 & 0 \\ 0 & 1 & 0 & 0 \\ 0 & 0 & -J_i\omega^2 & 0 \\ -m_i\omega^2 & 0 & 0 & 1 \end{bmatrix}, \tag{4.39}$$

$$\left[H_{Fi}\right] = \begin{bmatrix} 1 & l_i & \frac{l_i^2}{2EI_i} & \frac{l_i^3}{-6EI_i} + \frac{l_i}{k'GA_i} \\ 0 & 1 & \frac{l_i}{EI_i} & \frac{-l_i^2}{-2EI_i} \\ 0 & 0 & 1 & -l_i \\ 0 & 0 & 0 & 1 \end{bmatrix}. \tag{4.40}$$

Therefore, complete transfer matrix of entire Timoshenko beam is equal to

$$\left[H\right] = \left[H_{S_{n+1}}\right]\left[H_{F_n}\right]\left[H_{S_n}\right]\left[H_{F_{n-1}}\right]\left[H_{S_{n-1}}\right]\cdots\left[H_{F_1}\right]\left[H_{S_1}\right], \tag{4.41}$$

$$\left[H\right] = \left[H_{S_{n+1}}\right]\prod_{i=0}^{n}\left[H_i\right] = \begin{bmatrix} H_{11} & H_{12} & H_{13} & H_{14} \\ H_{21} & H_{22} & H_{23} & H_{24} \\ H_{31} & H_{32} & H_{33} & H_{34} \\ H_{41} & H_{42} & H_{43} & H_{44} \end{bmatrix}. \tag{4.42}$$

Finally, correlation between first node and end node of Timoshenko beam can be obtained as follows

$$\begin{bmatrix} Y_{n+1}^R \\ \psi_{n+1}^R \\ M_{n+1}^R \\ Q_{n+1}^R \end{bmatrix} = \left[H\right]\begin{bmatrix} Y_1^L \\ \psi_1^L \\ M_1^L \\ Q_1^L \end{bmatrix}. \tag{4.43}$$

Fundamental purpose of this section is to estimate dynamic response of structure by analyzing simplified mathematical model of Timoshenko beam with Transfer Function Method. In this mathematical problem, one of boundary condition is fixed while other boundary condition is free.

Therefore, frequencies of simplified mathematical model can be estimated by

$$\Big[\Delta(\omega)\Big] = \begin{vmatrix} H_{33} & H_{34} \\ H_{43} & H_{44} \end{vmatrix} = H_{33}H_{44} - H_{34}H_{43} = 0. \tag{4.44}$$

Corresponding mode shape of each ω can be estimated by obtaining transverse displacement of each node (Y_i) at points whose determinant of the matrix is zero.

Simplified mathematical model was updated using Equation 4.16 given in Stepped Timoshenko Beam section. Similarly with previous section, initial values of G^* are separately calculated from shear beam formula ($G^*_{initial} = \rho(4Lf_1)^2$) for each direction and correlation between E^* and G^* are provided by using C values calculated based on modal frequency ratios of FEM for both directions [82].

Algorithm updates mass and G^* value in each step until it finds minimum error value between the results of FEM and discrete Timoshenko beam model. In the analyses, it was assumed that there were sensors at only five points of modelled tall building (Story 0, Story 5, Story 18, Story 31 and Story 45).

Updated modal frequencies and mode shapes were represented for both directions in Figure 4.31 and Figure 4.32. In algorithm, non-updated models are beam models of the structure whose geometry, mass and stiffness distribution is uniform. On the other hand, updated models represent the numerical beam models of the structure consisting of six different sections with different mechanical properties.

According to mathematical representation of Timoshenko beam, dynamic properties of uniform numerical beam model are highly dependent on the ratio between the flexural rigidity and shear rigidity (C value).

In addition to C value, proper definition of geometry, mass and stiffness distribution in numerical model is critical to estimate consistent modal frequencies and mode shapes with identification results for non-uniform discrete models.

It is obvious from modal frequencies and MAC values that updating algorithm creates most suitable numerical model by calibrating mass, G^* and E^* values for six different sections to obtain minimum error value between results of FEM and discrete Timoshenko beam model.

Although the contribution of MAC values to error value is limited, obtaining consistent mode shapes with identification results is essential to estimate more reliable acceleration values of non-instrumented floors.

Floor displacements of mathematical model analyzing with TMM were estimated using the same procedure explained in STBM. Figure 4.33 - Figure 4.54 represent the recorded floor displacements and estimated floor displacements for X direction and Y direction.

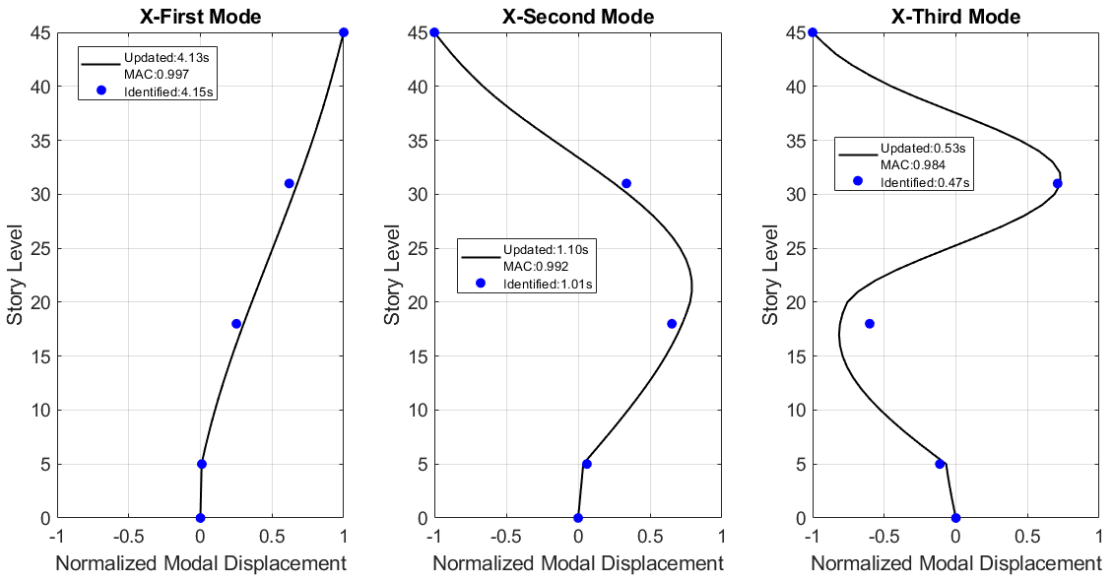

Figure 4.31. DTBM-X: updated and identified modal properties.

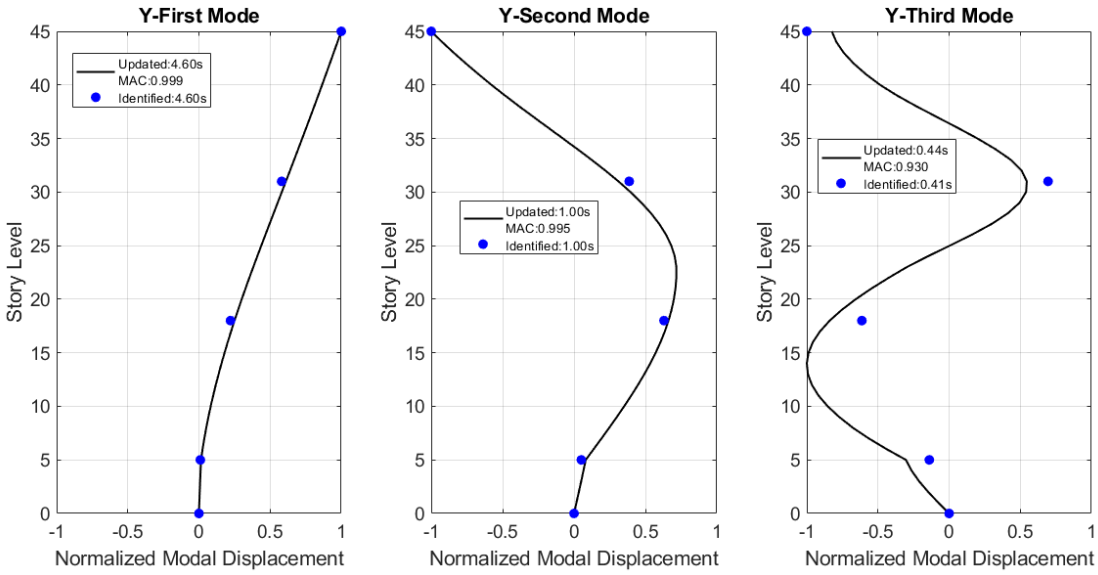

Figure 4.32. DTBM-Y: updated and identified modal properties.

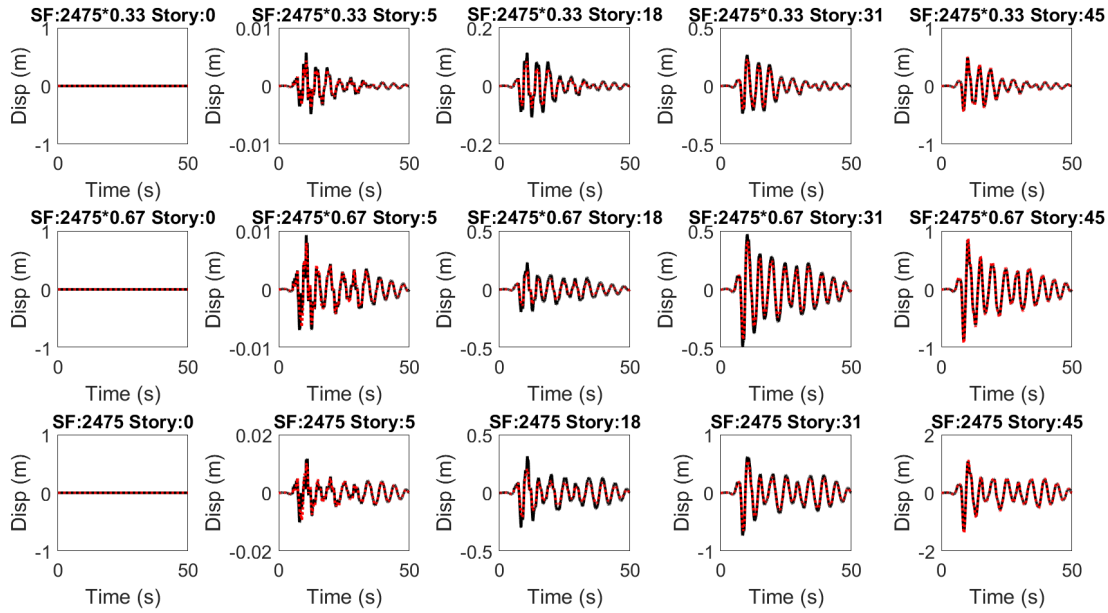

Figure 4.33. DTBM-X: recorded (black solid line) and estimated (red dashed line) floor displacements, eq id: 178.

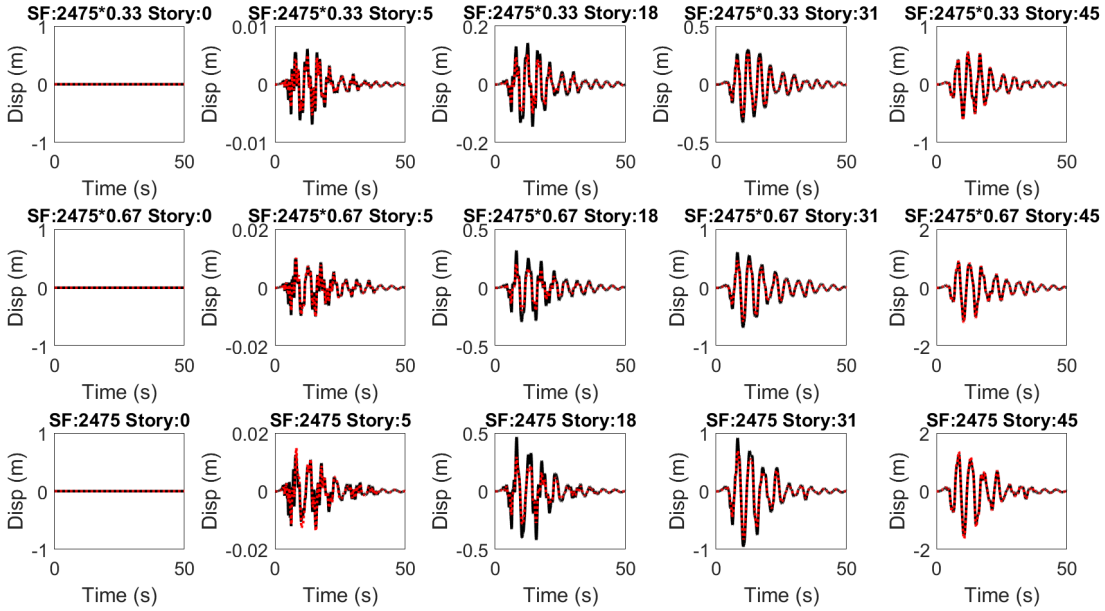

Figure 4.34. DTBM-X: recorded (black solid line) and estimated (red dashed line) floor displacements, eq id: 549.

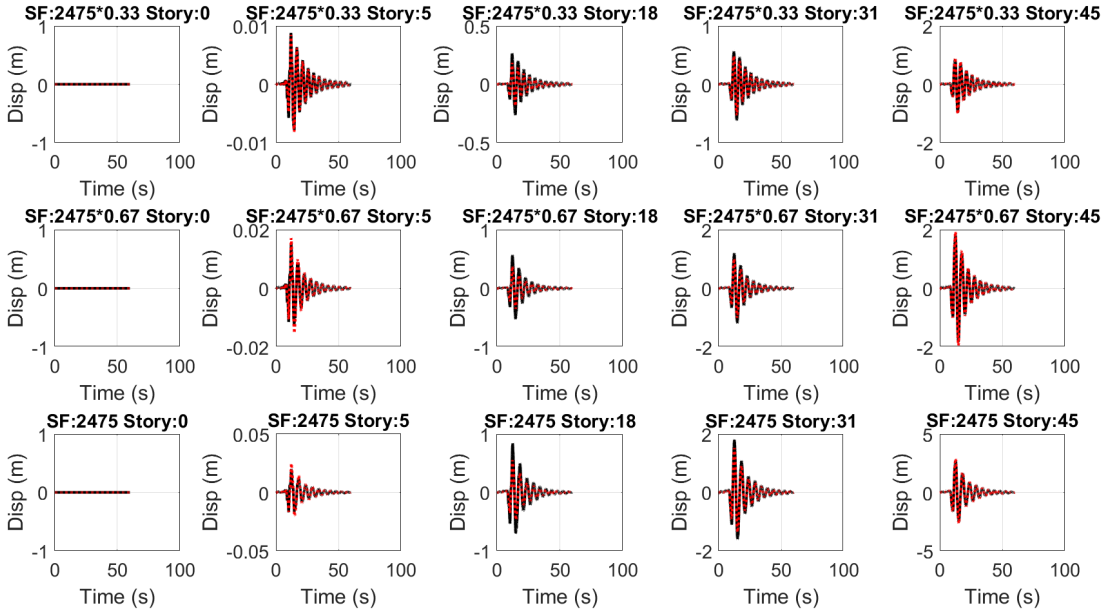

Figure 4.35. DTBM-X: recorded (black solid line) and estimated (red dashed line) floor displacements, eq id: 879.

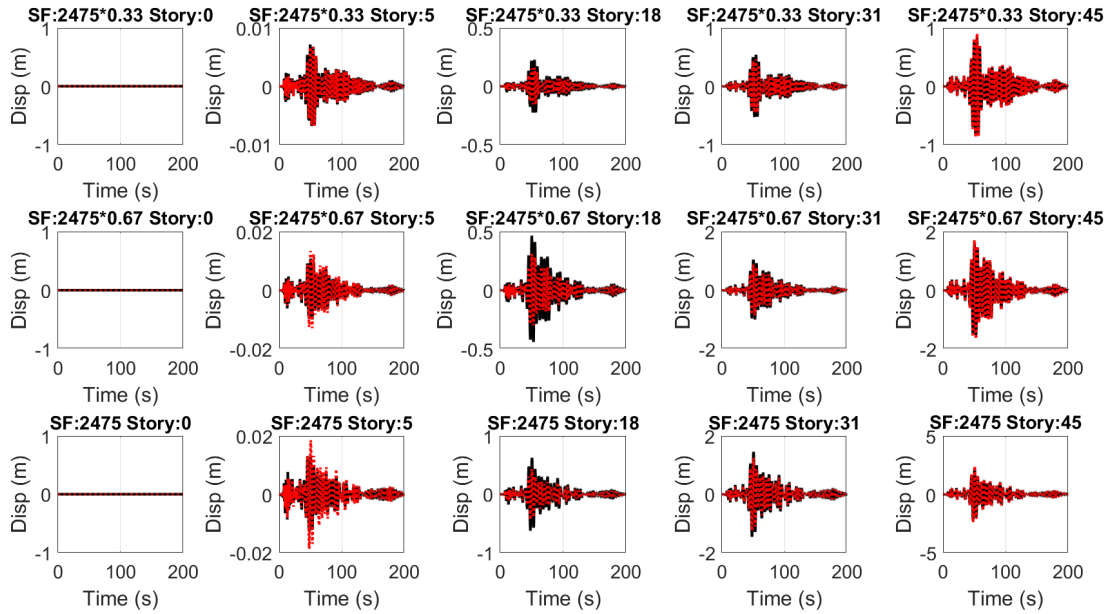

Figure 4.36. DTBM-X: recorded (black solid line) and estimated (red dashed line) floor displacements, eq id: 1115.

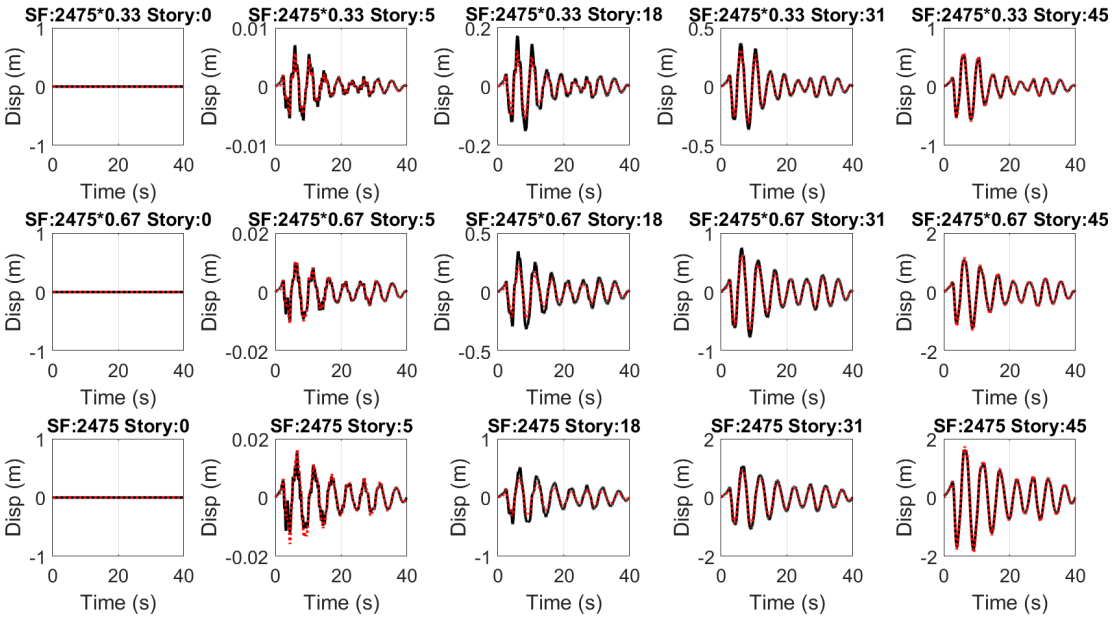

Figure 4.37. DTBM-X: recorded (black solid line) and estimated (red dashed line) floor displacements, eq id: 1165.

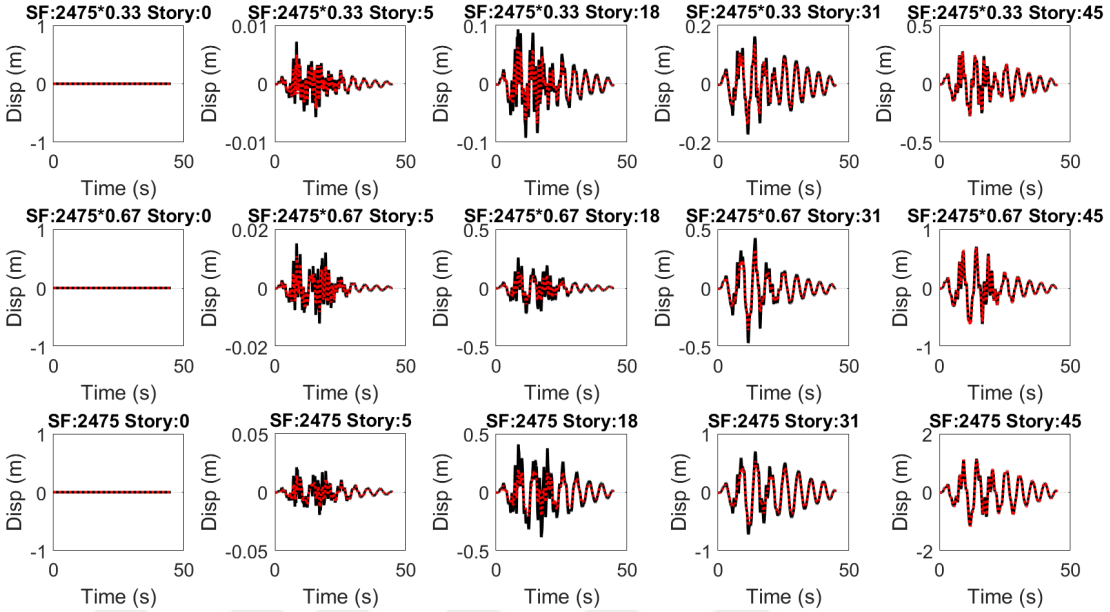

Figure 4.38. DTBM-X: recorded (black solid line) and estimated (red dashed line) floor displacements, eq id: 1615.

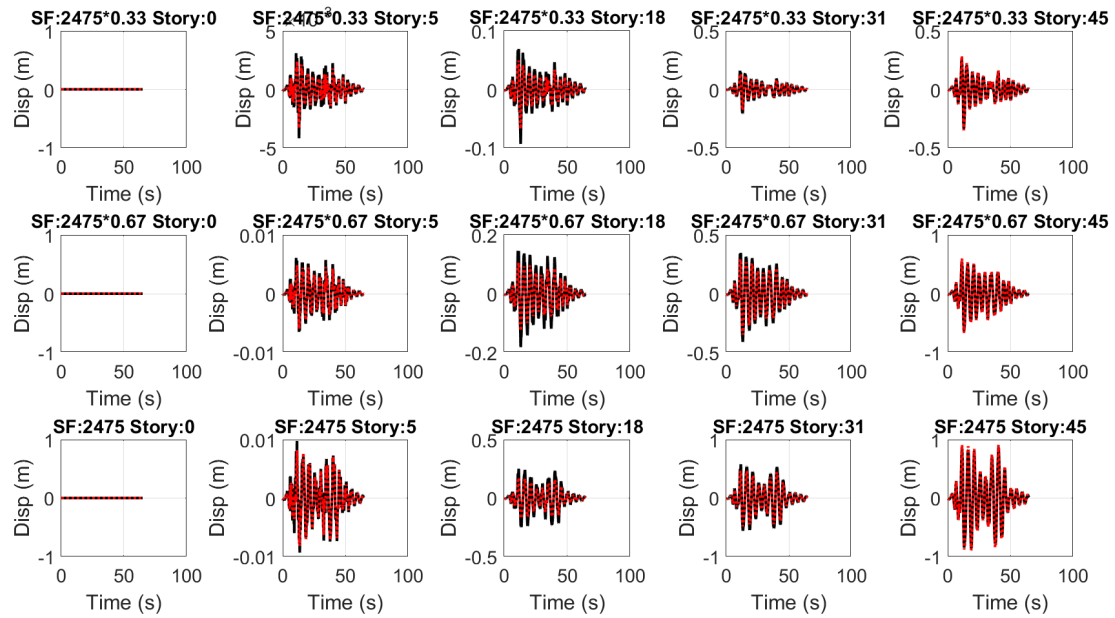

Figure 4.39. DTBM-X: recorded (black solid line) and estimated (red dashed line) floor displacements, eq id: 1633.

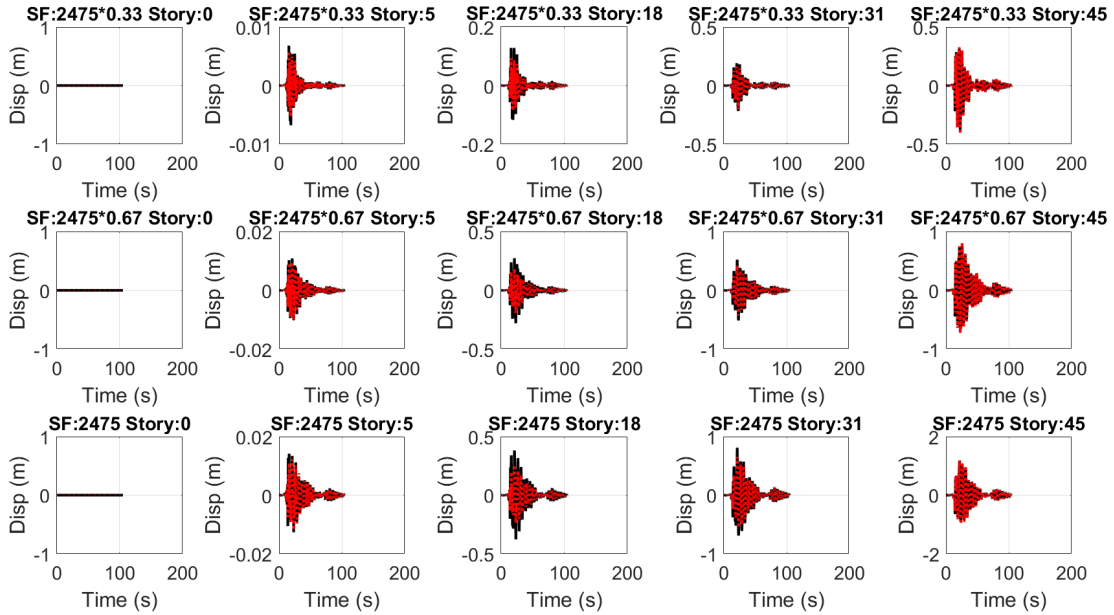

Figure 4.40. DTBM-X: recorded (black solid line) and estimated (red dashed line) floor displacements, eq id: 1794.

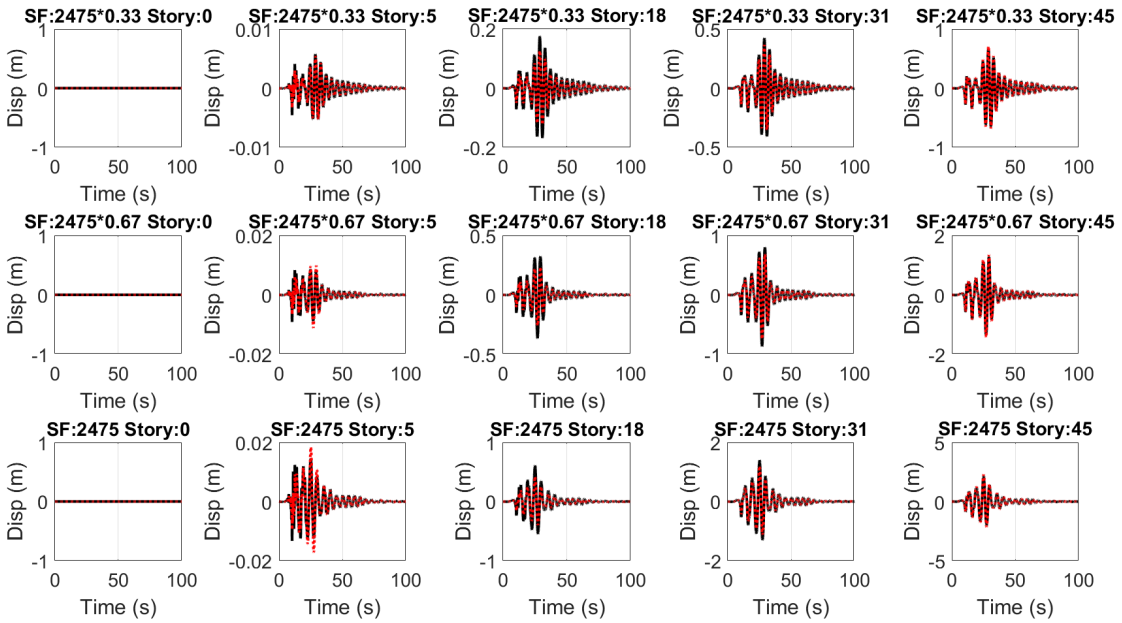

Figure 4.41. DTBM-X: recorded (black solid line) and estimated (red dashed line) floor displacements, eq id: 3954.

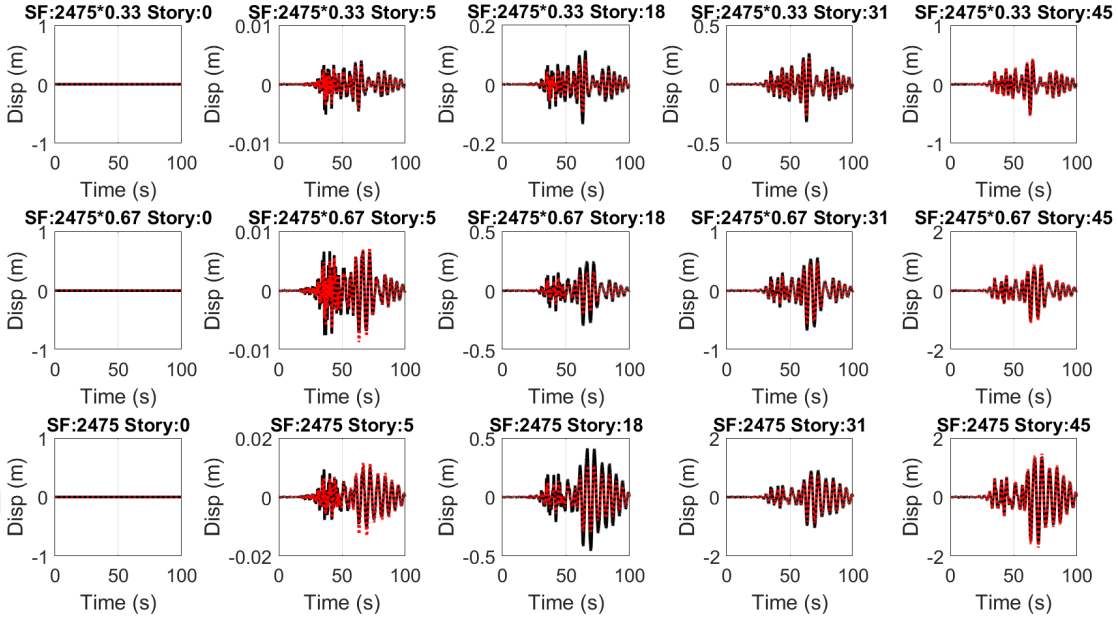

Figure 4.42. DTBM-X: recorded (black solid line) and estimated (red dashed line) floor displacements, eq id: 5836.

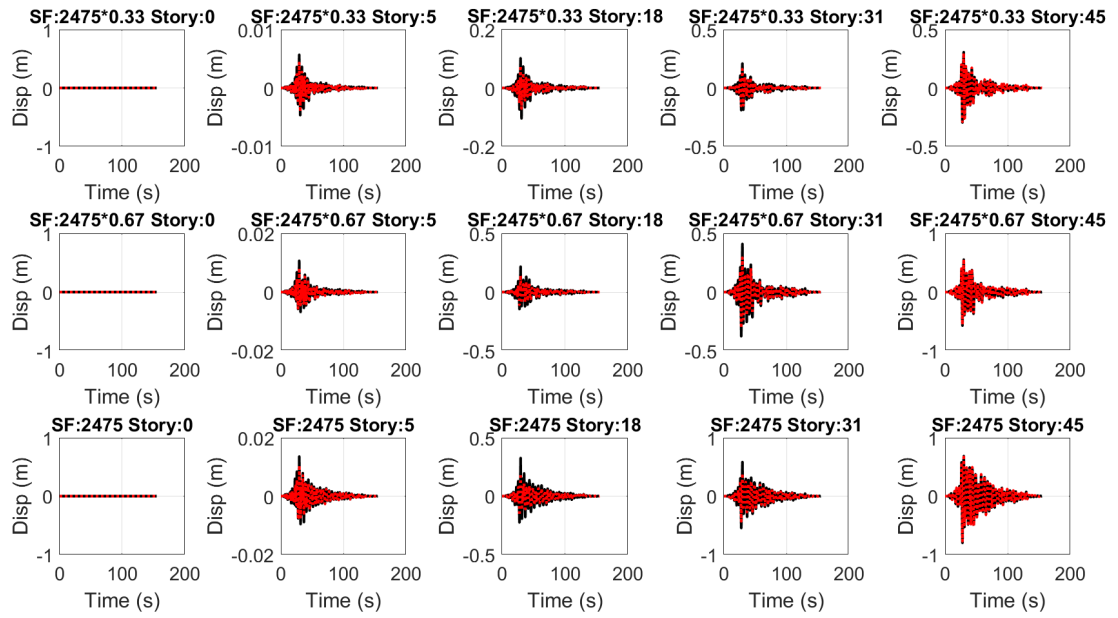

Figure 4.43. DTBM-X: recorded (black solid line) and estimated (red dashed line) floor displacements, eq id: 6980.

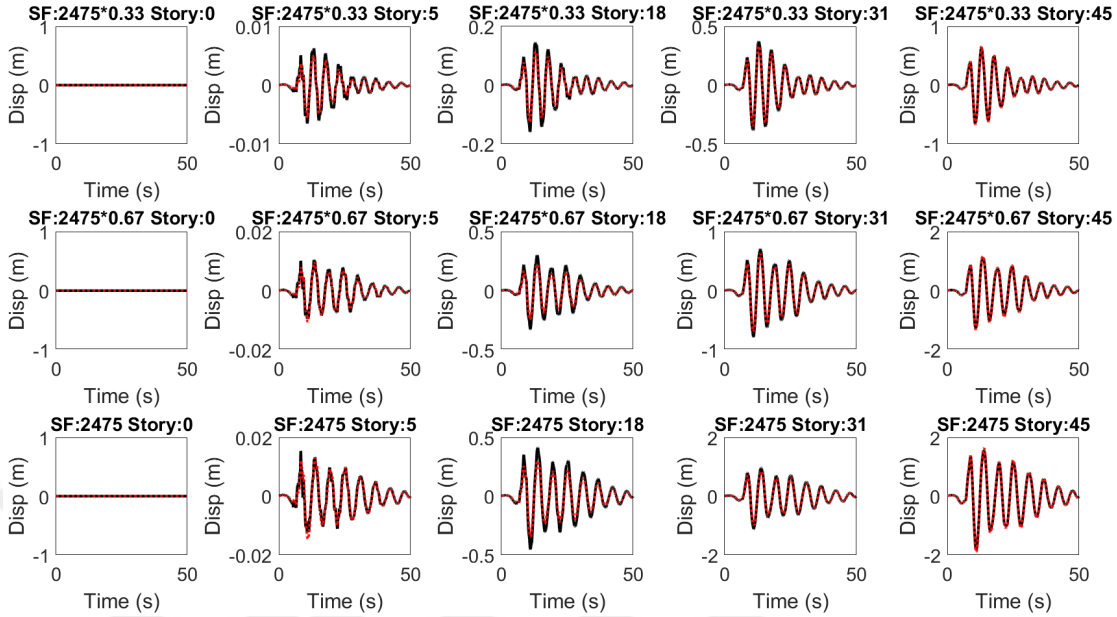

Figure 4.44. DTBM-Y: recorded (black solid line) and estimated (red dashed line) floor displacements, eq id: 178.

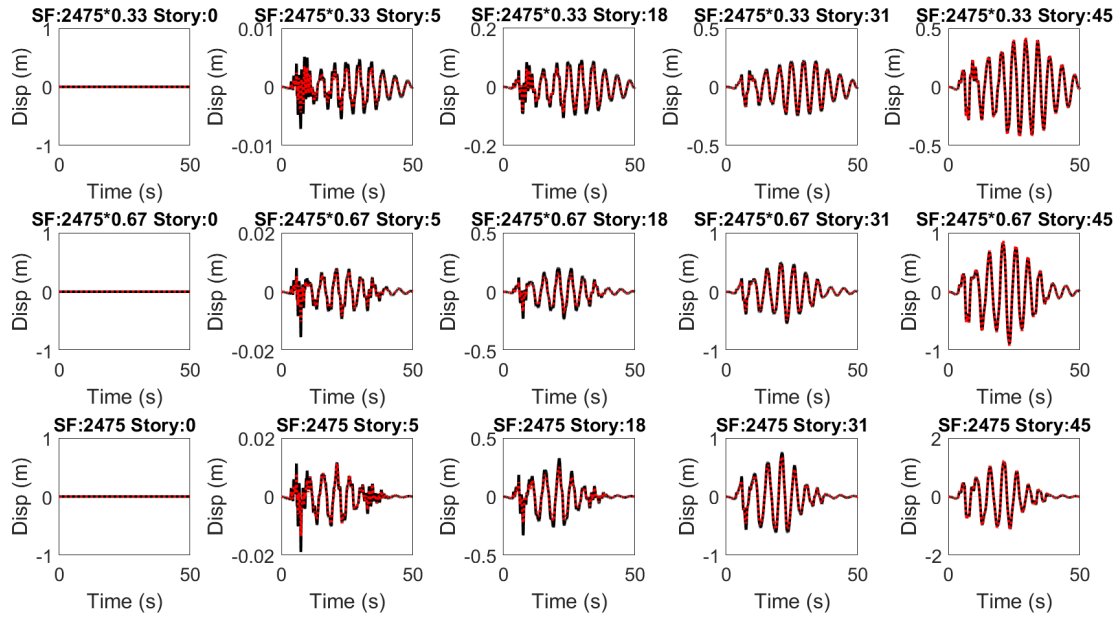

Figure 4.45. DTBM-Y: recorded (black solid line) and estimated (red dashed line) floor displacements, eq id: 549.

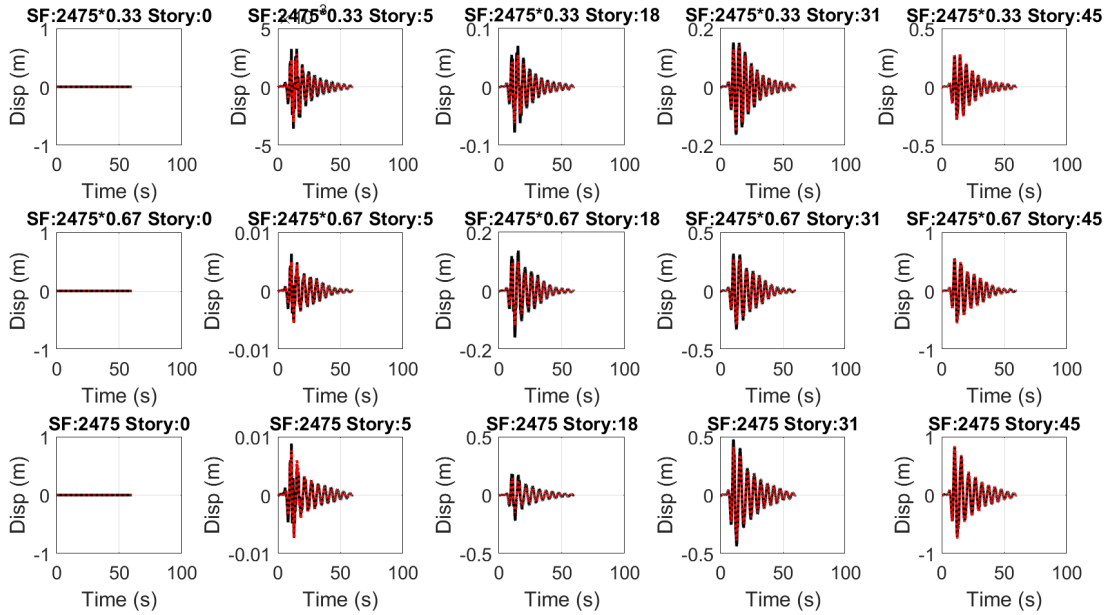

Figure 4.46. DTBM-Y: recorded (black solid line) and estimated (red dashed line) floor displacements, eq id: 879.

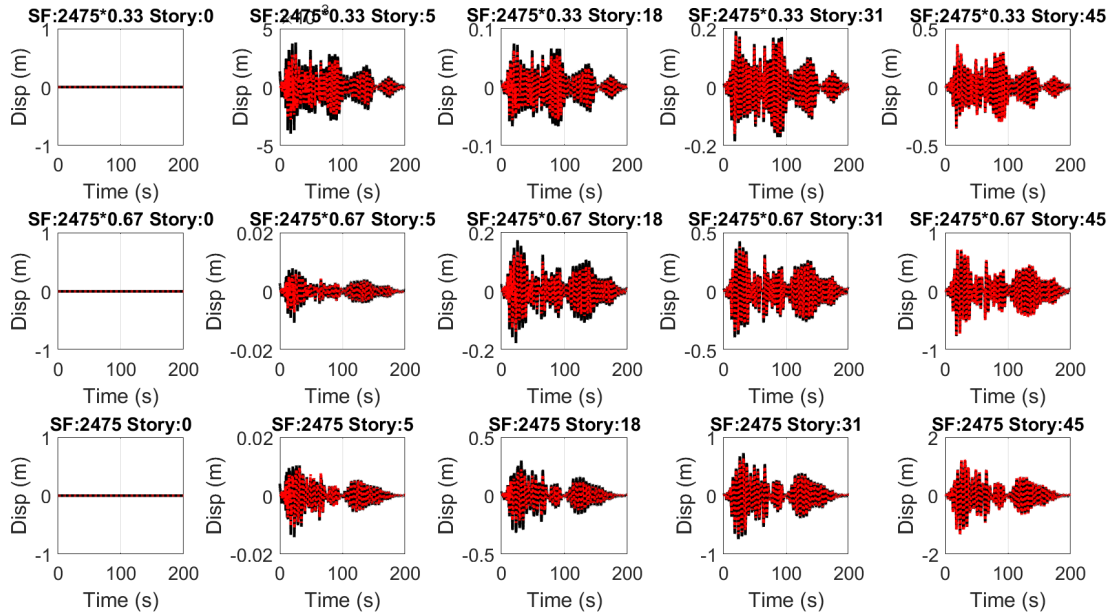

Figure 4.47. DTBM-Y: recorded (black solid line) and estimated (red dashed line) floor displacements, eq id: 1115.

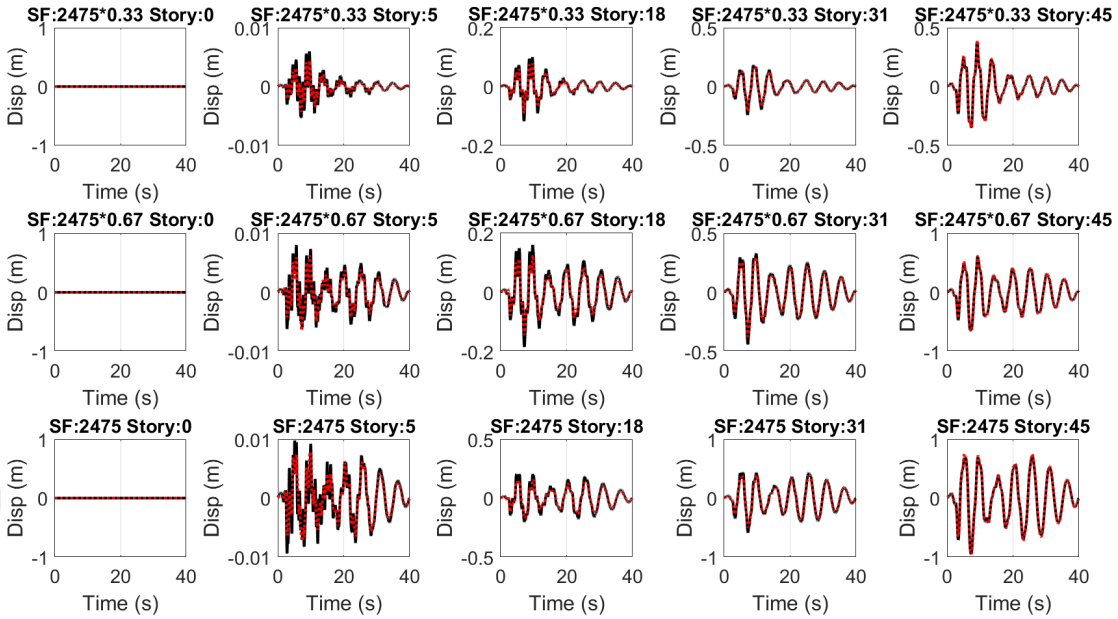

Figure 4.48. DTBM-Y: recorded (black solid line) and estimated (red dashed line) floor displacements, eq id: 1165.

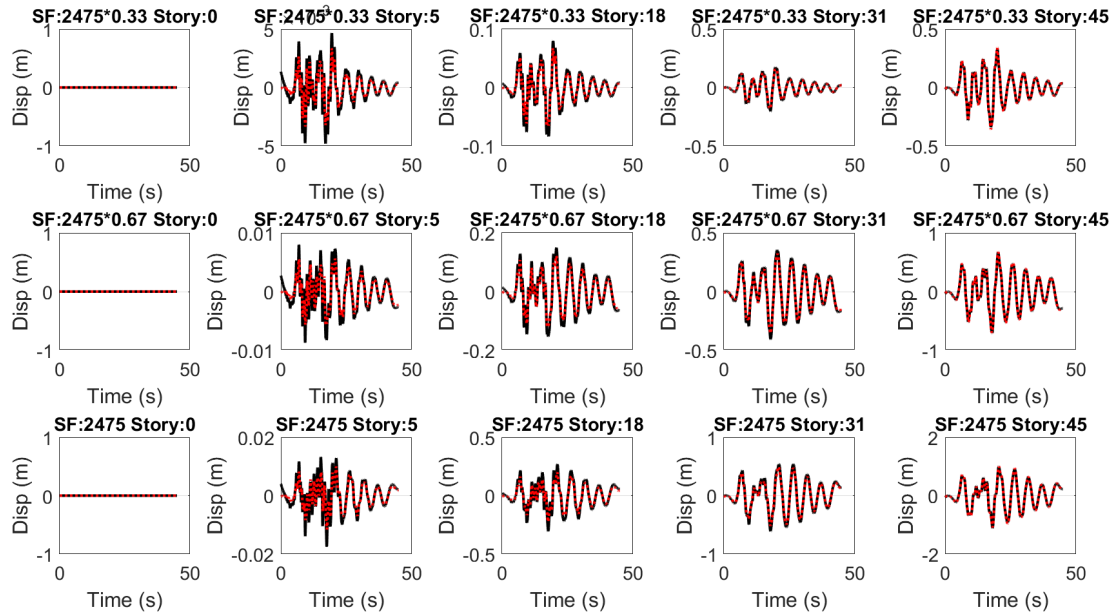

Figure 4.49. DTBM-Y: recorded (black solid line) and estimated (red dashed line) floor displacements, eq id: 1615.

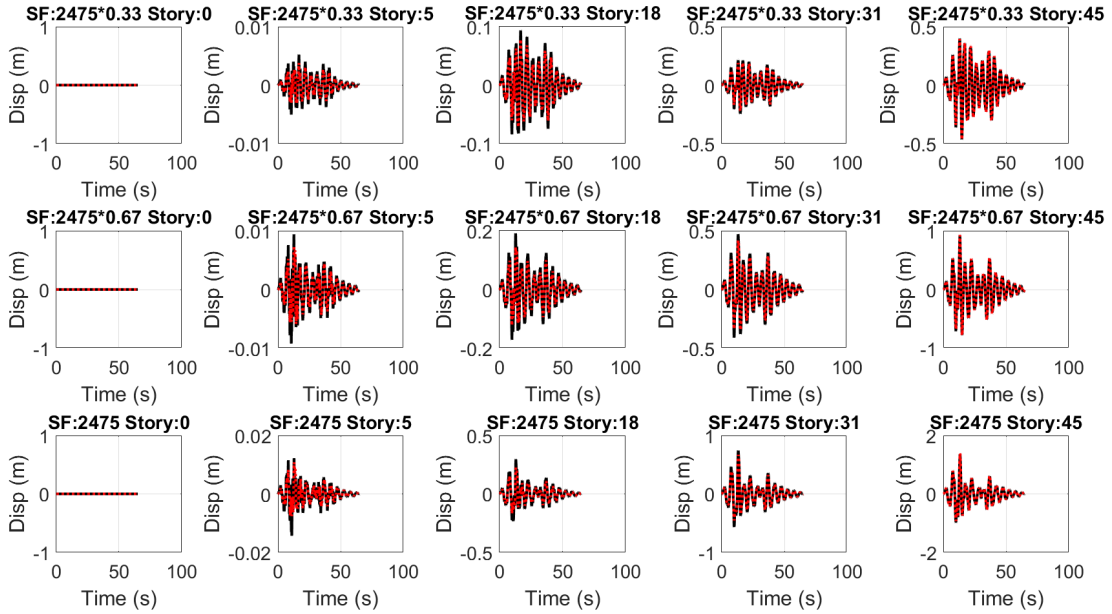

Figure 4.50. DTBM-Y: recorded (black solid line) and estimated (red dashed line) floor displacements, eq id: 1633.

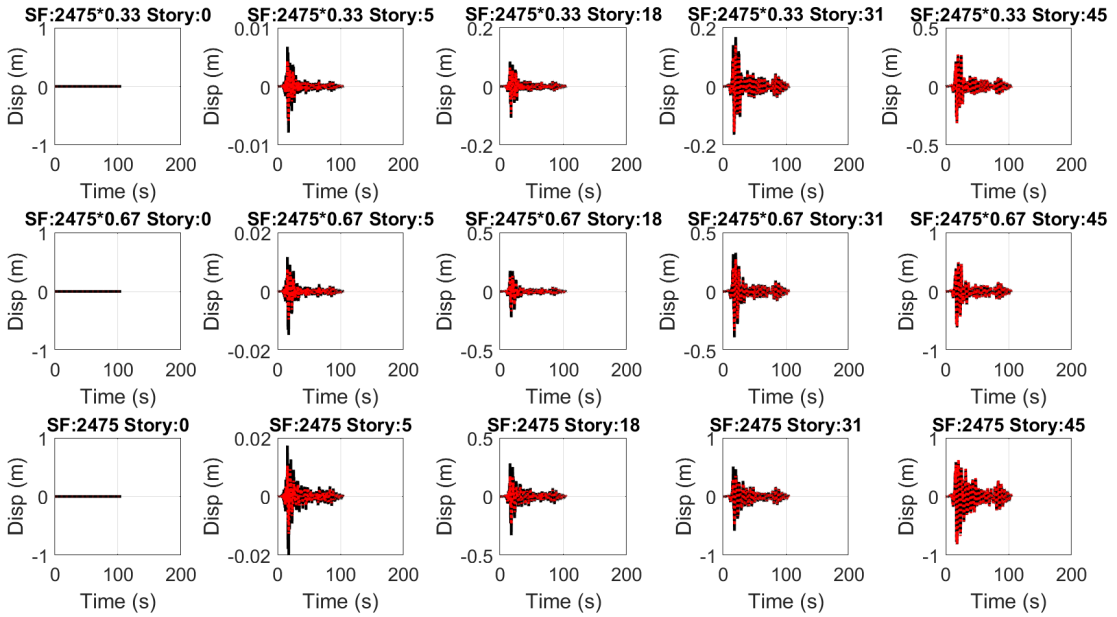

Figure 4.51. DTBM-Y: recorded (black solid line) and estimated (red dashed line) floor displacements, eq id: 1794.

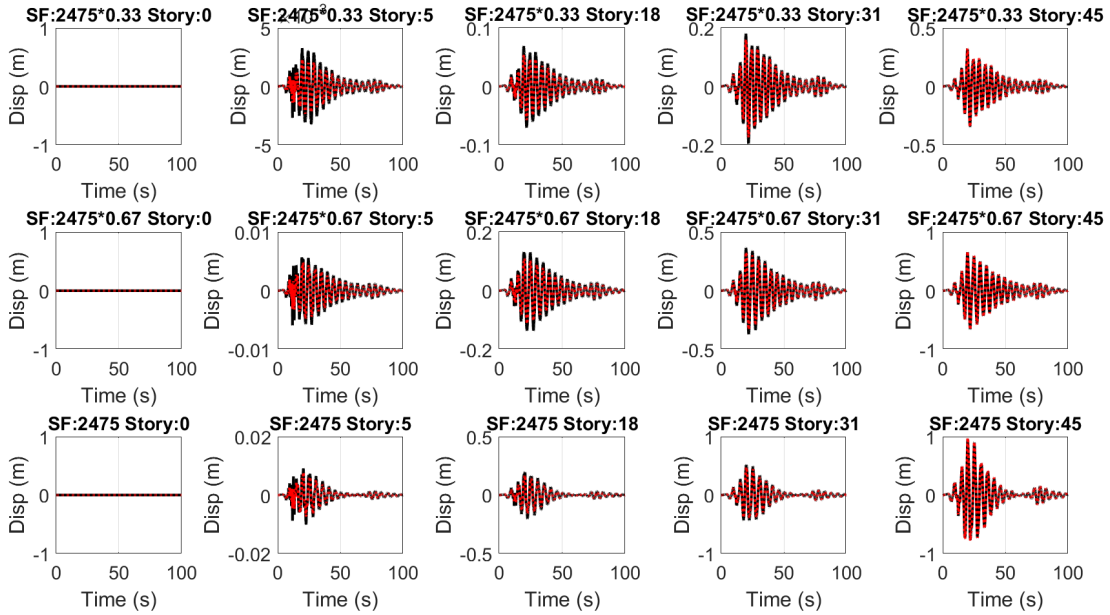

Figure 4.52. DTBM-Y: recorded (black solid line) and estimated (red dashed line) floor displacements, eq id: 3954.

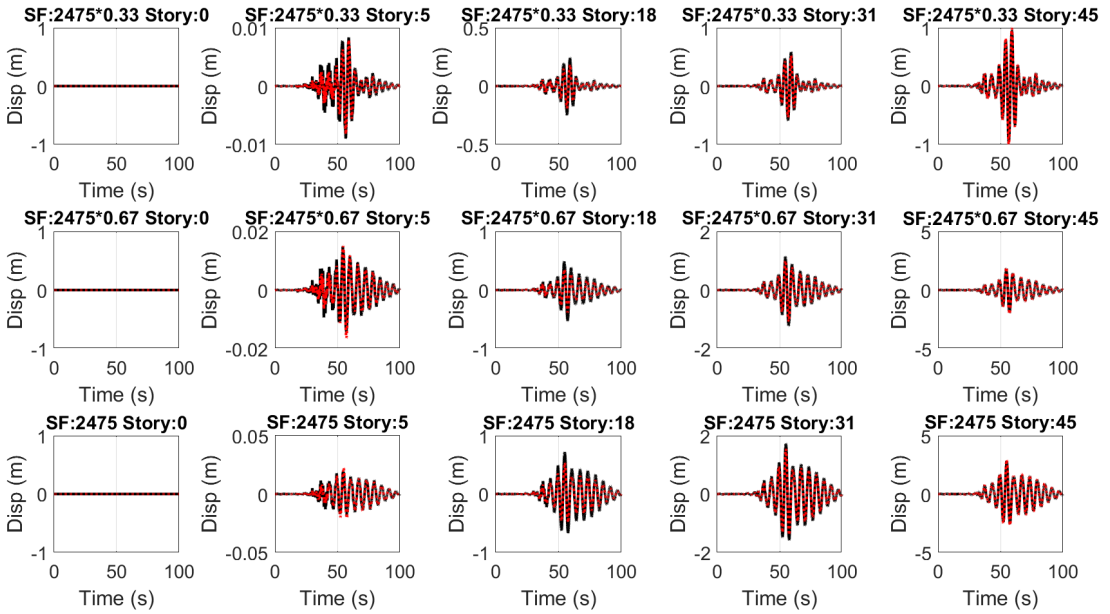

Figure 4.53. DTBM-Y: recorded (black solid line) and estimated (red dashed line) floor displacements, eq id: 5836.

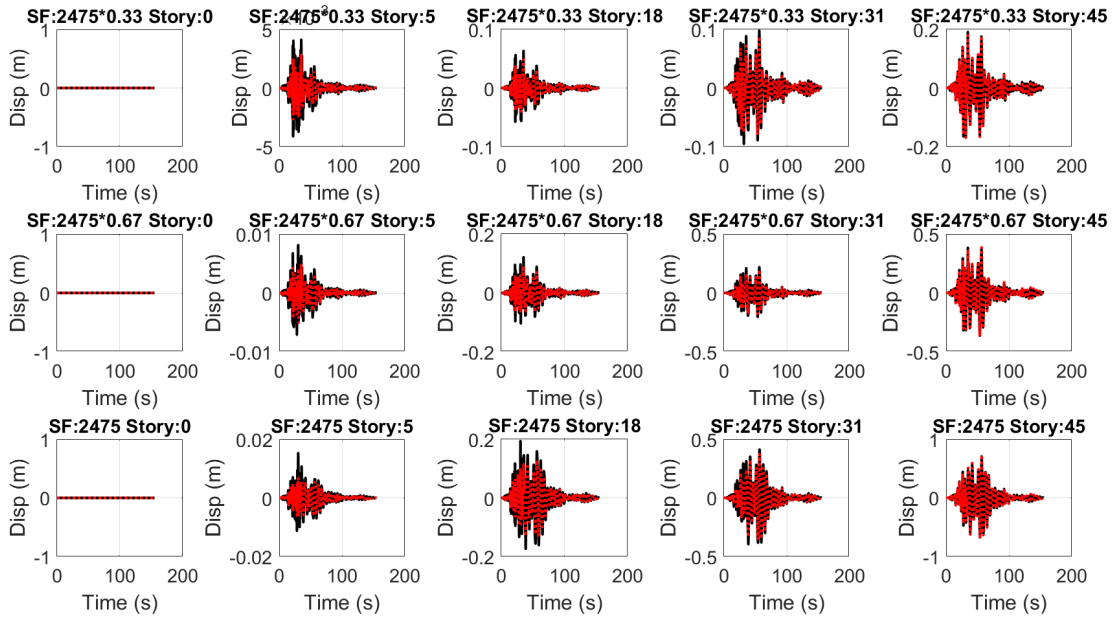

Figure 4.54. DTBM-Y: recorded (black solid line) and estimated (red dashed line) floor displacements, eq id: 6980.

Difference between recorded and estimated responses were calculated with Equation 4.22 and error values are presented for X and Y directions in Figure 4.55.

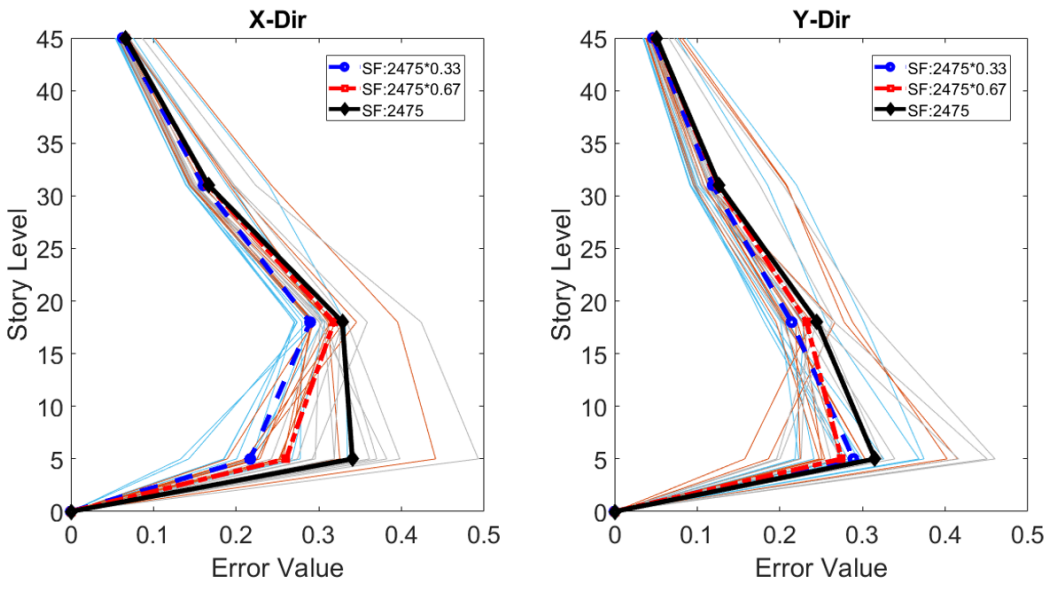

Figure 4.55. DTBM: error values between recorded and estimated floor displacements.

It can be clearly observed that recorded and estimated floor displacements show good agreement for instrumented floors. Since structural elements start to pass from elastic region to plastic region with increasing scale factors, error values of instrumented floors increase. Also, maximum error value was obtained at 5th and 18th floor because stiffness of structure changes abruptly at 5th floor with finished basement walls.

After updating simplified mathematical model of the structure, dynamic responses at all floors were estimated and inter-story drift ratios were calculated at each floor along the entire structure. Figure 4.56 and Figure 4.57 represent inter-story drift ratios of the structure for both directions under earthquakes with different scale factors.

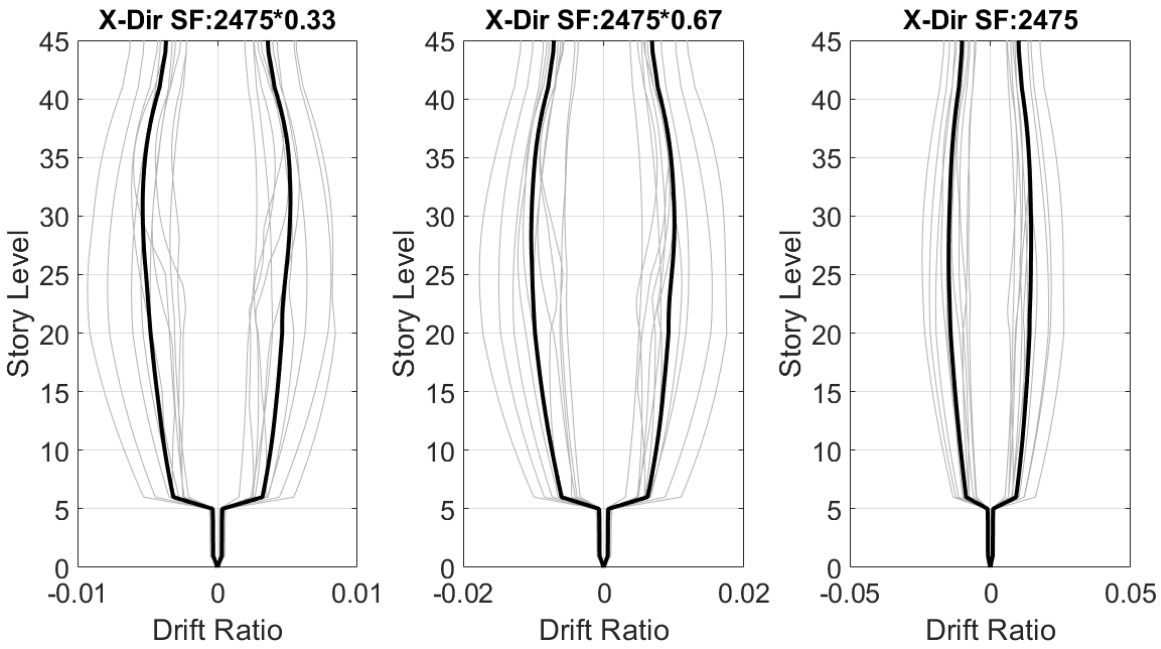

Figure 4.56. DTBM-X: estimated inter-story drift ratios.

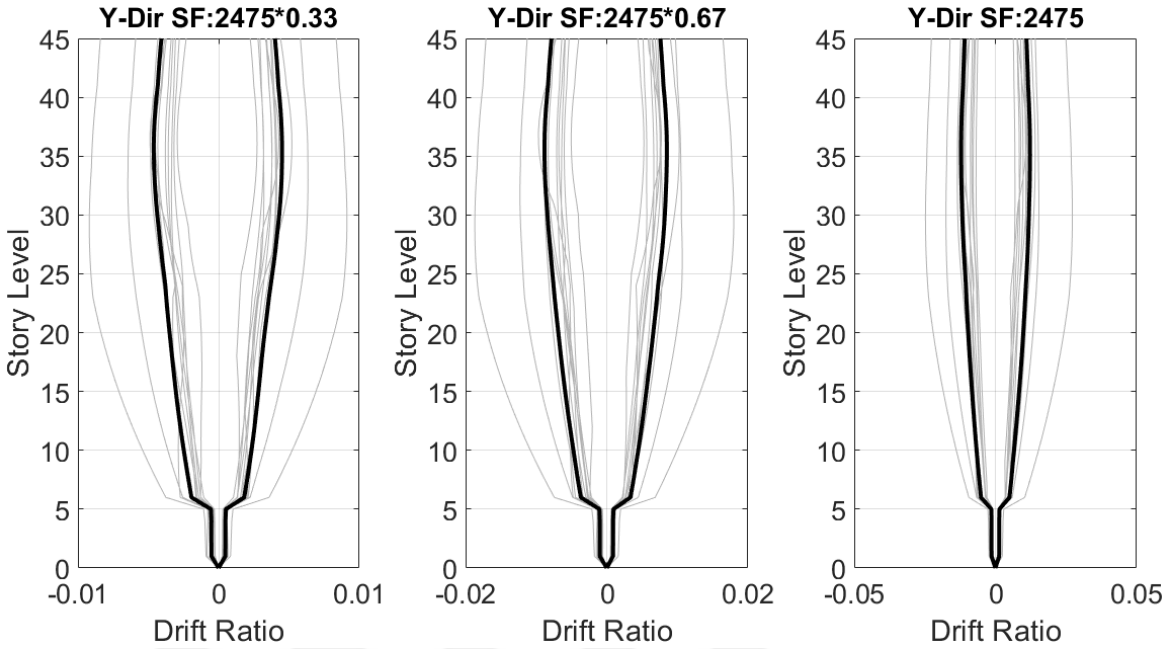

Figure 4.57. DTBM-Y: estimated inter-story drift ratios.

4.3. Nonlinear Simplified Model (NLSM)

In previous sections, non-instrumented floor responses of the structure were estimated from response of instrumented floors with stepped and discrete Timoshenko beam mathematical models. These models does not consider nonlinear behavior effects of structural members on dynamic responses. Therefore, development for a simplified mathematical model of multi-storey structures with a new technique that considers nonlinear behavior of structural elements may provide more reliable prediction of non-instrumented floor responses.

Today, tall buildings are designed by using coupled shear walls at the center and moment-resisting frame around walls. Therefore, while deformation of structure at lower floors is limited by coupled core walls, deformation at upper floors is prevented by moment-resisting frame. Since behavior of moment-resisting frame and behavior of coupled wall can be mathematically defined by using shear-type beam and flexural-type beam, respectively, simplified mathematical model of tall buildings can be created

by combination of shear-type beam and flexural-type beam. There are significant studies in literature that create continuum elastic mathematical model of tall buildings based on this approach and analyze their behavior under earthquakes [39, 40], [86, 87]. However, effect of nonlinear properties of structural components were not considered for dynamic response prediction of structure.

Some studies [88, 89] proposed to discretize shear-type beam and flexural-type beam at each floor level and used backbone curves in order to consider nonlinear behavior of structure. In these studies, elastic properties of shear and flexural springs are estimated based on correlation between frequency ratio and shear-flexural ratio as in suggested aproaches [39], [71], [88]. On the other hand, nonlinear behaviors of shear and flexural elements or springs are calibrated according to recommendations and assumptions in technical reports and guidelines. These methods assume that structure is designed for certain performance level at specific earthquake level and predefined coefficients according to structure type should be used to determine yield and peak points of nonlinear curves. However, it may not be known which performance level is assumed to design of structure. Also, suggested coefficients to determine nonlinear behavior of structure may not be appropriate for different types of structure.

In this study, simplified mathematical model of structure was created by using nodes at each floor level. Shear springs and flexural springs were used to simulate behavior of moment resisting frame and behavior of coupled core wall, respectively. In addition, nodes at each floor were linked with rigid element in order to provide compatibility conditions for deformation. Unique contribution of this study is that elastic and nonlinear behavior of shear and flexural springs are predicted from recorded response of structure by SHM system.

In NLSM approach, firstly, mass of each story and elastic properties of springs were determined. Mass of each story was assumed as 300 kg/m^3 because it is recommended to assume mass of 300 kg/m^3 - 400 kg/m^3 for structures with heavy shear walls [82]. Besides, linear rigidities of springs were calculated according to stiffness matrices

of pure shear beam and pure flexural beam. Initial values of G^* are separately calculated from shear beam formula ($G^*_{initial} = \rho(4Lf_1)^2$) for each direction and Figure 4.2 shows correlation between E^* and G^* by using relation between the effective flexural rigidity and the effective shear rigidity based on suggested method in literature [81]. This relation is created based on modal frequency ratios obtained from modal analysis of FEM. Finally, mass of each story and stiffness of springs were updated based on dynamic properties of modelled structure.

In this study, FEM is considered as a real structure with SHM system consisting of accelerometers at certain floors (Story 0, Story 5, Story 18, Story 31 and Story 45). Algorithm updates G^* value and mass in each step until it finds minimum error value between identified results of FEM and simulated results of NLSM. Detailed information about updating procedure to determine mass and elastic properties of NLSM is shown in Figure 4.58.

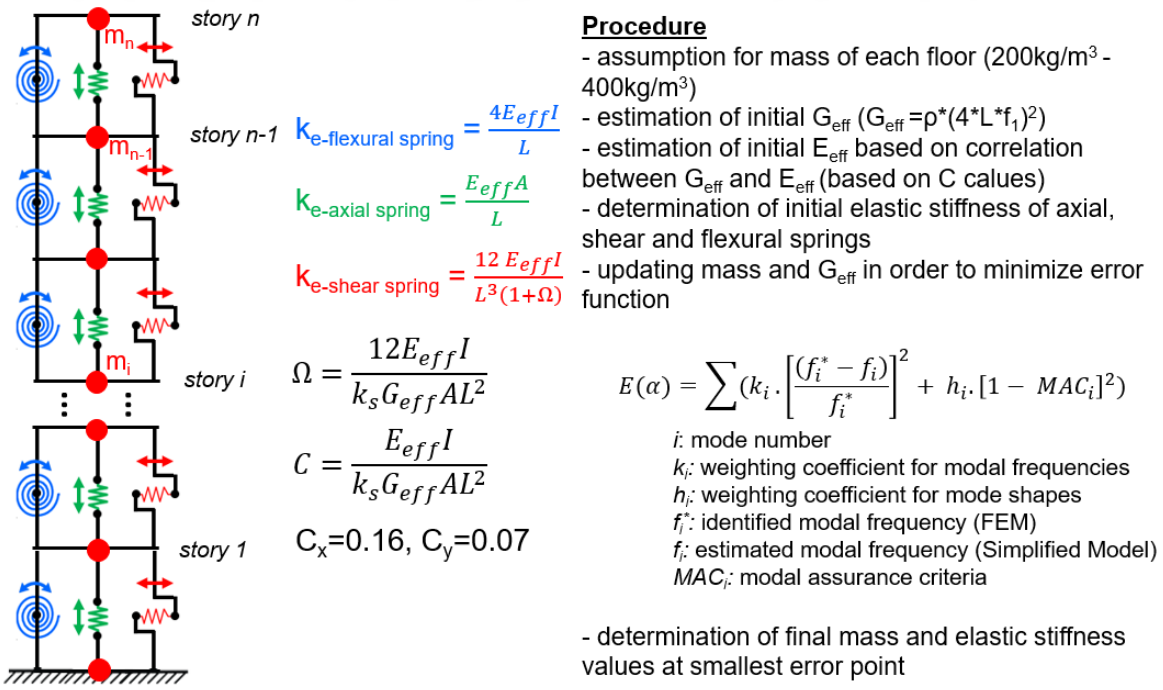

Figure 4.58. NLSM: detailed information about procedure to determine mass and elastic stiffness of springs.

Figure 4.59 represents error values calculated after each iteration and change in minimum error values for both directions.

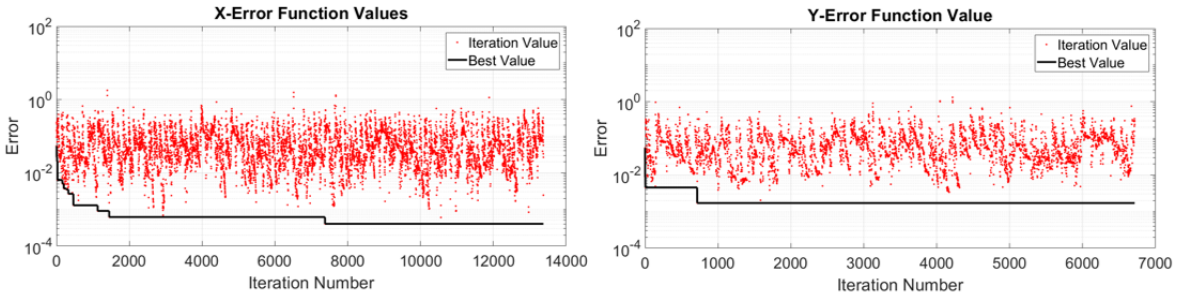

Figure 4.59. NLSM: changes in error values during updating.

In addition, changes in mass and stiffness of each section during updating are shown in Figure 4.60 and Figure 4.61 for both direction.

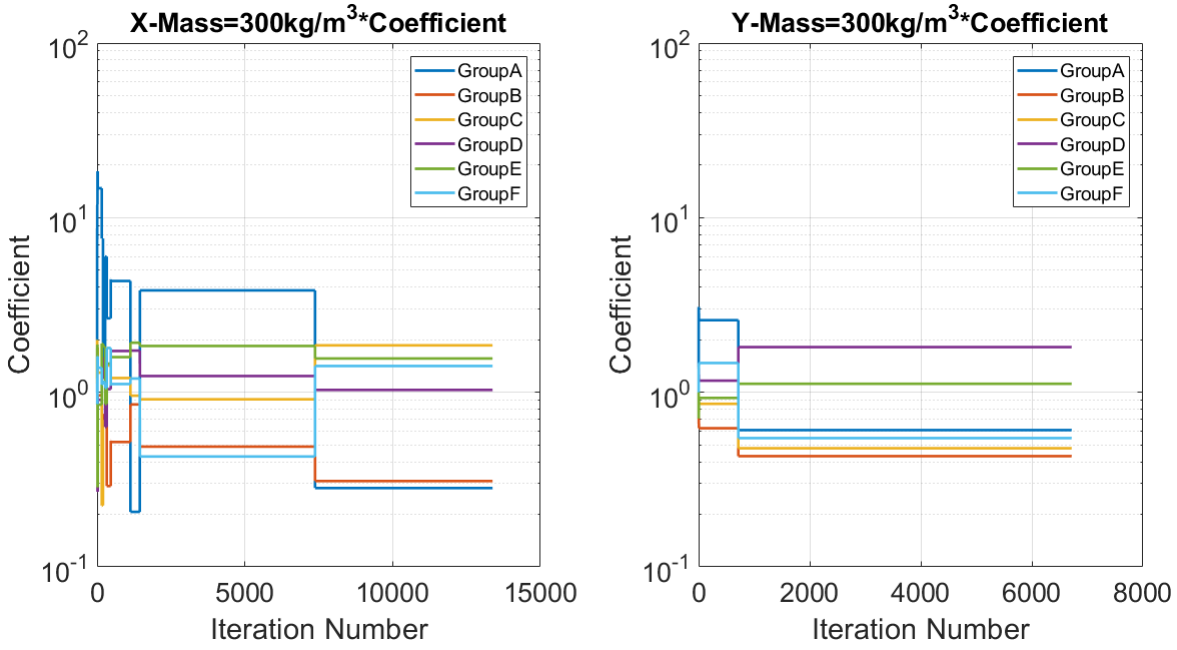

Figure 4.60. NLSM: changes in mass distribution of structure during updating.

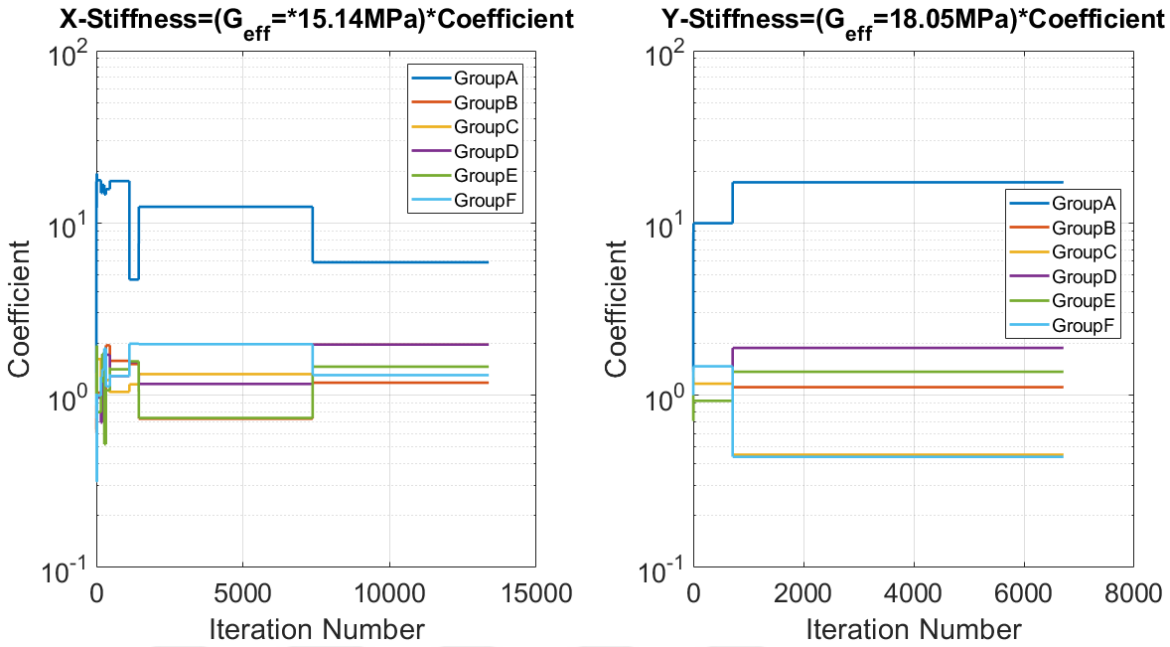

Figure 4.61. NLSM: changes in elastic stiffness distribution of structure during updating.

As can be seen from graphs, updating algorithm enables reasonable mass and elastic stiffness for simplified nonlinear mathematical model. The most important sign for reasonable updating procedure is that rigidity of stories with basement walls is expected to be high and algorithm estimates high stiffness values for these stories. Updated modal frequencies and mode shapes are presented for both directions in Figure 4.62 and Figure 4.63.

In addition to estimation of story masses and elastic properties of shear and flexural springs, another significant issue is to determine backbone curves of nonlinear springs. There are limited studies in literature considering nonlinear behavior of structures in simplified model [89]. In these studies, nonlinear properties of structural members are estimated according to recommendations and assumptions in technical reports and guidelines. On the other hand, in this study, nonlinear properties of shear and flexural springs in simplified nonlinear mathematical model for tall building were firstly determined based on total mass and defined earthquake load. Finally, estimated

nonlinear curves were updated with different optimization algorithms by using vibration records to obtain more accurate nonlinear relations.

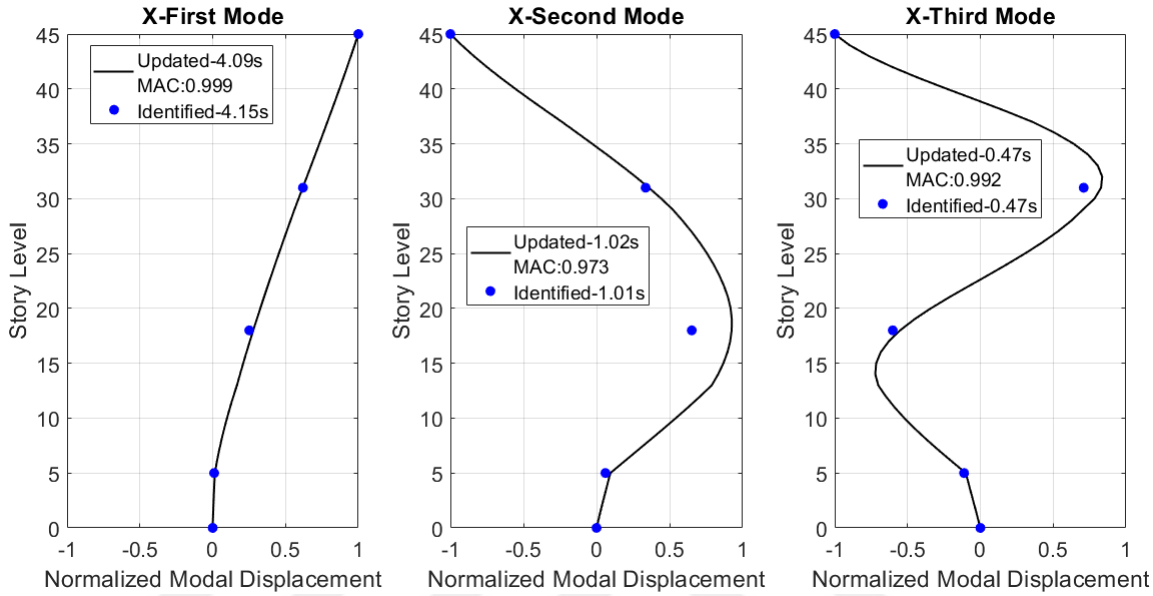

Figure 4.62. NLSM-X: updated and identified modal properties.

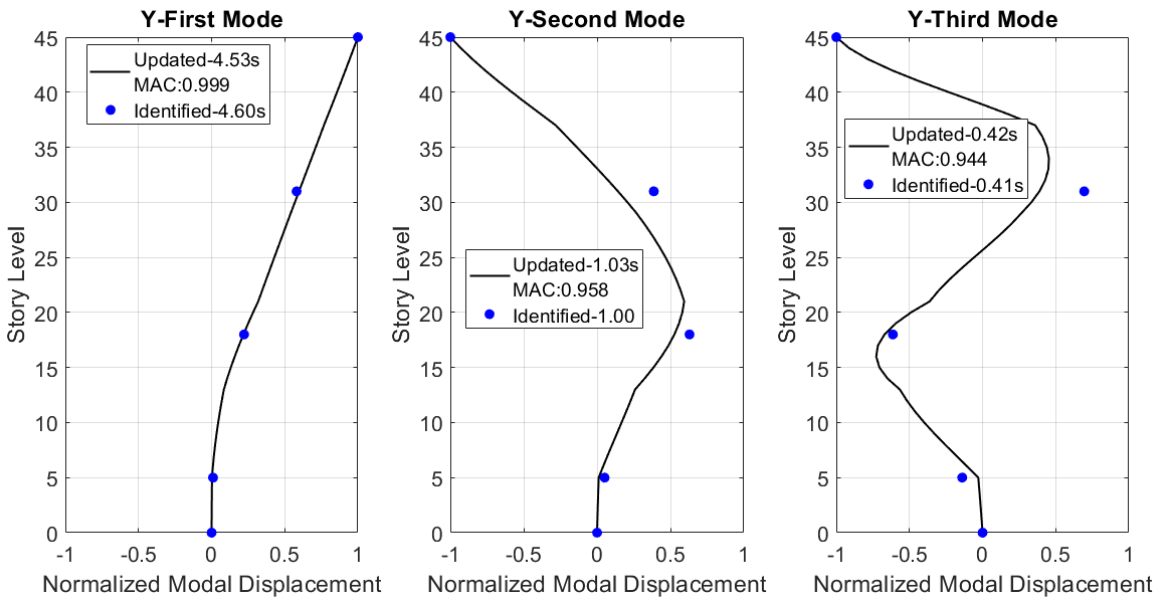

Figure 4.63. NLSM-Y: updated and identified modal properties.

Two different optimization techniques were utilized in order to determine more accurate nonlinear curves of springs in this study. One of them is Kalman Filter which is used in many studies [90, 91]. Kalman Filter is an optimization algorithm that estimates subsequent response of dynamic system based on previous state. The algorithm observes difference between simulated response of nonlinear mathematical model and measured data of real system by calculating Kalman Gain. The decrease in Kalman Gain during process indicates that created nonlinear mathematical model of dynamic system approaches to real dynamic model. Kalman Filter has been updated and improved in order to increase its efficiency with significant studies in literature [92-99]. Unscented Kalman Filter (UKF) was used to update simplified nonlinear mathematical model of structure in this study. Detailed information about the algorithm is given in Figure 4.64.

Algorithm of Unscented Kalman Filter

Step1:

$\{Q\}_0$: initial state vector

$[P]_0$: initial covariance matrix

$[P]_0$:*diag(coeff* $\{Q\}_0^2$)*

$[Q_n]$: noise covariance matrix

$[Q_n]$:*diag(coeff* $\{Q\}_0^2$)*

$[R_m]$: noise of measurement covariance matrix

$\{Q\}_1 = \{Q\}_0$

$[P]_1 = [P]_0 + [Q_n]$

parameters used in algorithm:

$\kappa=0$, $\alpha=1$, $\beta=2$, $n_Q=10$

$\lambda=[\alpha^*\alpha^*(n_Q+\kappa)]-n_Q$

$\gamma=\mathrm{sqrt}(n_Q+\lambda)$

$WeCoeff_{m,1}=\lambda/(n_Q+\lambda)$

$WeCoeff_{c,1}=[\lambda/(n_Q+\lambda)]+[1-(\alpha^*\alpha)+\beta]$

$WeCoeff_{m,j}=WeCoeff_{c,j}=0.5/(n_Q+\lambda)$; $j=2:1:2^*n_Q+1$

Step2:

for k=1:1:L*(L=step number)*

calculation *of* sigma points: $\sigma_k=[\{Q\}_k\ \{Q\}_k+\gamma\mathrm{sqrt}([P]_k)\ \{Q\}_k-\gamma\mathrm{sqrt}([P]_k)]$

calculation of simulation mean: $Y_{meanofsim,k}=WeCoeff_{m,k}{}^*Y_{sim,k}$

calculation of difference: $D_k=Y_{mea,k}-Y_{meanofsim,k}$

innovation-based coaverince matrix: $[I]_k=\mathrm{diag}(\sum_{j=1}^{2*L_Q+1} WeCoeff_{c,k}\ (Y_{sim,k}-Y_{meanofsim,k})^*\mathrm{transpose}((Y_{sim,k}-Y_{meanofsim,k})))$

updating of $[R_m]$: $[R_m]=\alpha[R_m]+(1-\alpha)\mathrm{diag}((D_k{}^*\mathrm{transpose}(D_k))-[I]_k)$

calculation of Kalman Gain:

$[P_{yy}]_k=[I]_k+[R_m]$

$[P_{0y}]_k=\sum_{j=1}^{2*L_Q+1} WeCoeff_{c,k}\ (\sigma_k-\{Q\}_k)^*\mathrm{transpose}((Y_{sim,k}-Y_{meanofsim,k}))$

Kalman Gain: $KG_k=[P_{0y}]_k{}^*\mathrm{inverse}([P_{yy}]_k)$

updating parameters:

$\{Q\}_{k+1}=\{Q\}_k+KG_k$

$[P]_{k+1}=[P]_k-KG_k\ [Pyy]_k\ \mathrm{transpose}(KG_k)$

end

Figure 4.64. Steps of unscented kalman filter.

In addition, estimated nonlinear curves of springs were updated by using Simulated Annealing (SA) [93], [100-102]. Structure of the algorithm was developed for material engineering to effectively perform annealing of solid elements such as iron. Simulated Annealing is an optimization algorithm that is capable to find global minimum of defined objective function by comparing objective function values at different points with probabilistic approach. The algorithm estimates global minimum of objective function by calculating difference between randomly determined simulated solutions. If difference is negative, current solution is updated; however, when difference is positive, Boltzmann Probability is utilized at points where simulated values in two cases are very close each other. Therefore, the algorithm continues by passing local minimums to properly identify global minimum. Detailed information about the algorithm is given in Figure 4.65.

Algorithm of Simulated Annealing

```
f:objective function
s:inital value
s':randomly selected value around s
L:step number

for ii=1:1:L
   Δf=f(s)-f(s')
   if Δf<0                          (obtaining better result condition)
     s=s'                           (updating of parameter)
   elseif exp(-Δf/s)>rand(0,1)      (obtaining better result condition according to Boltzmann Probability)
     s=s'                           (updating of parameter)
end
```

Figure 4.65. Steps of simulated annealing.

Simulated Annealing was utilized to update nonlinear spring properties in simplified model by using below objective function. The function is expressed as

$$Error_k = \sqrt{\frac{\sum_{t=0}^{NPT}[z_k(t) - y_k(t)]^2}{\sum_{t=0}^{NPT}[z_k(t)]^2}}, \tag{4.45}$$

where $z_k(t)$ the simulated floor displacements of FEM, $y_k(t)$ is the estimated floor displacements from simplified model and NPT is time length of data. The algorithm

updates $y_k(t)$ by changing nonlinear spring properties of simplified model based on defined boundary limits in order to estimate optimum values at global minimum of objective function. Simulated Annealing algorithm uses recorded responses of FEM and simulated responses NLSM at assumed instrumented floors. Detailed information about nonlinear curve of springs and nonlinear updating procedure is shown in Figure 4.66.

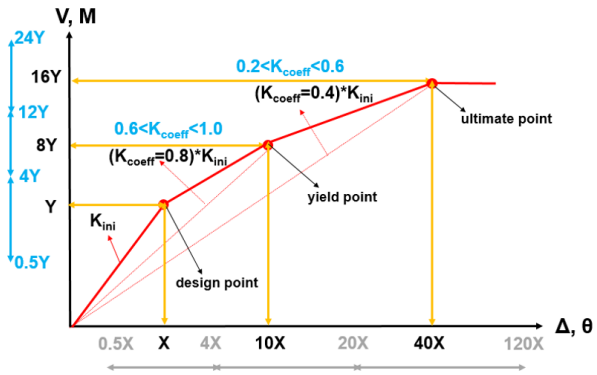

Procedure
- estimation of base shear $V_{total}=m_t*S_{DS}$ and Equivalent Seismic Load Analysis based on TBSC
- determination initial design point (X,Y)
  * K_{ini} was determined from elastic properties of springs
- determination of initial yield and ultimate points (10X,8Y and 40X,6Y)
  * initial secant stiffness of yield and ultimate points were determined **$0.8*K_{ini}$** and **$0.4*K_{ini}$** ,respectively
  * effect of initial values on the results was limited

Kalman Filter:
- estimation optimum design, yield and ultimate points based on Kalman Gain by updating shear force, bending moment and stiffness values of design, yield and ultimate points

Simulated Annealing:
- determination of boundary conditions (represented by blue color)
  * boundary conditions were determined by considering
    - all ground motion levels in TBSC
    - different overstrength factors
    - different system behavior factors
    due to uncertain design parameters
- estimation optimum design, yield and ultimate points based on objective function by updating shear force, bending moment and stiffness values of design, yield and ultimate points

Figure 4.66. Information about nonlinear curve of springs and nonlinear updating procedure.

In this study, Unscented Kalman Filter and Simulated Annealing were performed to properly predict nonlinear properties of shear and flexural springs using one earthquake record for 2475 return period and results are compared. Figure 4.67 and Figure 4.68 represent comparison of displacements and inter-story drift ratios.

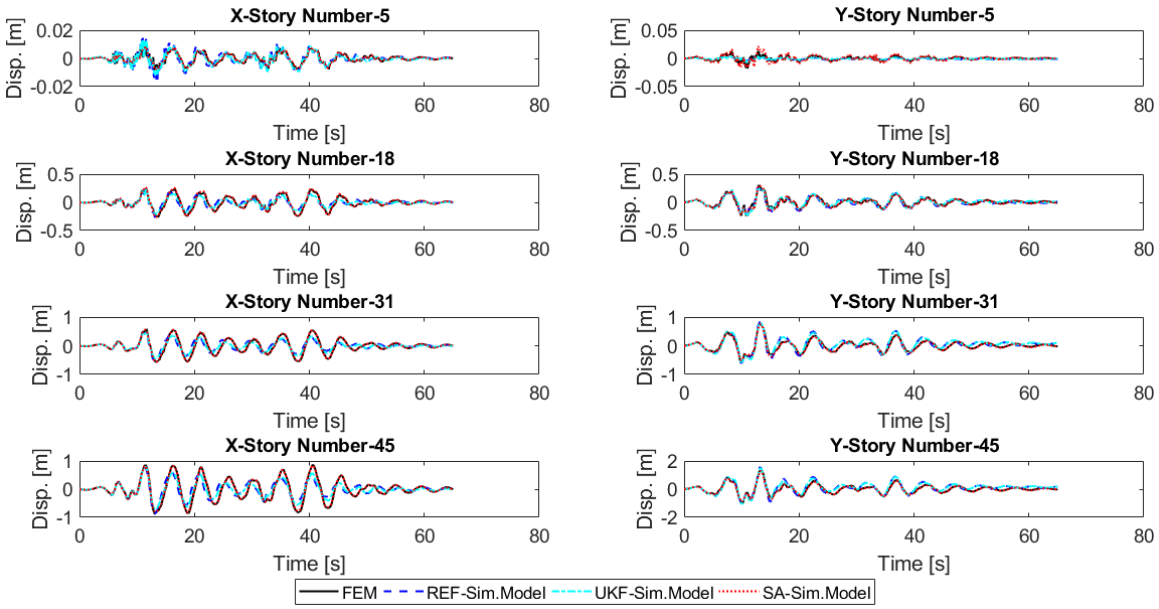

Figure 4.67. NLSM: comparison of displacements.

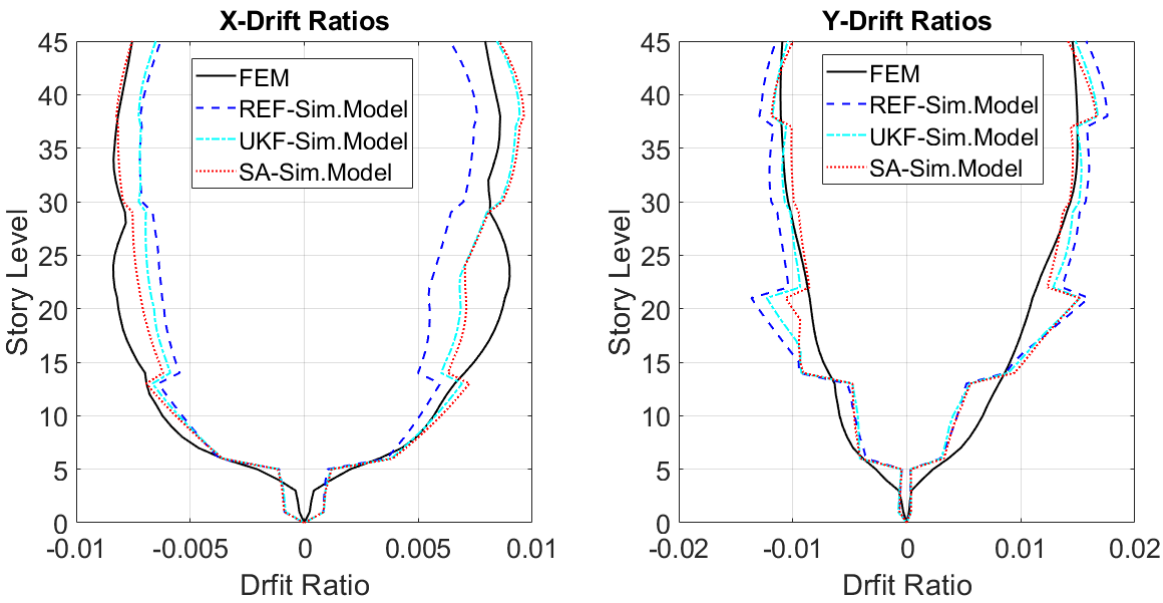

Figure 4.68. NLSM: comparison of inter-story drift ratios.

As can be clearly seen from comparison results, displacement and inter-story drift ratio of simplified nonlinear model updated by Simulated Annealing are much closer to displacement and inter-story drift ratio obtained from FEM. In addition, analysis time of Unscented Kalman Filter is long depending on step number of ground motion record. On the other hand, faster results can be obtained by Simulated Annealing regardless of step number of ground motion record. Besides, increase in number of updating parameters causes convergence problems for Unscented Kalman Filter. Therefore, nonlinear spring properties of simplified model were updated by Simulated Annealing for remaining ground motion records. Simulated and measured responses for instrumented floors are compatible for each selected earthquake after updating and comparison of simulated and measured responses for earthquakes are shown in Figure 4.69 - Figure 4.90.

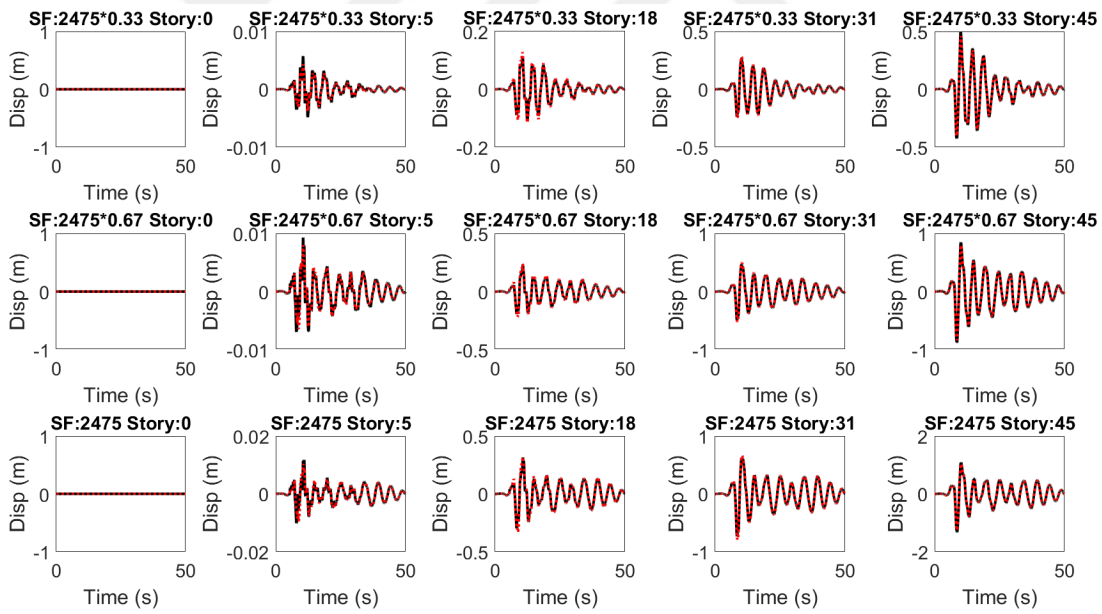

Figure 4.69. NLSM-X: recorded (black solid line) and estimated (red dashed line) floor displacements, eq id: 178.

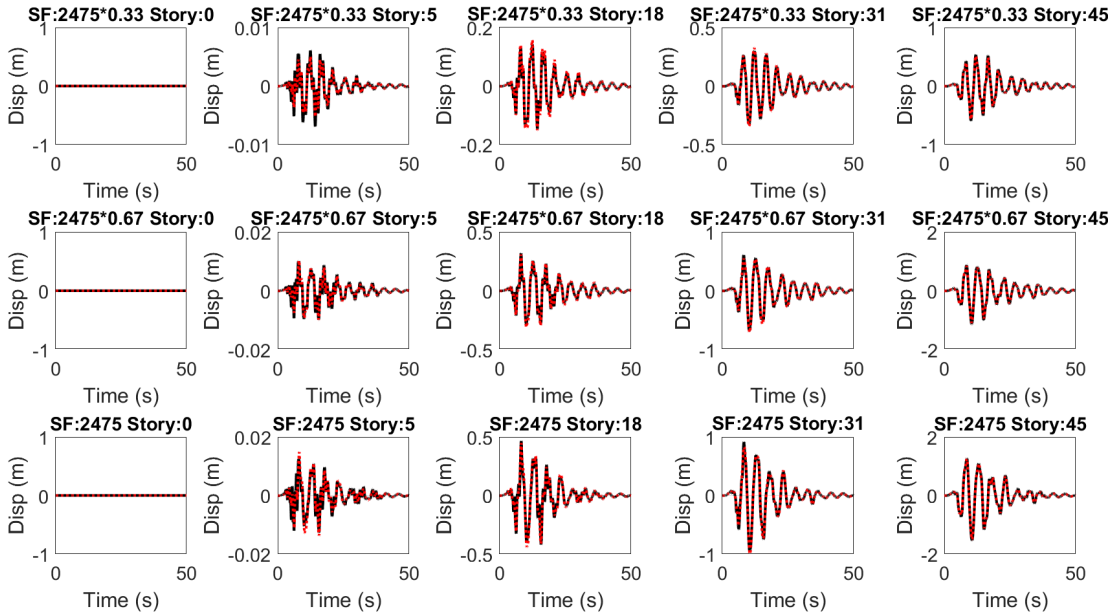

Figure 4.70. NLSM-X: recorded (black solid line) and estimated (red dashed line) floor displacements, eq id: 549.

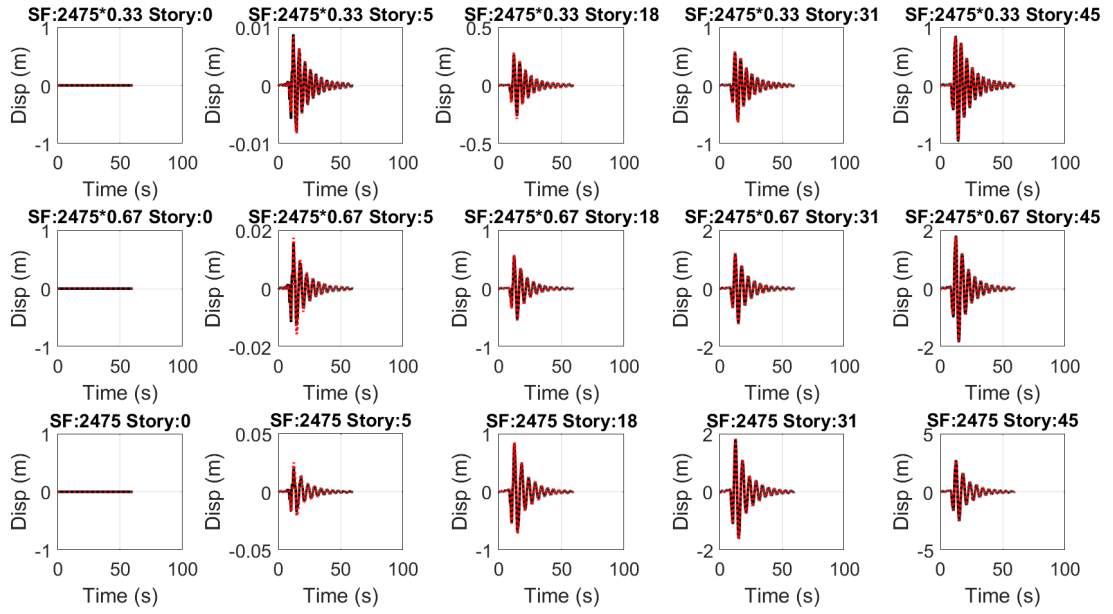

Figure 4.71. NLSM-X: recorded (black solid line) and estimated (red dashed line) floor displacements, eq id: 879.

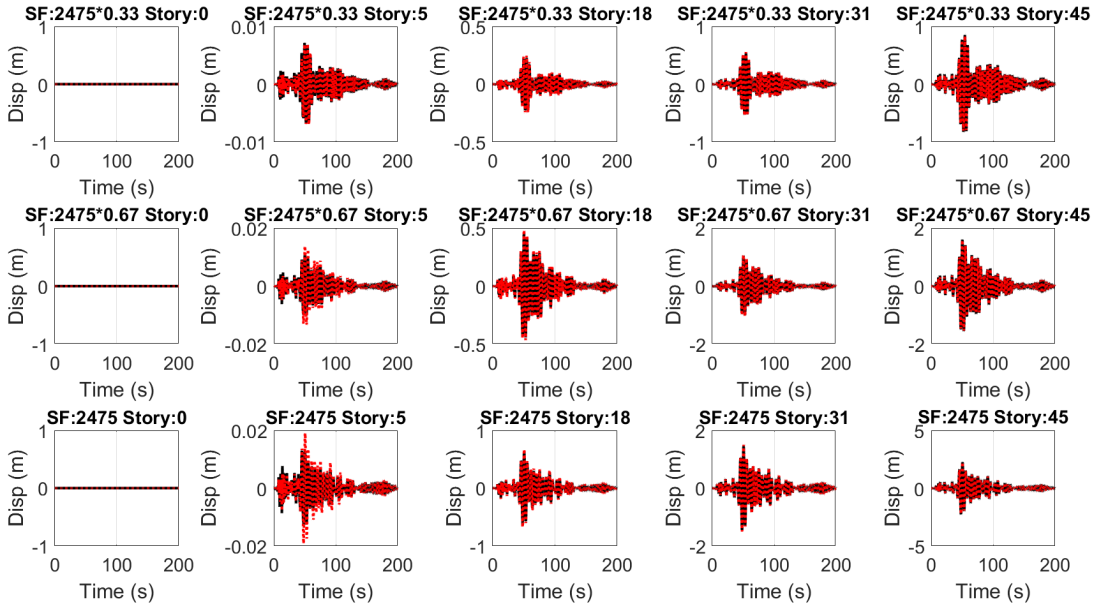

Figure 4.72. NLSM-X: recorded (black solid line) and estimated (red dashed line) floor displacements, eq id: 1115.

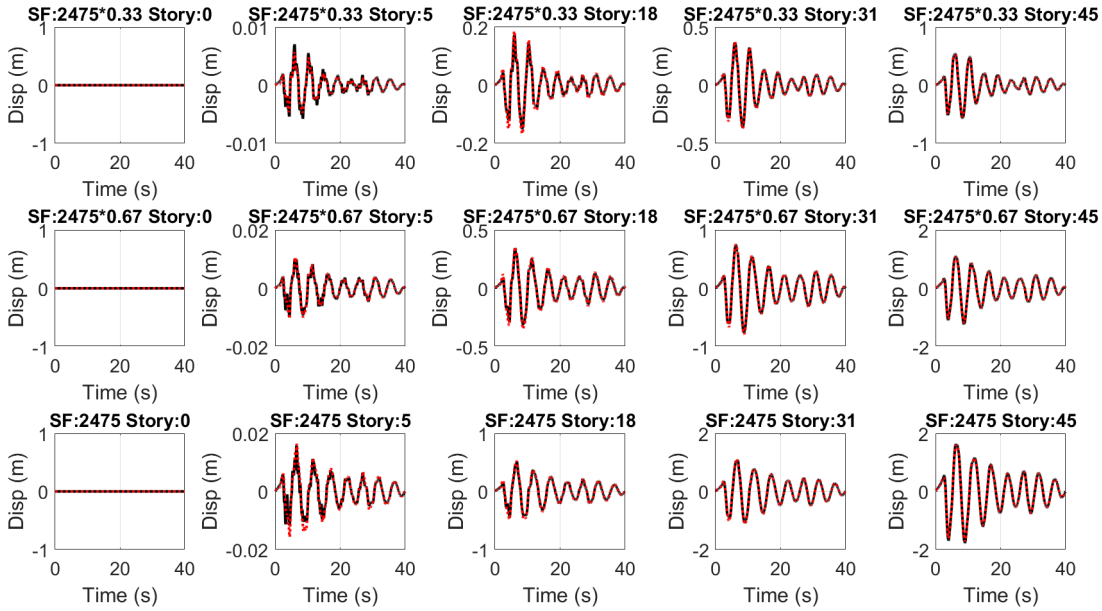

Figure 4.73. NLSM-X: recorded (black solid line) and estimated (red dashed line) floor displacements, eq id: 1165.

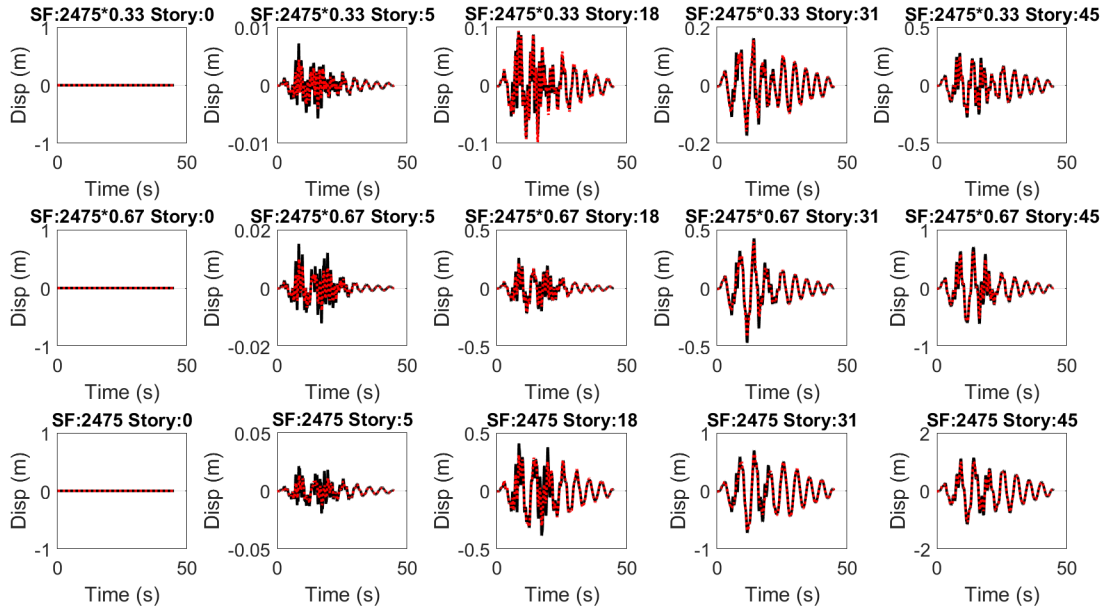

Figure 4.74. NLSM-X: recorded (black solid line) and estimated (red dashed line) floor displacements, eq id: 1615.

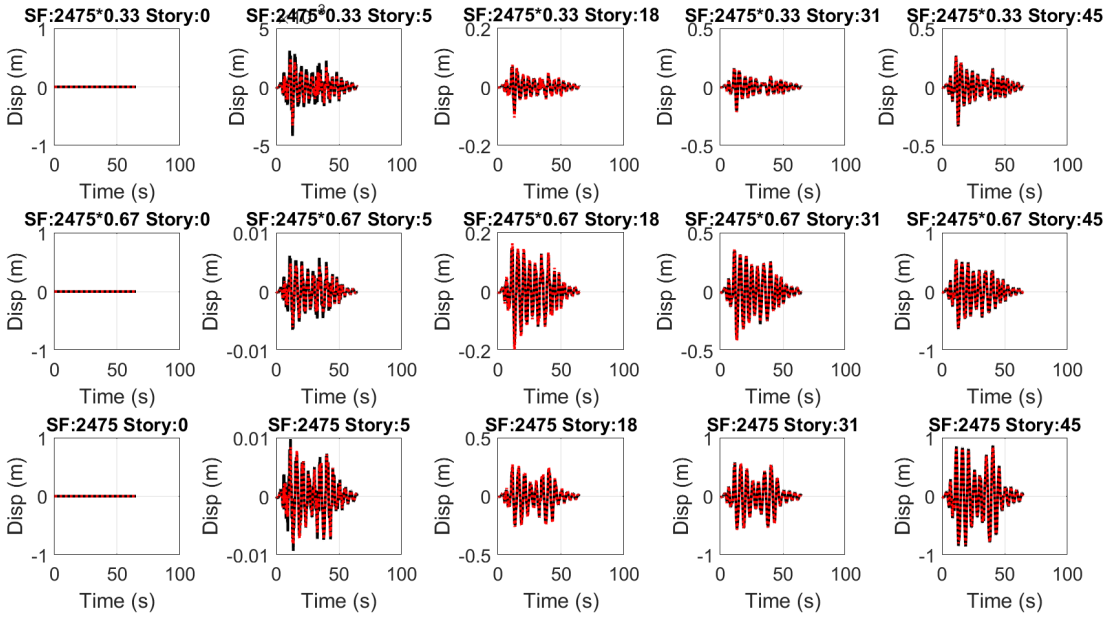

Figure 4.75. NLSM-X: recorded (black solid line) and estimated (red dashed line) floor displacements, eq id: 1633.

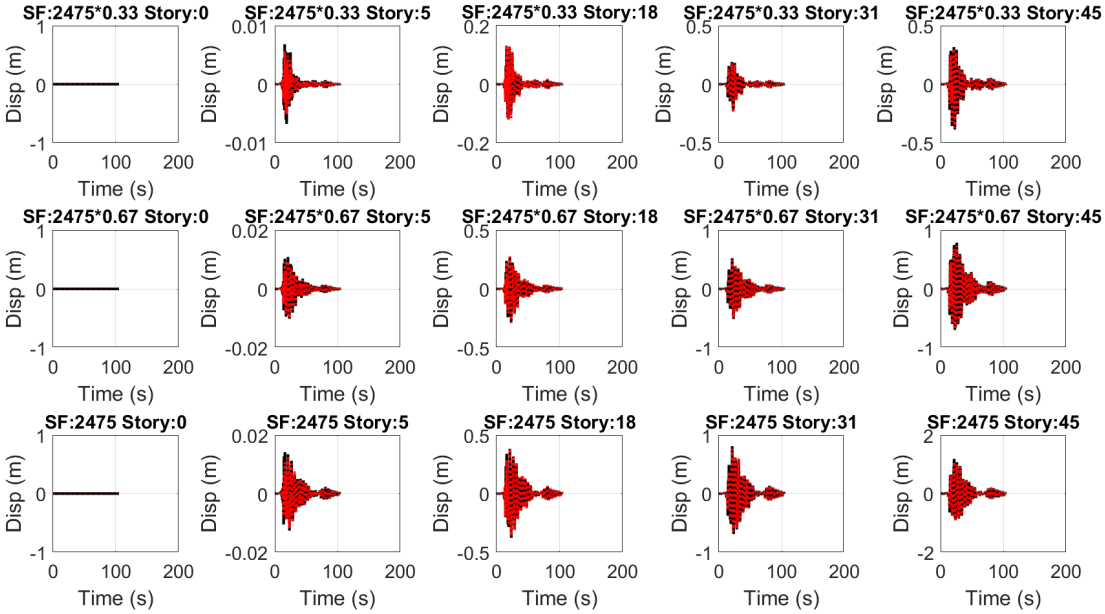

Figure 4.76. NLSM-X: recorded (black solid line) and estimated (red dashed line) floor displacements, eq id: 1794.

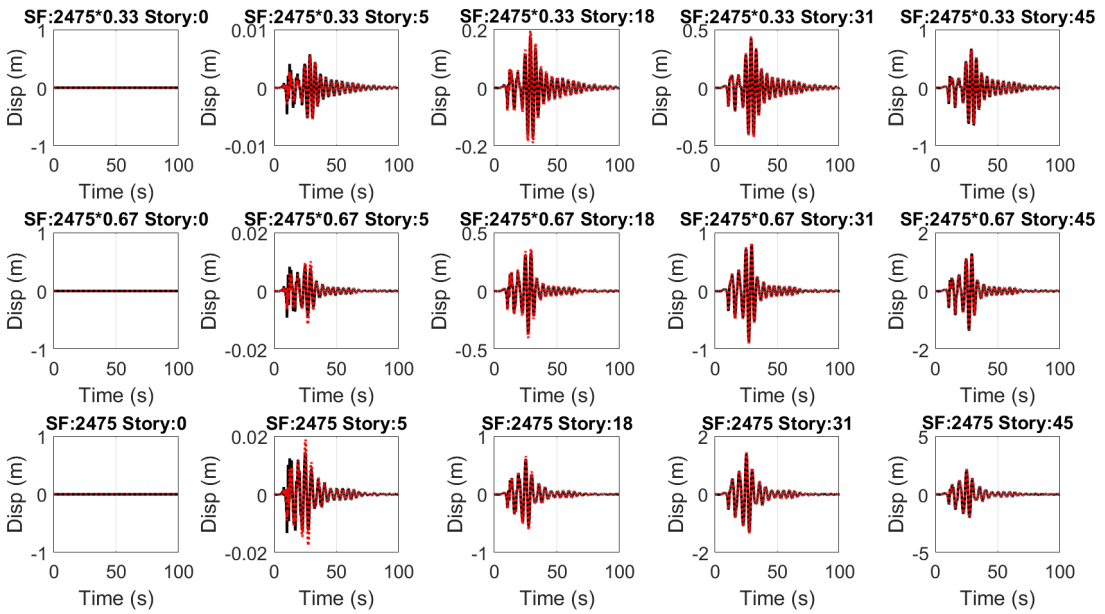

Figure 4.77. NLSM-X: recorded (black solid line) and estimated (red dashed line) floor displacements, eq id: 3954.

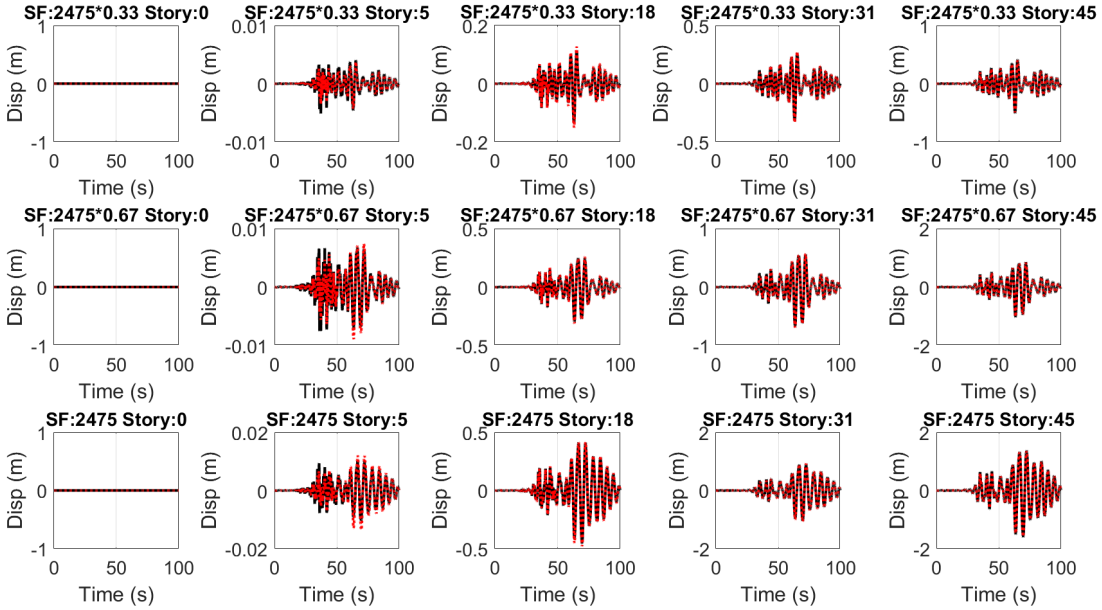

Figure 4.78. NLSM-X: recorded (black solid line) and estimated (red dashed line) floor displacements, eq id: 5836.

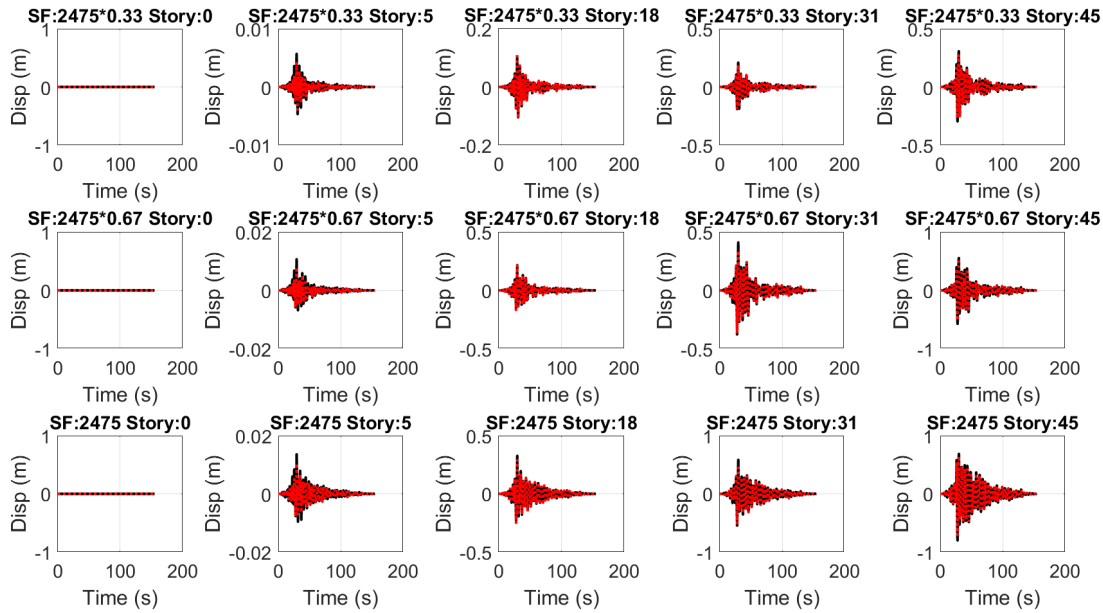

Figure 4.79. NLSM-X: recorded (black solid line) and estimated (red dashed line) floor displacements, eq id: 6980.

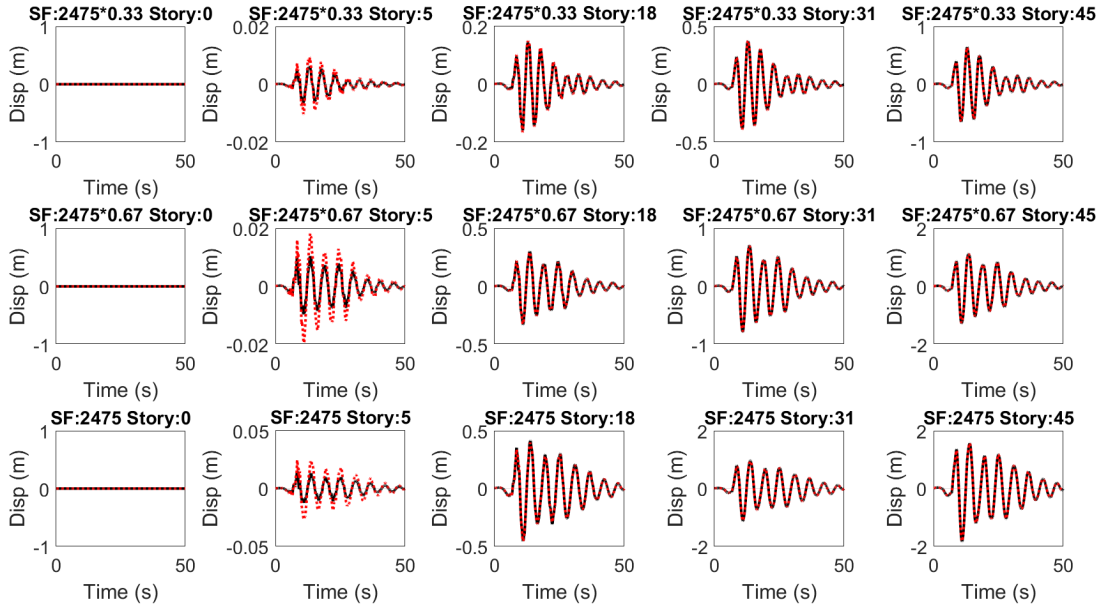

Figure 4.80. NLSM-Y: recorded (black solid line) and estimated (red dashed line) floor displacements, eq id: 178.

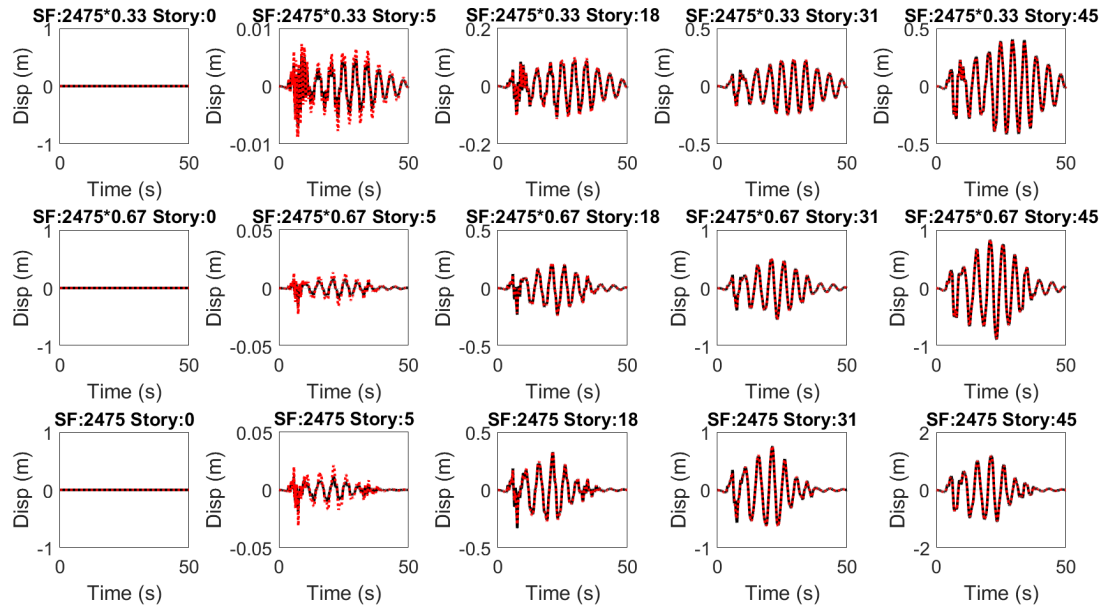

Figure 4.81. NLSM-Y: recorded (black solid line) and estimated (red dashed line) floor displacements, eq id: 549.

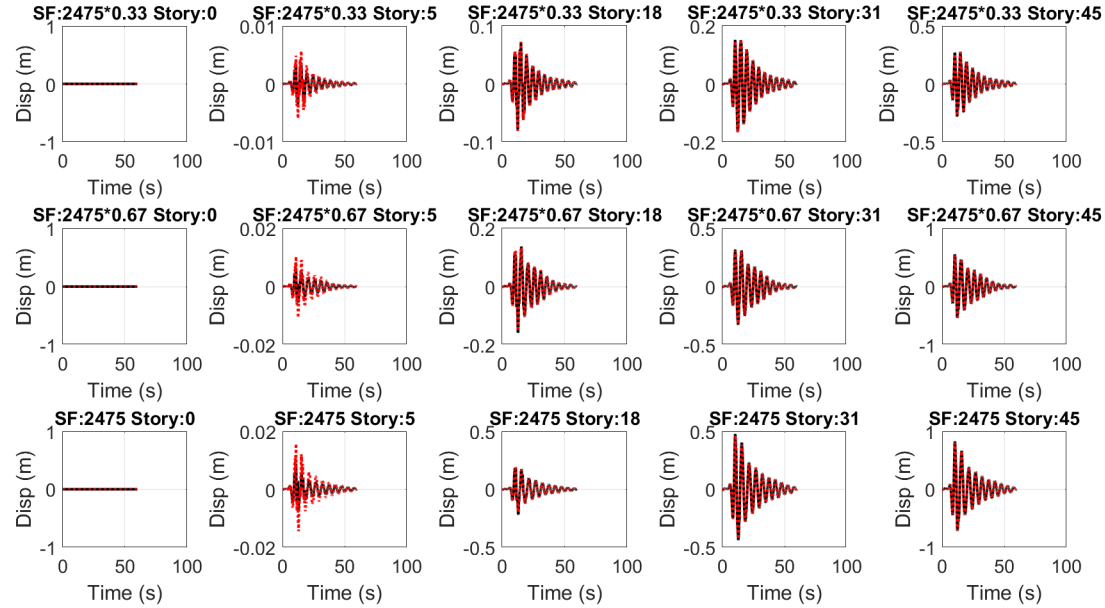

Figure 4.82. NLSM-Y: recorded (black solid line) and estimated (red dashed line) floor displacements, eq id: 879.

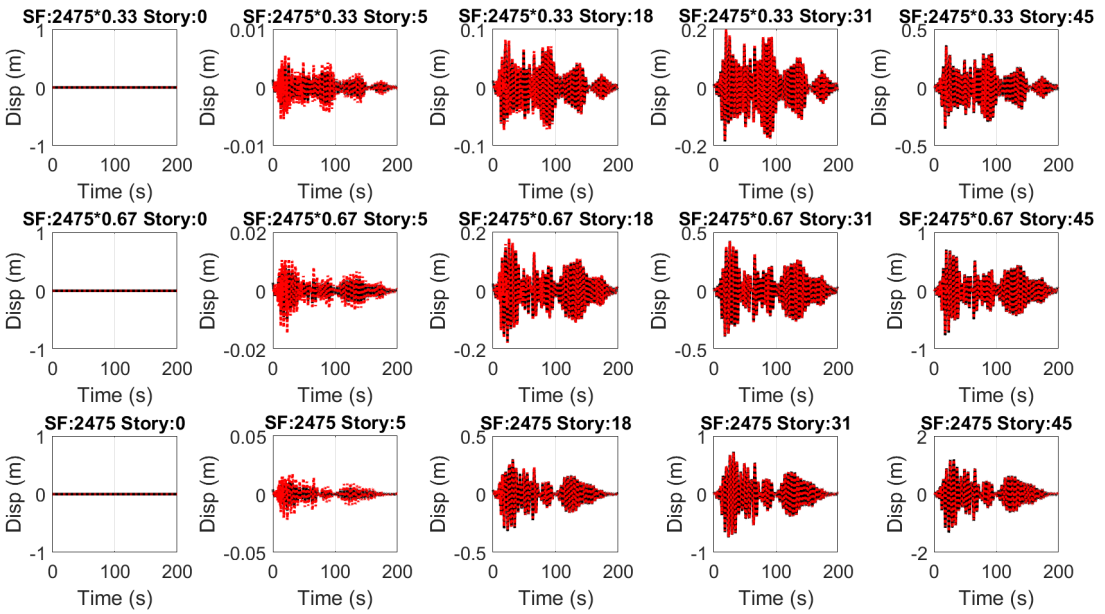

Figure 4.83. NLSM-Y: recorded (black solid line) and estimated (red dashed line) floor displacements, eq id: 1115.

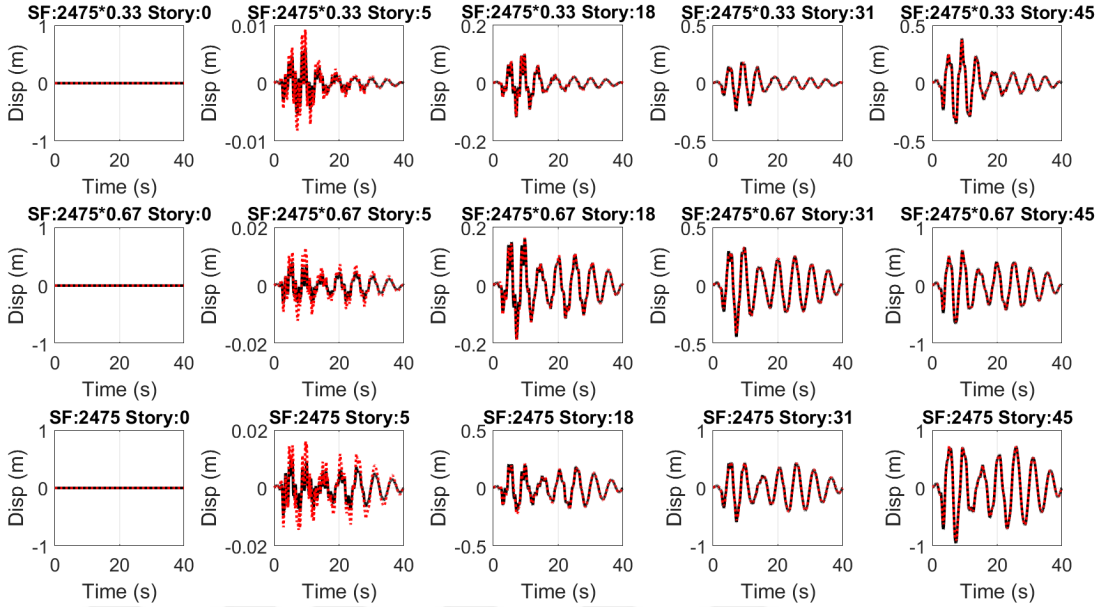

Figure 4.84. NLSM-Y: recorded (black solid line) and estimated (red dashed line) floor displacements, eq id: 1165.

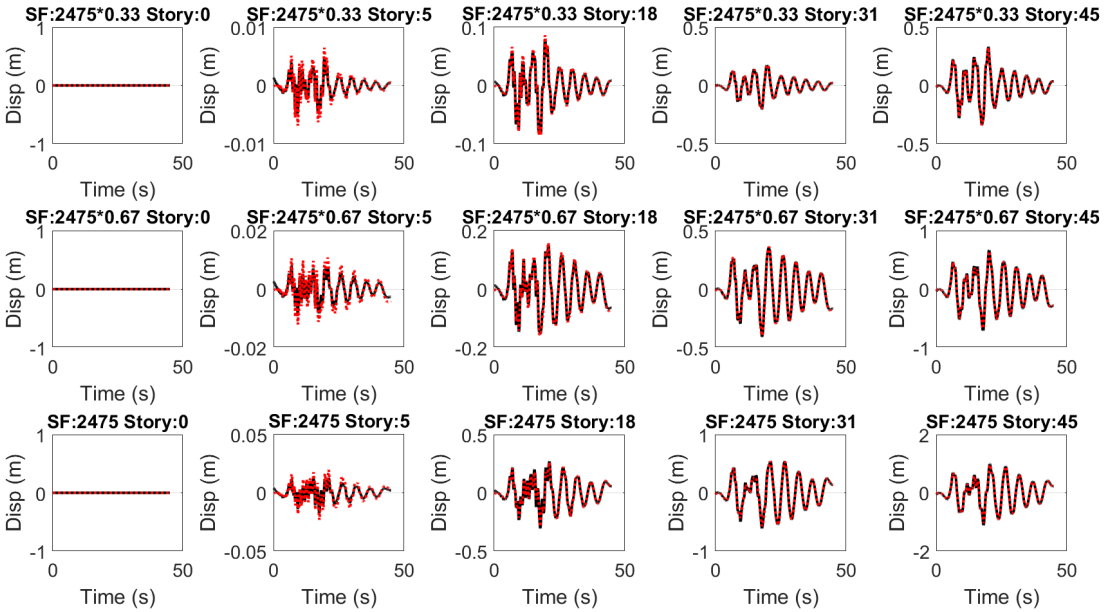

Figure 4.85. NLSM-Y: recorded (black solid line) and estimated (red dashed line) floor displacements, eq id: 1615.

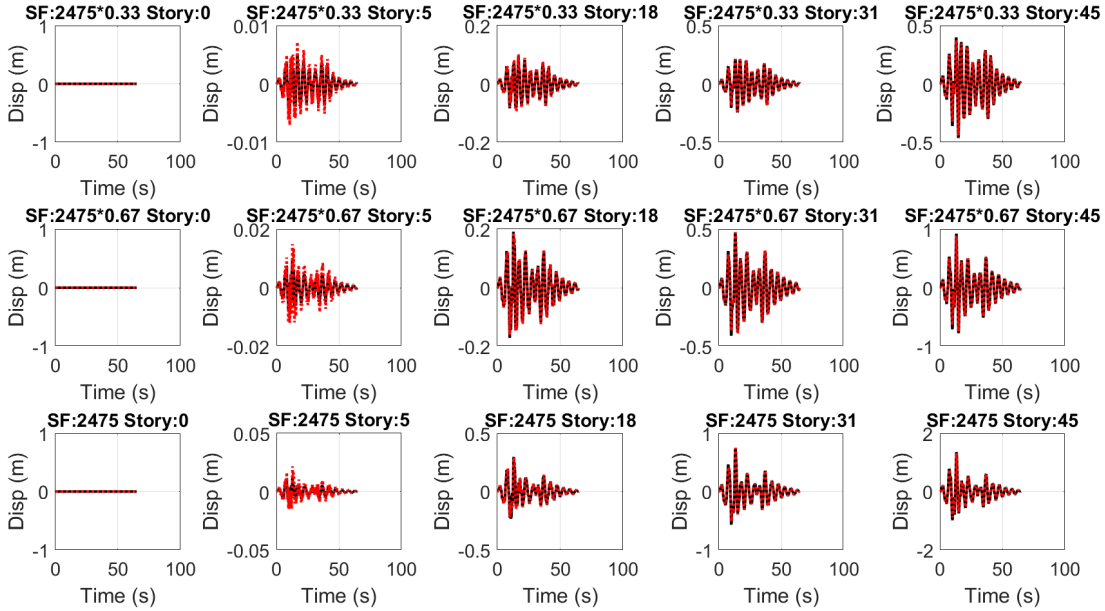

Figure 4.86. NLSM-Y: recorded (black solid line) and estimated (red dashed line) floor displacements, eq id: 1633.

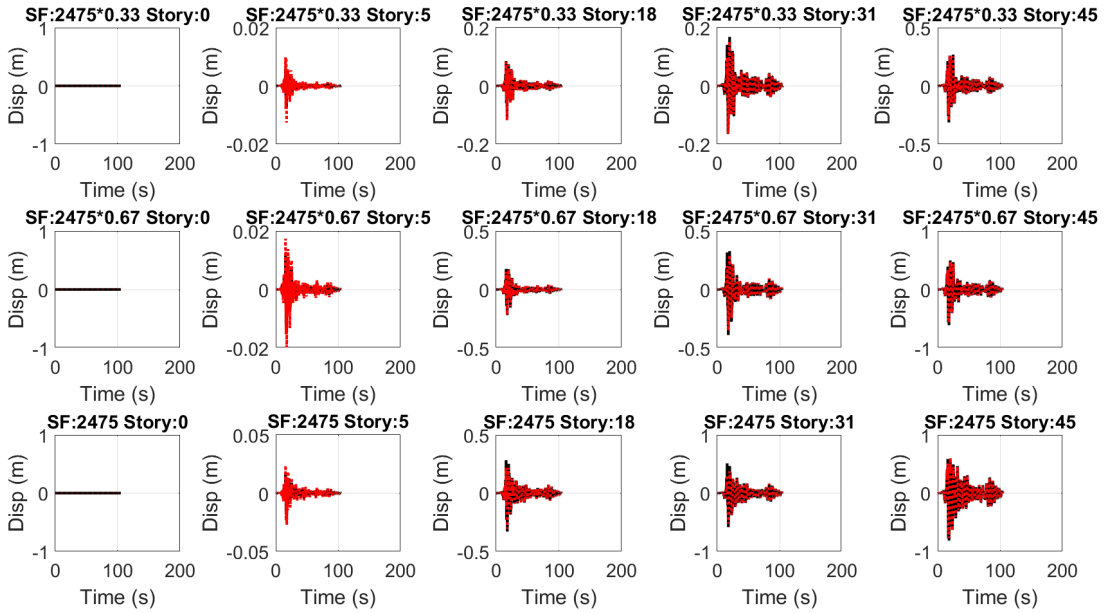

Figure 4.87. NLSM-Y: recorded (black solid line) and estimated (red dashed line) floor displacements, eq id: 1794.

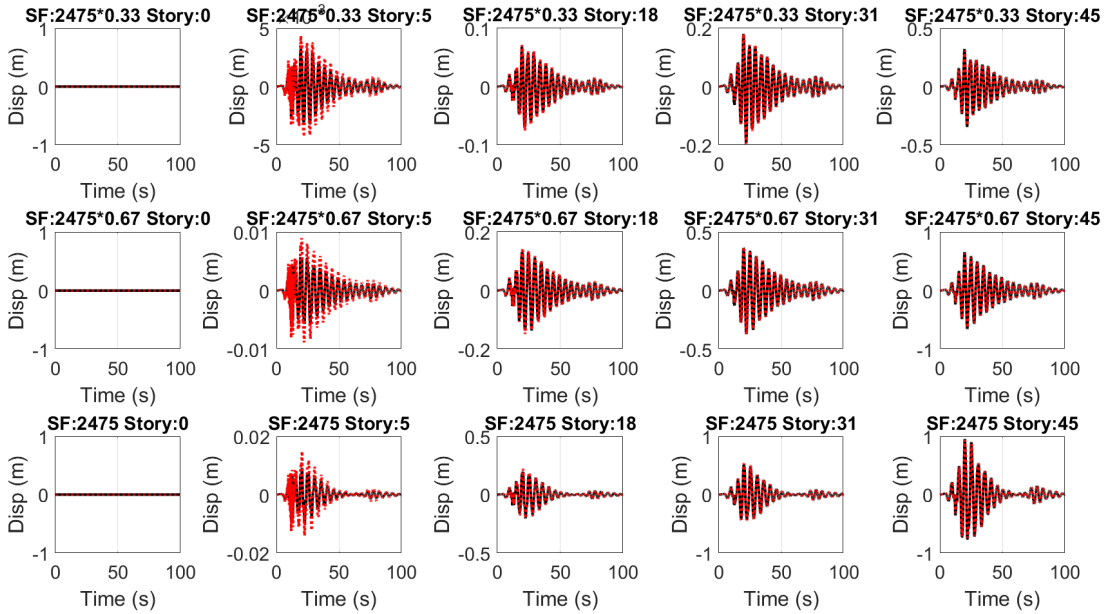

Figure 4.88. NLSM-Y: recorded (black solid line) and estimated (red dashed line) floor displacements, eq id: 3954.

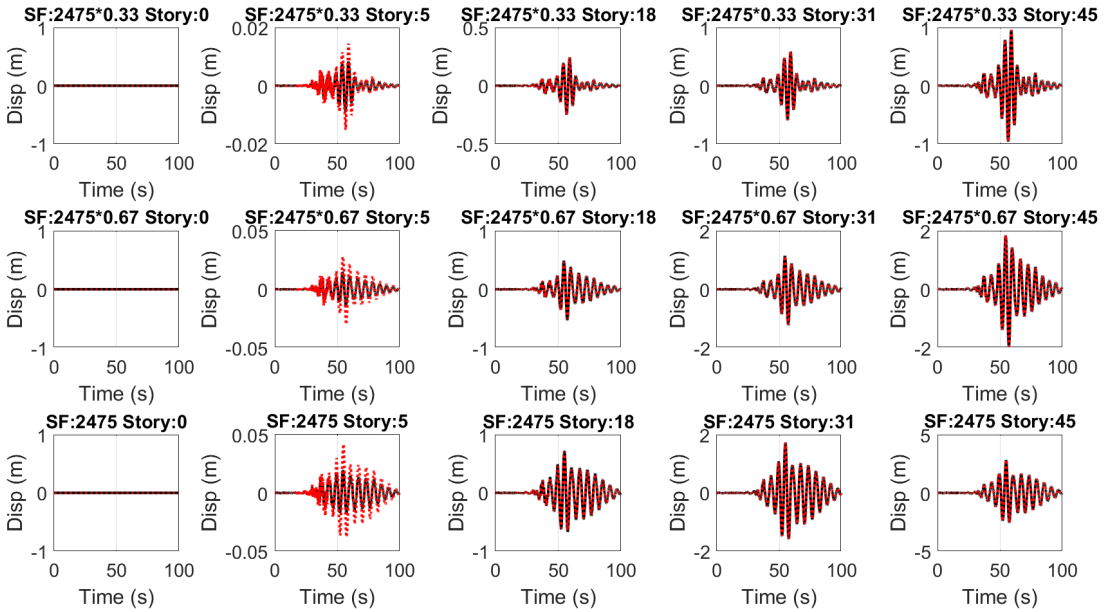

Figure 4.89. NLSM-Y: recorded (black solid line) and estimated (red dashed line) floor displacements, eq id: 5836.

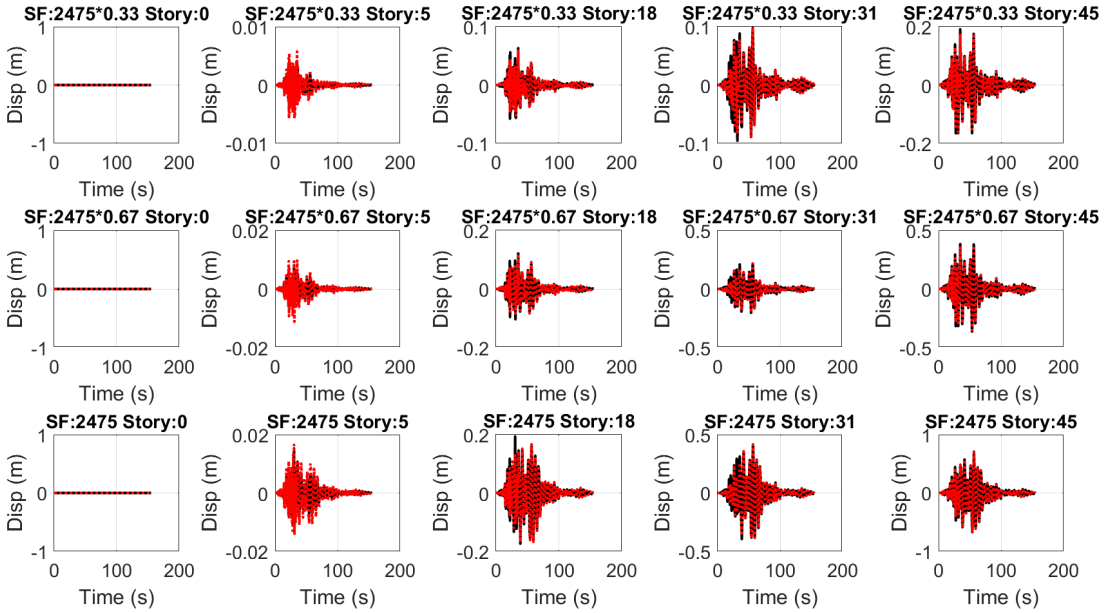

Figure 4.90. NLSM-Y: recorded (black solid line) and estimated (red dashed line) floor displacements, eq id: 6980.

Difference between recorded and estimated responses were calculated with Equation 4.22 and error values are presented for X and Y directions in Figure 4.91.

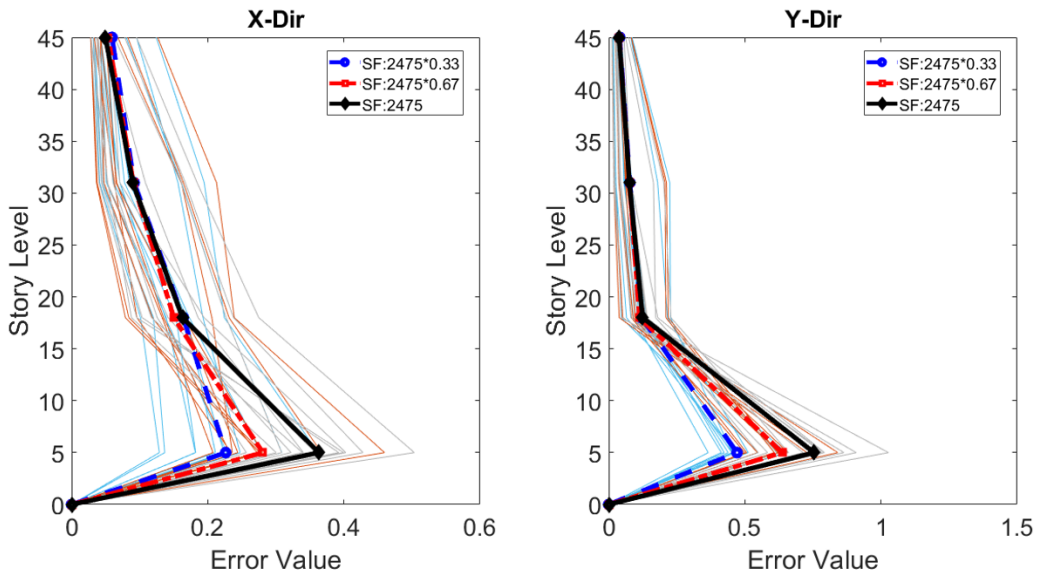

Figure 4.91. NLSM: error values between recorded and estimated floor displacements.

It can be clearly observed that recorded and estimated floor displacements show good agreement for instrumented floors. Since structural elements start to pass from elastic region to plastic region with increasing scale factors, error values of instrumented floors increase.

Also, maximum error value was obtained at 5th floor because stiffness of structure changes abruptly at 5th floor with finished basement walls.

After nonlinear simplified mathematical model updating of the structure, dynamic responses at all floors were estimated and inter-story drift ratios were calculated at each floor along the entire structure.

Figure 4.92 and Figure 4.93 represent inter-story drift ratios of the structure for both directions under earthquakes with different scale factors.

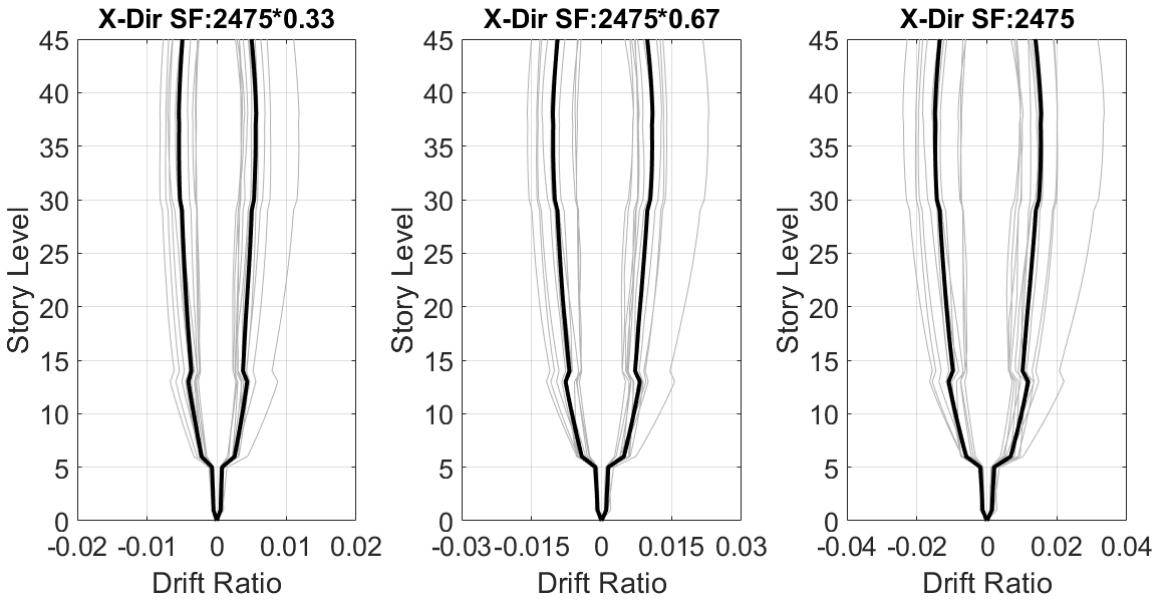

Figure 4.92. NLSM-X: estimated inter-story drift ratios.

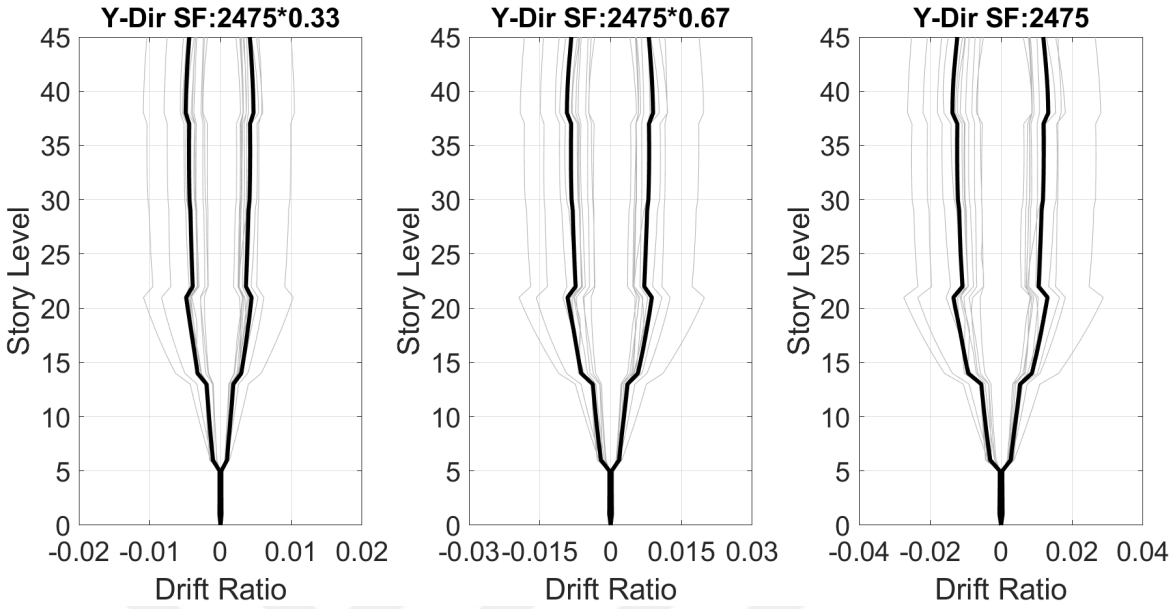

Figure 4.93. NLSM-Y: estimated inter-story drift ratios.

The main disadvantage of Simulated Annealing is that it may have more than one solution for same objective function. The main reasons are that boundary conditions of parameters in objective function cannot be strictly defined and defined boundary limits cannot be updated during process. In addition, comparison of objective function values are conducted by probabilistic approach with randomly selected parameters. For these reasons, results of Simulated Annealing after each earthquake were compared for each direction. (Figure 4.94 - Figure 4.121).

As can be seen from results of Simulated Annealing optimization, parameters of nonlinear springs are converged in certain ranges for more than half of ground motion records. However, significant deviations were observed especially for parameters of nonlinear shear springs. Actually, nonlinear shear springs in simplified nonlinear model were utilized to simulate frame system consisting of columns and beams. Since these members generally remain in elastic range under earthquakes, the effect of nonlinear shear spring properties to dynamic responses of the structure is limited. Therefore, deviations on parameters of nonlinear shear springs after updating were observed.

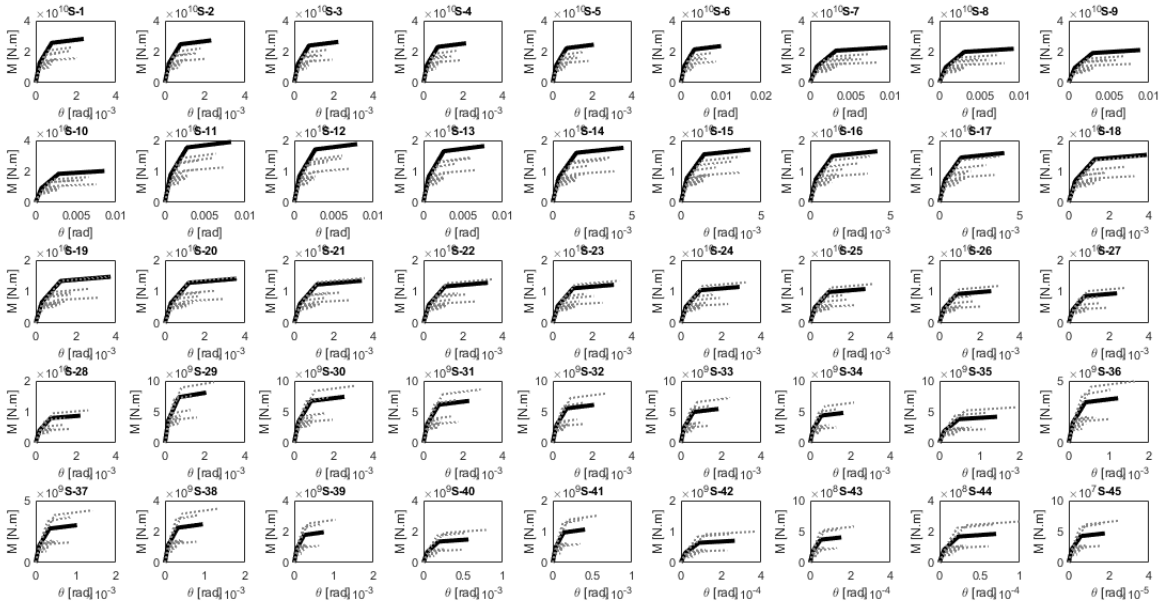

Figure 4.94. NLSM-X: nonlinear curves of flexural springs (initial curves: solid line, estimated curves: dashed line).

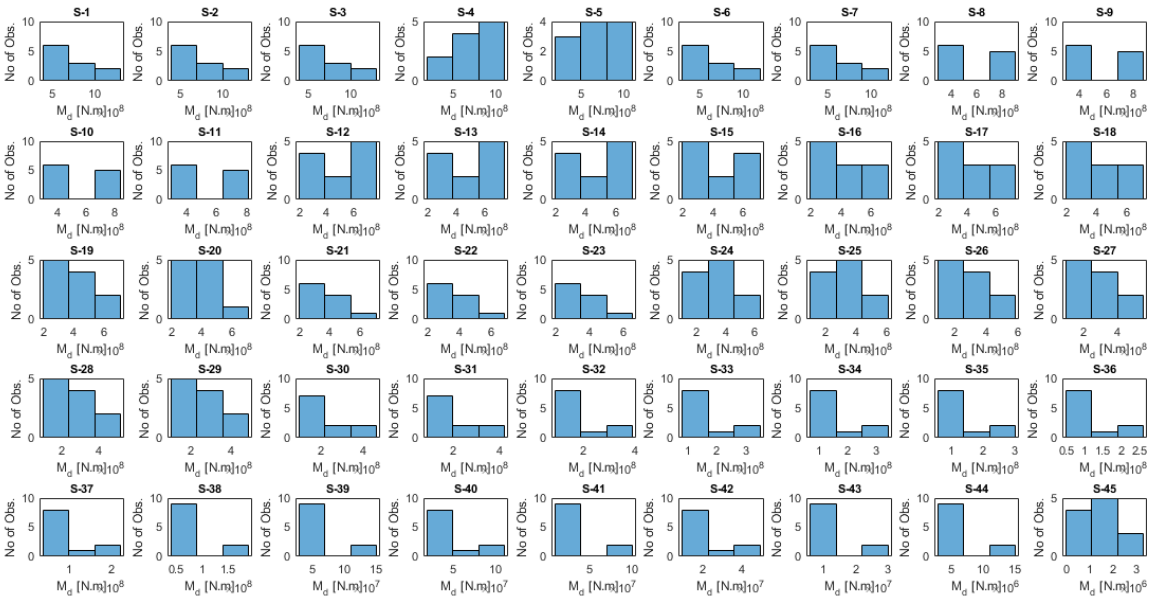

Figure 4.95. NLSM-X: distribution of estimated M_d.

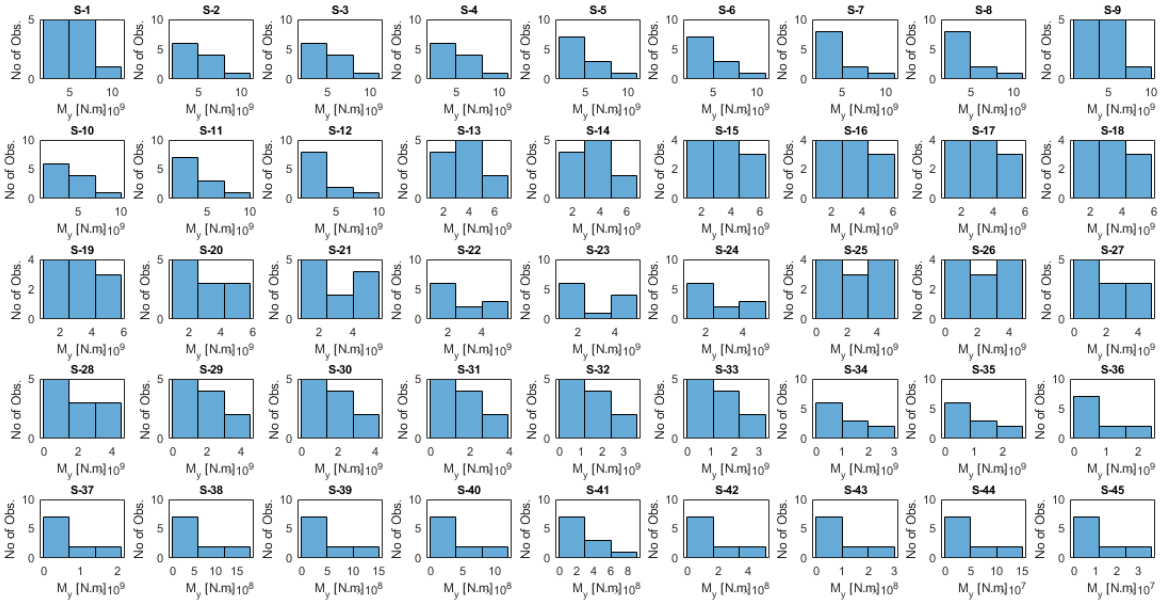

Figure 4.96. NLSM-X: distribution of estimated M_y.

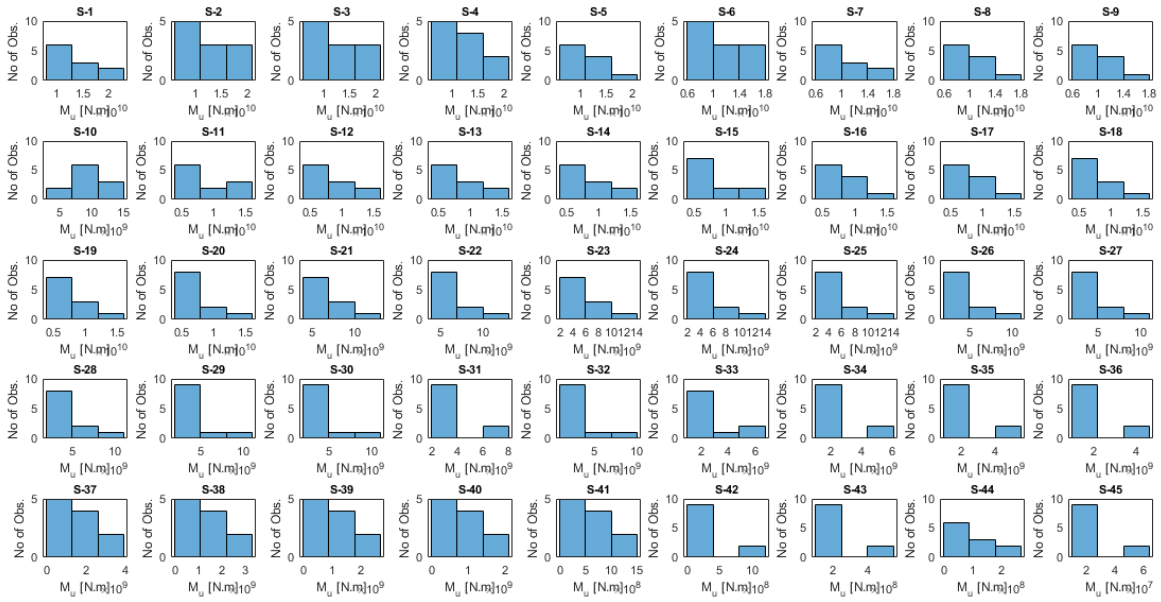

Figure 4.97. NLSM-X: distribution of estimated M_u.

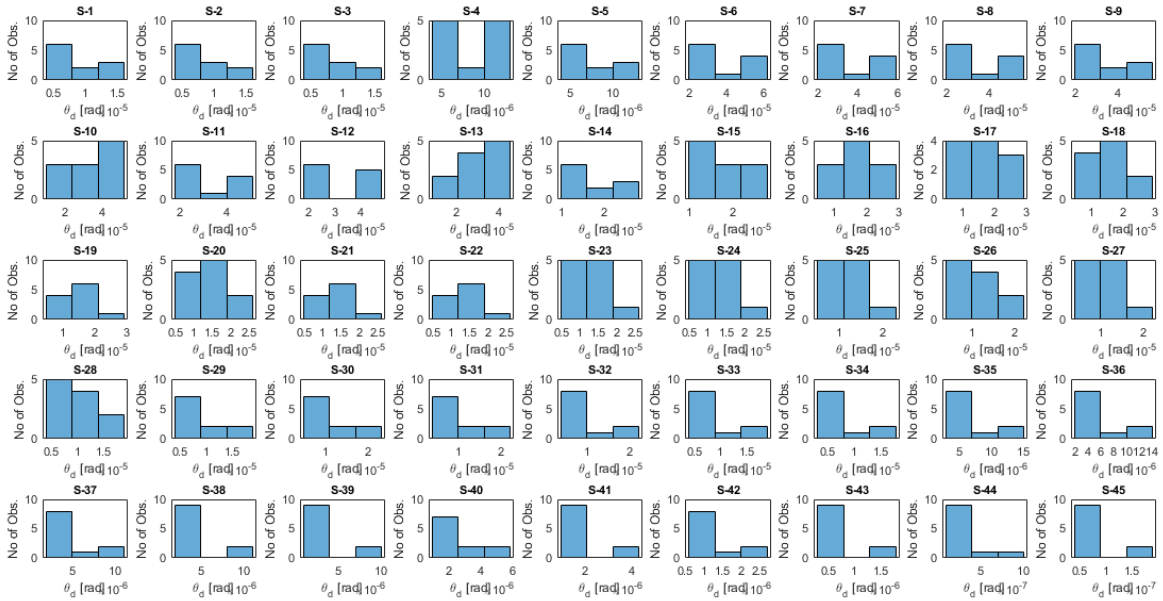

Figure 4.98. NLSM-X: distribution of estimated θ_d.

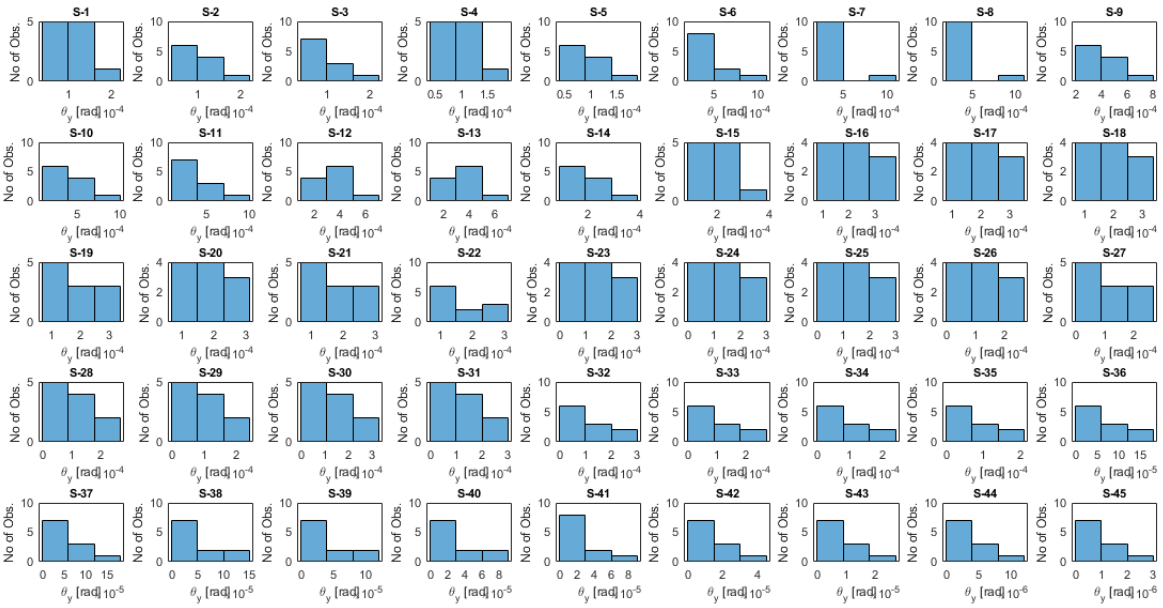

Figure 4.99. NLSM-X: distribution of estimated θ_y.

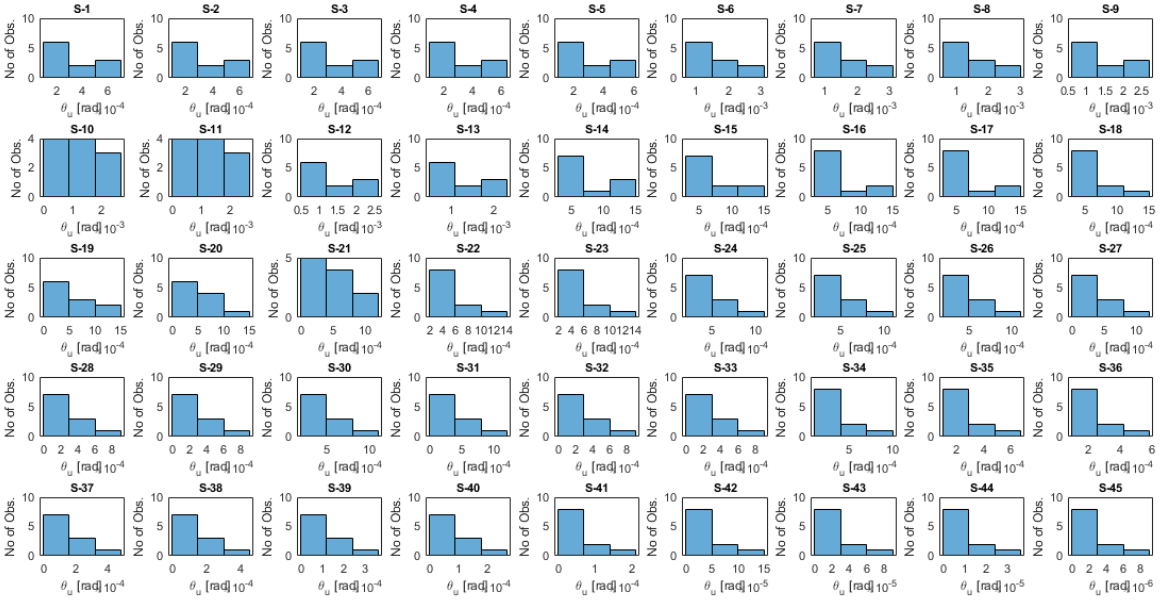

Figure 4.100. NLSM-X: distribution of estimated θ_u.

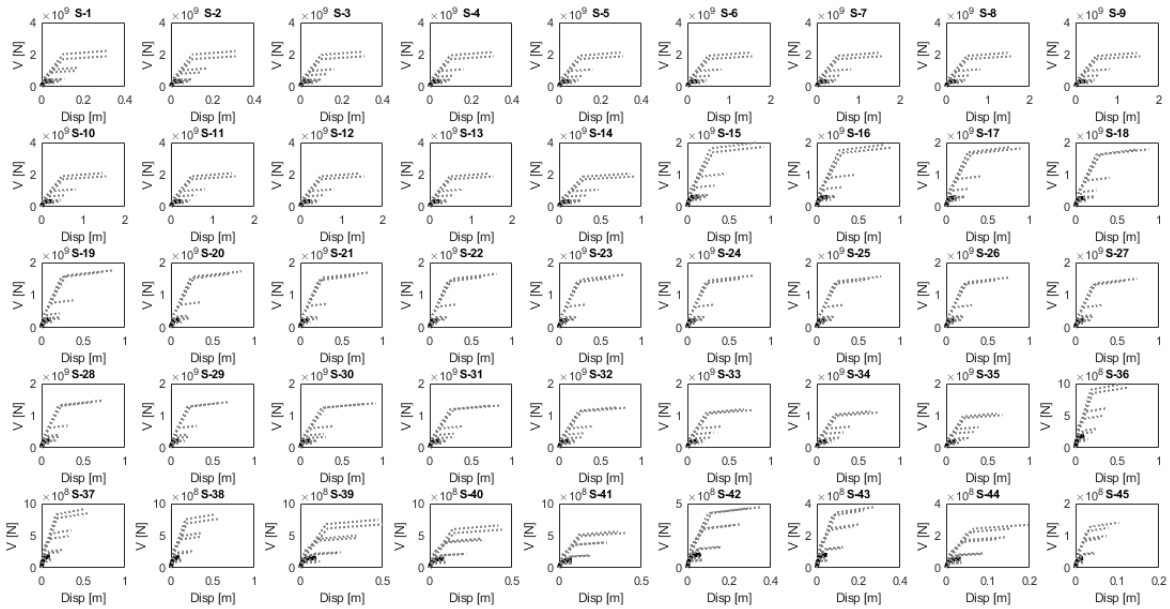

Figure 4.101. NLSM-X: nonlinear curves of shear springs (initial curves: solid line, estimated curves: dashed line).

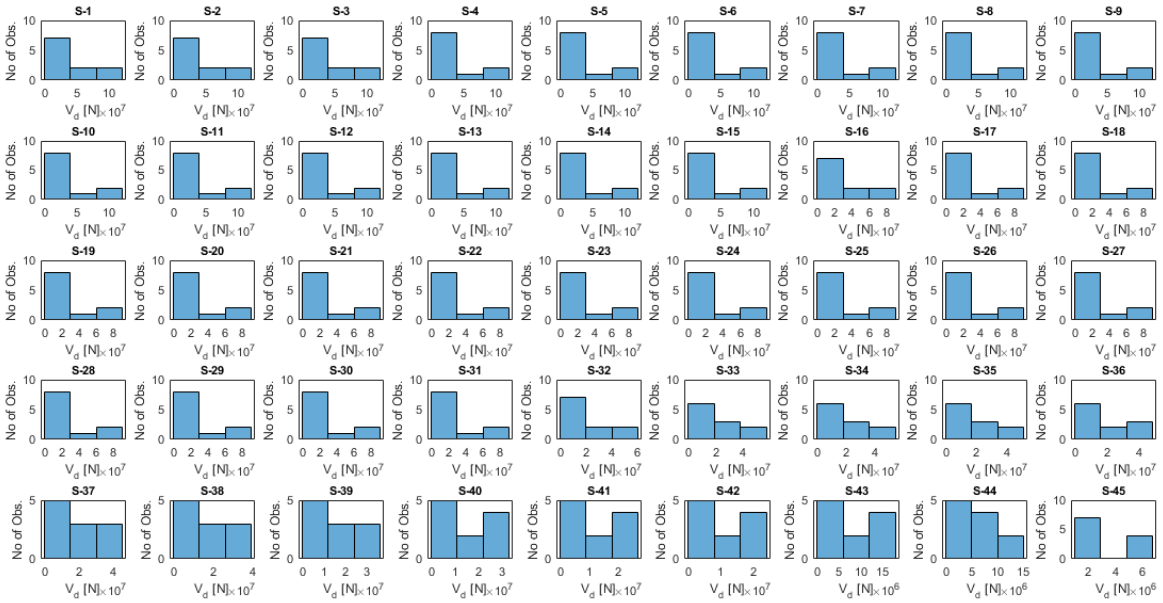

Figure 4.102. NLSM-X: distribution of estimated V_d.

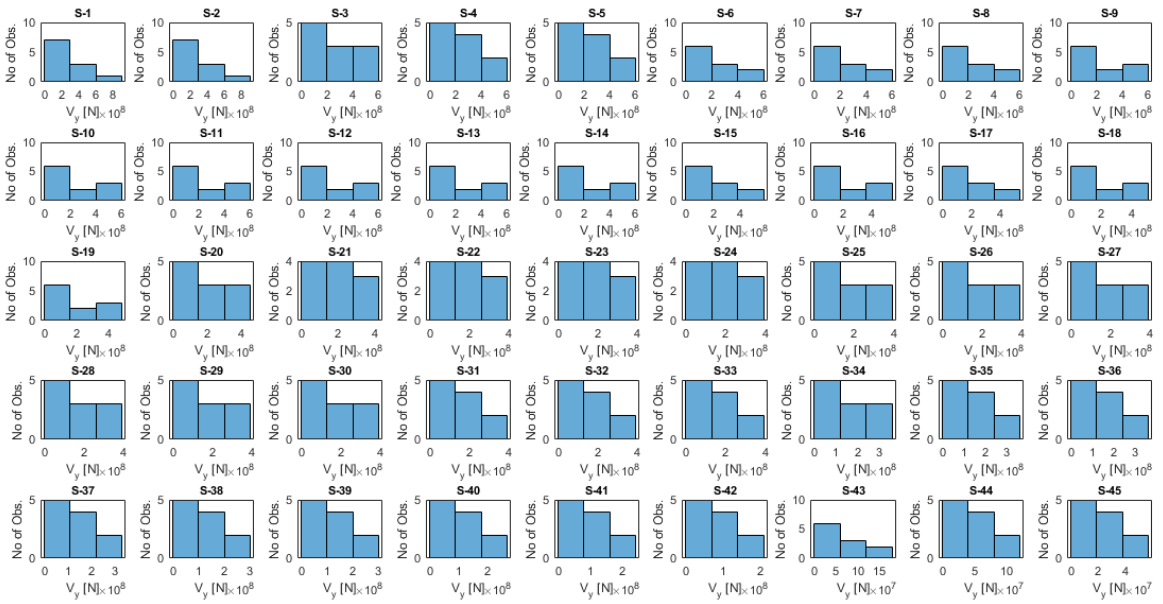

Figure 4.103. NLSM-X: distribution of estimated V_y.

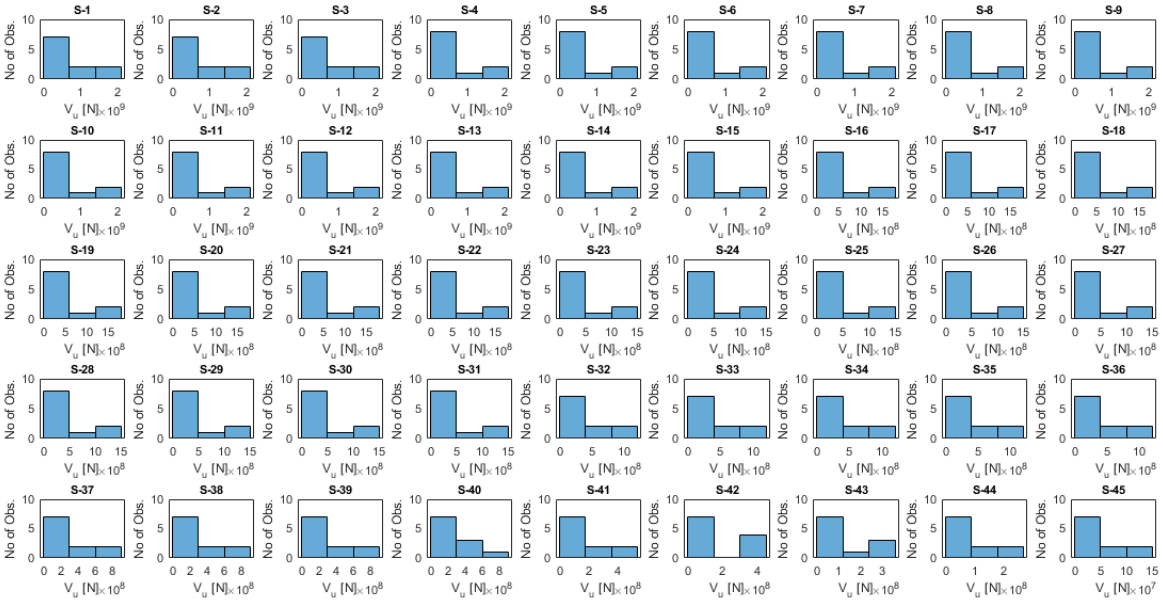

Figure 4.104. NLSM-X: distribution of estimated V_u.

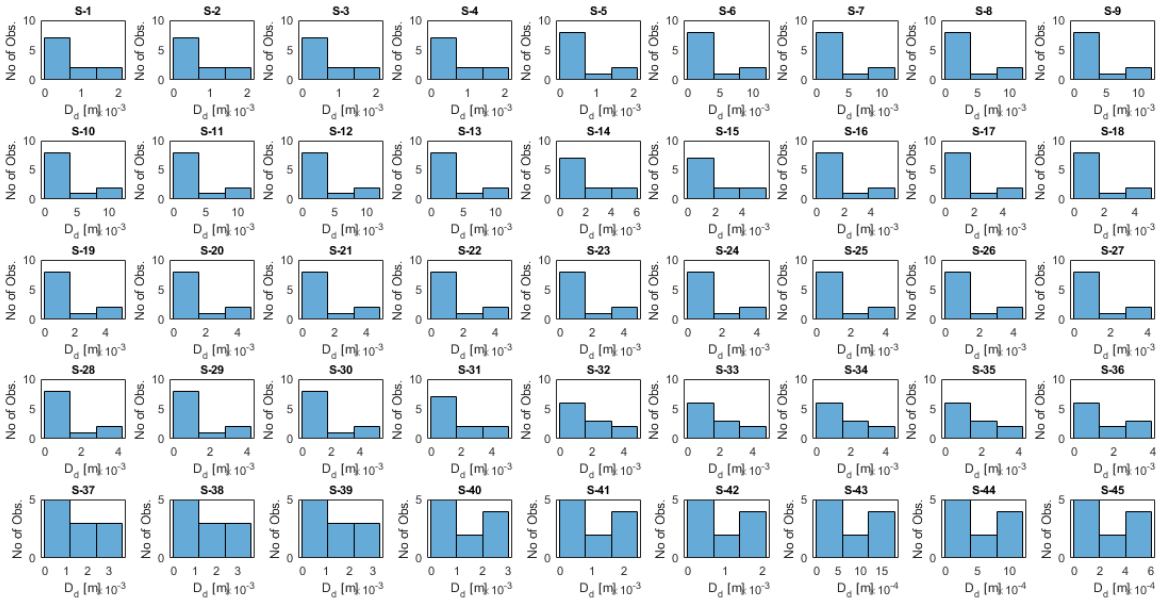

Figure 4.105. NLSM-X: distribution of estimated D_d.

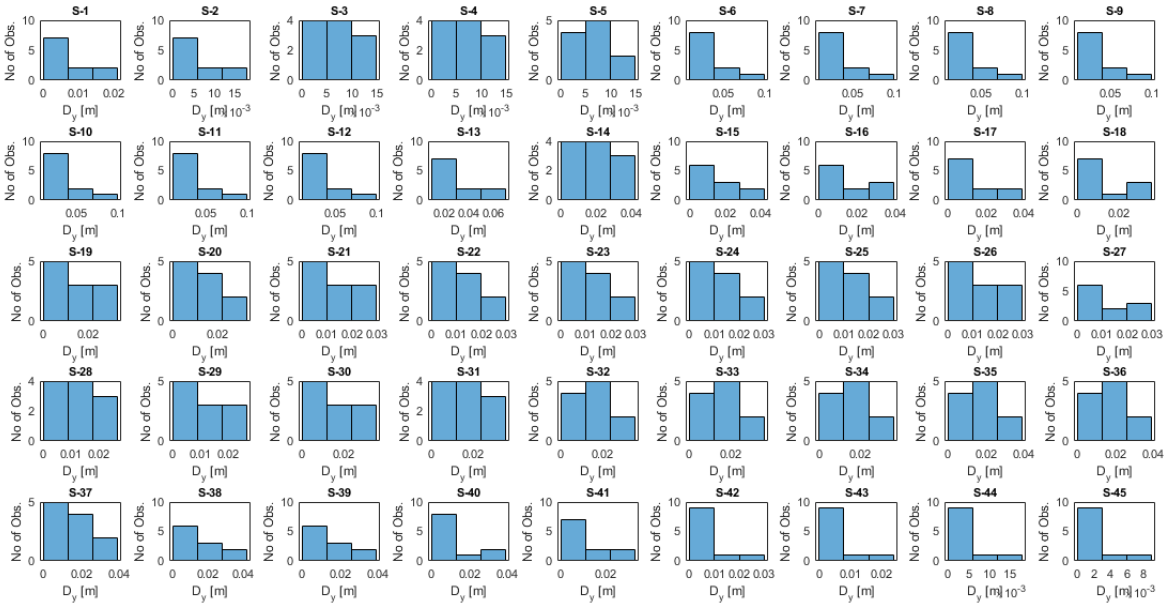

Figure 4.106. NLSM-X: distribution of estimated D_y.

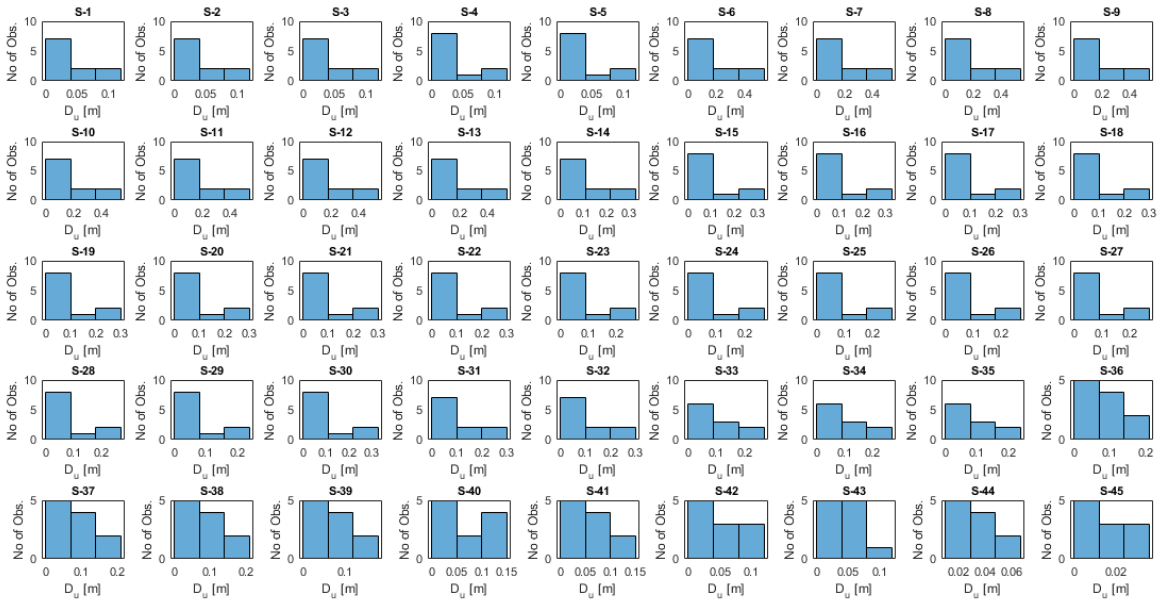

Figure 4.107. NLSM-X: distribution of estimated D_u.

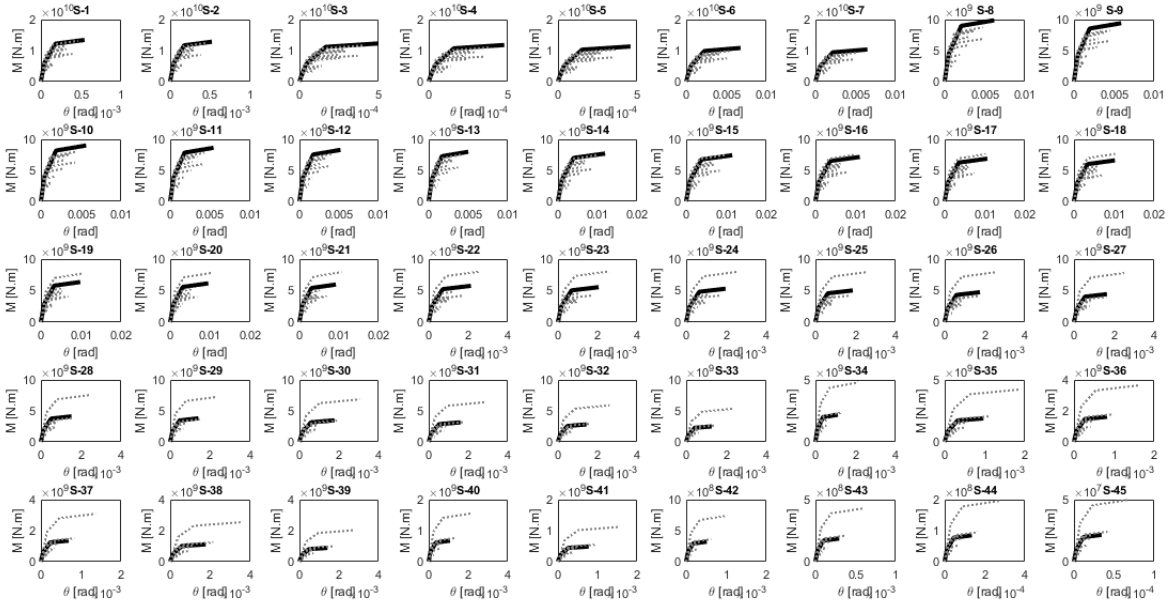

Figure 4.108. NLSM-Y: nonlinear curves of flexural springs (initial curves: solid line, estimated curves: dashed line).

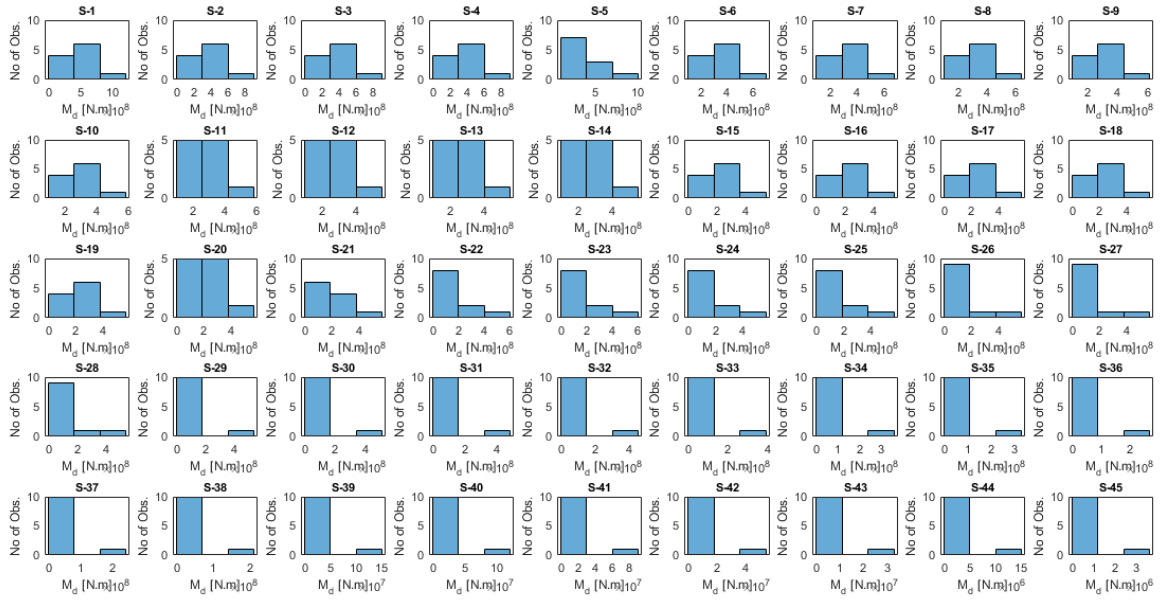

Figure 4.109. NLSM-Y: distribution of estimated M_d.

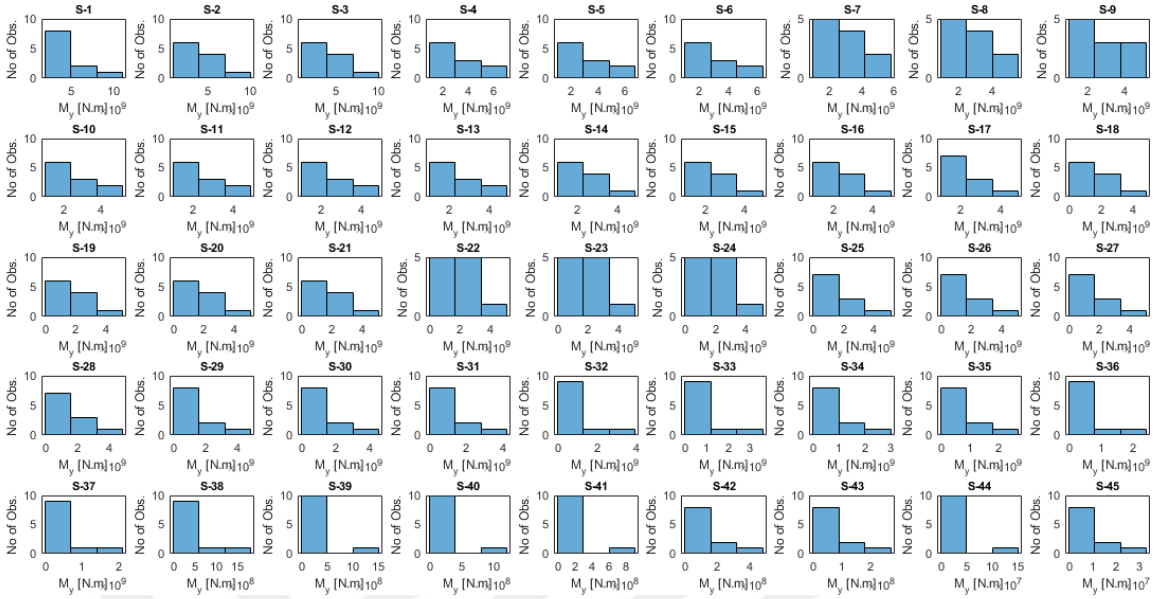

Figure 4.110. NLSM-Y: distribution of estimated M_y.

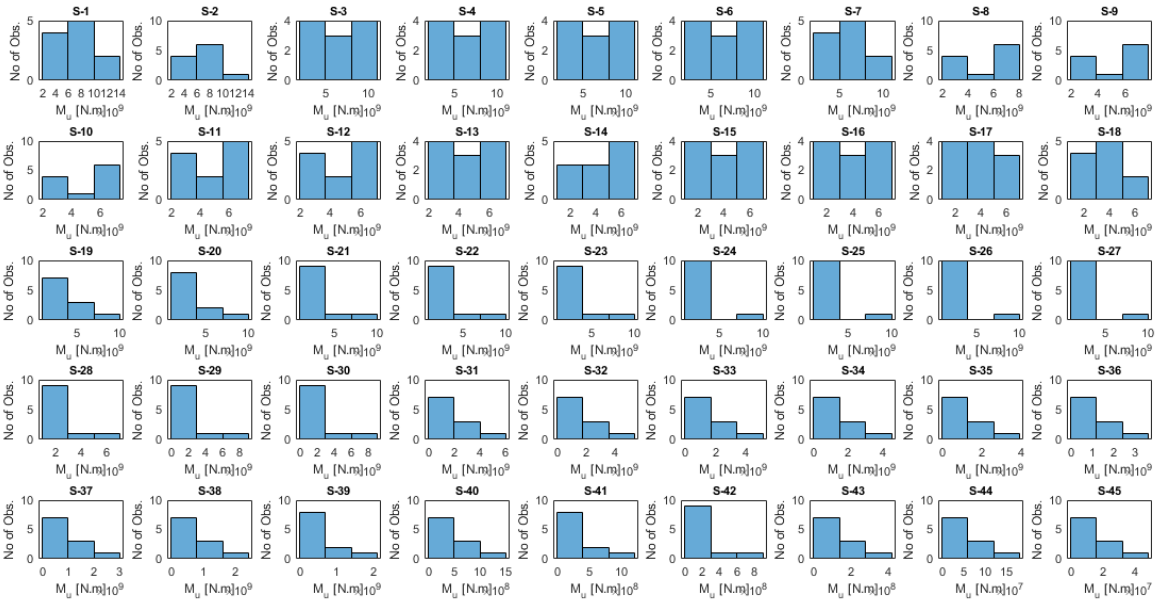

Figure 4.111. NLSM-Y: distribution of estimated M_u.

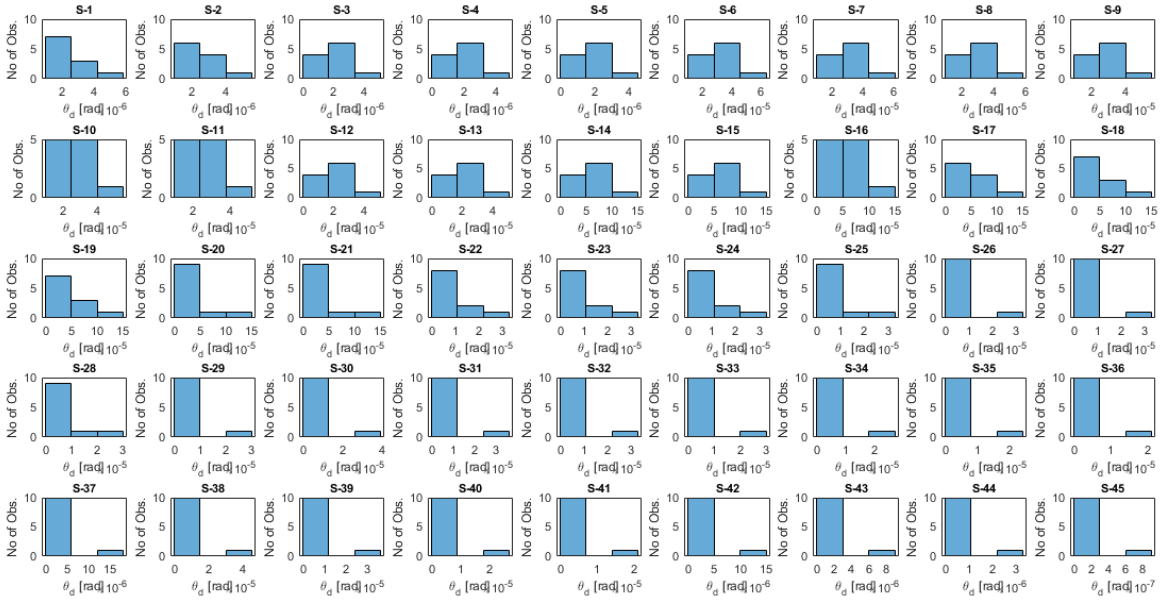

Figure 4.112. NLSM-Y: distribution of estimated θ_d.

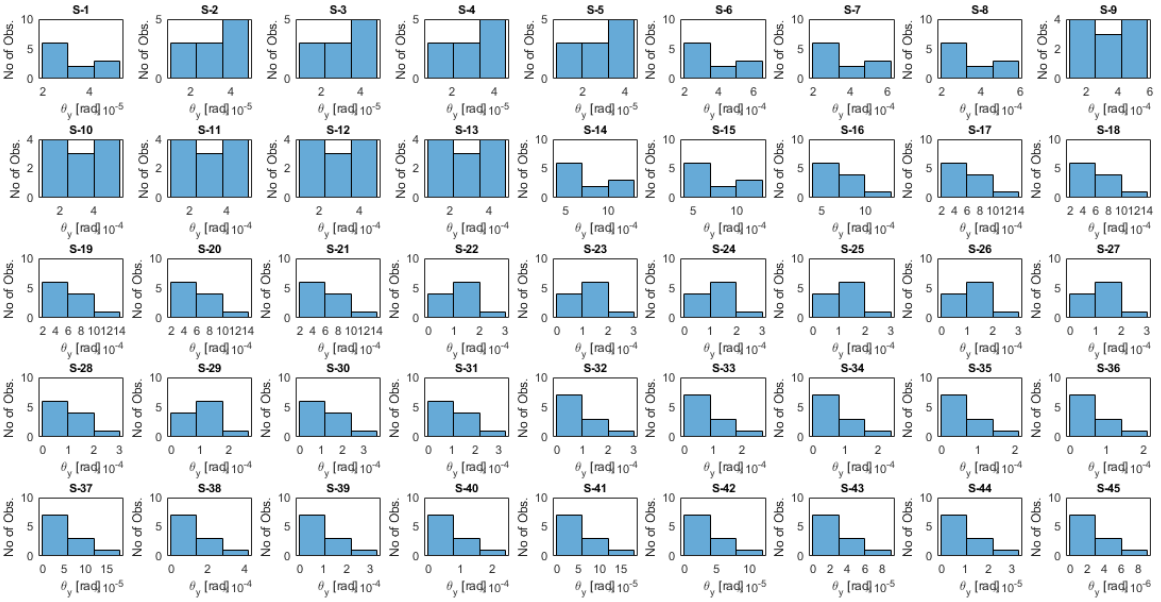

Figure 4.113. NLSM-Y: distribution of estimated θ_y.

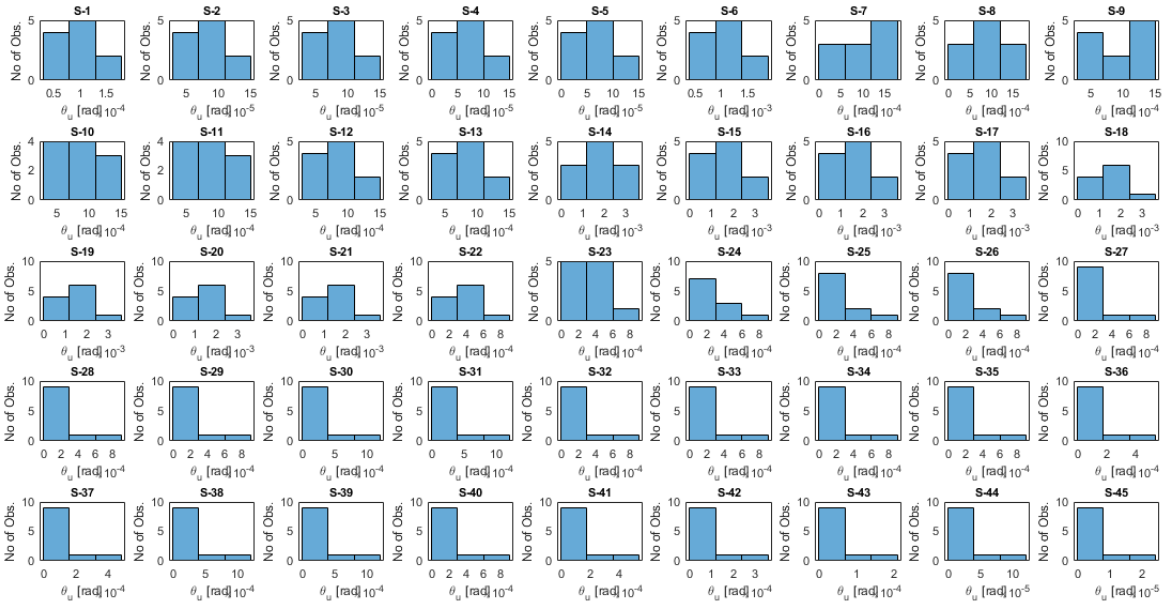

Figure 4.114. NLSM-Y: distribution of estimated θ_u.

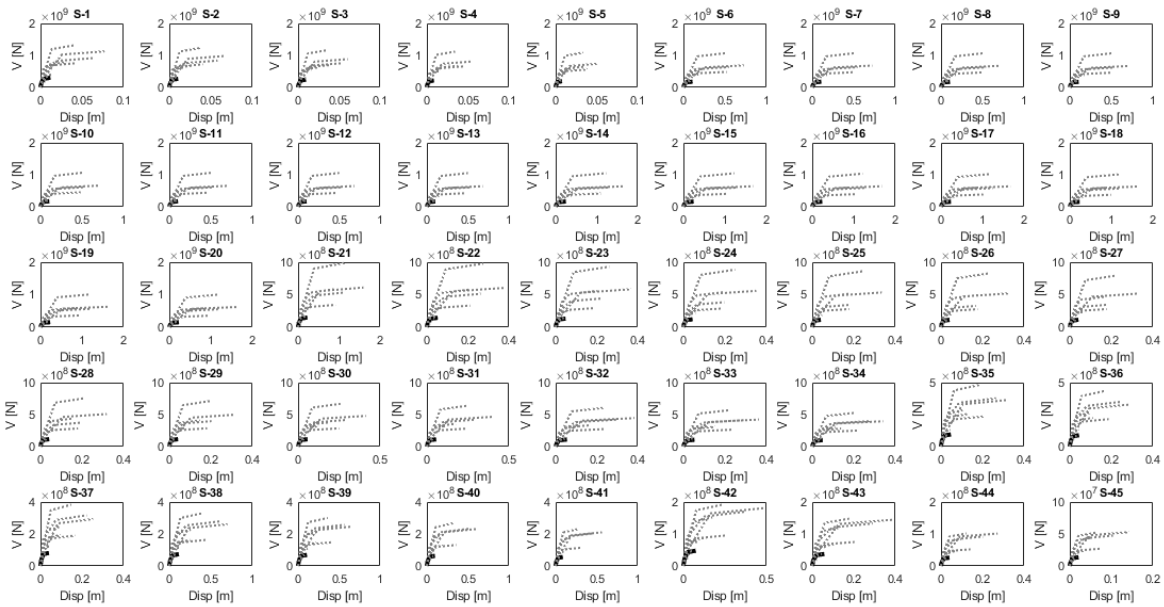

Figure 4.115. NLSM-Y: nonlinear curves of shear springs (initial curves: solid line, estimated curves: dashed line).

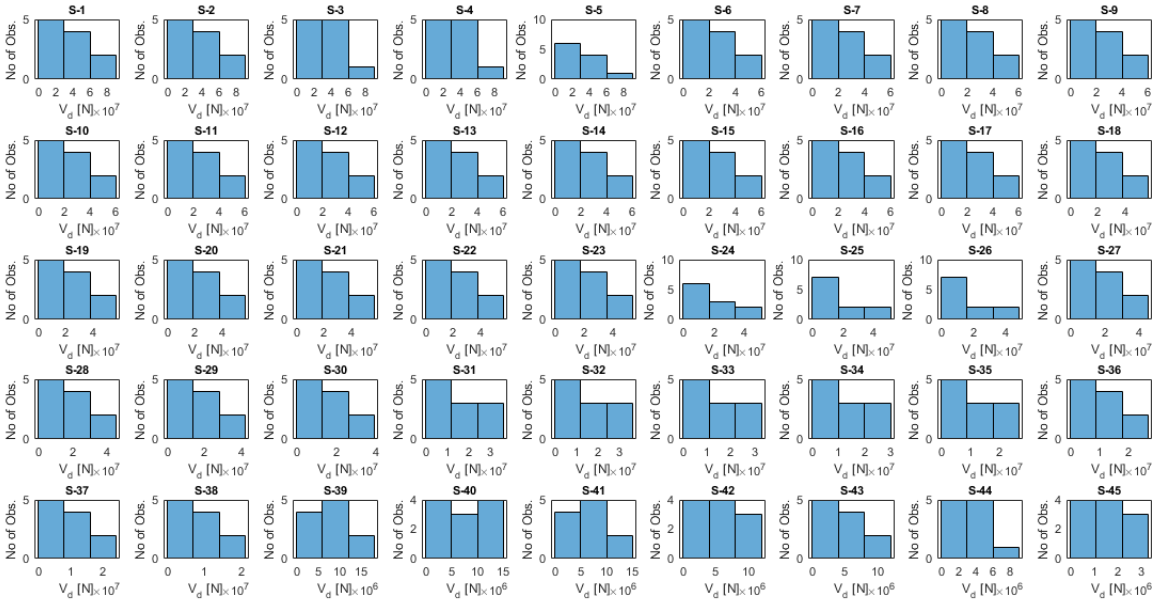

Figure 4.116. NLSM-Y: distribution of estimated V_d.

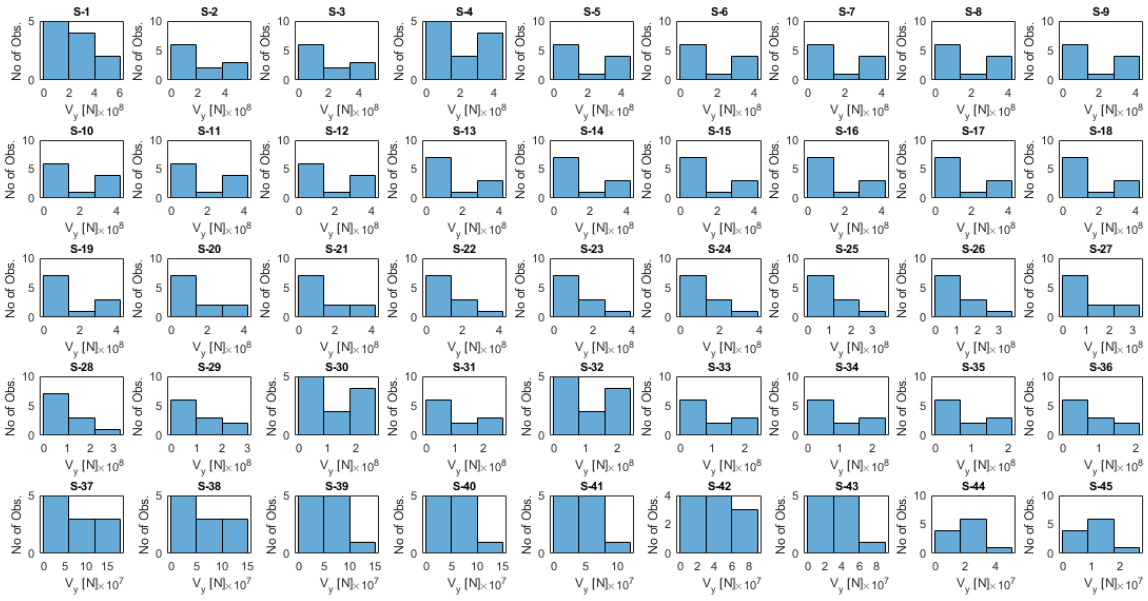

Figure 4.117. NLSM-Y: distribution of estimated V_y.

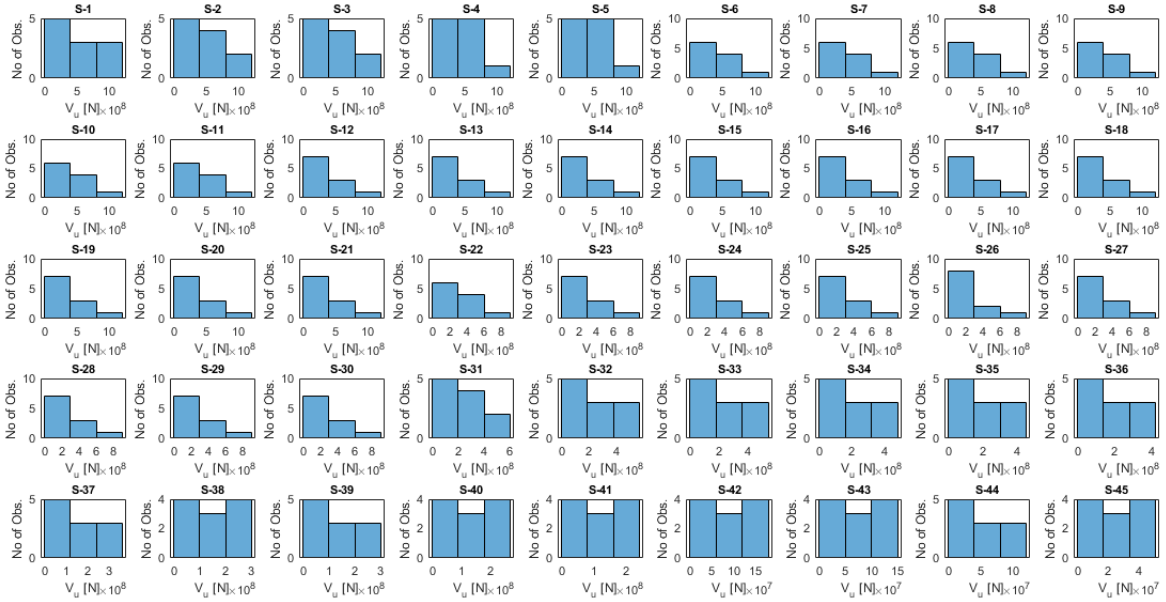

Figure 4.118. NLSM-Y: distribution of estimated V_u.

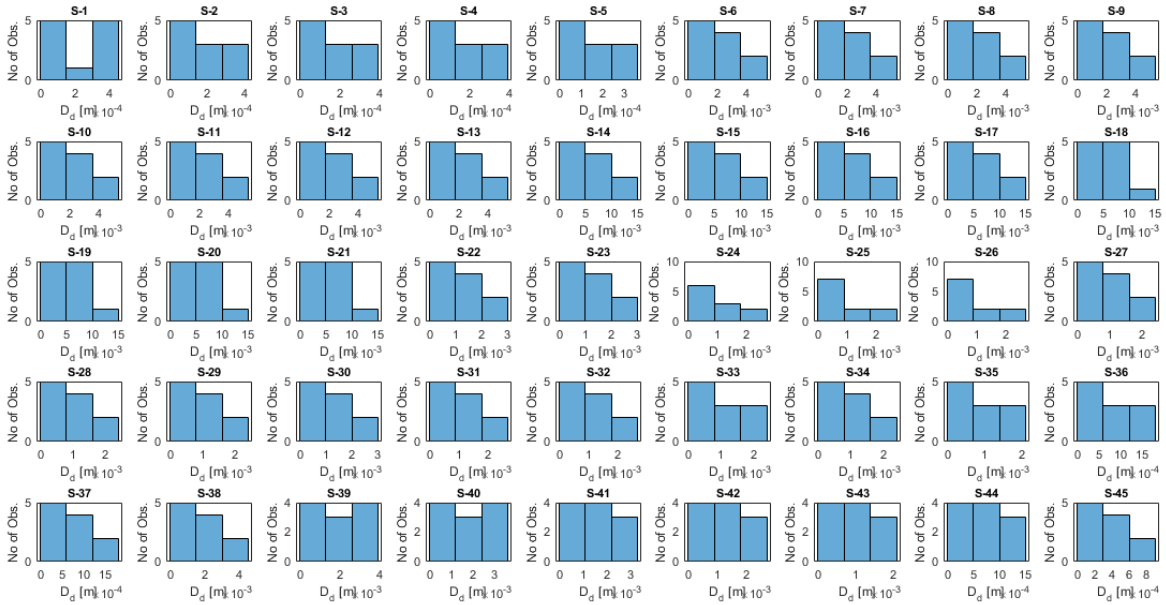

Figure 4.119. NLSM-Y: distribution of estimated D_d.

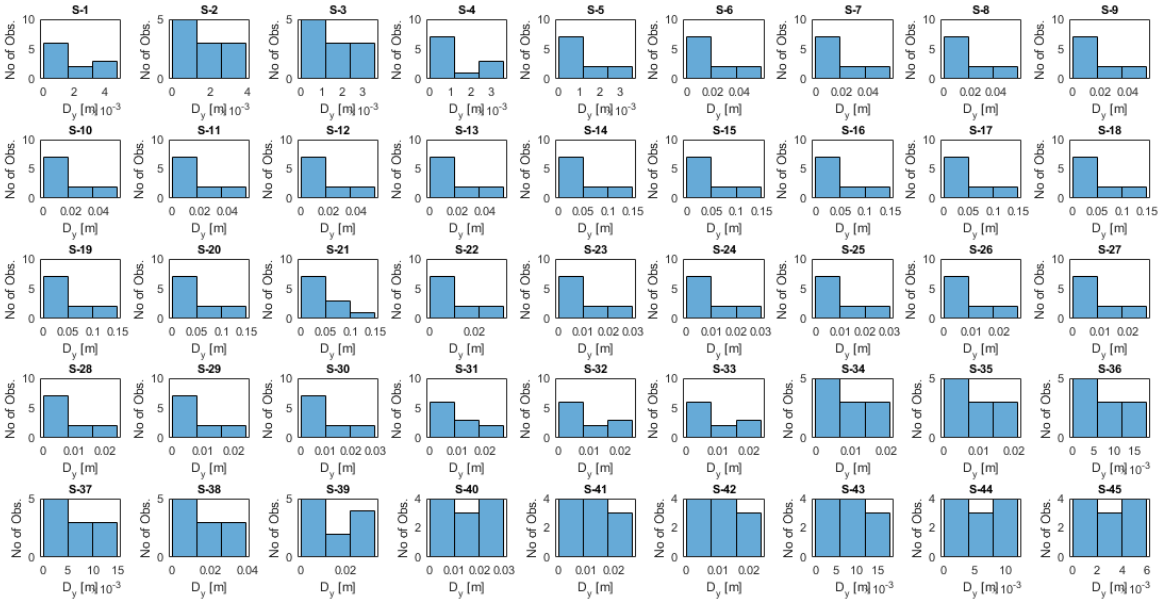

Figure 4.120. NLSM-Y: distribution of estimated D_y.

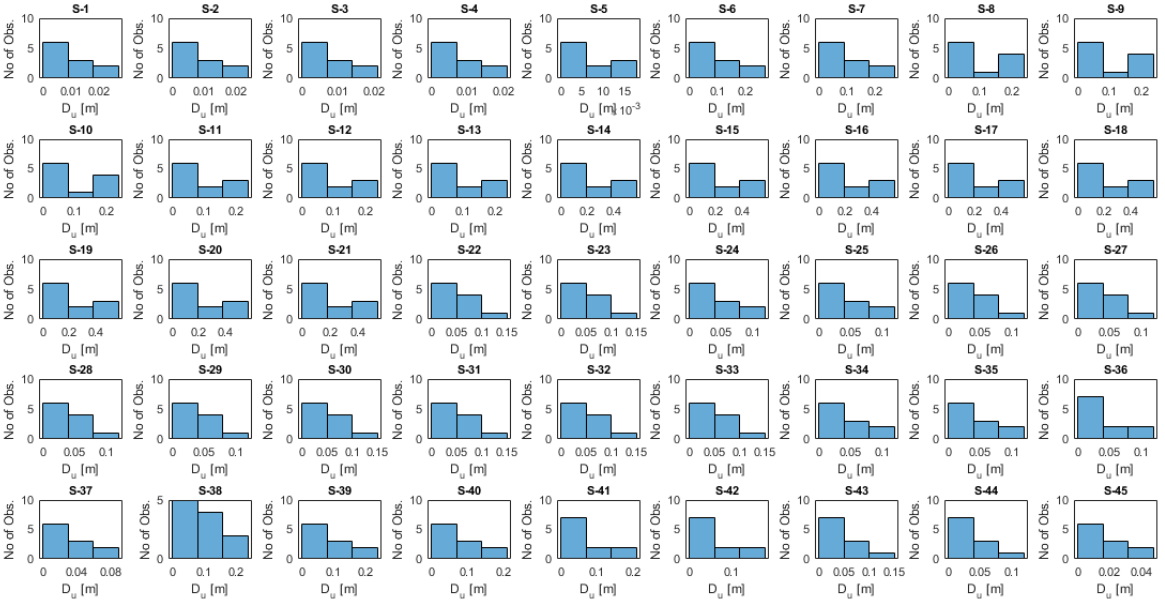

Figure 4.121. NLSM-Y: distribution of estimated D_u.

4.4. Comparison of Three Different Estimation Approaches

In this study, non-instrumented floor responses of multi-story structure were estimated from responses of instrumented floors by using different techniques. In this study, modelling tall building in OpenSees was considered as real structure with accelerometers at specific floors.

Firstly, elastic continuum mathematical model of modelled tall building was created by stepped Timoshenko beam model (STBM). In this approach, mechanical properties of different stories such as mass, stiffness, area and moment of inertia were considered with limited number of sections. If section number of STBM increases, convergence problems arise and analysis time increases due to complex compatibility equations. Besides, this approach does not consider nonlinear behavior effects.

Secondly, mathematical model of Timoshenko beam was discretized at story level in order to effectively consider different mass, stiffness and moment of inertia for each story. Dynamic response of simplified mathematical model was predicted by Transfer Matrix Method (TMM). Also, this method does not take into account nonlinear properties of structural components.

Finally, nonlinear simplified model of multi-story structure was created with nonlinear shear and flexural springs to consider effect of nonlinear properties on dynamic response of structure. Linear and nonlinear parameters of springs were updated by Simulated Annealing optimization method based on recorded responses of instrument floors.

Figure 4.122 and Figure 4.123 represent average errors calculated by three different approaches for selected ground motion records. Figure 4.124 and Figure 4.125 represent comparison of inter-story drift ratios of FEM (assumed as areal structure with SHM system) and simplified mathematical models created by different approaches.

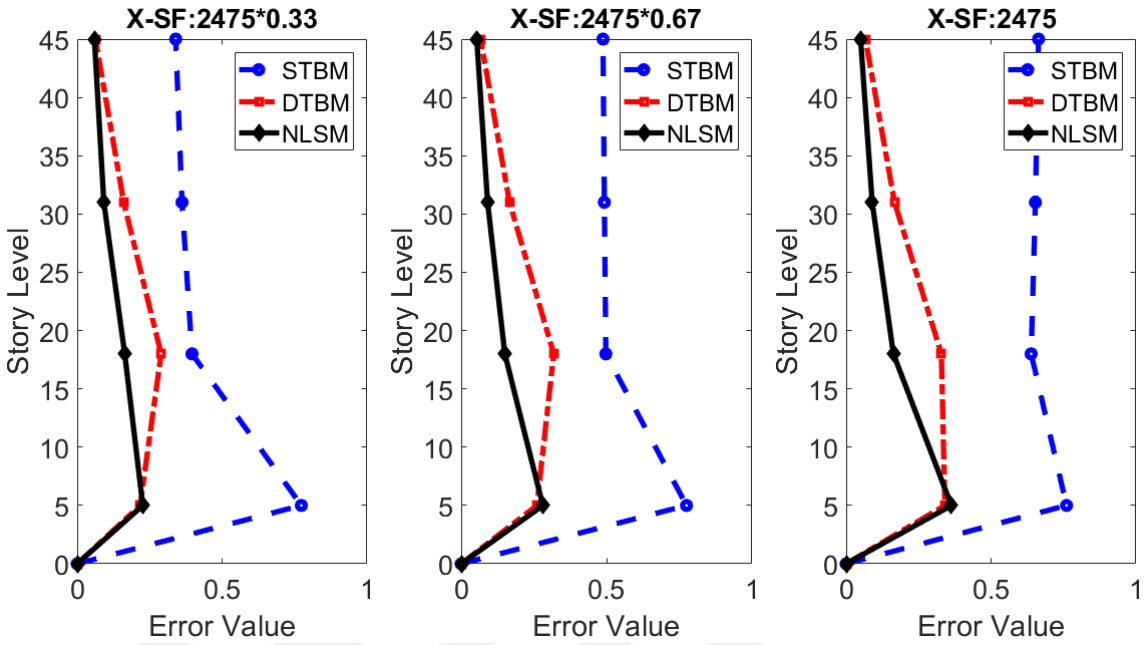

Figure 4.122. Comparison of error values between recorded and estimated floor displacements for x direction.

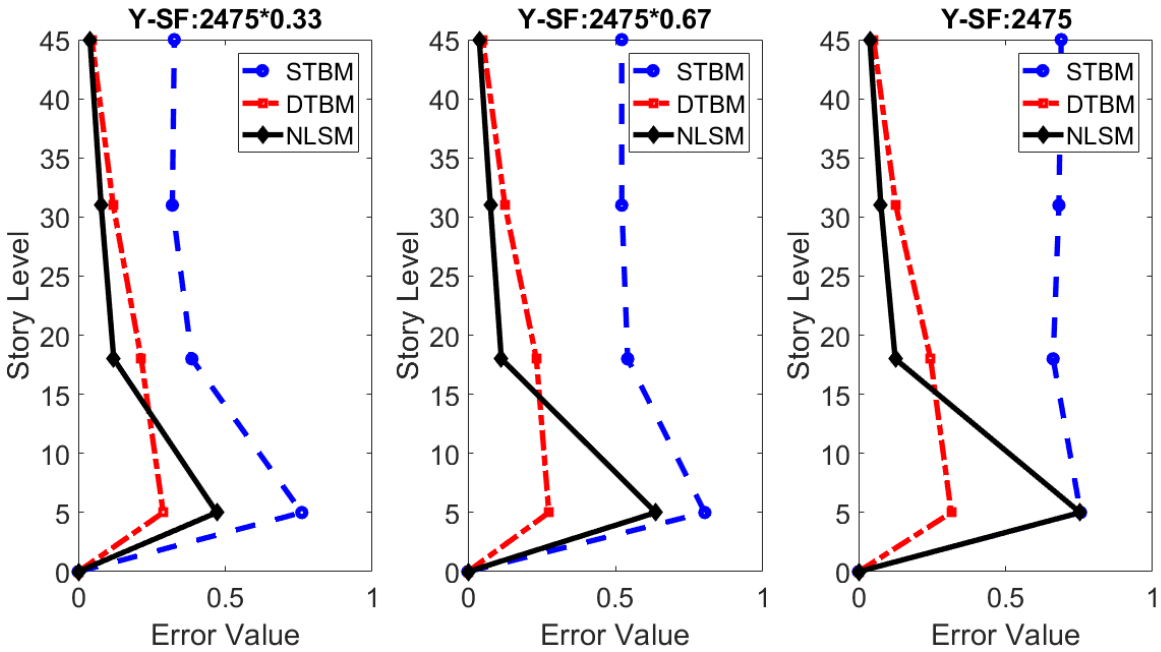

Figure 4.123. Comparison of error values between recorded and estimated floor displacements for y direction.

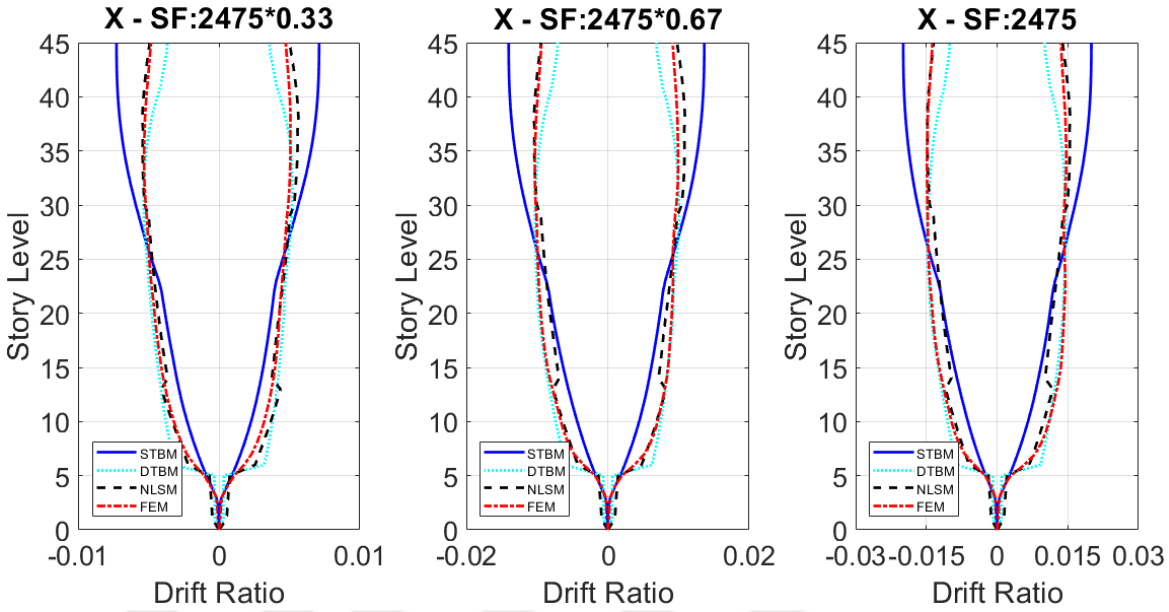

Figure 4.124. Comparison of inter-story drift ratios for x direction.

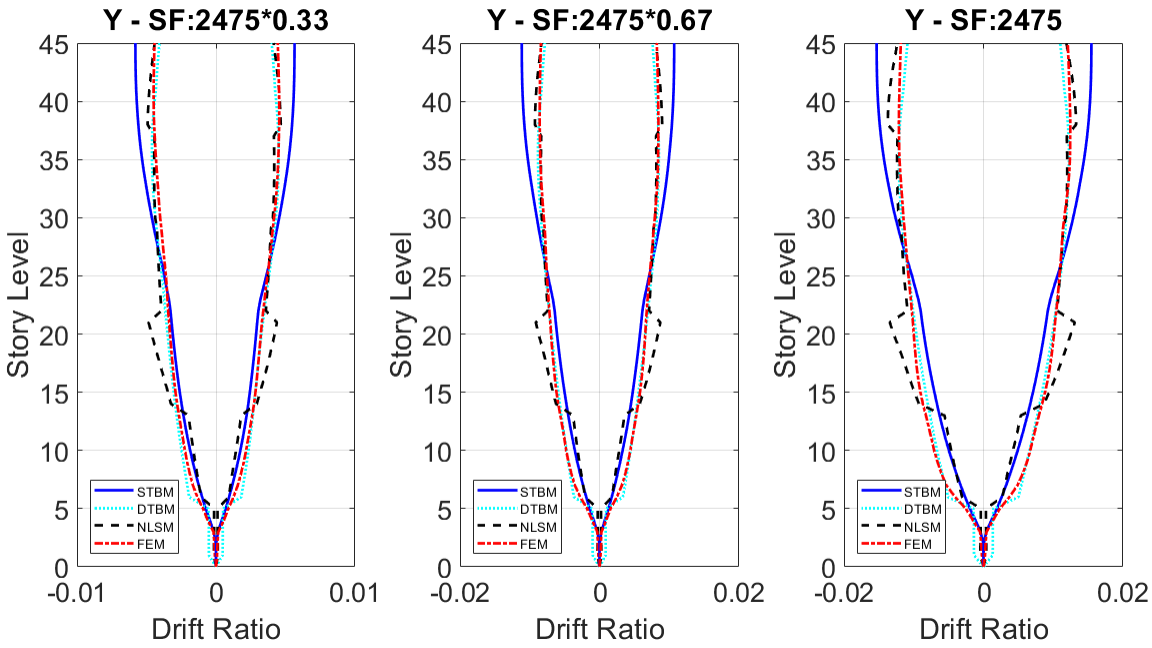

Figure 4.125. Comparison of inter-story drift ratios for y direction.

Continuous and discrete elastic mathematical models of the structure do not take into account nonlinear properties of structural components. Besides, mechanical properties of the structure such as mass, stiffness, area and moment of inertia at different stories are considered in limited ranges to satisfy compatibility equations due to convergence problems and analysis time. Comparison results show that considering different mechanical properties such ass mass and stiffness for different stories by discretizing of model at each story level and considering nonlinear properties of structural components increase accuracy of simulated dynamic responses of simplified models.

5. DAMAGE EVALUATION

Tall buildings are significant engineering solutions to respond needs of cities with rapidly increasing population. Many guidelines and seismic codes have been published and revised to increase performance of tall buildings against earthquakes in seismic regions. Since number of tall buildings increases with development of technology in seismically prone regions, reliable condition assessment of tall buildings after earthquakes is very significant. There are many recommendations such as visual inspection, controlling top displacement and residual drift for damage assessment in many studies and guidelines [103-112]. It is clear that stiffness of structure decreases due to damage during earthquake and dynamic properties of structure changes due to stiffness degradation. Changes in dynamic properties of structure (most significant change is reduction in modal frequencies) can be tracked by using recorded responses of instrumented floors to assess condition of structures after earthquakes. Also, peak inter-story drift ratio is a reliable indicator to determine condition of structures after earthquakes. However, it is difficult to obtain inter-story drifts profile for structures due to limited number of sensors.

In this study, damage evaluation of structure was performed by using changes in fundamental frequencies of structure and peak inter-story drift ratios as damage indicators [113]. The main reason for using two different parameters for damage assessment is that only using frequency change or only using inter-story drift ratio may not be reliable. For this purpose, new methodologies are presented to predict non-instrumented floor responses of structure from recorded responses of instrumented floors. Therefore, peak inter-story drift ratio of structure can be reliably predicted by using these methods. In addition, damage level determined by this method was compared by damage level of structural members obtained for FEM analyses. For this purpose, nonlinear behavior of coupling beams were used because they are critical structural components that significantly contribute to energy dissipation in tall buildings during earthquake.

Figure 5.1 – Figure 5.22 represents change in frequencies of structure during selected ground motions for different scale factors. Damage Index (DI) for assessment was calculated as $DI = 1 - (f_{1-min}/f_{1-init})^2$.

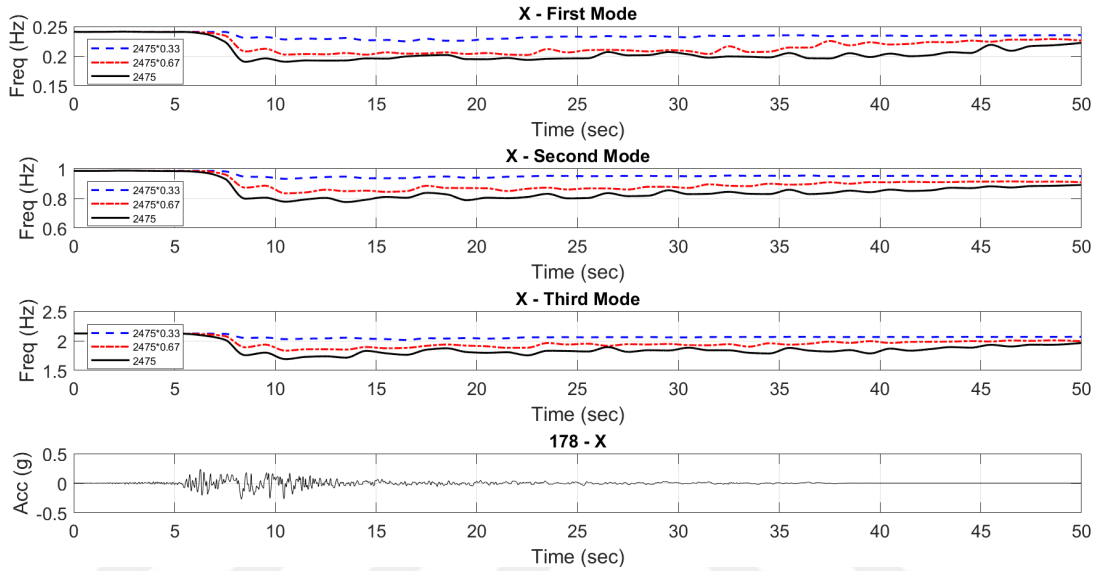

Figure 5.1. Changes in modal frequencies for x direction, eq id: 178.

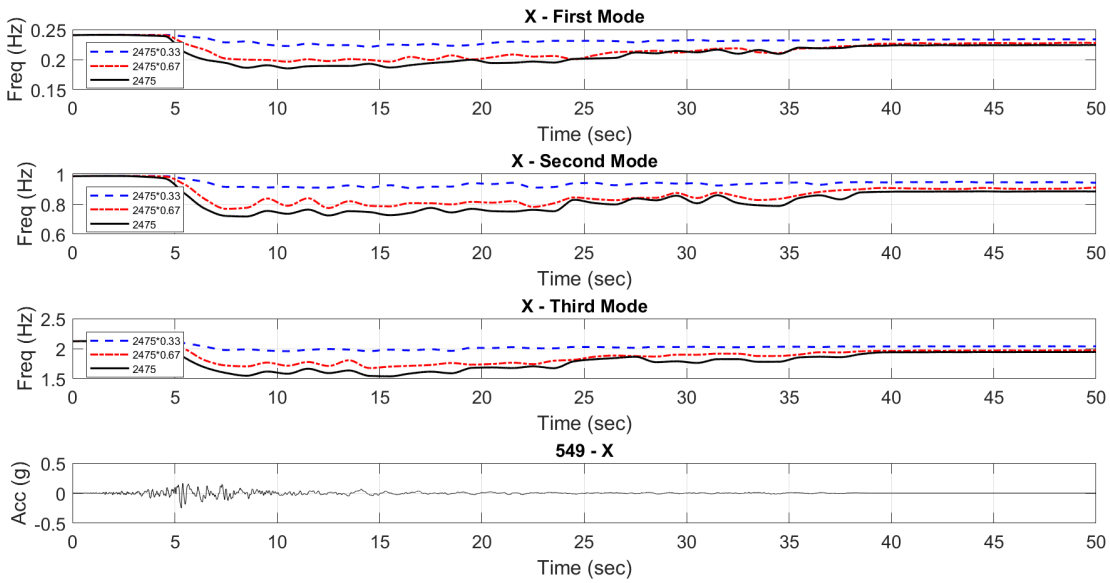

Figure 5.2. Changes in modal frequencies for x direction, eq id: 549.

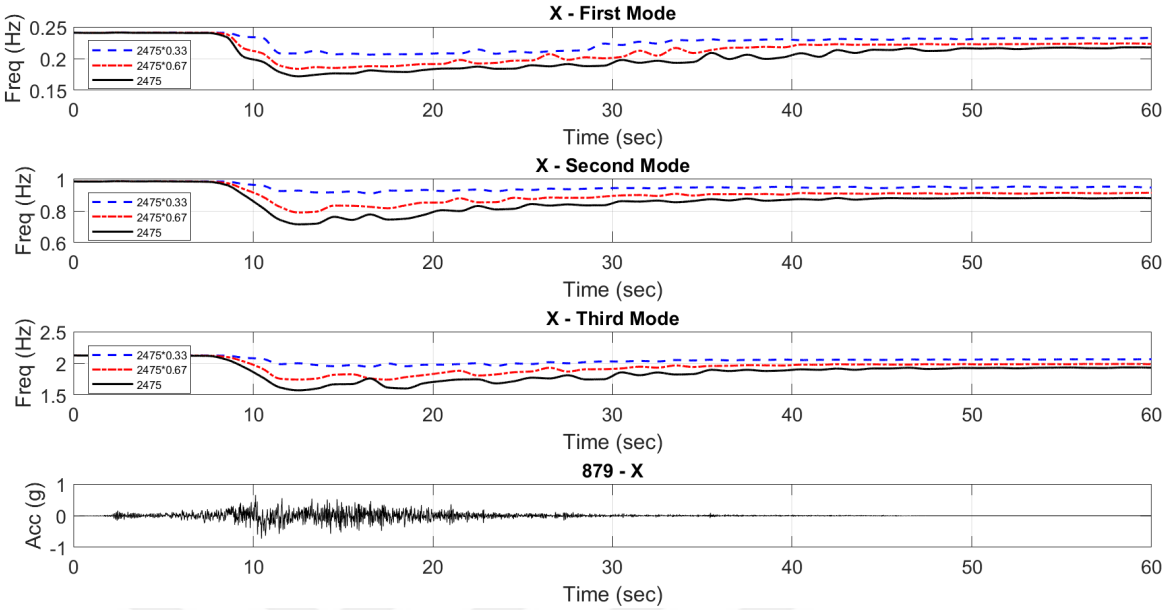

Figure 5.3. Changes in modal frequencies for x direction, eq id: 879.

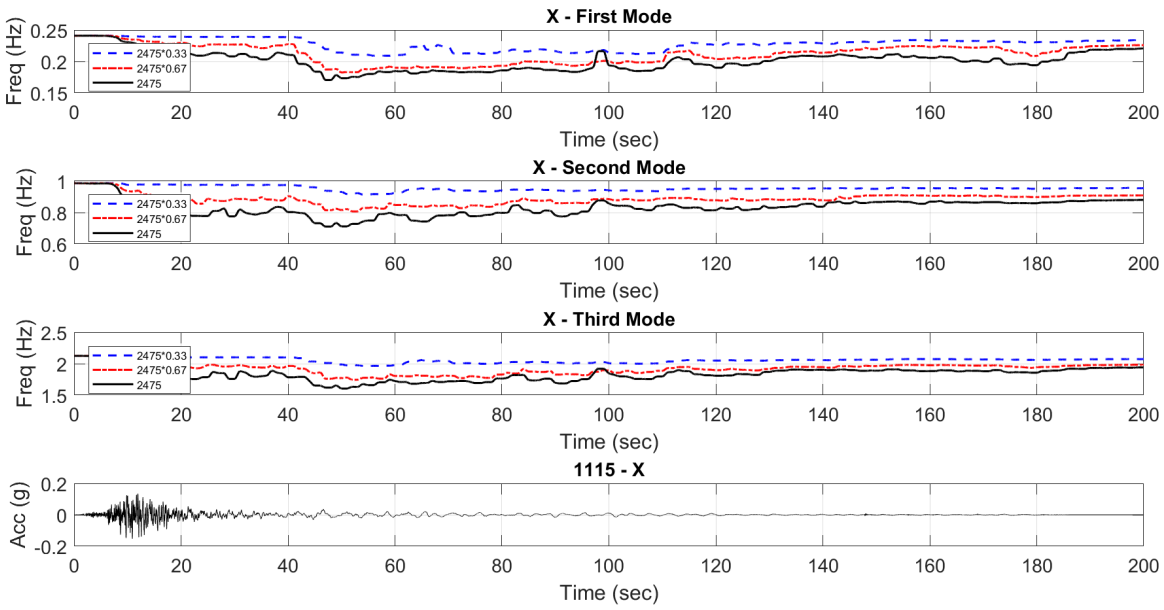

Figure 5.4. Changes in modal frequencies for x direction, eq id: 1115.

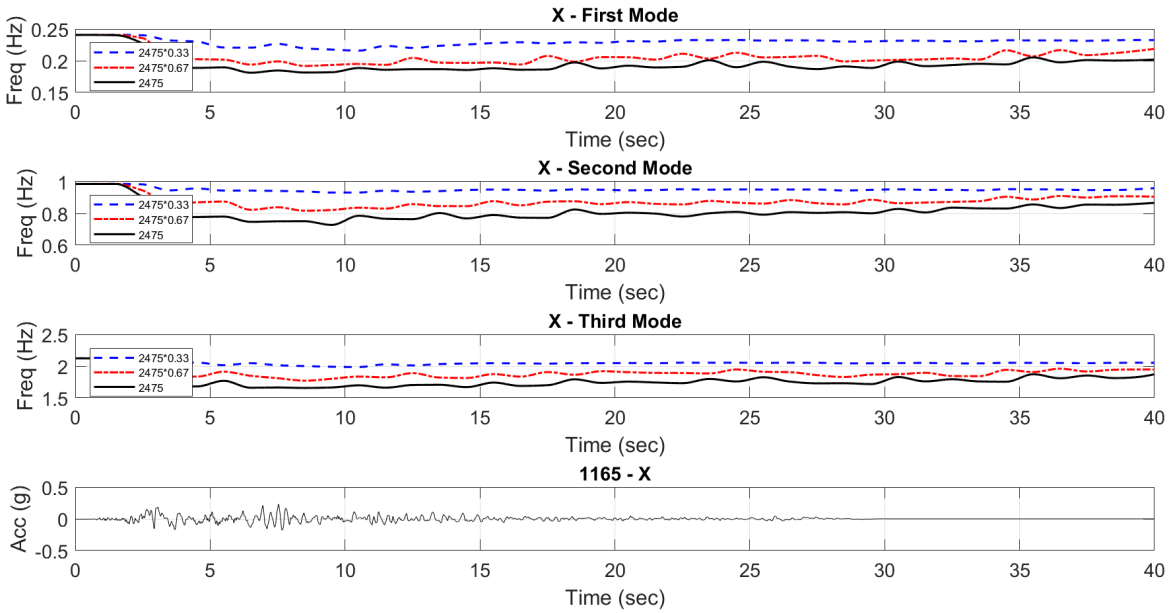

Figure 5.5. Changes in modal frequencies for x direction, eq id: 1165.

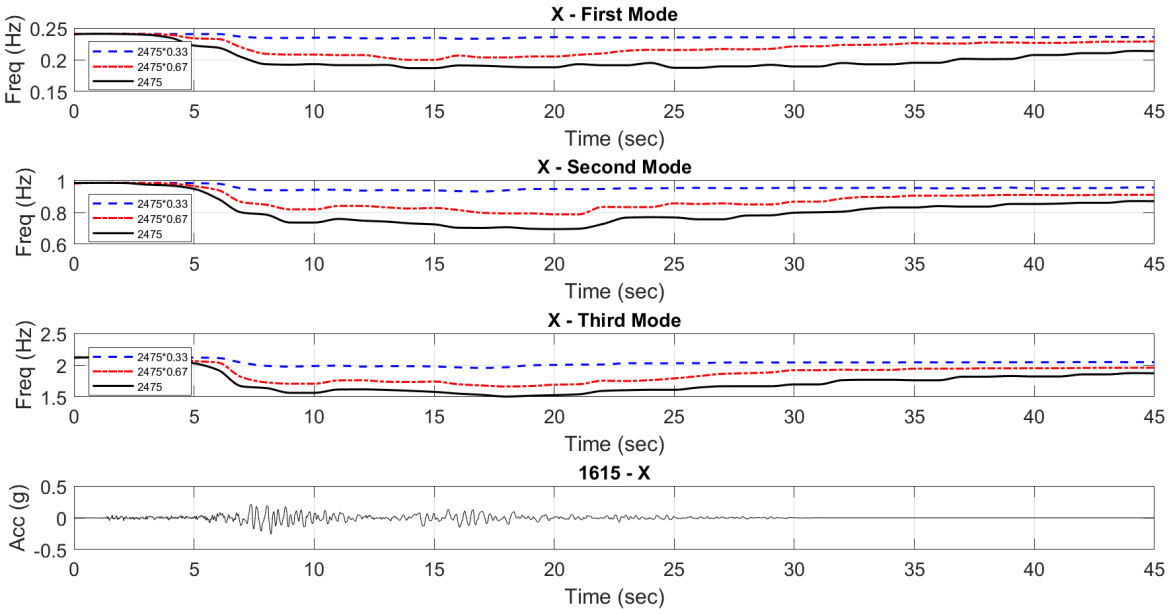

Figure 5.6. Changes in modal frequencies for x direction, eq id: 1655.

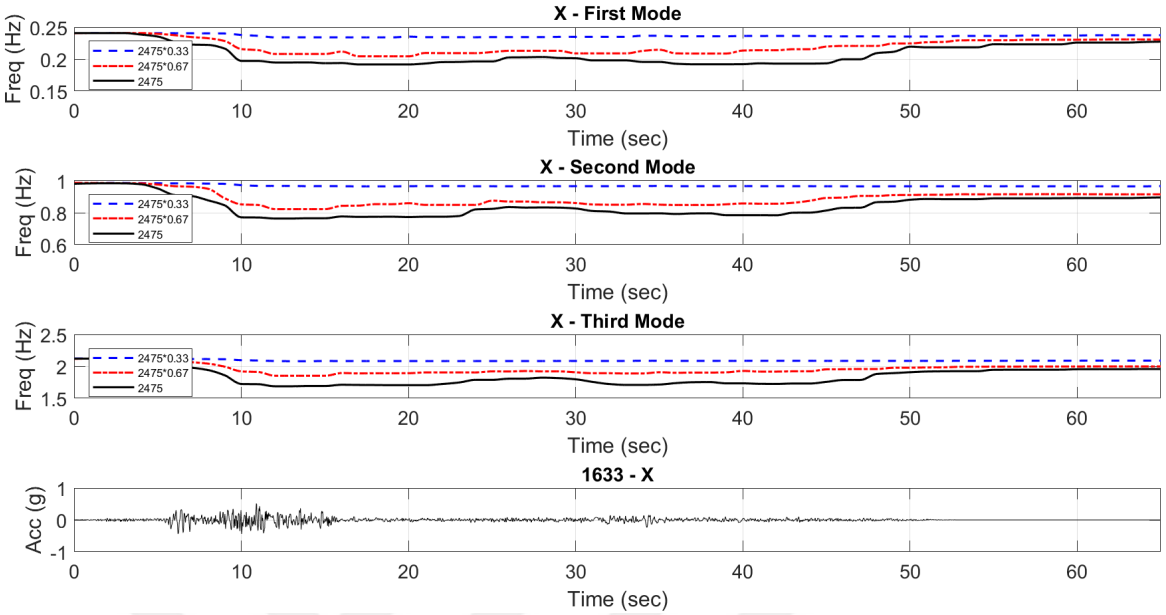

Figure 5.7. Changes in modal frequencies for x direction, eq id: 1633.

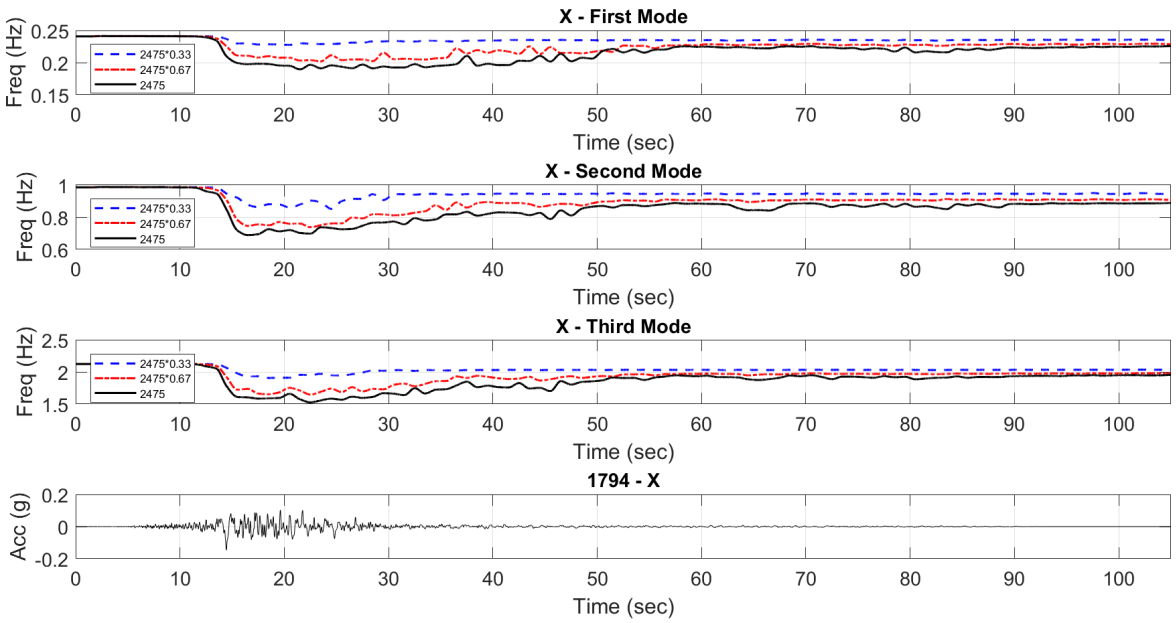

Figure 5.8. Changes in modal frequencies for x direction, eq id: 1794.

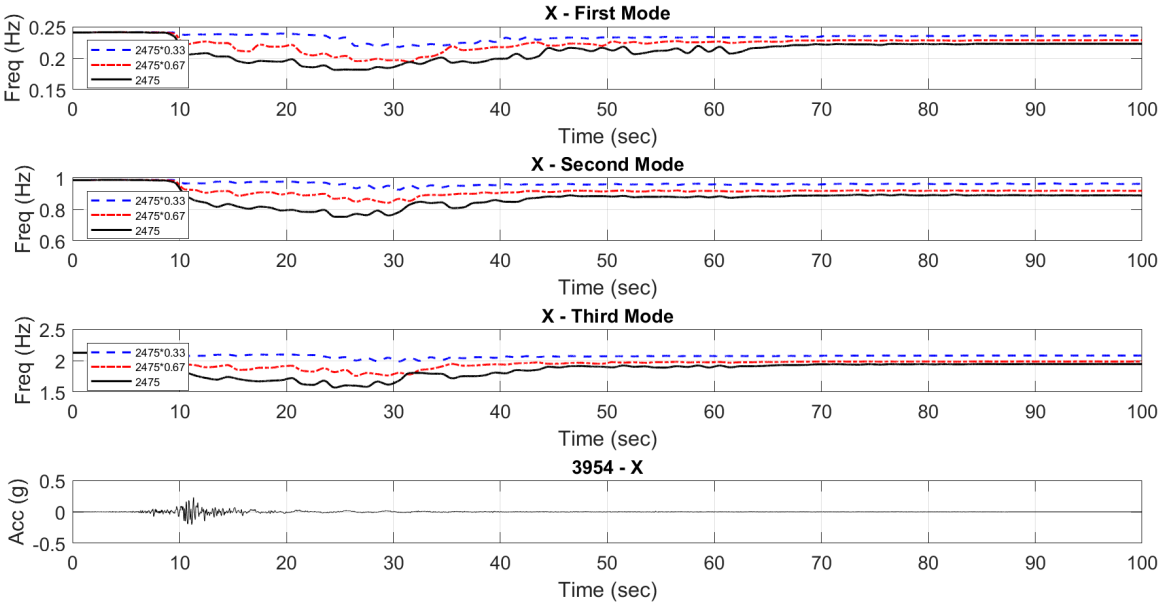

Figure 5.9. Changes in modal frequencies for x direction, eq id: 3954.

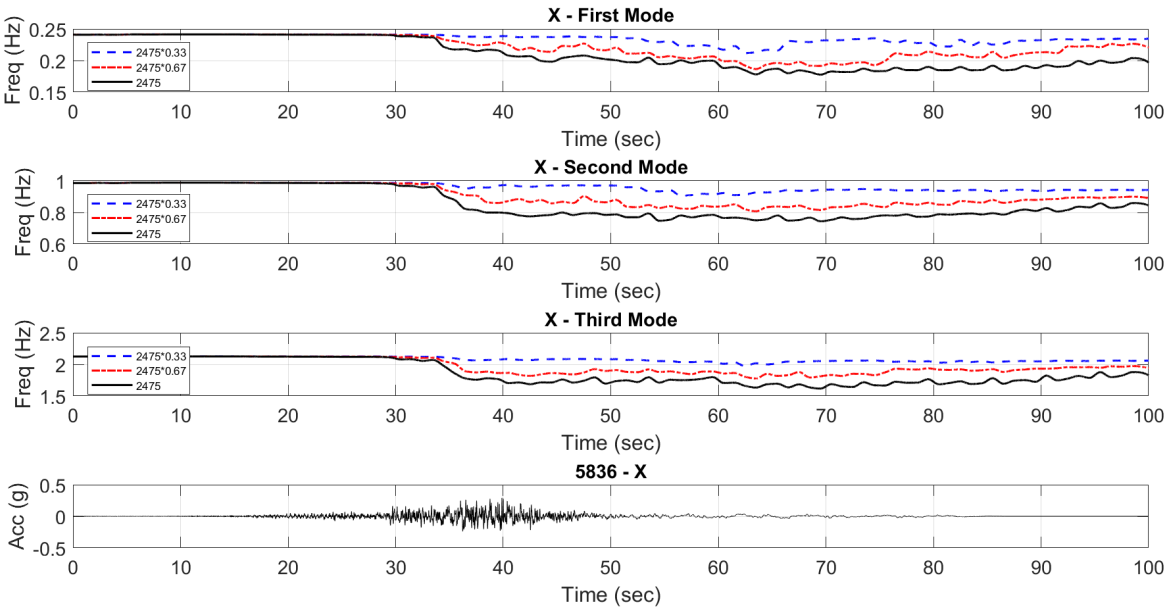

Figure 5.10. Changes in modal frequencies for x direction, eq id: 5836.

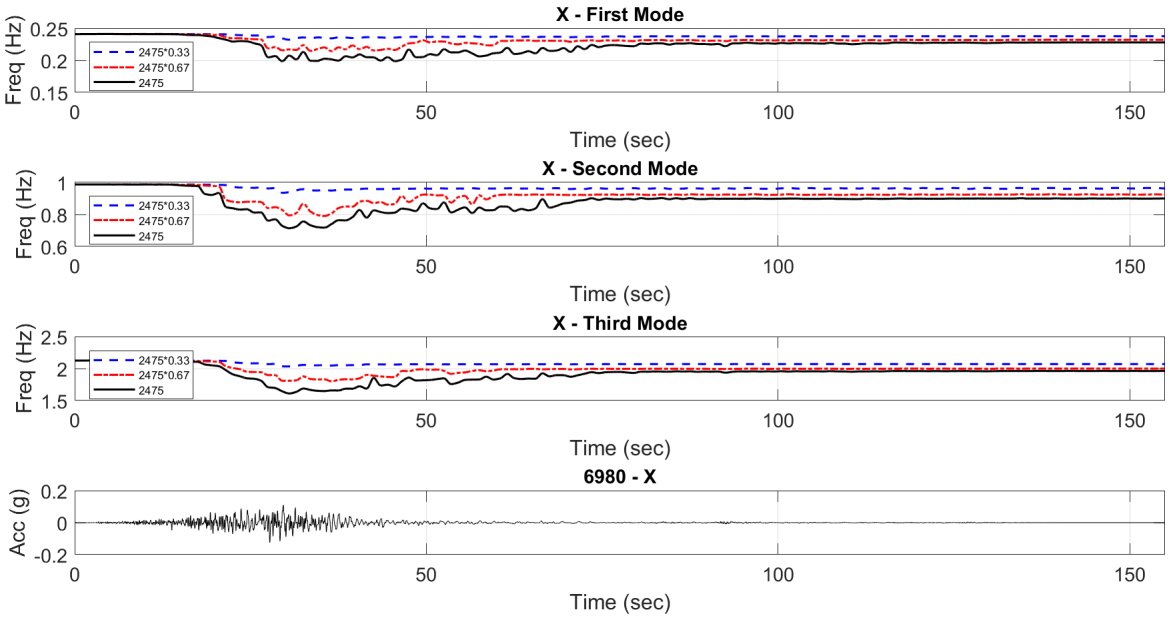

Figure 5.11. Changes in modal frequencies for x direction, eq id: 6980.

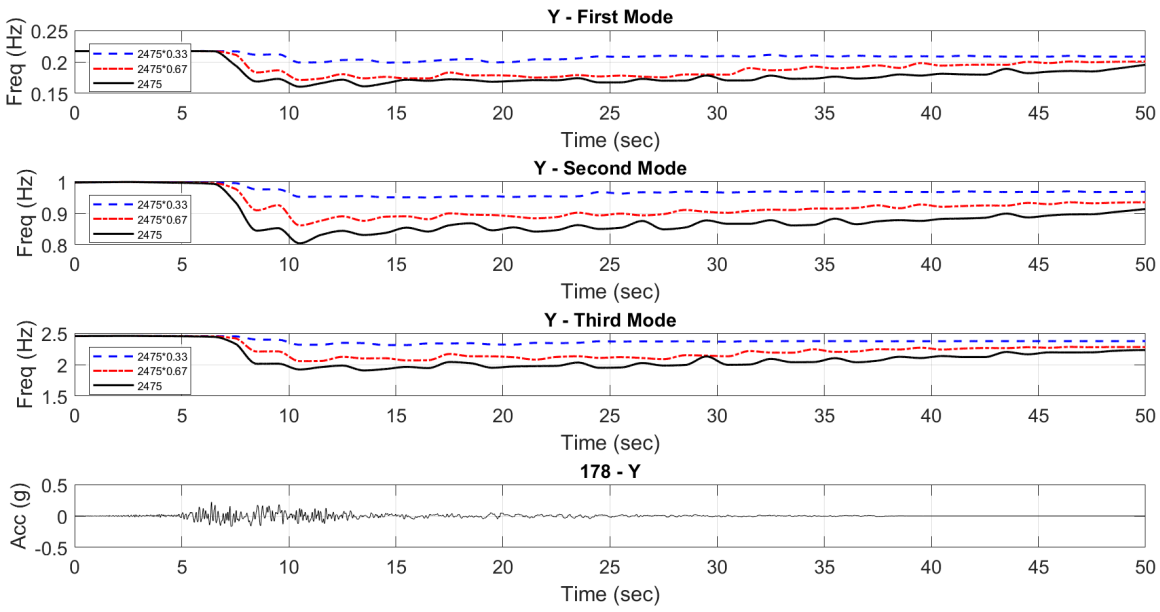

Figure 5.12. Changes in modal frequencies for y direction, eq id: 178.

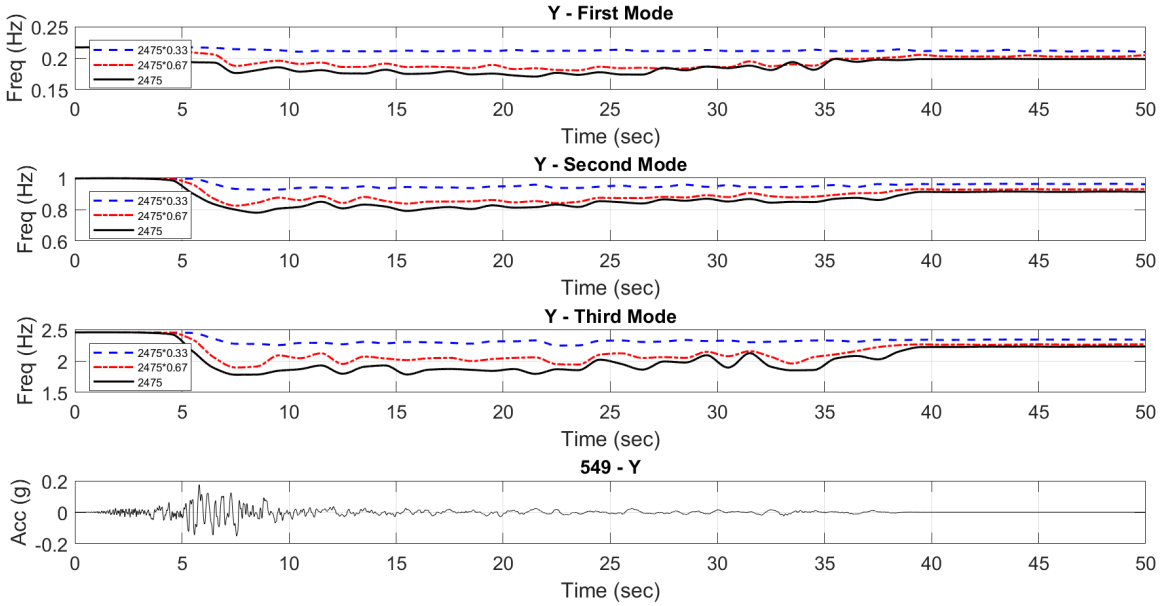

Figure 5.13. Changes in modal frequencies for y direction, eq id: 549.

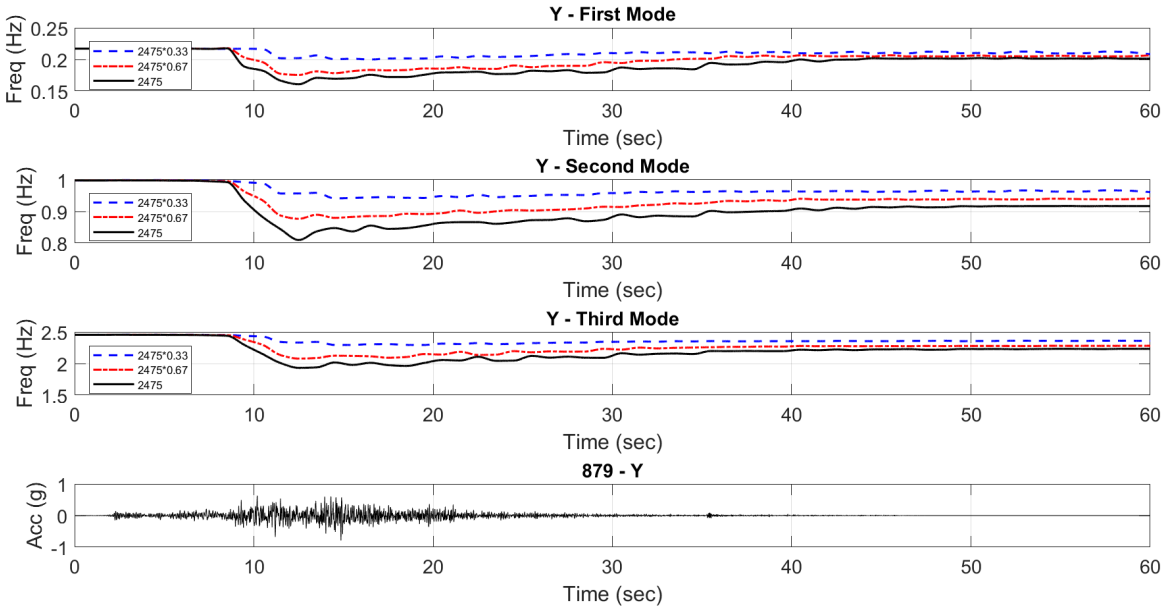

Figure 5.14. Changes in modal frequencies for y direction, eq id: 879.

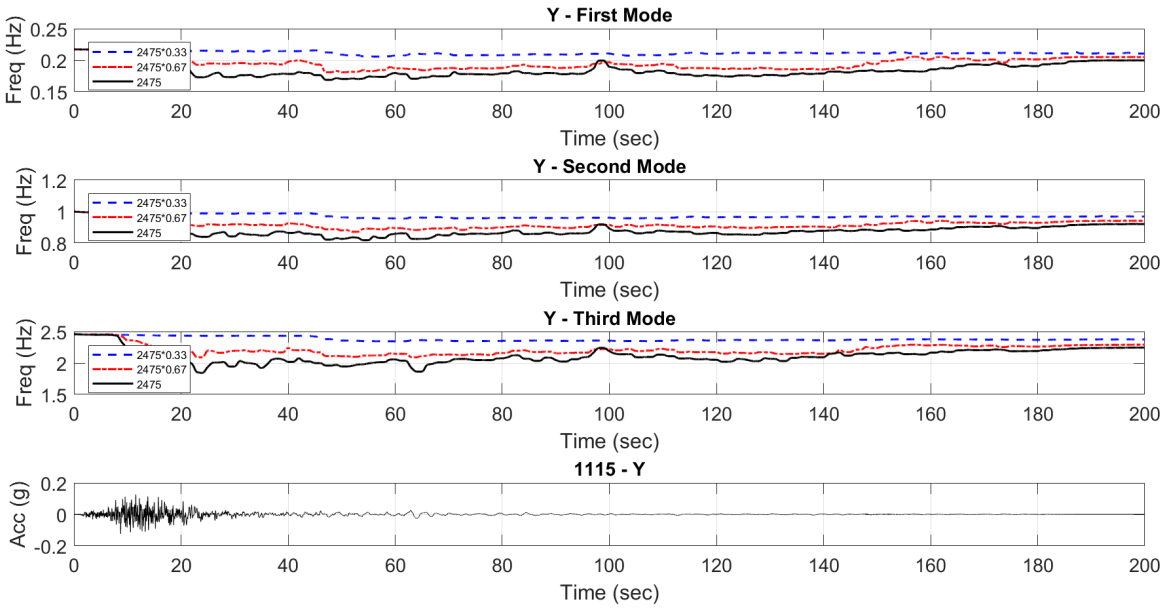

Figure 5.15. Changes in modal frequencies for y direction, eq id: 1115.

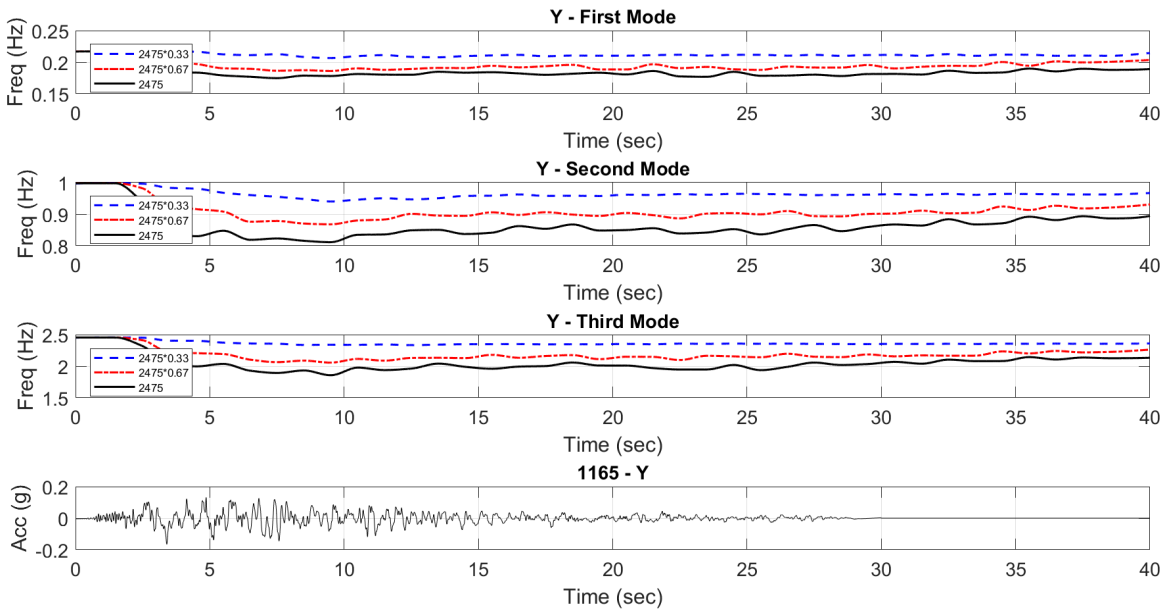

Figure 5.16. Changes in modal frequencies for y direction, eq id: 1165.

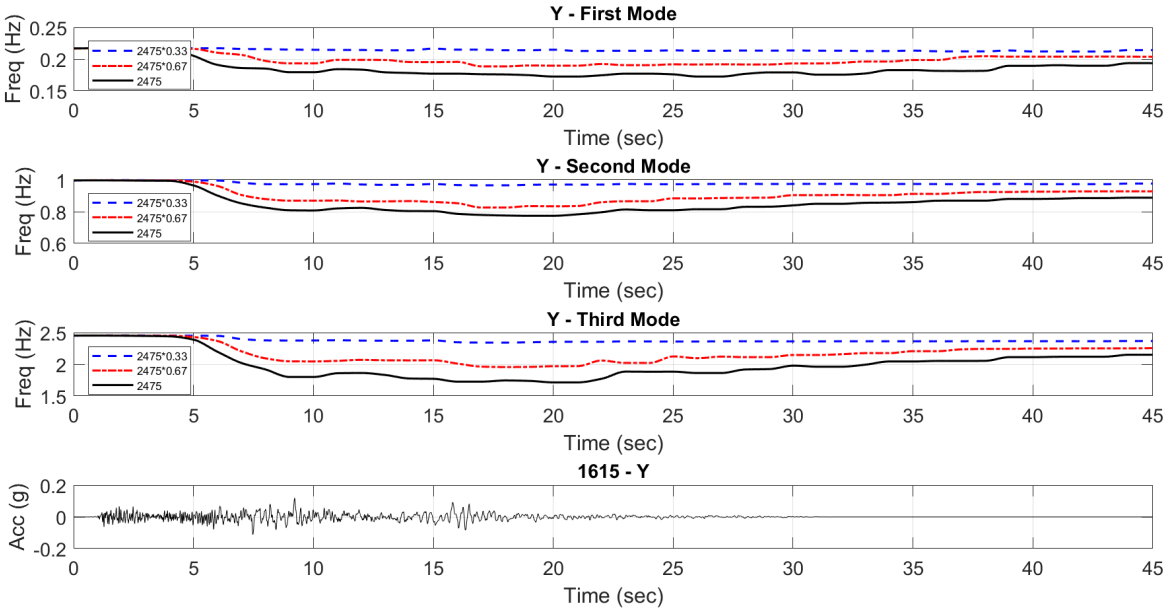

Figure 5.17. Changes in modal frequencies for y direction, eq id: 1655.

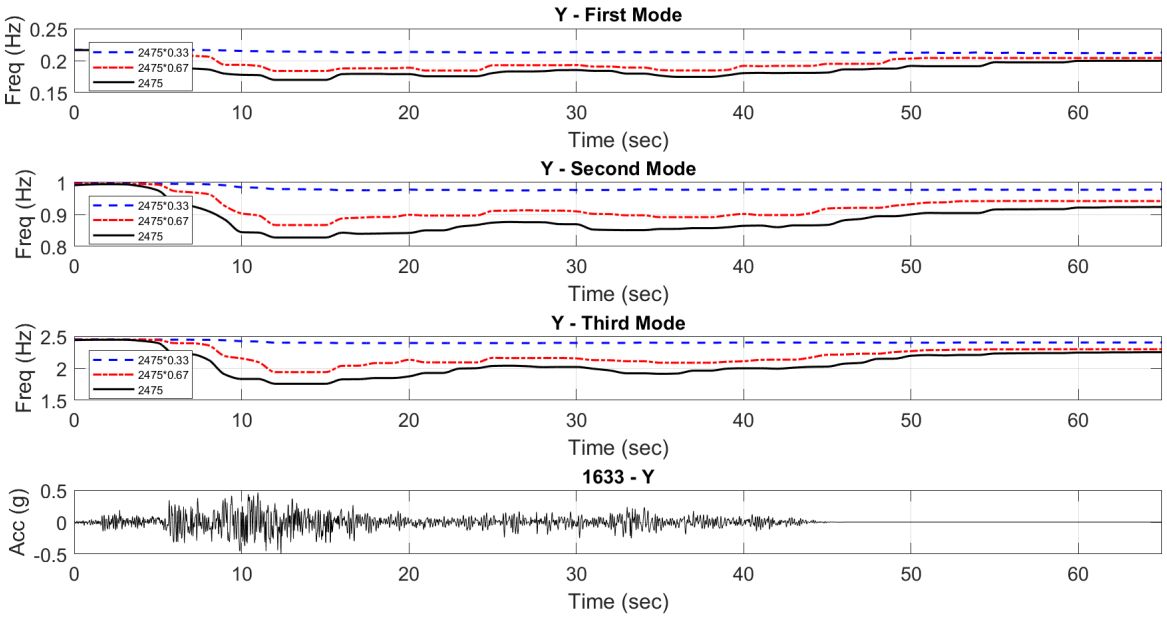

Figure 5.18. Changes in modal frequencies for y direction, eq id: 1633.

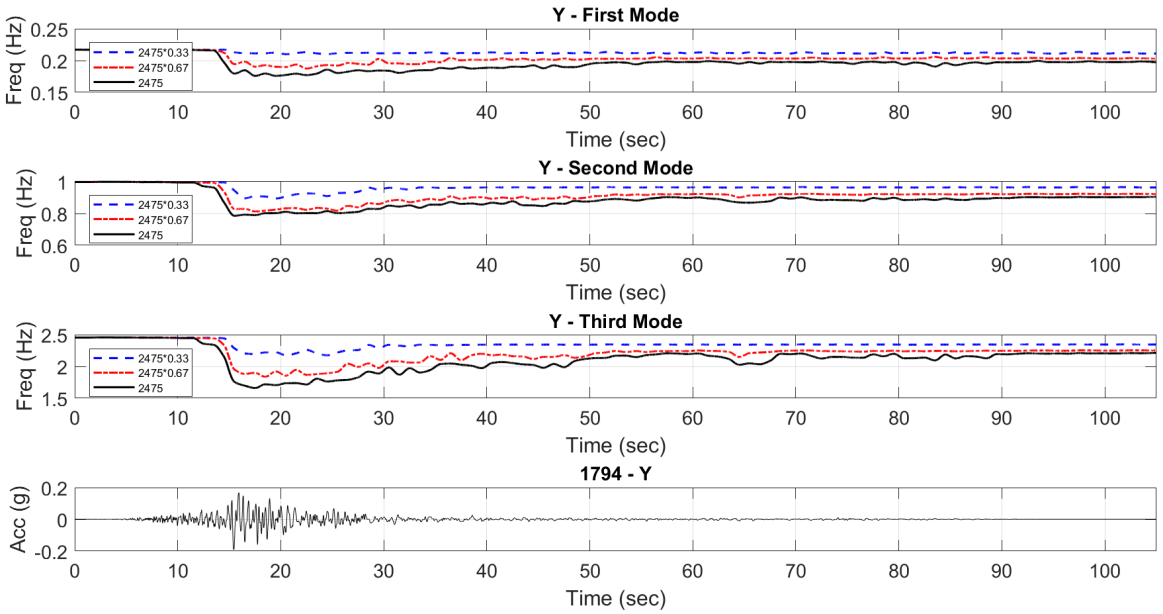

Figure 5.19. Changes in modal frequencies for y direction, eq id: 1794.

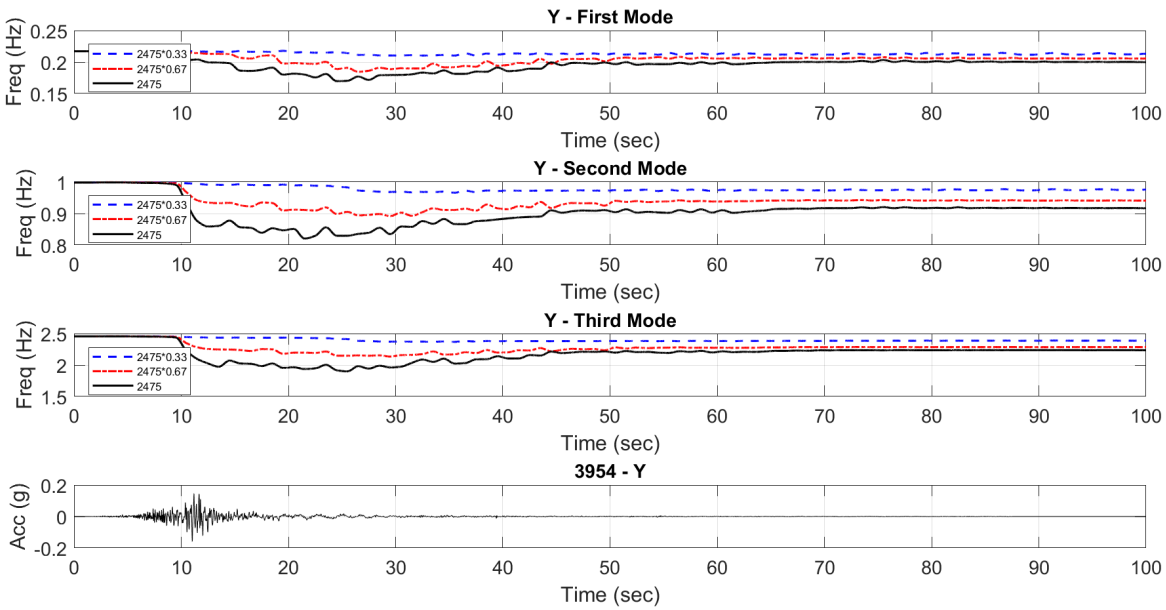

Figure 5.20. Changes in modal frequencies for y direction, eq id: 3954.

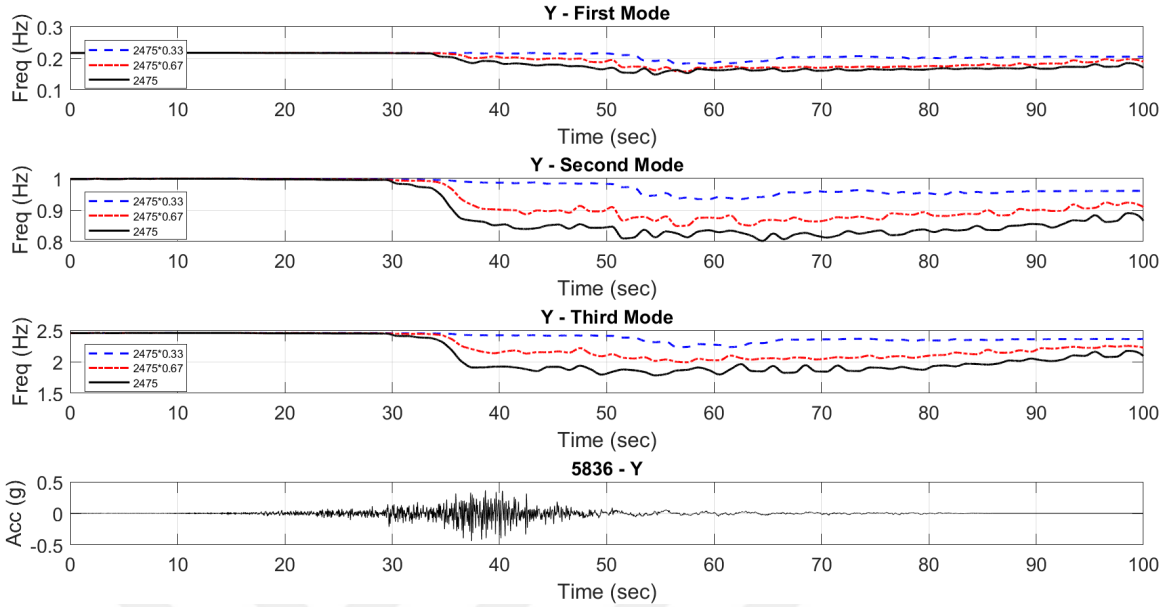

Figure 5.21. Changes in modal frequencies for y direction, eq id: 5836.

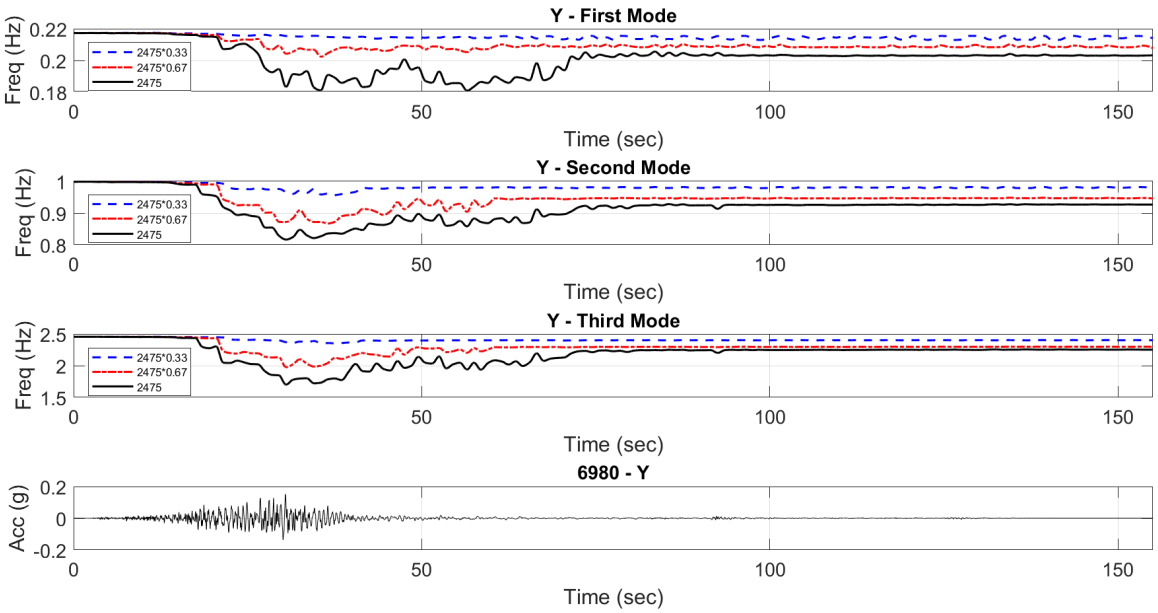

Figure 5.22. Changes in modal frequencies for y direction, eq id: 6980.

Table 5.1 summarizes changes in frequencies of structure during earthquakes with different scale factors. From analysis results, more frequency decrease was observed due to high stiffness degradation as scale factor increases. Maximum frequency decreases in X direction and Y direction for 2475 return period are 29% and 32%, respectively. In addition, minimum frequency decreases in X direction and Y direction for 2475 return period are 18% and 17%, respectively.

Table 5.1. Summary of frequency changes.

$\mathbf{f}_{1-min}(Hz)$													
EQ ID		**REF**	**178**	**549**	**879**	**1115**	**1165**	**1615**	**1633**	**1794**	**3954**	**5836**	**6980**
X	**2475*0.33**	0.241	0.225	0.221	0.206	0.209	0.216	0.233	0.234	0.228	0.218	0.212	0.232
	2475*0.67	0.241	0.202	0.196	0.184	0.182	0.192	0.200	0.204	0.202	0.194	0.186	0.214
	2475	0.241	0.190	0.185	0.172	0.170	0.181	0.187	0.192	0.190	0.181	0.178	0.199
Y	**2475*0.33**	0.217	0.199	0.210	0.200	0.206	0.207	0.212	0.212	0.210	0.210	0.183	0.213
	2475*0.67	0.217	0.171	0.181	0.176	0.181	0.186	0.189	0.184	0.187	0.184	0.158	0.202
	2475	0.217	0.161	0.171	0.161	0.169	0.175	0.172	0.170	0.176	0.170	0.149	0.181
change (%)													
X	**2475*0.33**	1.000	0.933	0.919	0.856	0.867	0.896	0.967	0.972	0.944	0.904	0.879	0.964
	2475*0.67	1.000	0.838	0.815	0.763	0.757	0.796	0.829	0.849	0.838	0.806	0.773	0.889
	2475	1.000	0.790	0.769	0.714	0.707	0.752	0.775	0.796	0.787	0.752	0.737	0.824
Y	**2475*0.33**	1.000	0.915	0.965	0.920	0.946	0.950	0.975	0.974	0.966	0.967	0.841	0.979
	2475*0.67	1.000	0.788	0.831	0.808	0.831	0.856	0.867	0.846	0.862	0.848	0.728	0.931
	2475	1.000	0.739	0.785	0.740	0.776	0.804	0.793	0.781	0.809	0.780	0.683	0.832

The most critical point is to determine reasonable threshold values to define performance level of structure after earthquake. Some threshold values are recommended in literature [107], [114].

In this study, new threshold values are used as shown in Table 5.2 which gives better correlation between damage indicators (damage index and peak inter-story drift ratio) and coupling beam deformation.

Table 5.2. Performance levels and suggested threshold values.

Performance Level ***Damage Level***	Damage Index (DI)	Peak Inter-Story Dirft Ratio (PIDR)	$\theta_{max}/\theta_{yield}$ of Coupling Beams
Uninterrupted Use (UU) ***No Damage***	0<=DI<0.05	0<=PIDR<0.0015	0<=$\theta_{max}/\theta_{yield}$<1.0
Immediate Occupancy (IO) ***Minor Damage***	0.05<=DI<0.18	0.0015<=PIDR<0.0053	1.0<=$\theta_{max}/\theta_{yield}$<3.5
Life Safety (LS) ***Moderate Damage***	0.18<=DI<0.39	0.0053<=PIDR<0.0105	3.5<=$\theta_{max}/\theta_{yield}$<6
Collapse Prevention (CP) ***Significant Damage***	0.39<=DI<0.60	0.0105<=PIDR<0.0150	6<=$\theta_{max}/\theta_{yield}$<10
Critical Level (CL) ***Severe Damage***	0.60<=DI<1.00	0.0150<=PIDR<0.0300	10<=$\theta_{max}/\theta_{yield}$<15

Figure 5.23 represents DI vs. Maximum Inter-story Drift Ratio graphs for earthquakes with different scale factors. The points in the figures show maximum inter-story drift ratios of each story for the corresponding DI. Generally, consistent performance levels for given DI and maximum inter-story drift ratio along the structure were observed.

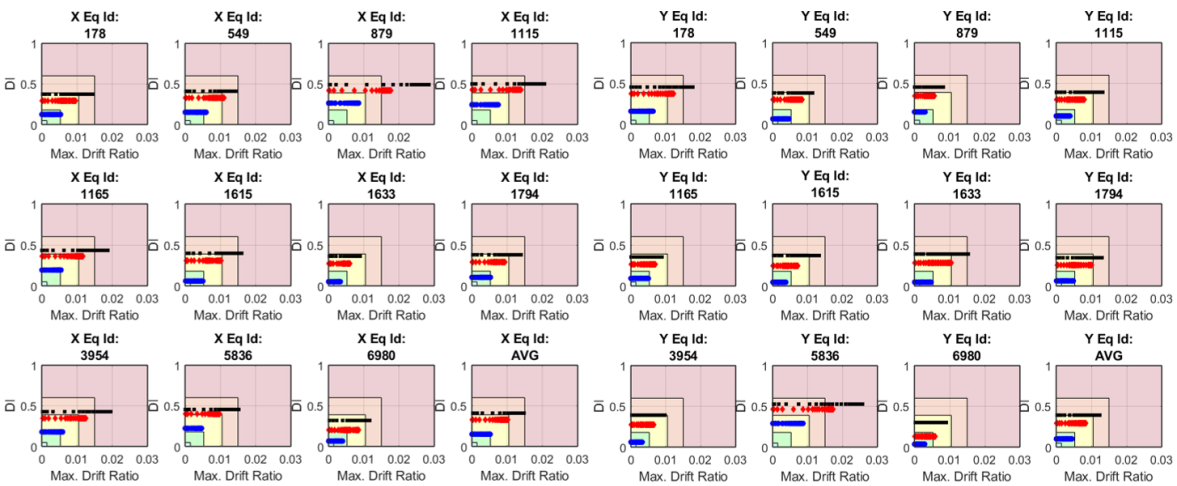

Figure 5.23. Damage index vs. maximum drift ratio graphs (blue points for sf: 2475*0.33, red points for sf: 2475*0.67, black points for sf: 2475).

Also, Figure 5.24 represents percentage distribution of maximum drift ratios based on determined performance levels. This results are compared with chord rotations of coupling beams to verify maximum inter-story drift ratio can be used as a damage indicator.

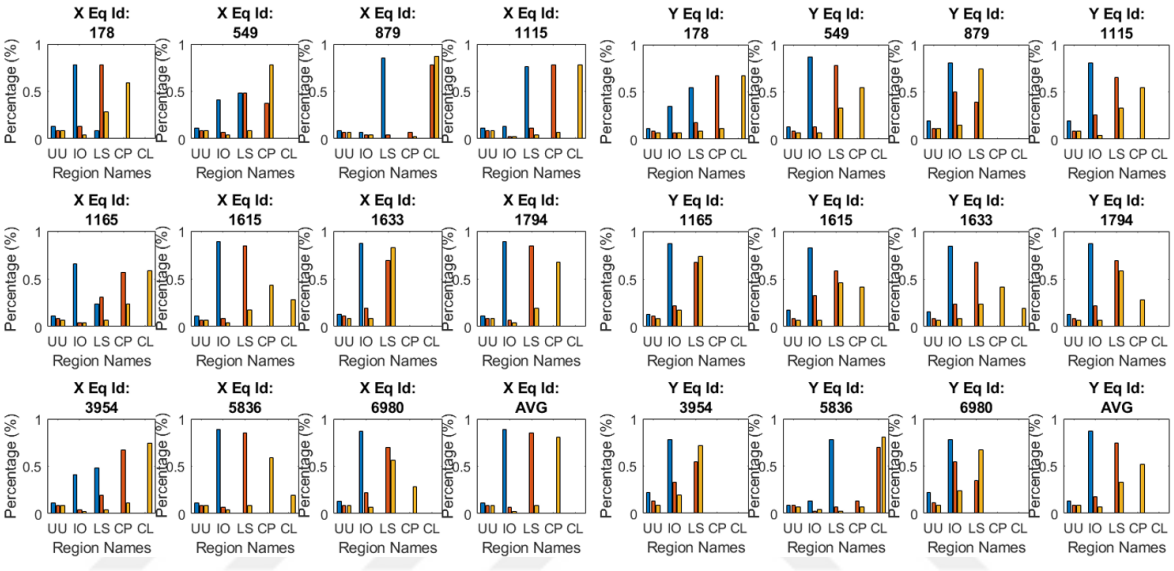

Figure 5.24. Damage distribution based on maximum drift ratio (blue bars for sf: 2475*0.33, red bars for sf: 2475*0.67, yellow bars for sf: 2475).

Figure 5.25 shows DI vs. $\theta_{max}/\theta_{yield}$ for coupling beams. Maximum chord rotation of coupling beams shown in figures by points increases with increasing scale factors. Also, percentage distribution of $\theta_{max}/\theta_{yield}$ for coupling beams is presented in Figure 5.26. The distributions of performance levels for maximum inter story drift ratio and coupling beams are generally compatible for given DI. Therefore, threshold values given in Table 5.2 may be used for condition assessment of structures. Also, this good agreement shows that proposed method is reliable to estimate damage level by DI and maximum inter-story drift ratio.

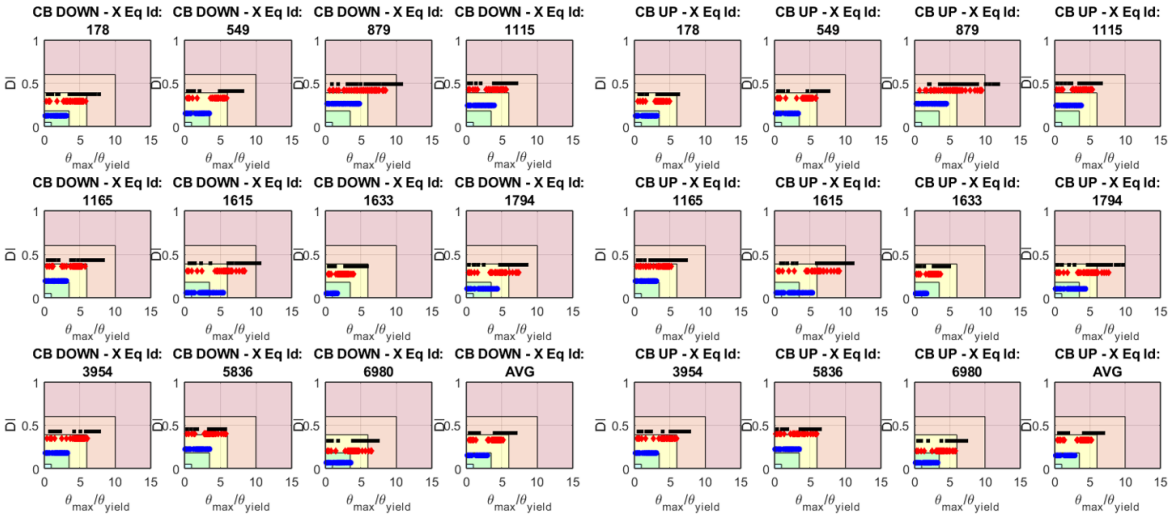

Figure 5.25. Damage index vs. maximum chord rotation/yield chord rotation ratio graphs for coupling beams (blue points for sf: 2475*0.33, red points for sf: 2475*0.67, black points for sf: 2475).

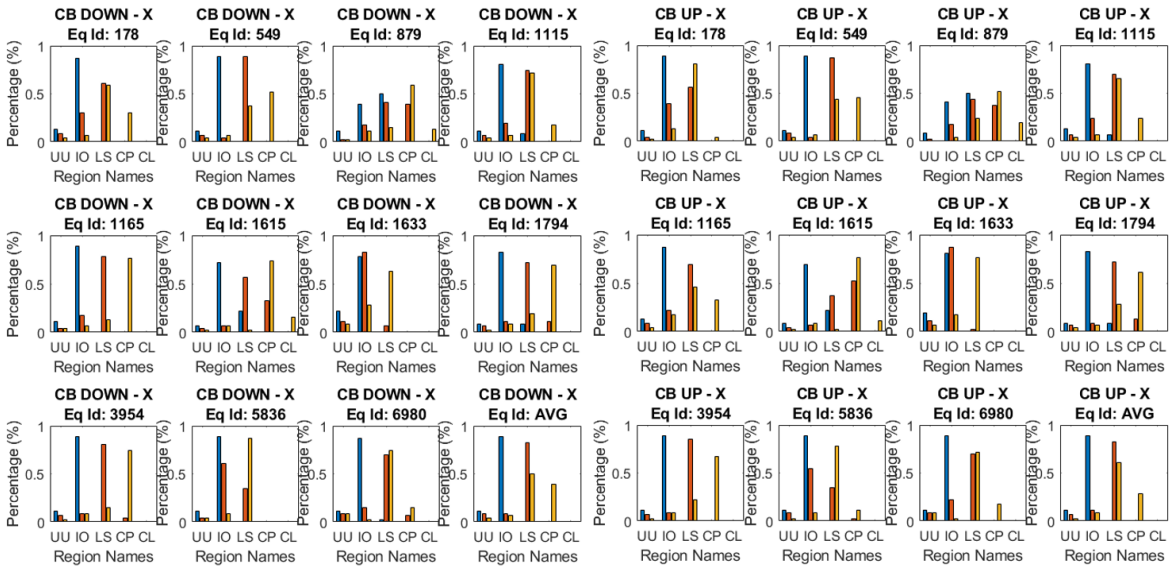

Figure 5.26. Damage distribution based on maximum chord rotation/yield chord rotation ratio for coupling beams (blue bars for sf: 2475*0.33, red bars for sf: 2475*0.67, yellow bars for sf: 2475).

Up to this point, DI values are fixed because each earthquake result is presented separately. Figure 5.27 summarizes DI vs. Maximum Inter-story Drift Ratio graphs for 11 earthquakes with different scale factors.

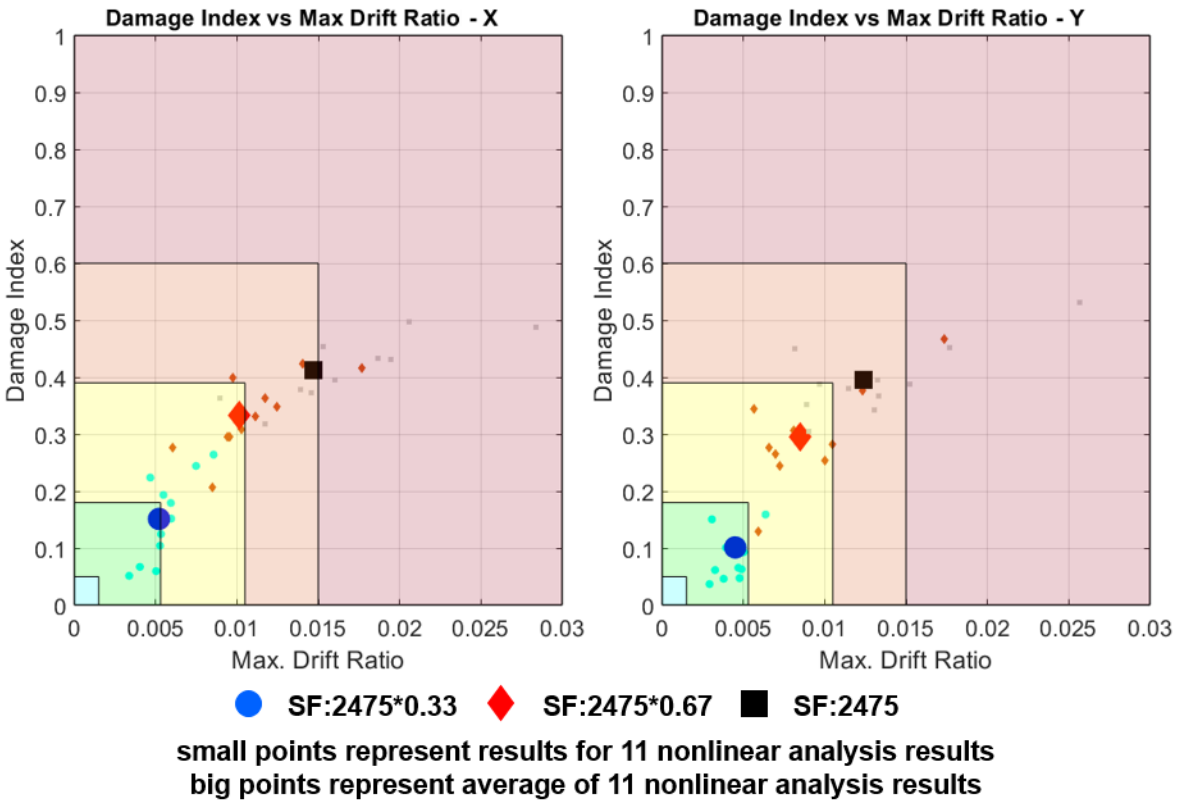

Figure 5.27. Summary of damage index vs. maximum inter-story drift ratio.

6. REAL WORLD APPLICATIONS

The proposed simplified models were used to estimate responses of non - instrumented floors from instrumented floors for two different structures. The first structure showed elastic behavior under a weak earthquake with no damage observed. On the other hand, the second structure was severely damaged under a strong earthquake.

6.1. Non-Damaged Tall Building

A tall building located in the business center of Istanbul has been monitored continuously since June 2019. General characteristics of the building and plan of the SHM system are shown in Figure 6.1.

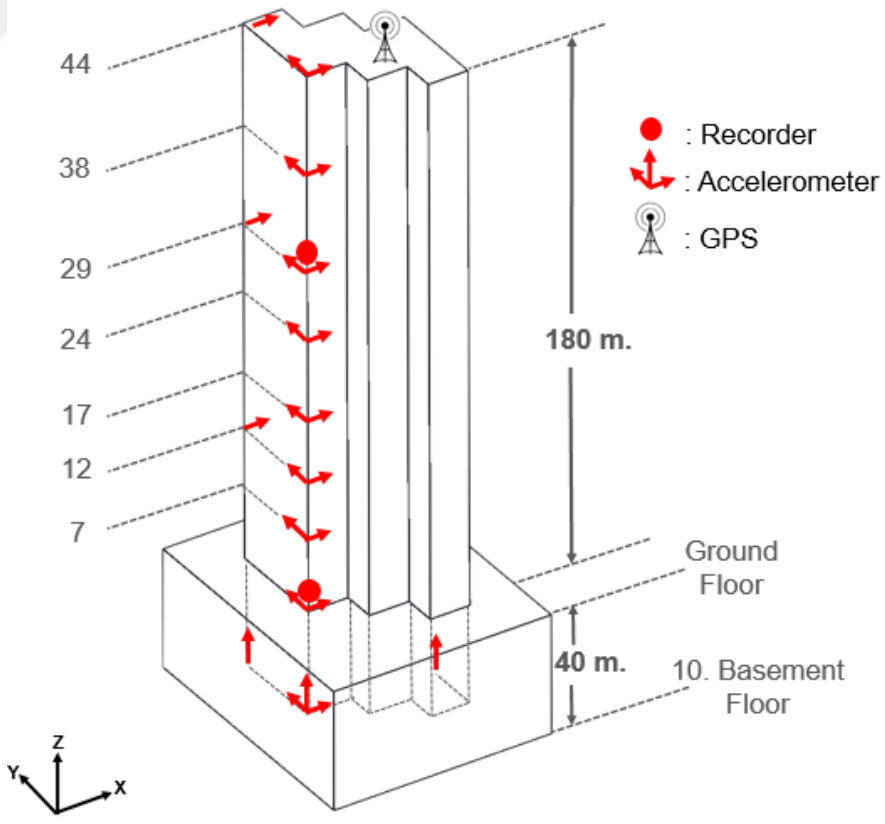

Figure 6.1. SHM system and sensor layout of tall building.

The building is instrumented with force balance accelerometers (SA107B, Columbia Research Laboratories, Inc.) with dynamic range of 130 dB, bandwidth of DC-200 Hz, and full-scale range of $\pm 2g$. There are at least two accelerometers in X and Y directions at specific floors with additional third accelerometer placed on top floors and certain middle floors to identify torsion modes. In addition, accelerometers on basement floors in vertical direction enable to detect rocking behavior. Also, two separate recorders; one on the ground floor and one on the 29th floor, exist and they are synchronized by GPS.

In building, vibration data are continuously collected at 200 Hz and analysis results are reported automatically. Table 6.1 represents modal identification results obtained using Enhanced Frequency Domain Decomposition (EFDD) method under ambient conditions [115]. In signal processing, Hanning window was utilized in order to prevent leakage and averaging was applied in time domain in order to decrease noise effect.

Table 6.1. System identification results of tall building in Istanbul under ambient condition.

Mode	**f (Hz)**	ξ (%)	**Mode**	**f (Hz)**	ξ (%)	**Mode**	**f (Hz)**	ξ (%)
X-1st Trans.	0.27	3.54	**Y-2nd Trans.**	1.15	1.25	**Y-3rd Trans.**	2.36	0.77
Y-1st Trans.	0.33	2.40	**X-2nd Trans.**	1.25	1.33	**X-3rd Trans.**	2.43	1.37
1st Torsion	0.58	1.98	**2nd Torsion**	1.71	0.90	**3rd Torsion**	2.58	1.21

Vibration data were collected from 285 tall buildings with different structural characteristics by research committee of Architectural Institute of Japan and dynamic properties of the buildings were identified. Empirical formulas were developed based on system identification results to estimate fundamental frequencies and damping ratios from heights and top displacements [116]. It is observed that the identified frequencies of tall building are in agreement with the estimated values from the recommended empirical equations. On the other hand, identified modal damping ratios of tall building were slightly higher than the estimated values from recommended empirical equations.

The data archive was created by recording the two-month uninterrupted vibration data and the changes in the modal properties of the structure were observed by analyzing these records (Figure 6.2, Figure 6.3 and Figure 6.4).

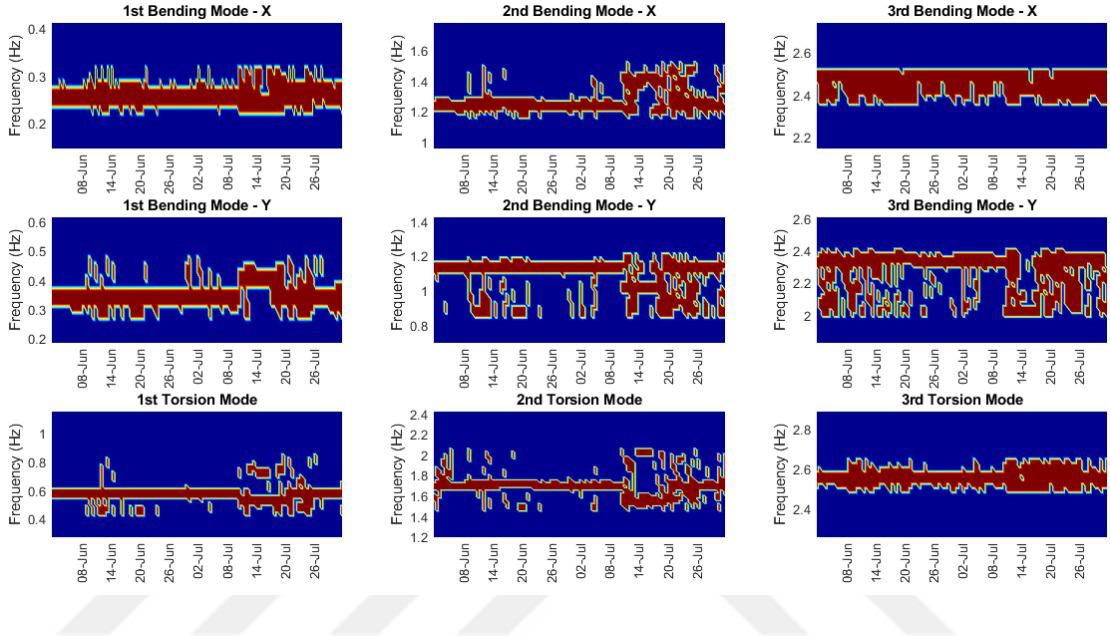

Figure 6.2. Scattering of modal frequencies.

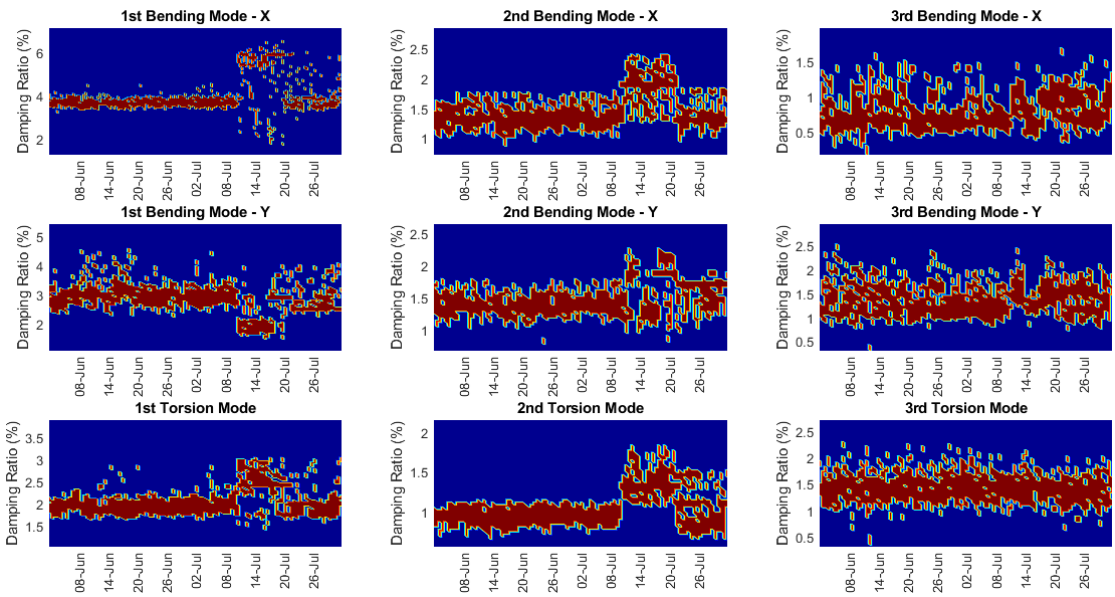

Figure 6.3. Scattering of modal damping ratios.

In Figure 6.2 and Figure 6.3, x-axis shows the vibration analysis results of one-hour data. Scatter of the modal frequencies observed in these figures constitutes a band such that identified frequencies out of this band would be an indication of possible damage.

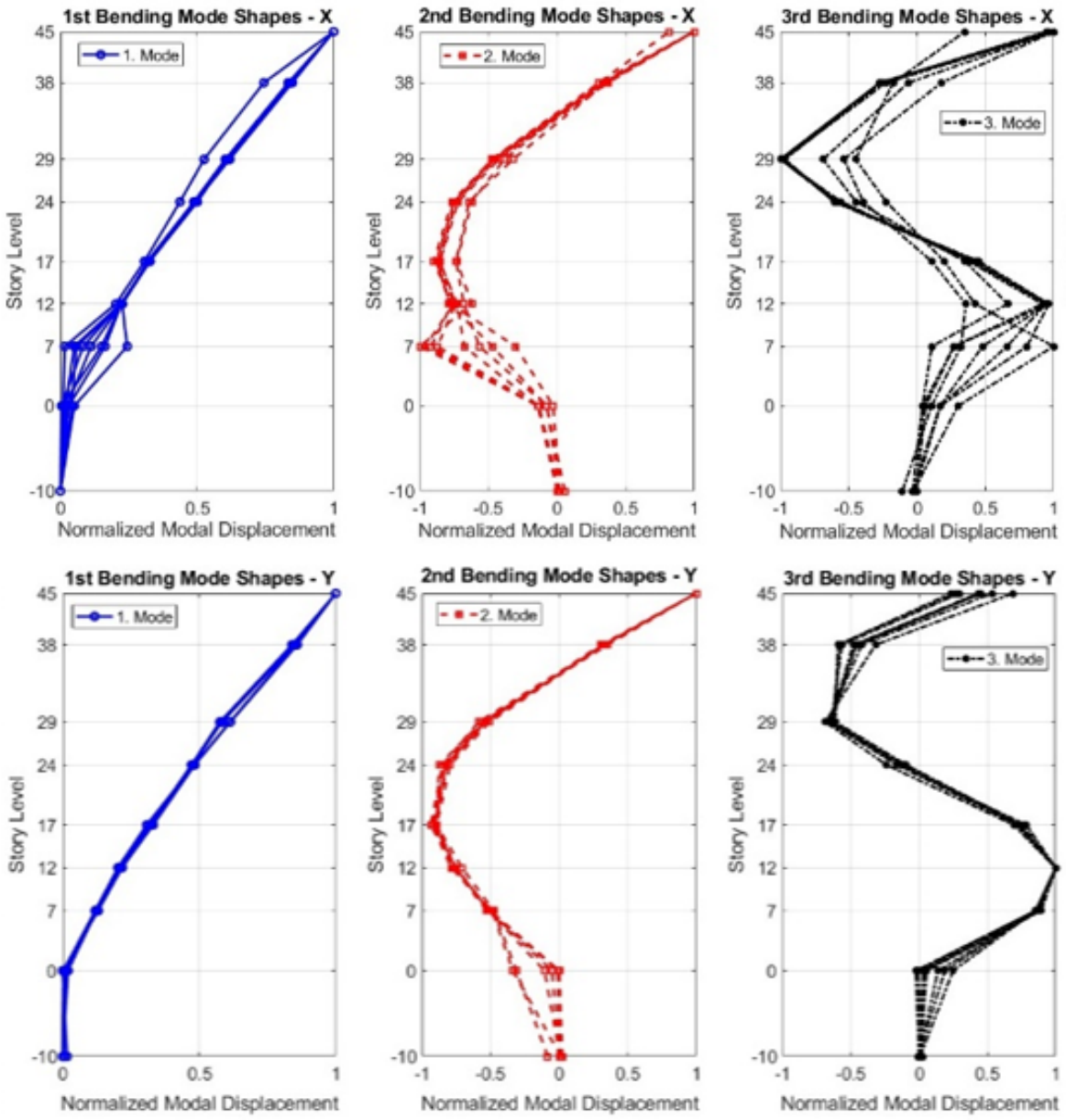

Figure 6.4. Changes in mode shapes.

Figure 6.5 and Figure 6.6 represent distribution of identified frequencies and damping ratios for two months continuous monitoring of the tall building. When the estimated values are outside $\pm 2\sigma$, possible damage situation and environmental effects are considered. Specified range for scattering of dynamic properties was determined according to mean and standard deviation results calculated by statistical analysis of long term monitoring vibration data. Analysis results show that changes in natural frequencies and modal damping ratios are within the specified range. Coefficient of variation is about 1-10% for modal frequencies. In addition, coefficient of variations calculated for identified modal damping ratios are higher than those for frequency values as expected.

Marmara Sea Earthquake on 27 September 2019 was also recorded by SHM system (Figure 6.7). Under this earthquake, the tall building remained in elastic range and no damage was observed. Therefore, it is appropriate to use STBM and DTBM approaches, which do not consider nonlinear behavior, to estimate response of non-instrumented floors from instrumented floor responses for this structure.

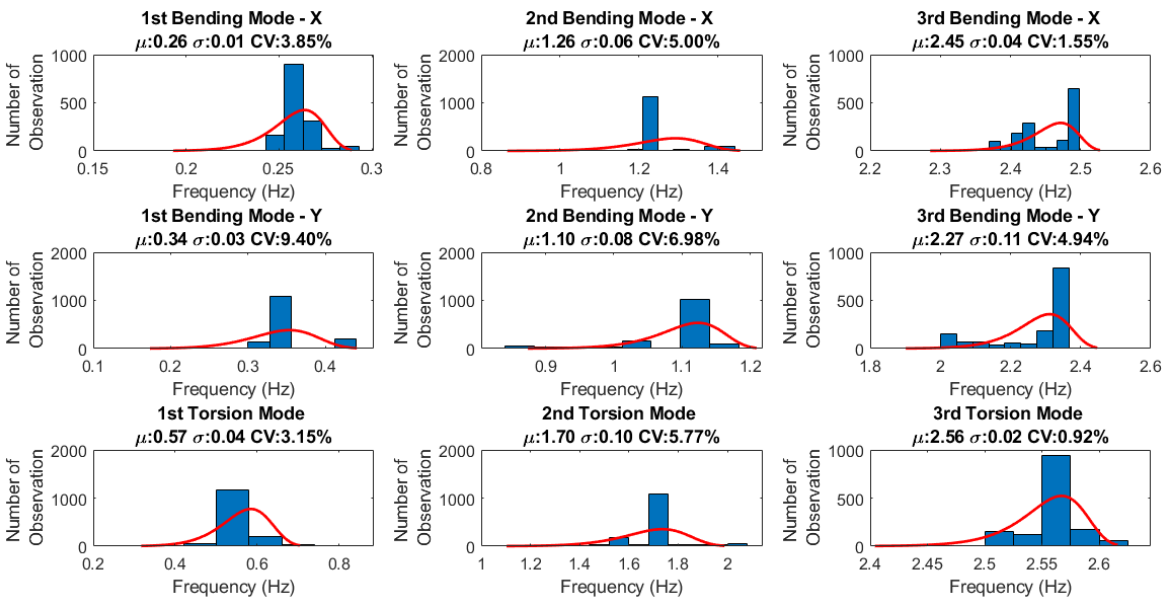

Figure 6.5. Distribution of identified modal frequencies.

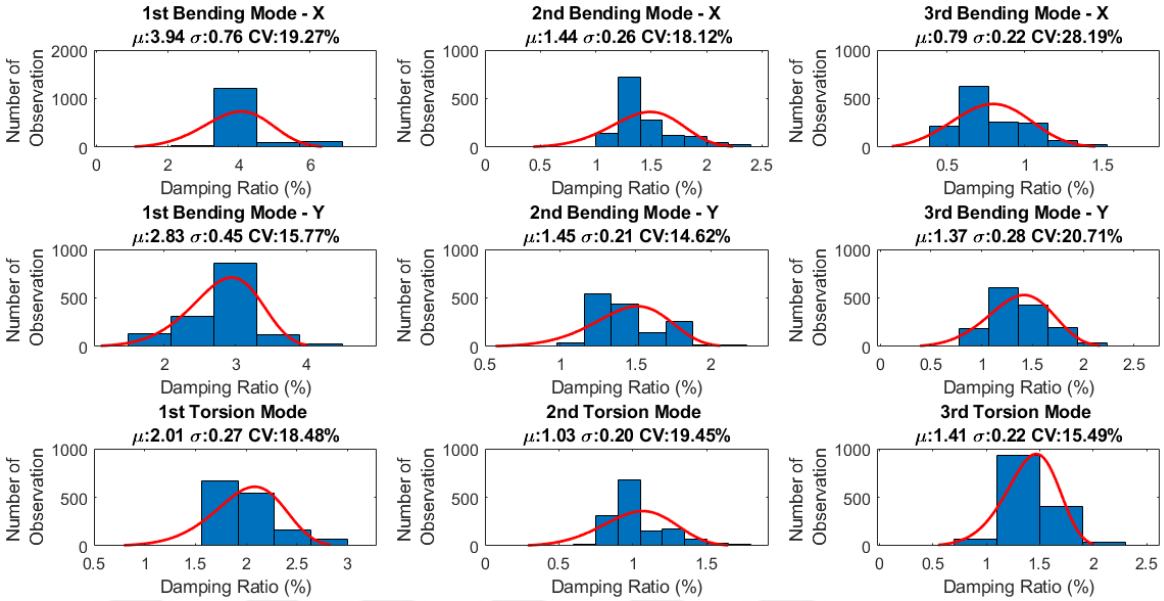

Figure 6.6. Distribution of identified modal damping ratios.

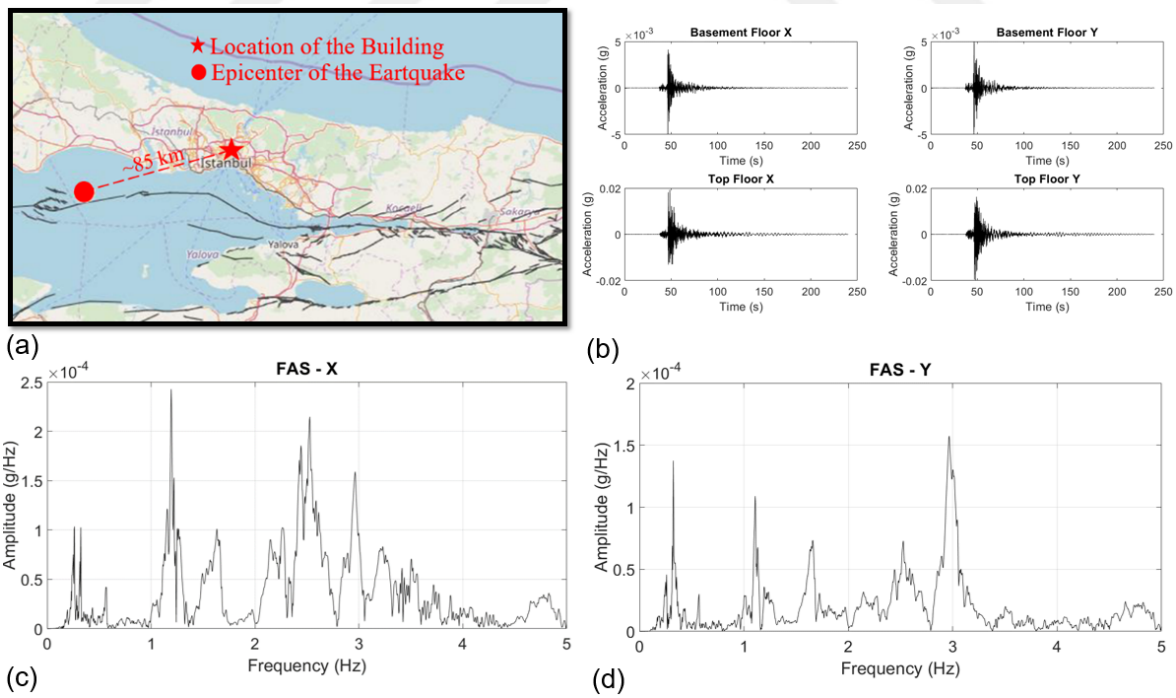

Figure 6.7. (a) Location of the building and the earthquake. (b) Vibration records from the building. (c) FAS of input motion – basement floor x direction. (d) FAS of input motion – basement floor y direction.

In order to identify modal parameters before, during and after the earthquake, numerical algorithm for subspace state-space system identification (N4SID) [117, 118] method was used. There are many studies in literature to estimate model order of a dynamic system. In many cases, model order is assumed to be 2N for N degree of freedom system [119]. However, high model order creates spurious modes and increases analysis time to identify dynamic properties of the structure. On the other hand, singular values of Hankel Matrix created by using recorded responses of the system present energy contribution of each order to whole system energy. Figure 6.8 shows singular values of Hankel matrices before, during and after the earthquake in X and Y directions. Although filtering techniques were applied to eliminate noise effect, singular values would not be zero. However, it can be clearly seen that the curves approach an asymptote around model order 100 for all cases, so an extra increase in model order after this state causes negligible contribution to whole dynamic energy of the system.

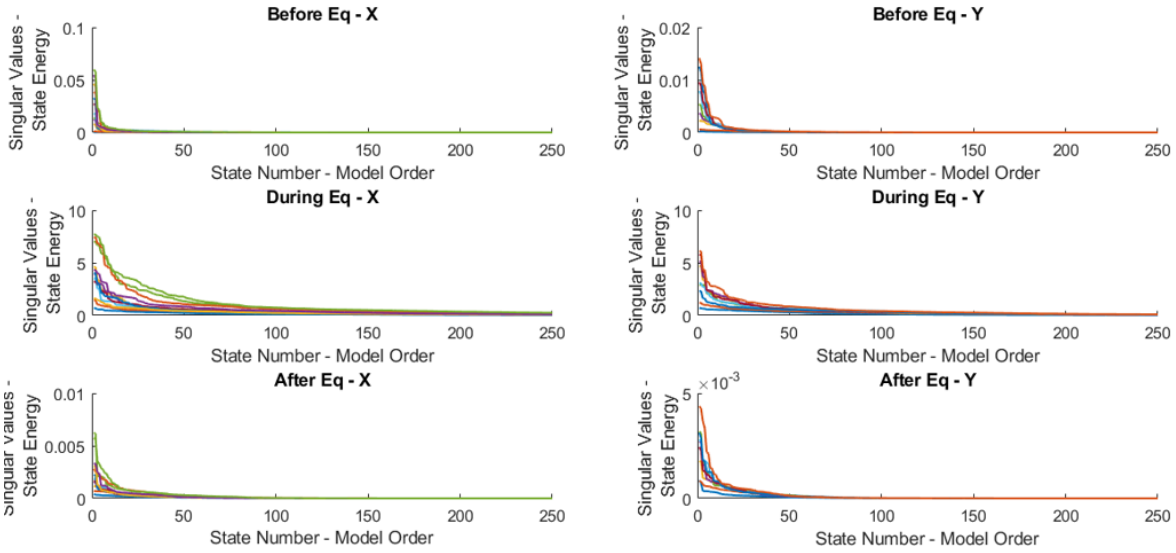

Figure 6.8. Singular values of Hankel matrices.

One of the most important system identification technique commonly used in literature is numerical algorithm for subspace state-space system identification (N4SID) [117, 118]. This algorithm determines stable dynamic system by calculating projection

of input and output data. Also, stability diagrams were created for this method. Relative frequency and damping less than 3% and 15%, modal assurance criteria (MAC) number greater than 0.95 are defined as convergence criteria for stable models. Figure 6.9 shows stability diagrams before, during and after the earthquake. In addition, mode shapes of the structure obtained from N4SID method are demonstrated in Figure 6.10. Table 6.2 presents identified natural frequencies and damping ratios obtained from N4SID method.

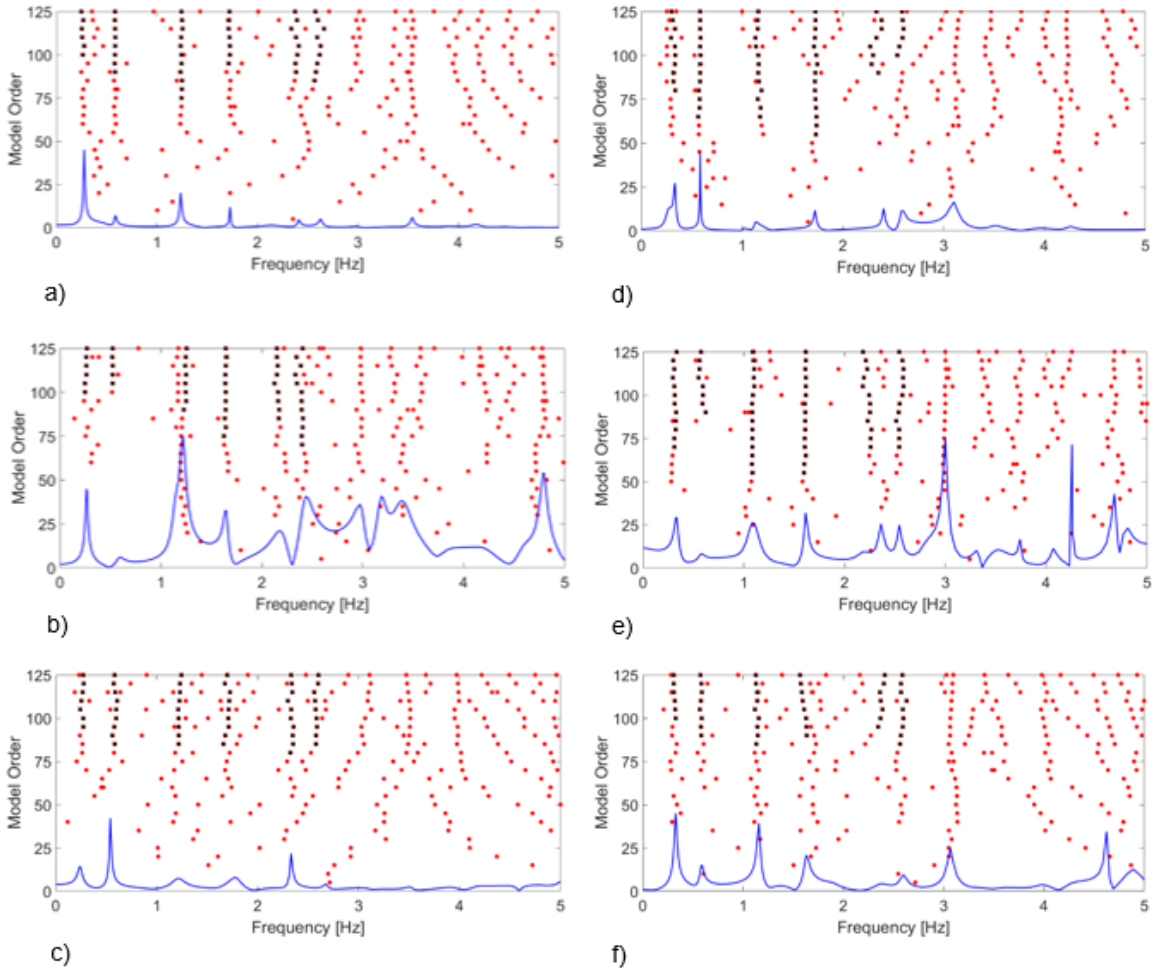

Figure 6.9. Stabilization diagrams for N4SID method - from up to bottom: before, during and after earthquake.

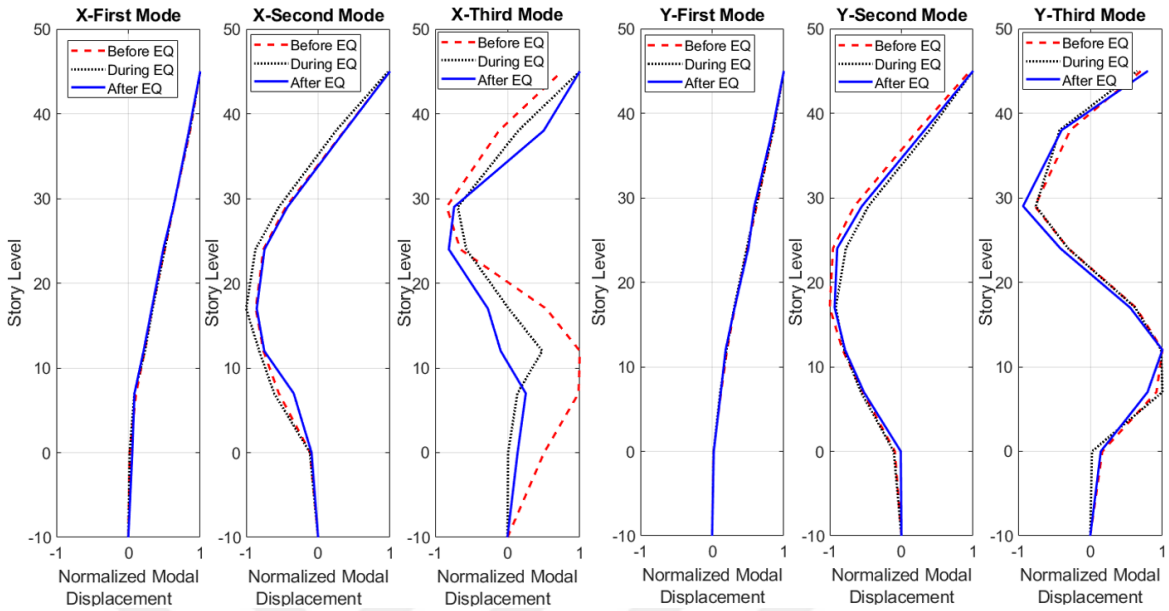

Figure 6.10. Identified mode shapes with N4SID method.

Table 6.2. Identified natural frequencies and damping ratios of tall building in Istanbul with N4SID method.

Modes	Before Earthquake		Earthquake		After Earthquake	
	f (Hz)	ξ (%)	f (Hz)	ξ (%)	f (Hz)	ξ (%)
X-1st Trans.	0.26	0.54	0.26	4.11	0.26	1.05
Y-1st Trans.	0.33	2.79	0.31	3.57	0.30	4.43
1st Torsion	0.58	0.78	0.59	6.39	0.58	0.61
Y-2nd Trans.	1.13	1.62	1.11	3.02	1.15	1.07
X-2nd Trans	1.25	0.76	1.22	2.44	1.24	0.27
2nd Torsion	1.72	0.68	1.65	1.31	1.70	1.06
X-3rd Trans.	2.40	0.85	2.17	3.69	2.34	0.35
Y-3rd Trans	2.40	0.46	2.25	8.24	2.32	0.99
3rd Torsion	2.60	0.74	2.43	2.62	2.54	1.62

As expected, second bending, third bending and torsional mode frequencies of the structure during the earthquake are generally smaller than those identified from ambient vibration records. Identification results also show that there are clear increases in modal damping ratios during the earthquake. Recovering of natural frequencies after the earthquake can again be clearly observed. It is also noted that changes in modal frequencies and damping ratios are within the scatter limits as shown in Figure 6.2 and Figure 6.3. In addition, no clear change in mode shapes of the structure before, during and after earthquake except the third bending mode in X direction is observed (Figure 6.10). However, similar changes in corresponding mode shape were also observed in the long-term monitoring (Figure 6.4).

Simplified mathematical models of the structure were created based on proposed methodologies in previous sections. Firstly, initial mass values of each section for stepped Timoshenko beam model and initial mass of each story for discrete Timoshenko beam model analyzed by Transfer Matrix Method were assumed as 300 kg/m3 according to recommendation in literature [82]. Besides, initial values of G^* for all mathematical models are separately calculated from shear beam formula ($G^*_{initial} = \rho(4Lf_1)^2$) for each direction and correlation between G^* and E^* are provided by using C values calculated based on ratios of identified modal frequencies for both directions [82]. Figure 6.11 represents calculated C values for X and Y directions.

Algorithm updates mass and G^* values in each step by using objective function (Equation 4.16) until it finds minimum error value between the identified modal properties with N4SID method and calculated modal properties of simplified mathematical models. Updated modal frequencies and mode shapes are presented for both directions in Figure 6.12 - Figure 6.15 for two different methods.

Besides, floor accelerations of simplified mathematical models were estimated with the procedure explained in Stepped Timoshenko Beam Model section. Figure 6.16 - Figure 6.23 represent recorded and estimated floor accelerations for X and Y directions for the whole duration of earthquake and for two seconds.

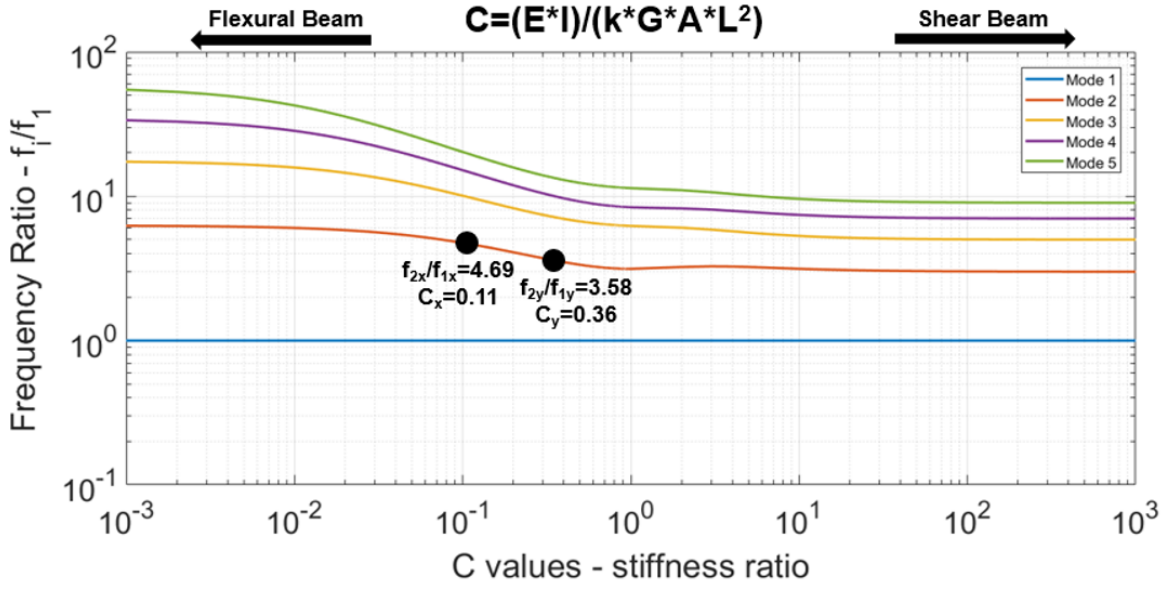

Figure 6.11. Relation between the effective bending rigidity and the effective shear rigidity.

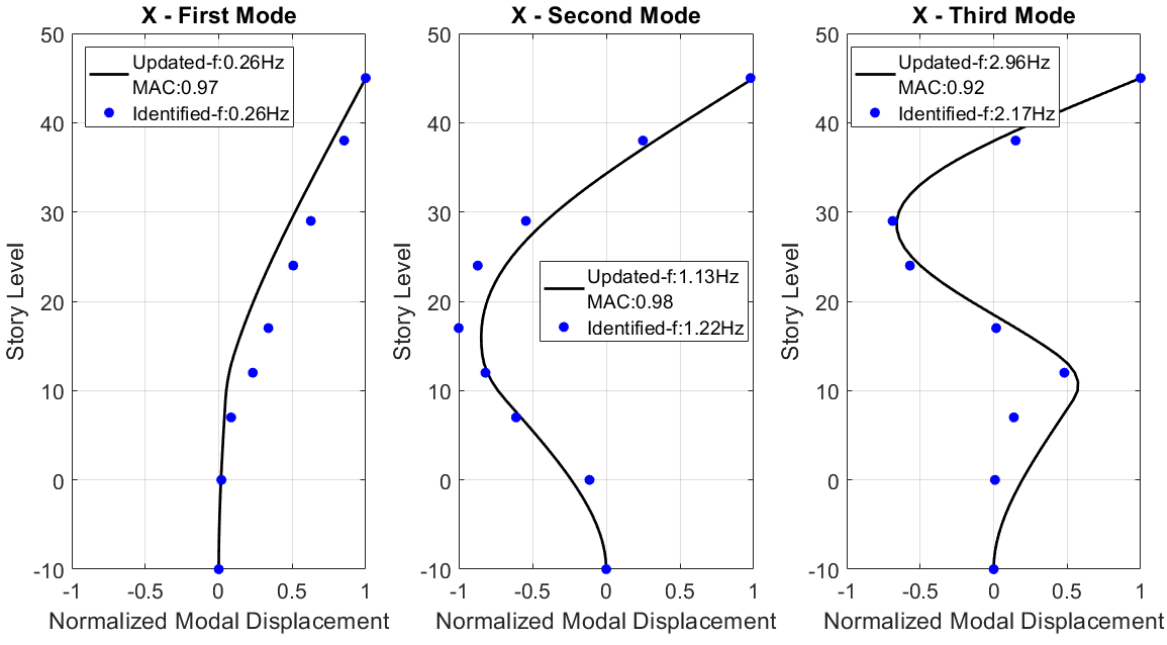

Figure 6.12. Updated and identified modal properties of STBM for x direction.

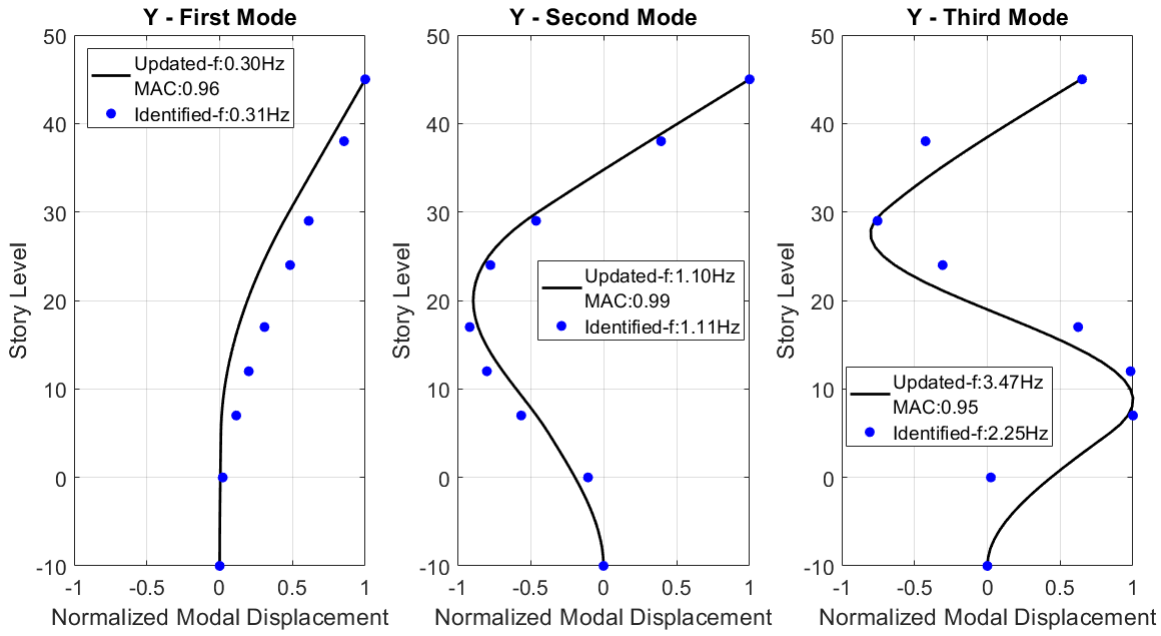

Figure 6.13. Updated and identified modal properties of STBM for y direction.

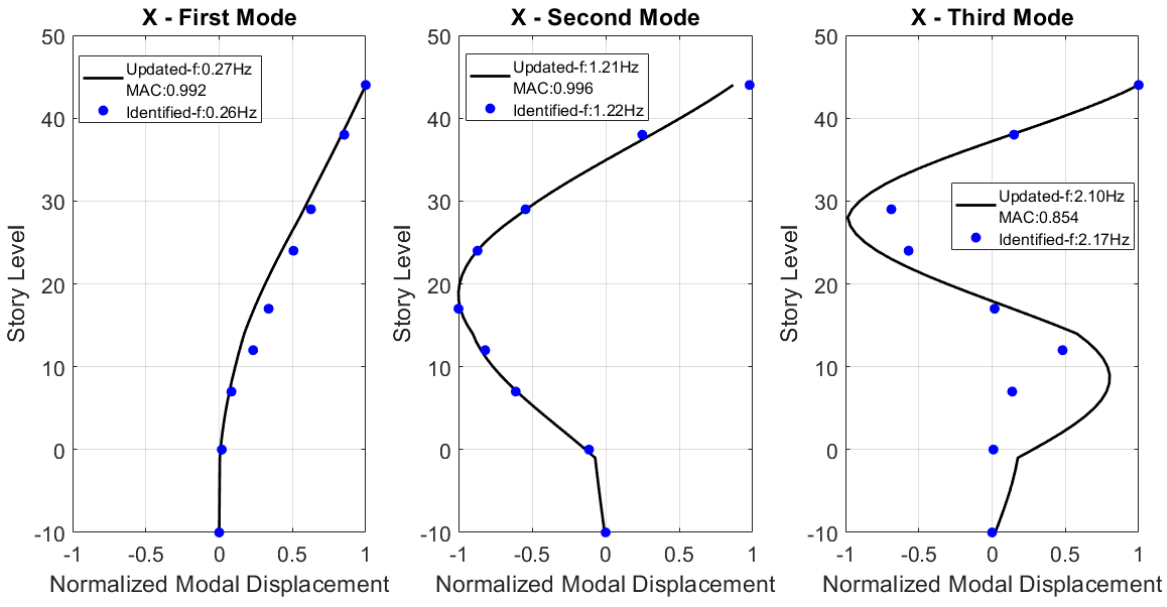

Figure 6.14. Updated and identified modal properties of DTBM for x direction.

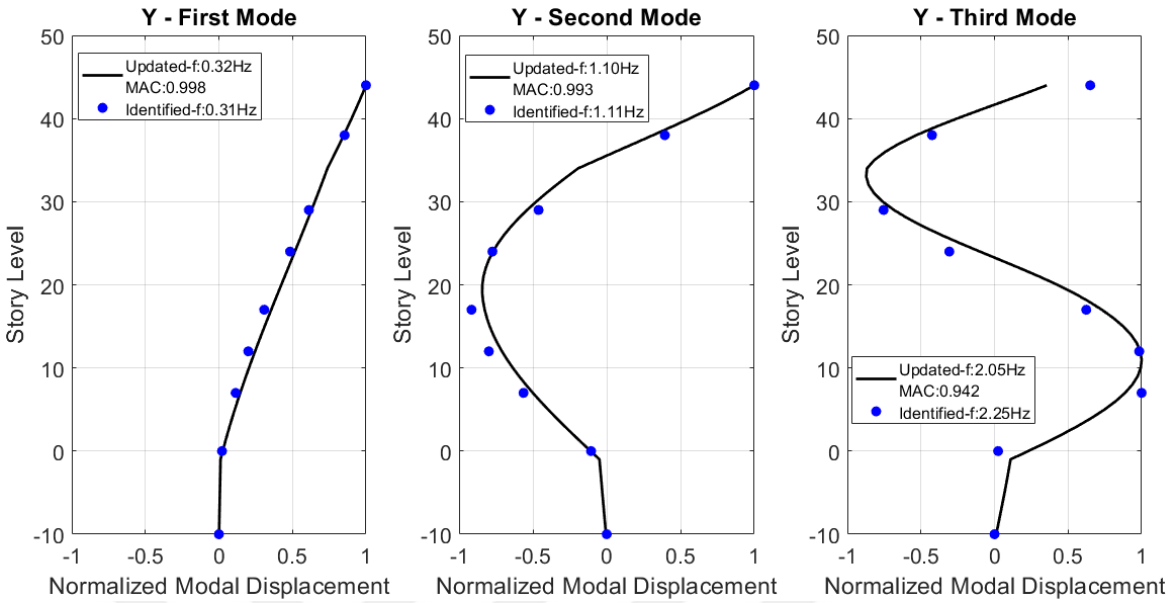

Figure 6.15. Updated and identified modal properties of DTBM for y direction.

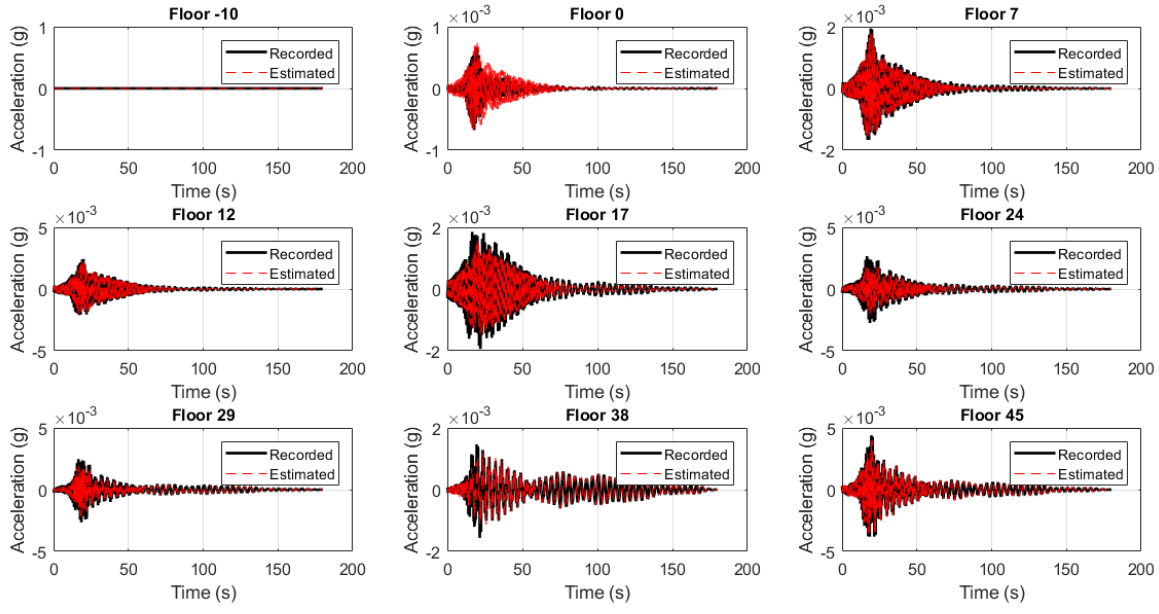

Figure 6.16. Recorded and estimated floor accelerations for whole duration for x direction (STBM).

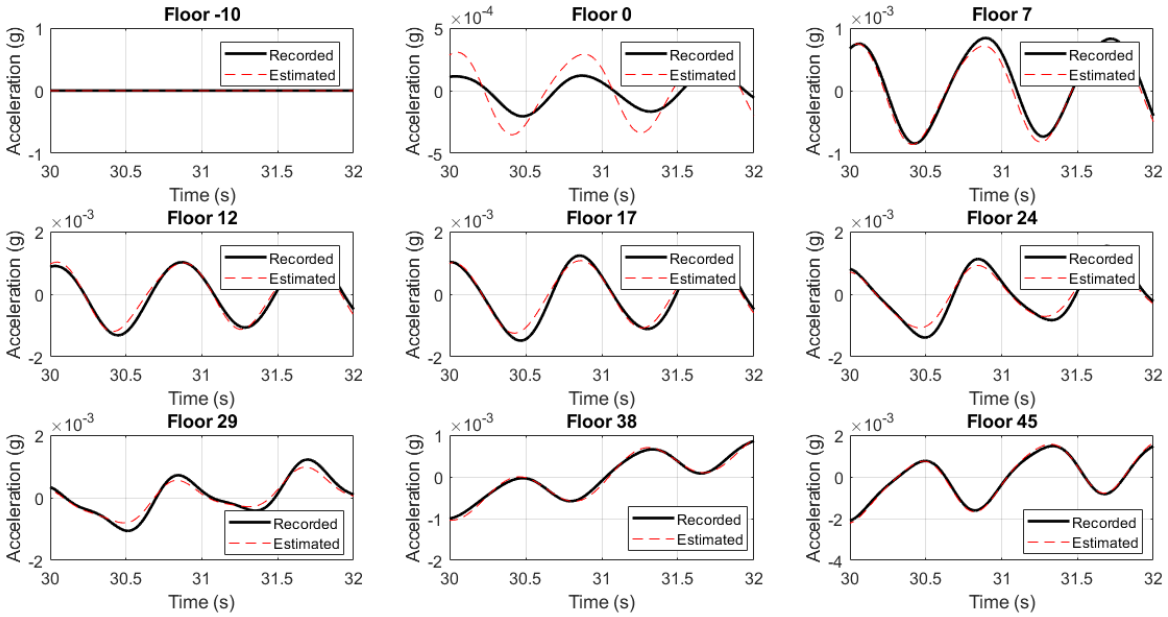

Figure 6.17. Recorded and estimated floor accelerations for two seconds for x direction (STBM).

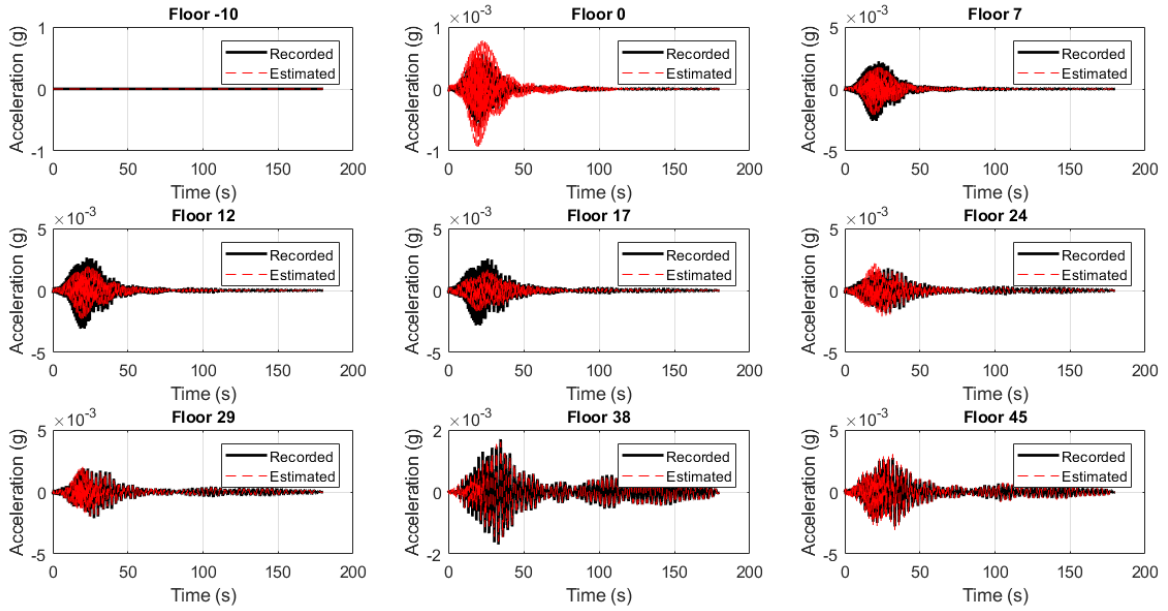

Figure 6.18. Recorded and estimated floor accelerations for whole duration for y direction (STBM).

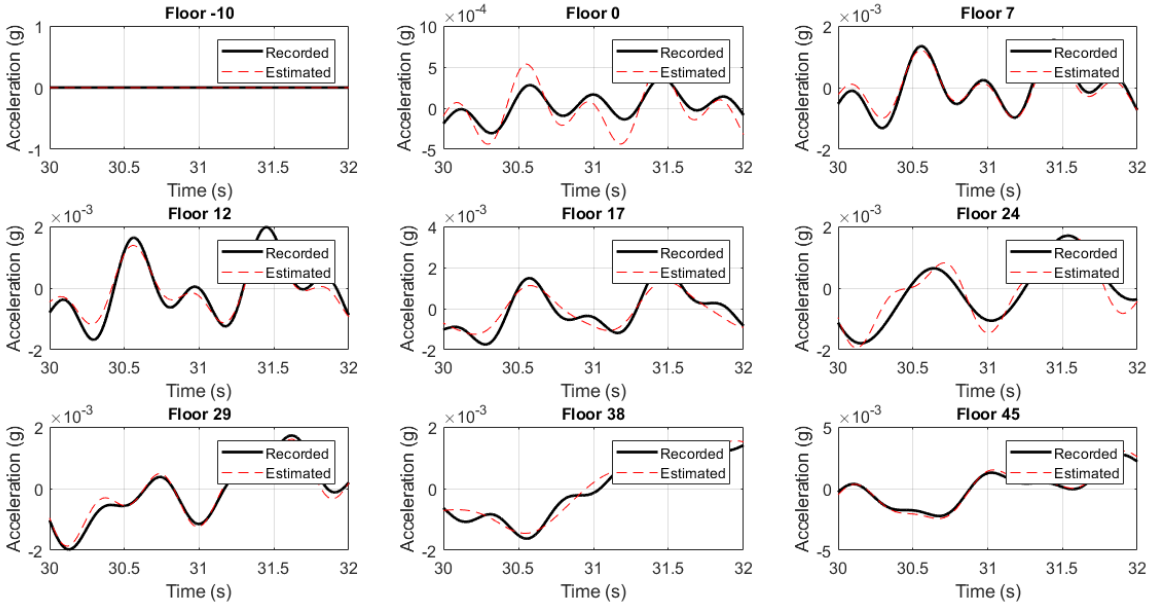

Figure 6.19. Recorded and estimated floor accelerations for two seconds for y direction (STBM).

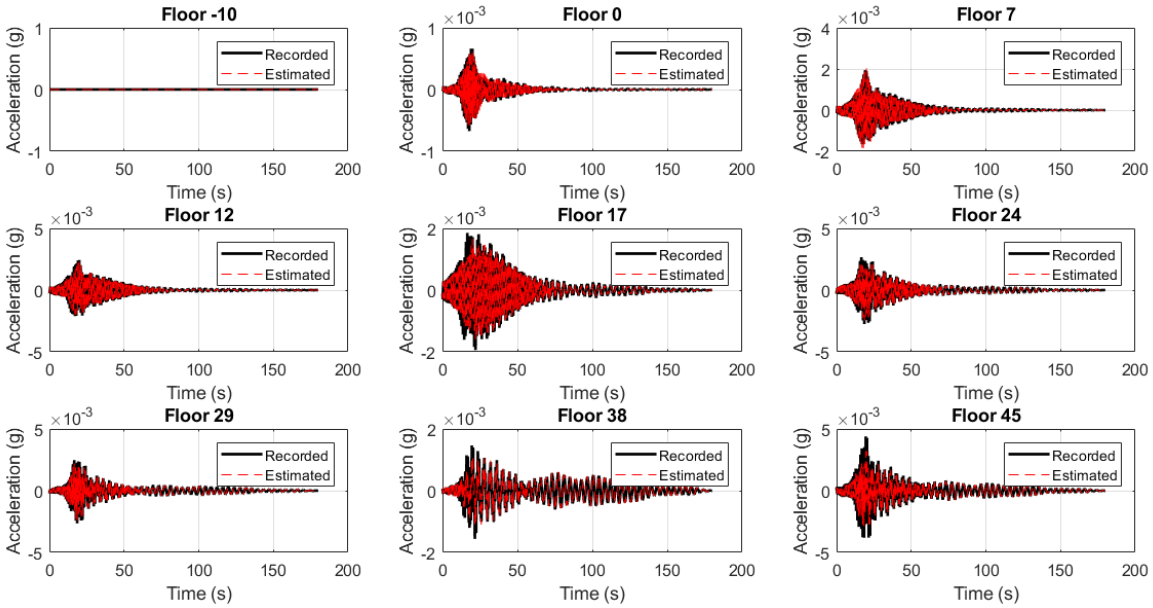

Figure 6.20. Recorded and estimated floor accelerations for whole duration for x direction (DTBM).

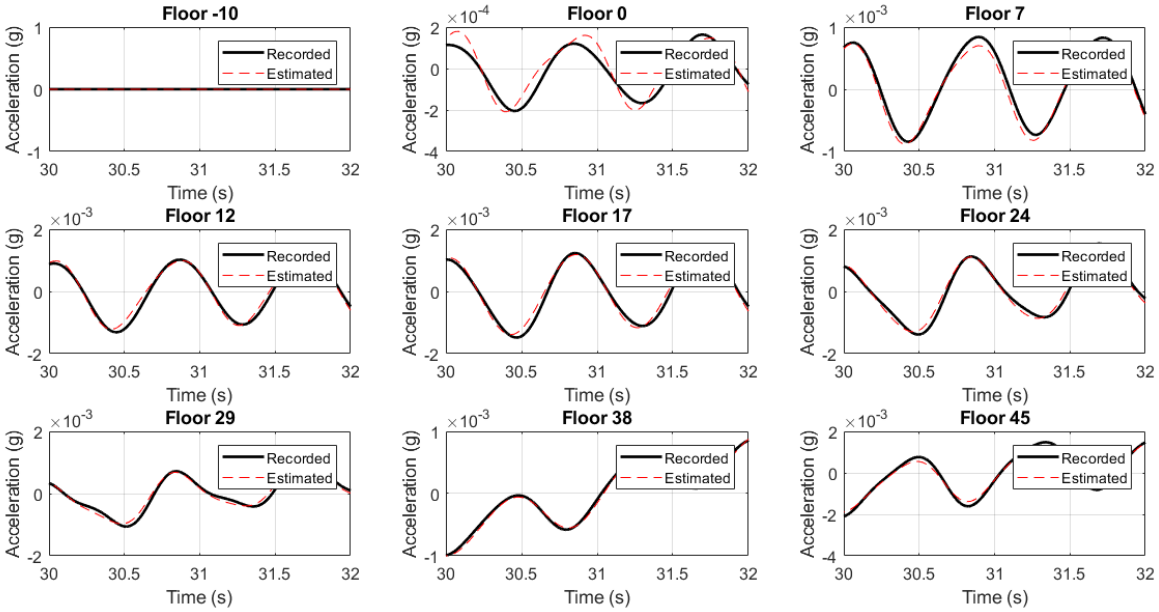

Figure 6.21. Recorded and estimated floor accelerations for two seconds for x direction (DTBM).

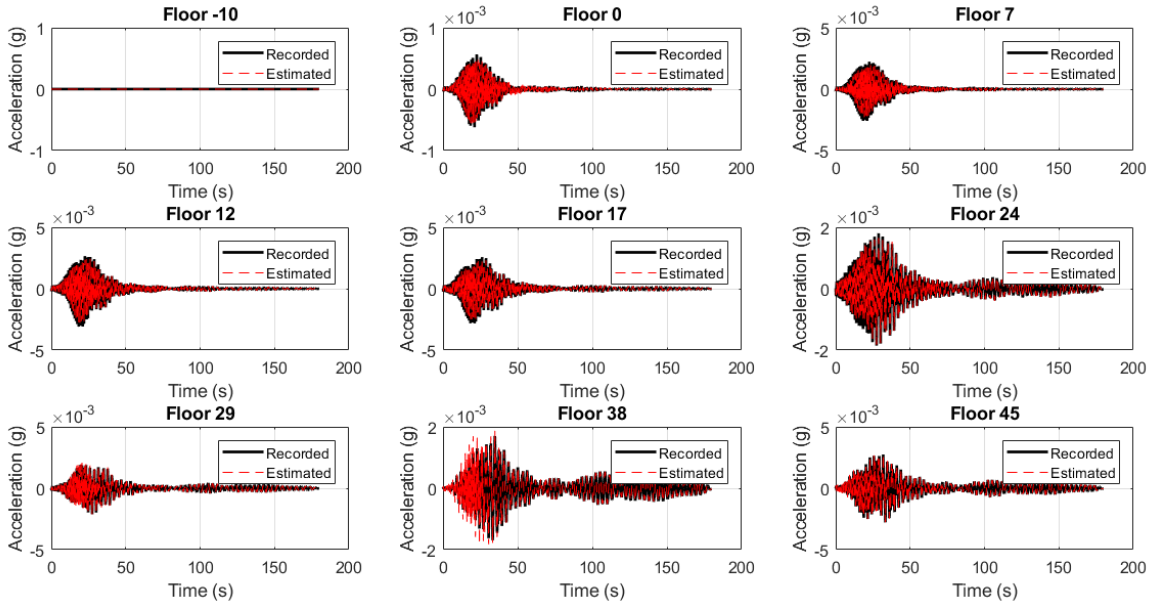

Figure 6.22. Recorded and estimated floor accelerations for whole duration for y direction (DTBM).

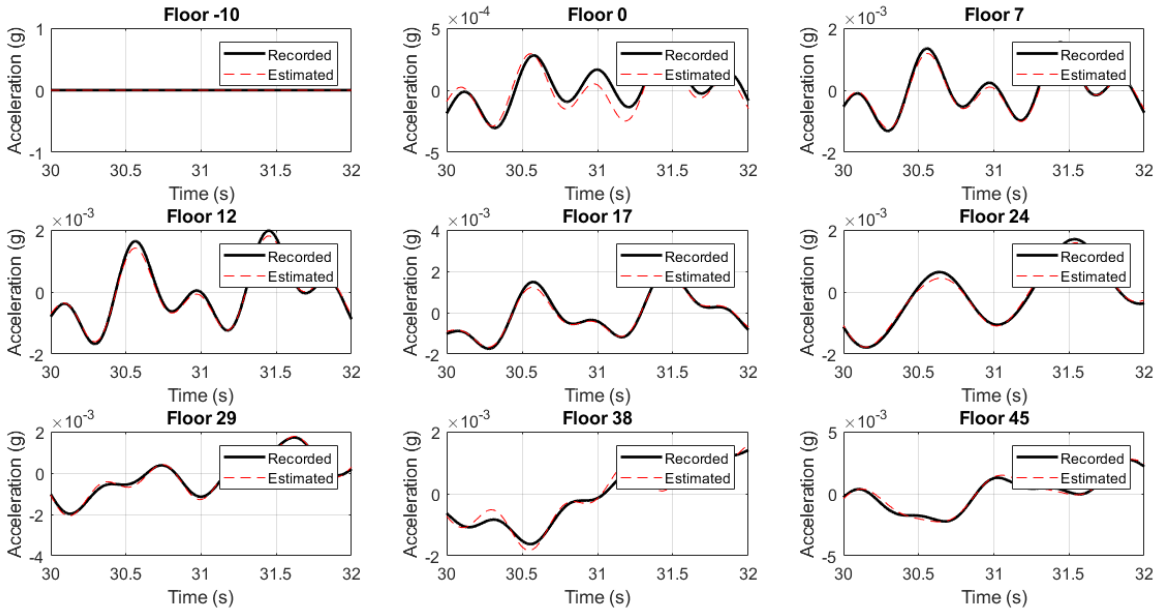

Figure 6.23. Recorded and estimated floor accelerations for two seconds for y direction (DTBM).

It can be clearly observed that recorded and estimated floor accelerations show good agreement for instrumented floors. Figure 6.24 represents inter-story drift ratios of the structure for both directions under the earthquake. It can be seen that the inter-story drifts are significantly lower than threshold values given in Table 5.2.

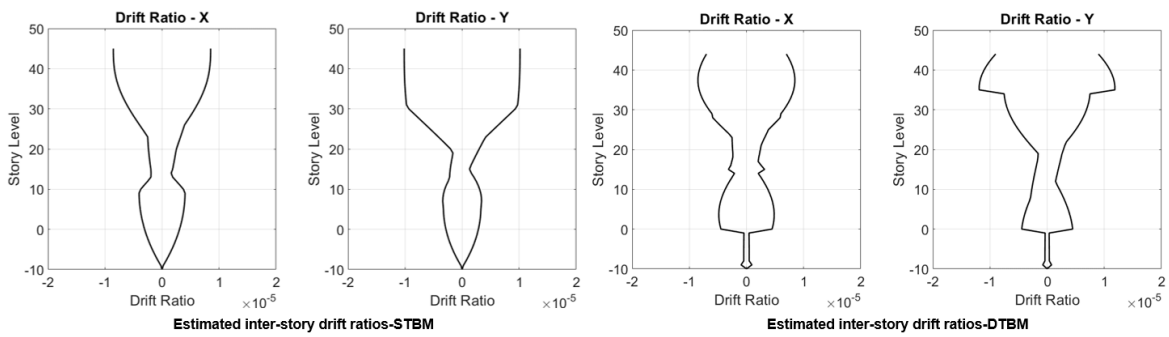

Figure 6.24. Estimated inter-story drift ratios for STBM and DTBM.

Figure 6.25 shows DI vs. Maximum Inter-story Drift Ratio for Marmara Sea Earthquake. As can be seen from the figure, the recommended intervals for different damage levels are appropriate even for low damage conditions. However, although low inter-story drift ratios were estimated during Marmara Sea Earthquake, changes in fundamental frequencies are higher than expected. This may be due to effect of other mechanism such as soil-structure interaction. Also, it is imperative to highlight that since changes in modal frequencies of the tall building during the seismic event are in the scatter limits observed during long term monitoring presented in Figure 6.2, it is difficult to use only DI index in order to determine damage level. On the other hand, maximum inter-story drift ratio can be utilized in addition to DI to decide reliable damage level. Therefore, proposed relationship between frequency change and maximum inter-story drift ratio provides significant advantage for reliable condition assessment of structures.

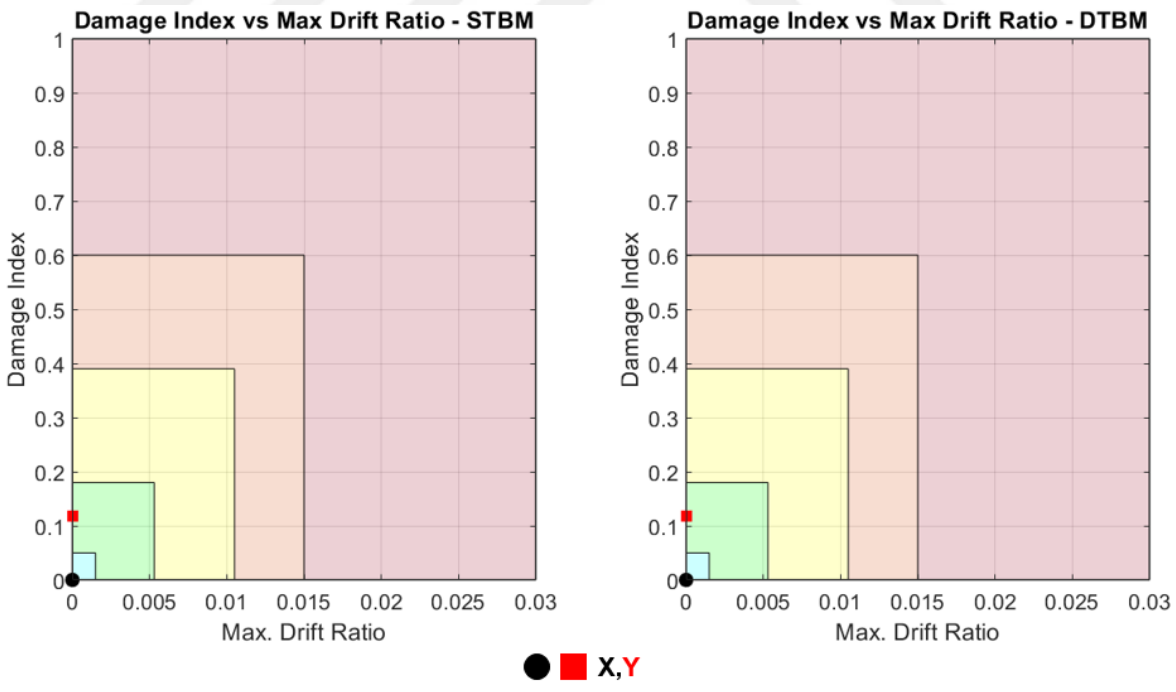

Figure 6.25. Damage index vs. maximum inter-story drift ratio graphs for STBM and DTBM.

6.2. Damaged RC Building

Since there is no publicly available dynamic response of a tall building damaged after a severe earthquake in literature, dynamic response of 7-story building in Van Nuys, recorded during 1994 Northridge earthquake, were used in order to validate proposed methodology for NLSM in this study.

The building was constructed in 1966 according to seismic code used in Los Angeles City and survived after significant earthquakes. Vertical load-bearing system of the building only consists of columns with different dimension and there are no shear walls. However, brick walls are utilized in some sections of entrance floor. In addition, spandrel beams are used to control torsional behavior of the building. Pile foundation is preferred since the building is constructed on soft soil. Figure 6.26 represents side view, typical floor plan and foundation system of the building.

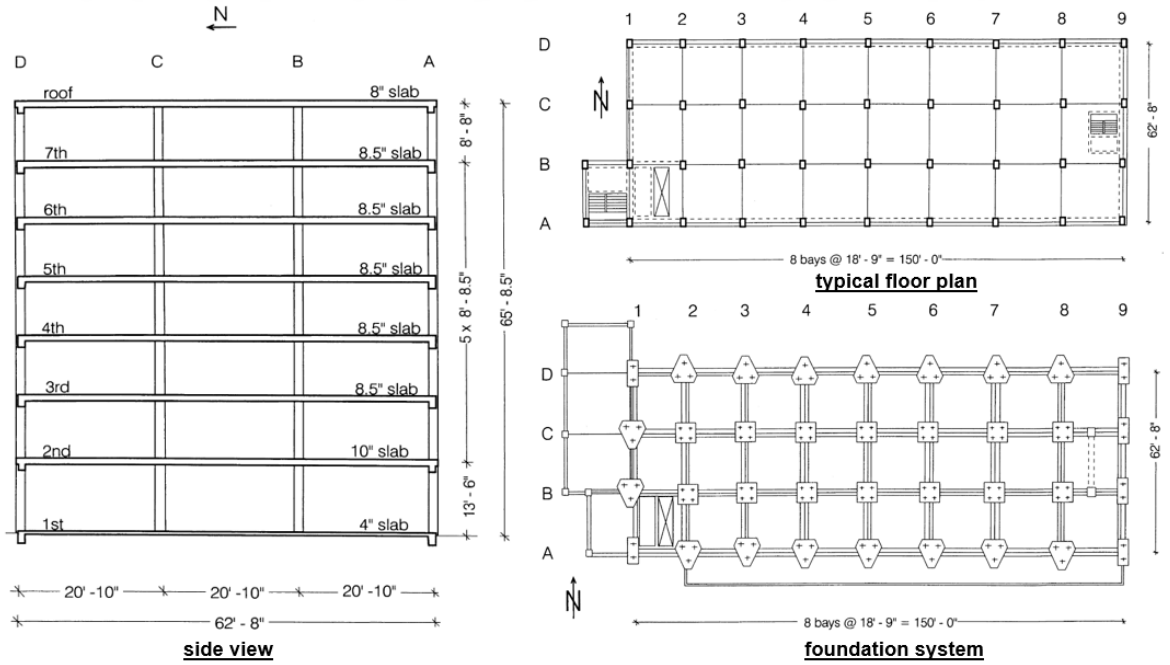

Figure 6.26. General overview of the building [48].

Instrumentation of the building was updated and improved over time and number of sensors increased to 16 before significant earthquakes occurred. Figure 29 represents sensor layout of the building.

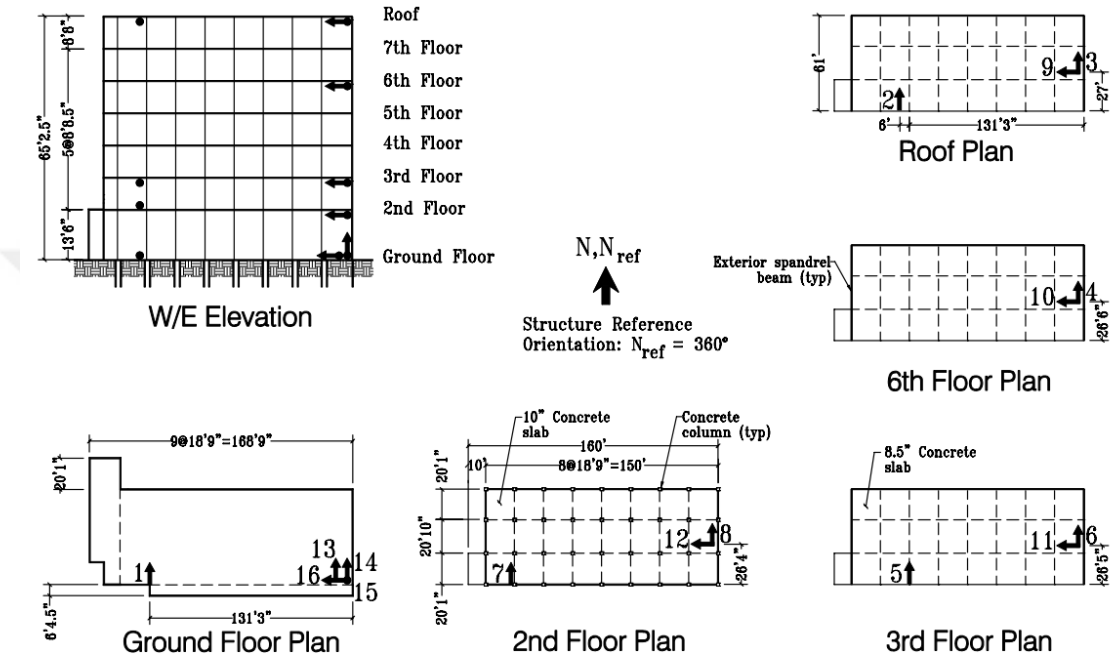

Figure 6.27. SHM system and sensor layout of the building.

The system recorded dynamic response of the structure during Big Bear Earthquake (28 June 1992, 6.6MI), Landers Earthquake (28 June 1992, 7.3Ml) and Northridge Earthquake (17 January 1994, 6.4Ml). The vibration data recorded under these earthquakes were analyzed by different techniques in many studies to understand behavior and to detect damages of building [26], [120-123]. In addition, dynamic properties of the building which are identified from vibration records and estimated from modal analysis of finite element model were compared in some studies [121], [124]. Although significant damages were not observed during Big Bear and Landers Earthquakes, Northridge Earthquake caused important structural damages [120]. Figure 6.28 represents recorded vibration data of the structure under Northridge Earthquake ($PGA_{NS} : 0.42g, PGA_{EW} : 0.45g, PGA_V : 0.27g$).

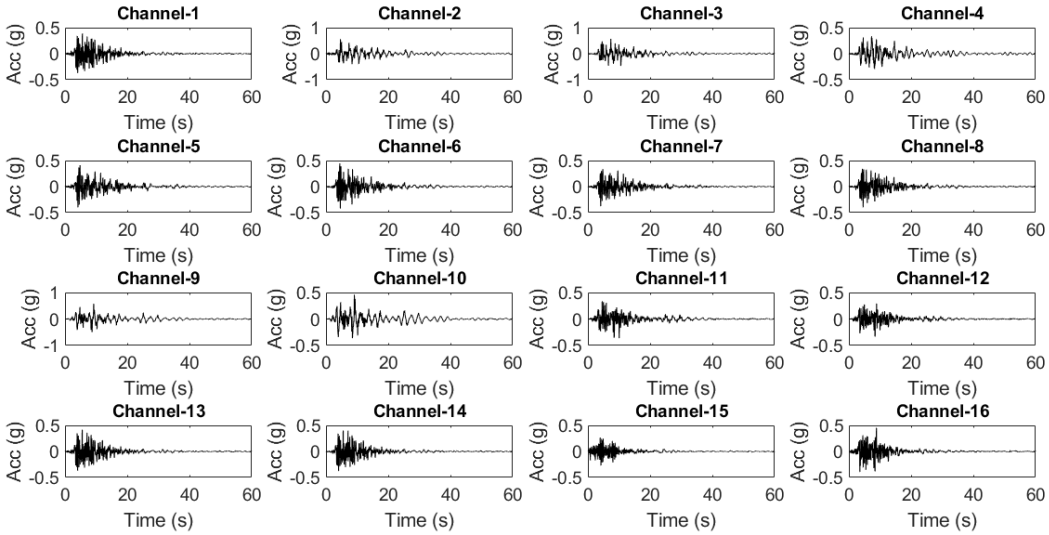

Figure 6.28. Time history graphs for Northridge Earthquake.

Figure 6.29 and Figure 6.30 present structural damages of the building after Northridge Earthquake.

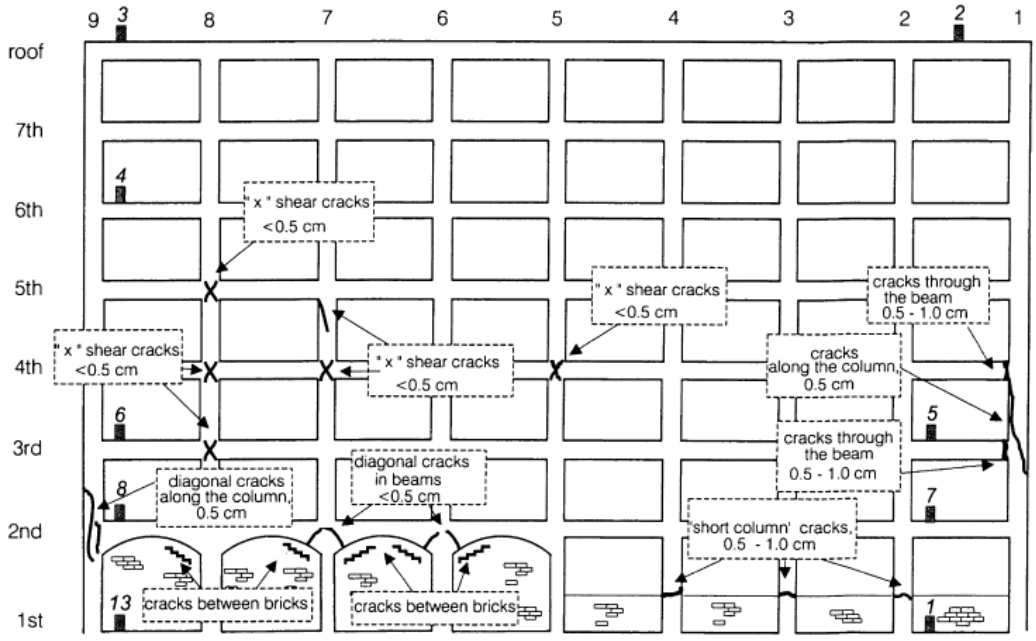

Figure 6.29. Observed structural damages on building after Northridge Earthquake – north view [120].

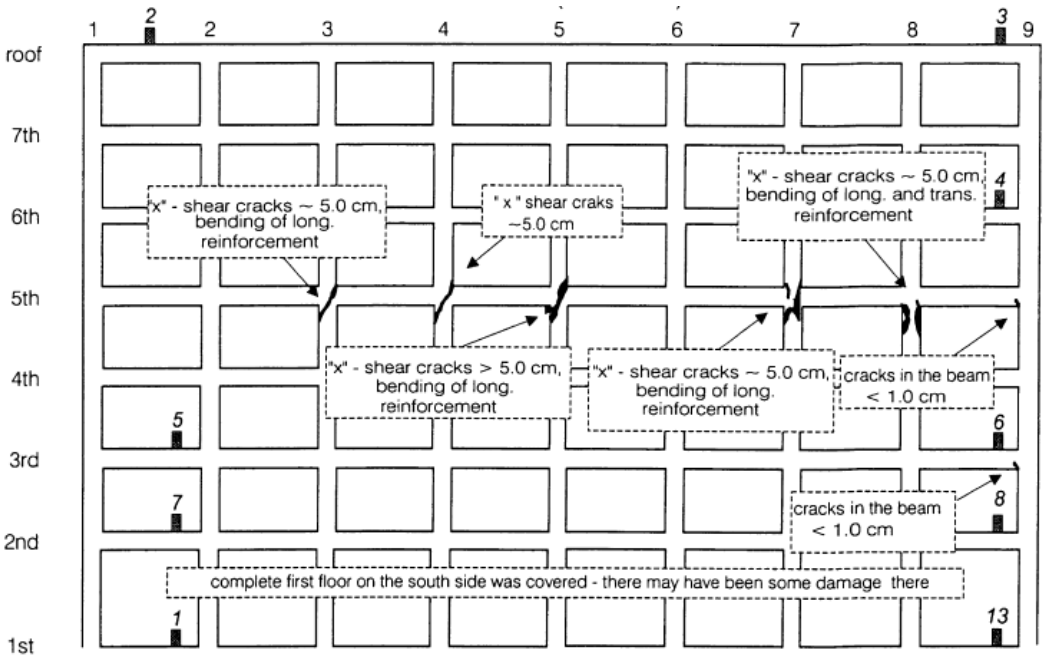

Figure 6.30. Observed structural damages on building after Northridge Earthquake – south view [120].

In this study, dynamic properties of the building was identified with N4SID [117, 118]. Figure 6.31 represents frequency changes of the building.

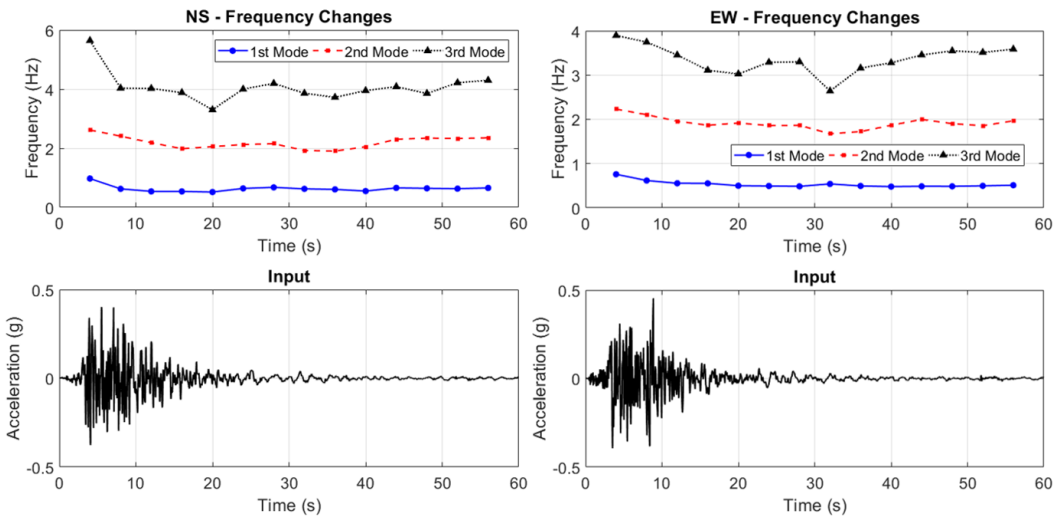

Figure 6.31. Changes in modal frequencies under Northridge Earthquake.

Also, identified mode shapes before and after earthquake was compared in Figure 6.32.

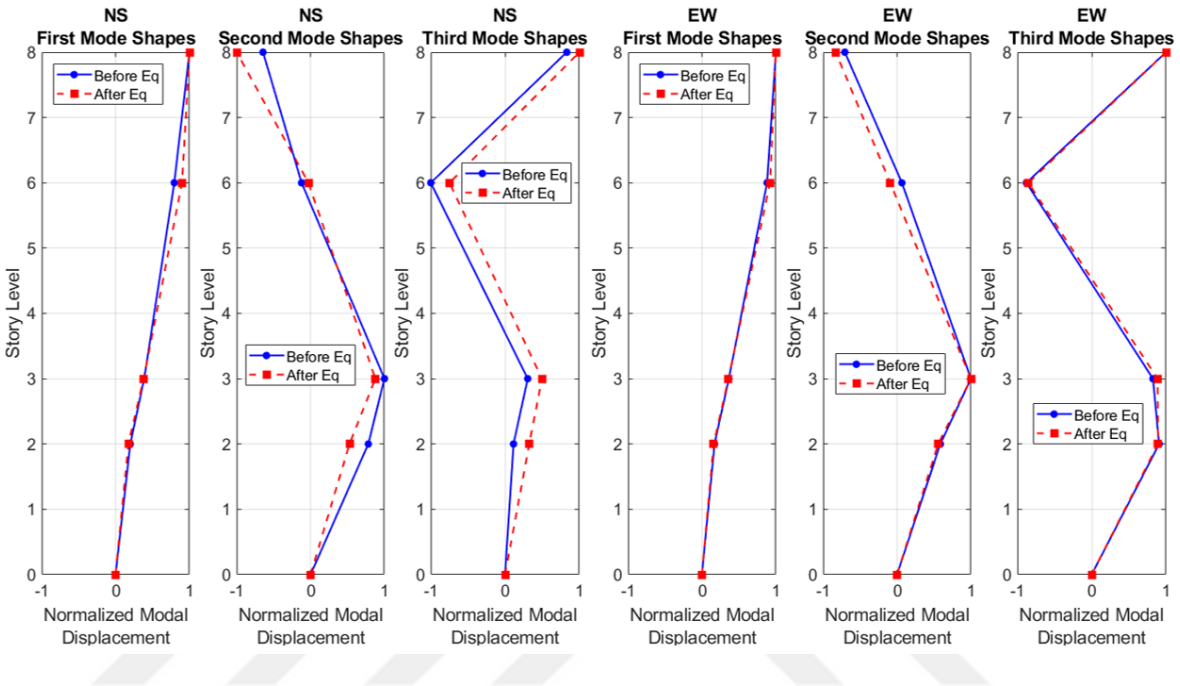

Figure 6.32. Identified mode shapes before and after Northridge Earthquake.

Table 6.3 presents comparison of identification results of this study and previous study in literature.

Table 6.3. Comparison of identified modal frequencies with results of other studies.

	This Study	**Trifunac, Ivonovic, Todorovska [122]**
NS – f_{beg}	0.97 Hz	0.90 Hz
NS – f_{end}	0.66 Hz	0.60 Hz
NS – f_{min}	0.52 Hz	0.50 Hz
EW – f_{beg}	0.76 Hz	0.95 Hz
EW – f_{end}	0.51 Hz	0.60 Hz
EW – f_{min}	0.48 Hz	0.45 Hz

NLSM of the structure was created based on the proposed methodology. Firstly, mass of each story and elastic properties of nonlinear springs were estimated by using recorded vibration data. Initial mass for each story was assumed as 200 kg/m^3 base on recommendation in literature [82]. Initial values of G^* are separately calculated from shear beam formula for each direction and correlation between G^* and E^* are provided by using C values calculated based on modal frequency ratios of model for both directions. Figure 6.33 shows C values of the building. Since there are no coupling beams and structural shear walls in the structure, it is reasonable that behavior of the structure is close to shear beam behavior.

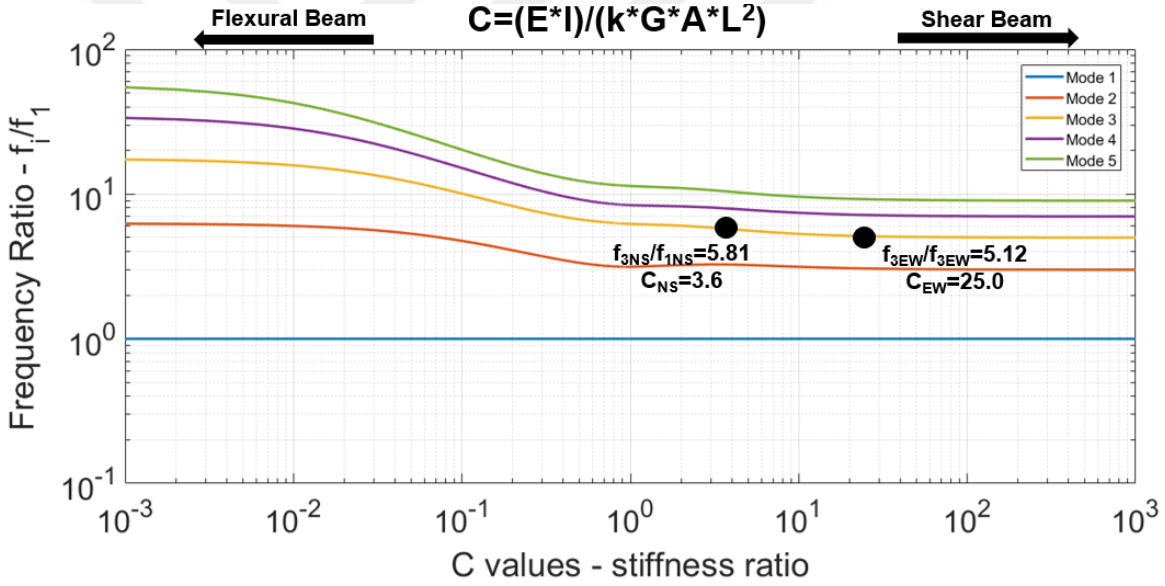

Figure 6.33. Relation between the effective bending rigidity and the effective shear rigidity.

Optimum mass and elastic properties of nonlinear springs were predicted by updating NLSM with the steps described in Figure 4.58. Error values of objective function after each iteration and change in minimum error values for both direction were shown in Figure 6.34.

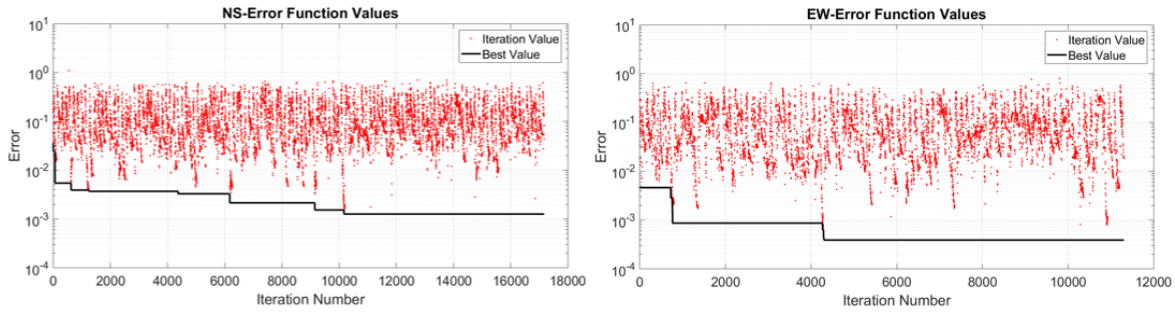

Figure 6.34. Changes in error values during updating.

Also, changes in mass and elastic stiffness of each story were presented in Figure 6.35 and Figure 6.36.

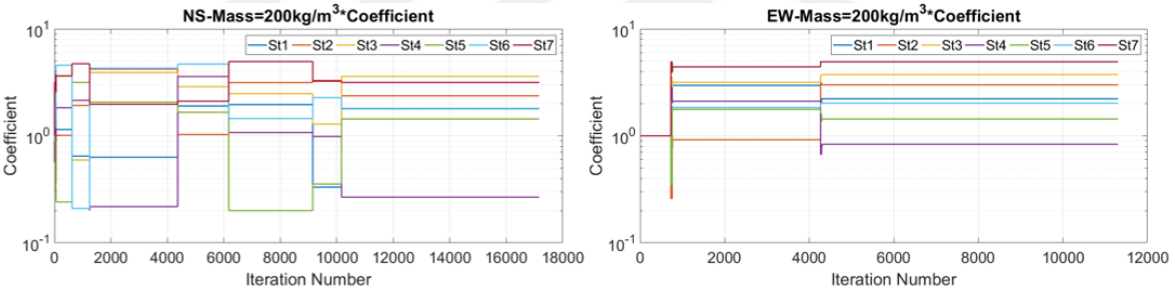

Figure 6.35. Changes in mass distribution of building in Van Nuys during updating.

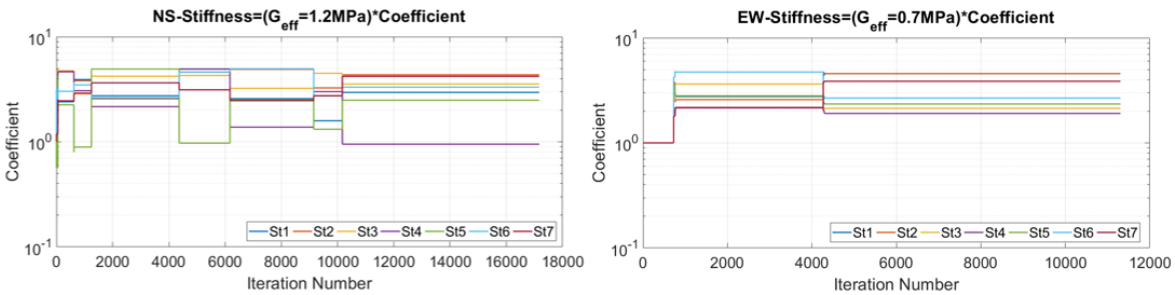

Figure 6.36. Changes in elastic stiffness distribution of building in Van Nuys during updating.

Updated modal frequencies and mode shapes were represented for both directions in Figure 6.37.

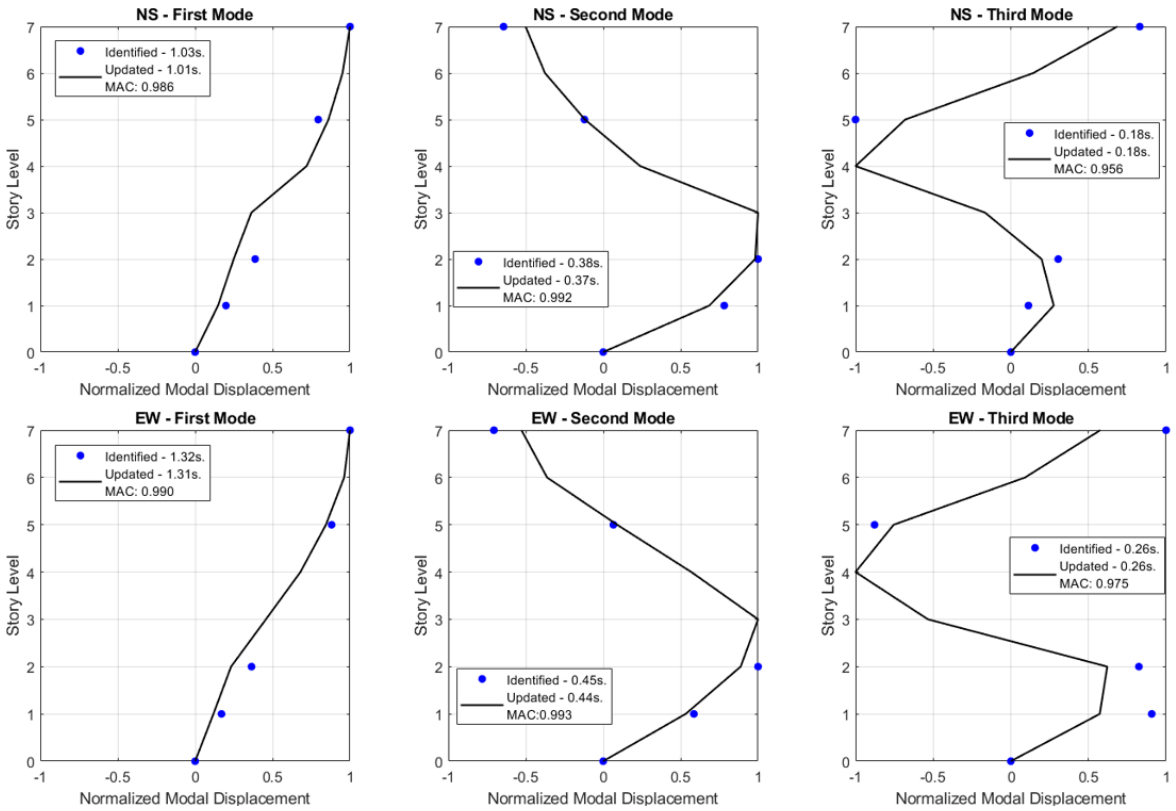

Figure 6.37. Updated and identified modal properties.

Finally, NLSM was updated with Simulated Annealing with the steps described in Figure 4.66. In updating, dynamic response of the structure recorded by accelerometers on second floor were excluded from algorithm. At the end of updating, simulated and measured responses of the structure at second floor compared in order to quantify efficiency of updating algorithm. Figure 6.38 and Figure 6.39 represent comparison of simulated and measured responses of the structure. As can be clearly seen from graphs, simulated and measured responses show good agreement.

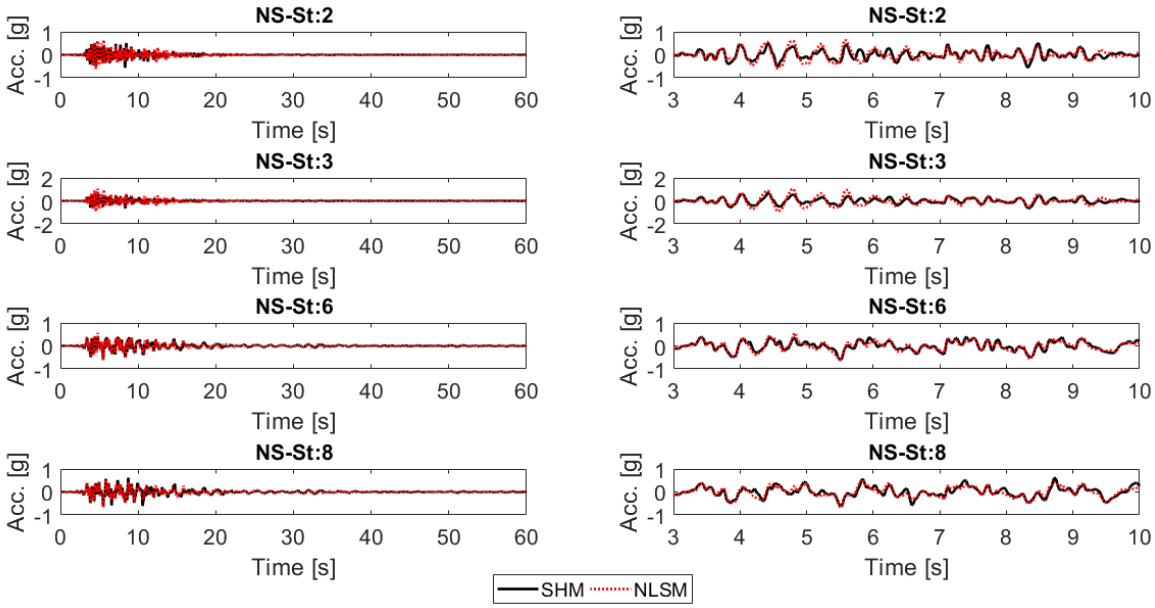

Figure 6.38. Recorded and estimated floor accelerations for north-south.

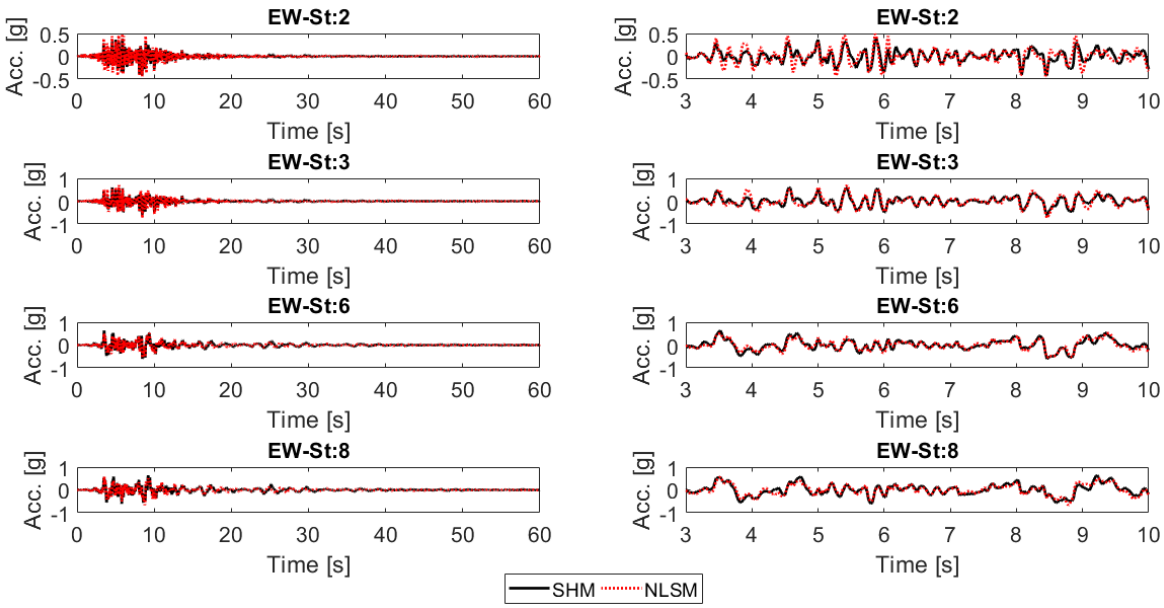

Figure 6.39. Recorded and estimated floor accelerations for east-west.

Nonlinear behaviors of springs were presented in Figure 6.40 and Figure 6.41. As can be seen from the results, more than half of nonlinear shear and flexural springs exceeded design points and showed nonlinear behavior.

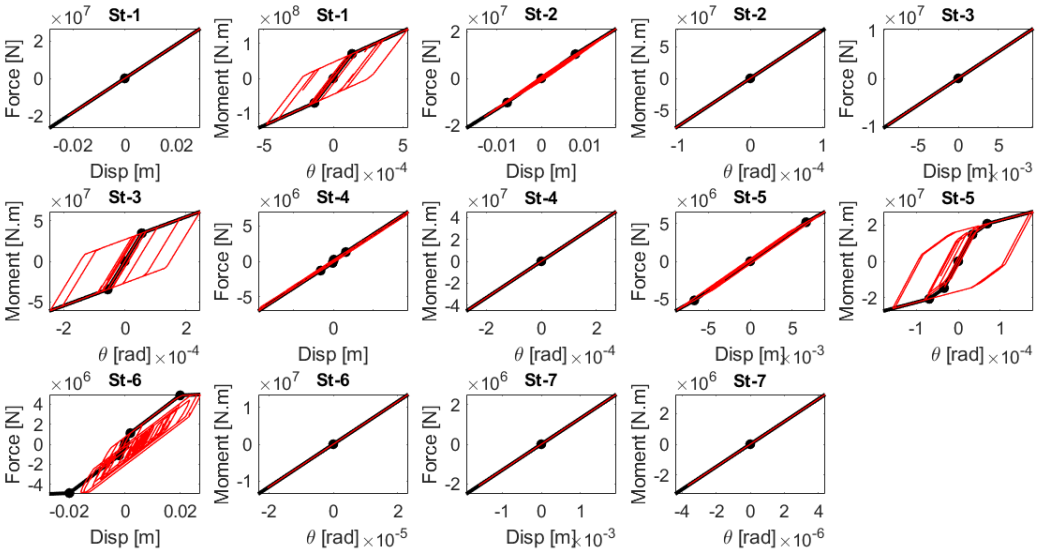

Figure 6.40. Nonlinear behavior of springs after updating for north-south.

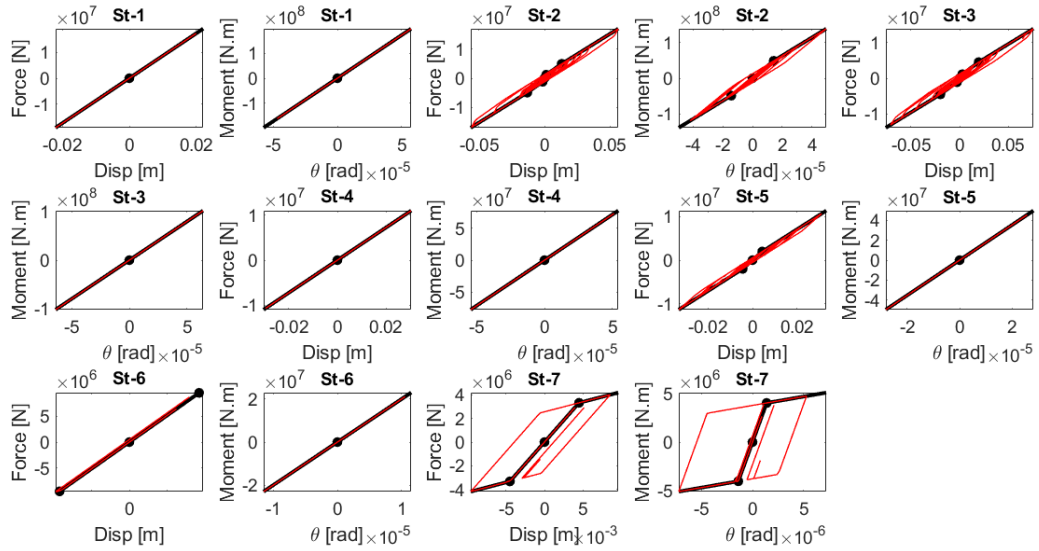

Figure 6.41. Nonlinear behavior of springs after updating for east-west.

The hysteretic behavior of nonlinear shear and flexural springs of NLSM under earthquakes can provide significant benefits for condition assessment of structures. Since each story is modeled separately with nonlinear shear and flexural components in NLSM, the amount of non-linearity in shear and flexural springs can be an important indicator in evaluating damages of structural members that contribute to shear behavior and flexural behavior in these floors. Therefore, local condition assessment of structures can be reliably conducted based on non-linearity of springs in NLSM after an earthquake.

In addition, estimated inter-story drift ratios were presented in Figure 6.42. Dynamic response of the structure was also simulated by using Big Bear and Landers earthquakes in order to validate proposed ranges for low damage conditions. Figure 6.43 shows DI vs. Maximum Inter-story Drift Ratio for three earthquakes. As can be seen from the graph, the recommended intervals for different damage levels are appropriate even for low damage conditions.

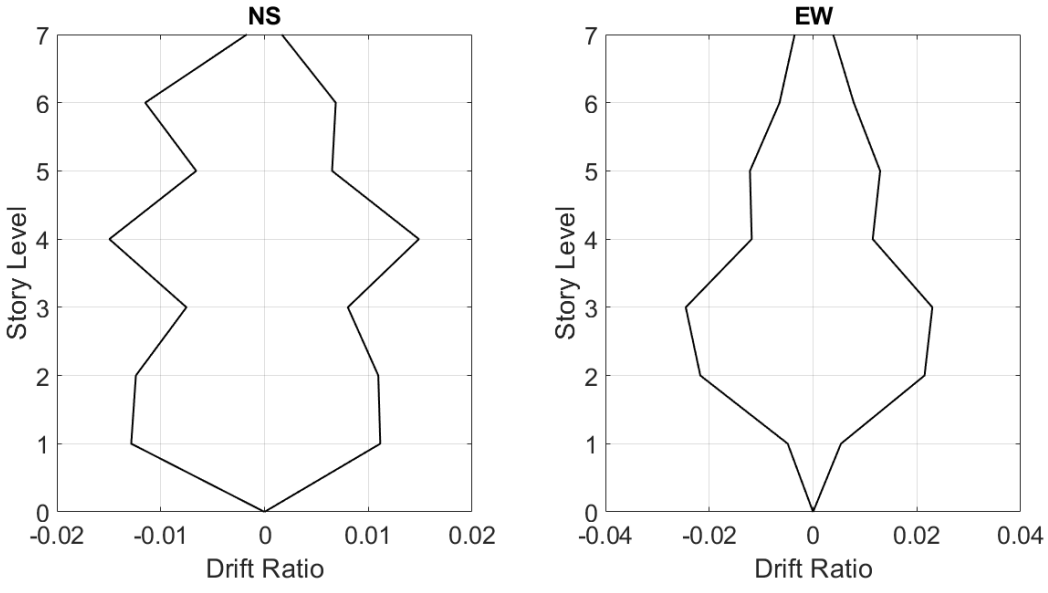

Figure 6.42. Estimated inter-story drift ratios.

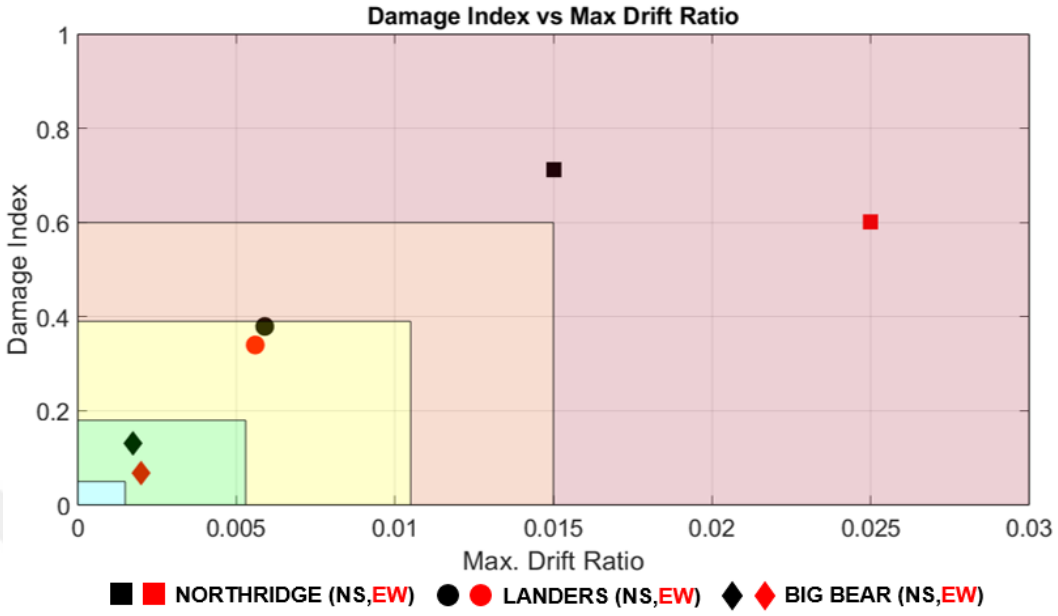

Figure 6.43. Damage index vs. maximum inter-story drift ratio graph for damage assessment of building.

7. SOFTWARE DEVELOPMENT

There are various versions of real – time monitoring software in literature which identify dynamic properties of structures by using Fourier transforms and calculate the responses of the structure in terms of displacements and story drifts [77], [125, 126]. In addition to these, responses of floors between instrumented floors are predicted by using linear and cubic interpolation techniques.

In this study, a software was developed to perform remote and automatic data transfer from structures and to analyze collected data automatically/manually. This software collects vibration records from structures remotely and wirelessly, conducts modal analysis and determines dynamic properties of structures (modal frequencies, shapes and damping ratios) by using different identification techniques. Identification results are saved to SQLite database in real time to control structures. Figure 7.1 shows graphical interface for Real Time Monitoring Module of in-house developed software.

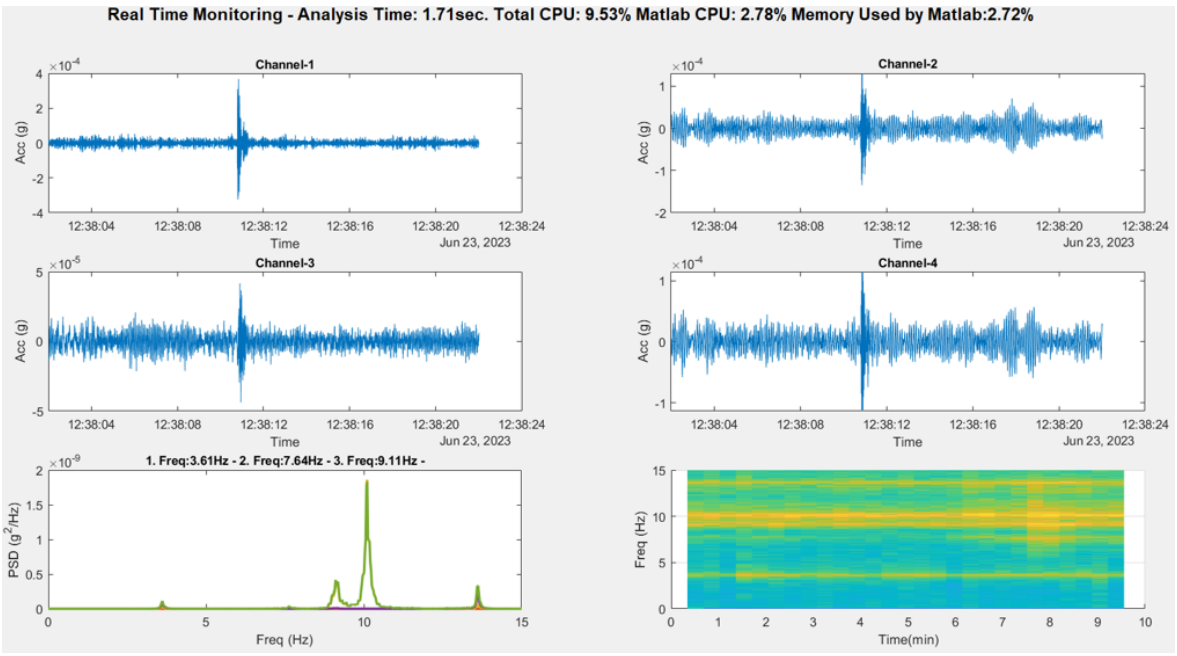

Figure 7.1. Graphical user interface of real time monitoring module.

Besides, the software has additional modules to manually analyze recorded vibration data by using frequency and time domain system identification techniques. Figure 7.2 and Figure 7.3 represents graphical interface of these modules.

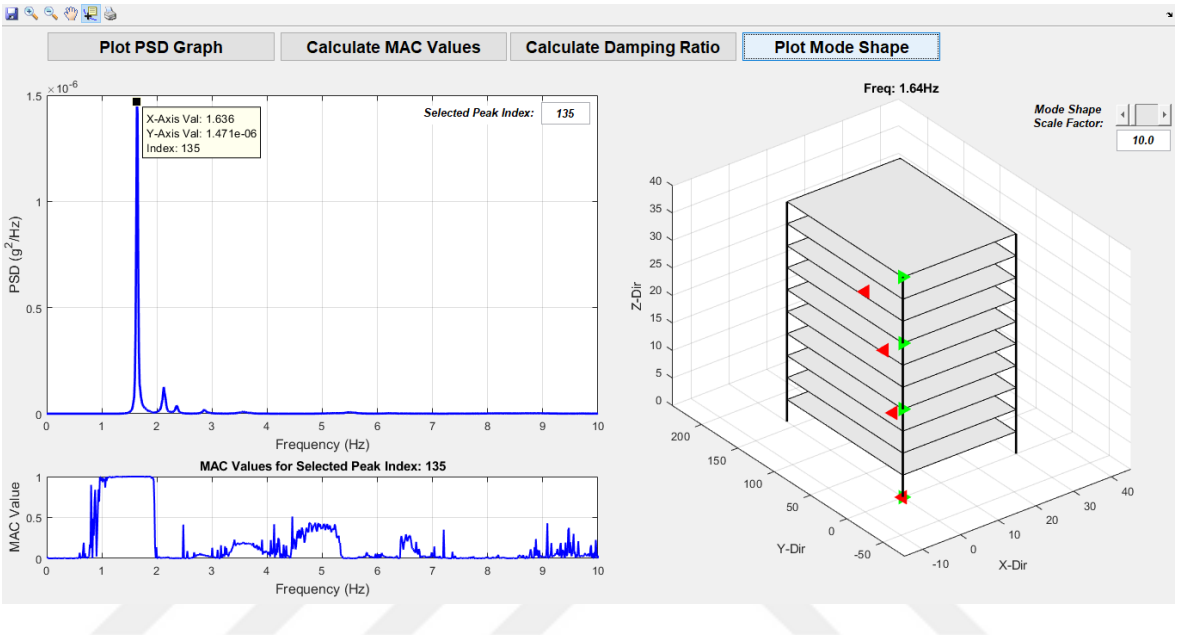

Figure 7.2. Graphical user interface of system identification (freq domain) module.

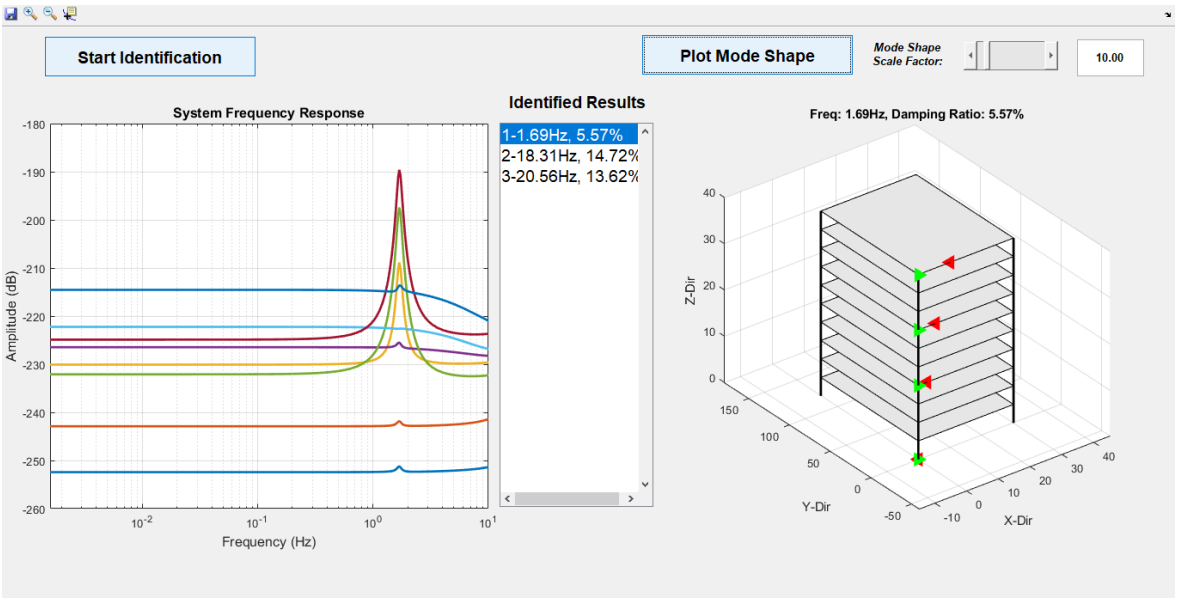

Figure 7.3. Graphical user interface of system identification (time domain) module.

In addition, velocity and displacement values are calculated by integration with Butterworth filter technique can be utilized while calculating velocity and displacement values to get more accurate results. Module for calculation of displacement and velocity values from acceleration values is presented in Figure 7.4.

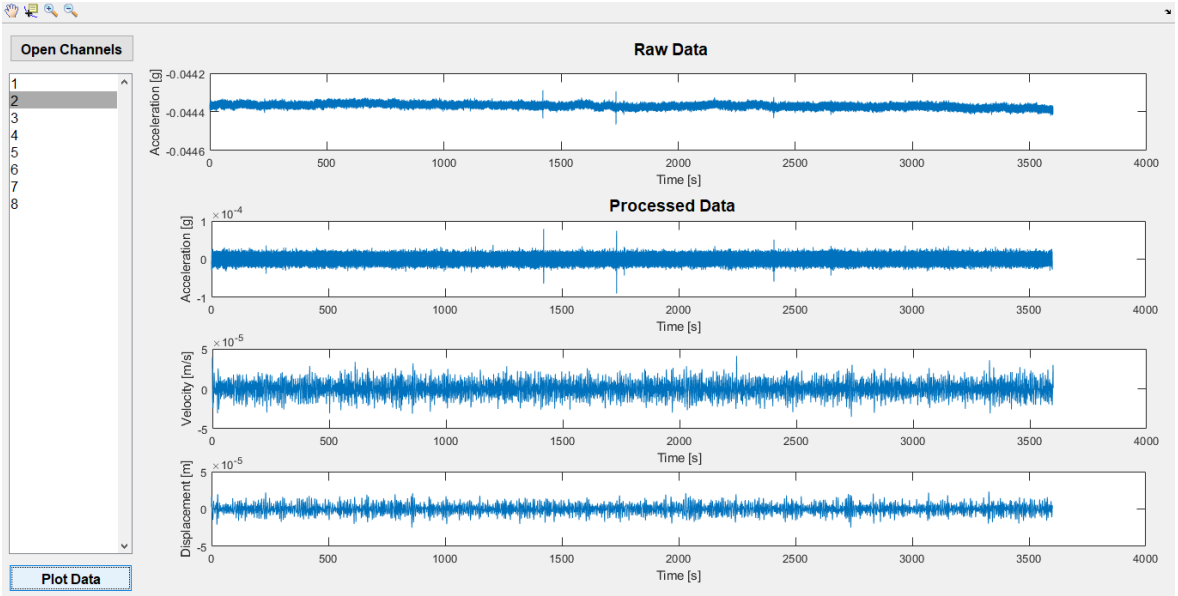

Figure 7.4. Graphical user interface of signal processing module.

The software also performs condition assessment of the structure by tracking changes in modal values and inter-story drift ratios. In the event of an earthquake, the software gives different warning messages if changes in modal frequencies and inter-story drift ratios exceed the pre-determined threshold values. Also, detailed report is prepared about current condition of structure according to analysis of vibration responses recorded before, during and after earthquake. Automatically created report example is shown in Figure 7.5.

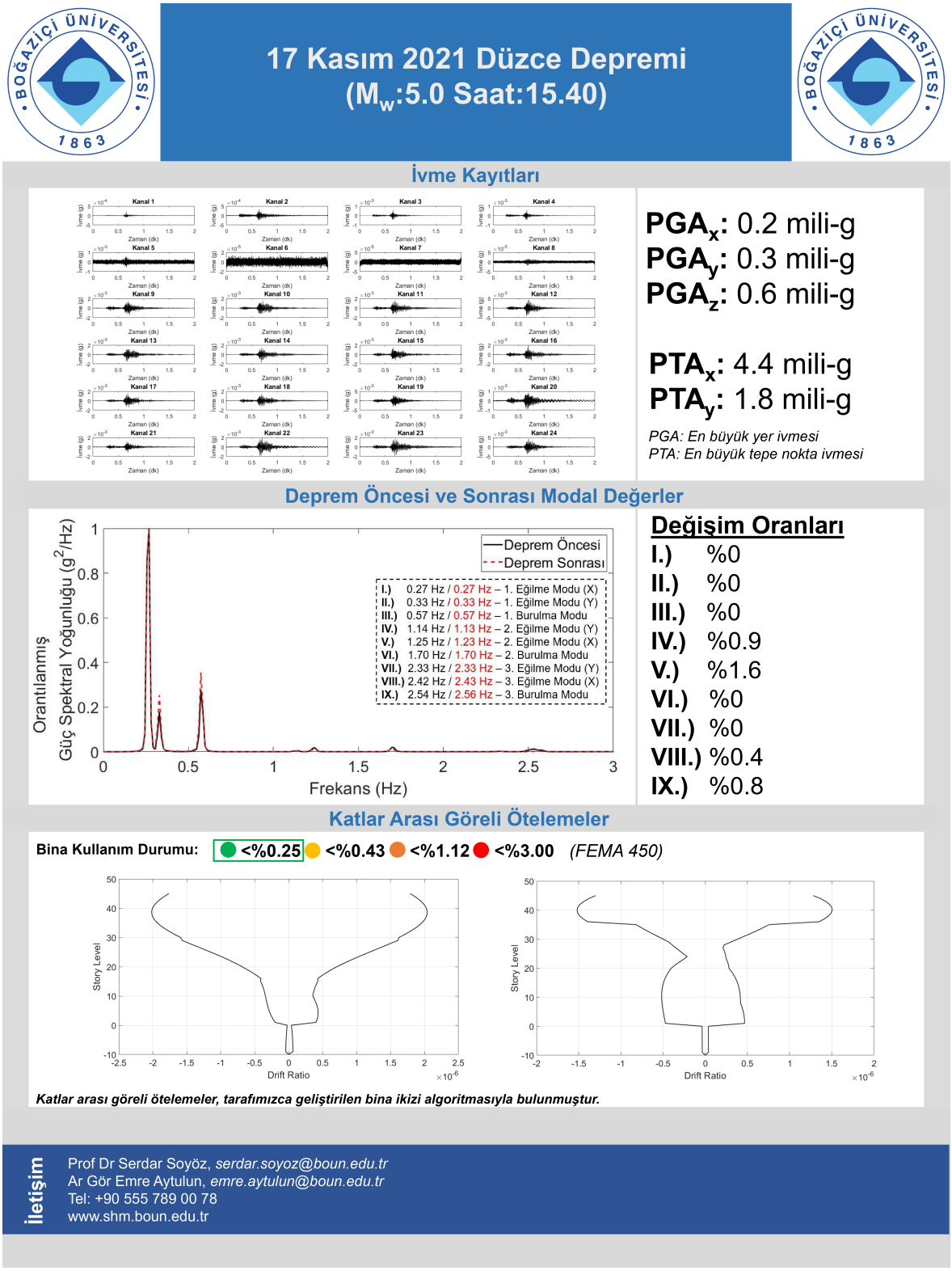

Figure 7.5. Automatically created report by in-house developed software.

8. SUMMARY AND CONCLUSION

The number of tall buildings in cities with high seismicity has been significantly increasing. Performing quick and reliable assessment on functionality of structure after a possible earthquake provide more efficient post-earthquake management. Analysis of dynamic response recorded by SHM system enables reliable and objective condition assessment of structures by controlling changes in dynamic properties and inter-story drift ratio. However, sensors are generally located at certain floors of structures due to economic reasons. Therefore, it is essential to obtain response of non-instrumented floors to reliably conduct damage assessment of structures.

In this study, dynamic response of non-instrumented floors was predicted from dynamic response of instrumented floors. For this aim, a representative tall building was modelled in OpenSees. Nonlinear analyzes of the FEM were performed with selected 11 ground motion records selected to determine relationship between changes in modal parameters and inter-story drift ratios and structural deformations. Because, modal parameters and inter-story drift ratios can be obtained from analysis of vibration data recorded by SHM.

Three different methods were used to estimate responses of non-instrumented floors from instrumented floor responses. Firstly, simplified mathematical model of the structure was created by Timoshenko Beam approach. Since Timoshenko Beam considers effects of shear and flexural behavior, it enables great advantage to estimate dynamic response of tall buildings. However, it is limited to predict dynamic response of structures because it does not take into account nonlinear behavior of structural components and convergence problems are faced while solving compatibility equations. Also, increase in section numbers with different mechanical properties increases analysis time.

Secondly, a simplified mathematical model of the structure was created by discretizing Timoshenko beam model and analyzed with Transfer Matrix Method. This approach provides better modelling of stories with different mechanical properties. Although estimated responses by this method are more satisfactory than responses predicted by first approach, this technique also does not consider nonlinear behavior of structural components.

Finally, nonlinear simplified model of the structure was created by nonlinear shear and flexural springs. Initial parameters of nonlinear springs were estimated based on total mass of the structure and assumed earthquake load. Afterwards, Unscented Kalman Filter and Simulated Annealing algorithms were utilized in order to update nonlinear parameters of springs. Error values of simulated responses obtained by Simulated Annealing are smaller than error values of simulated responses obtained by Unscented Kalman Filter updating. Also, Unscented Kalman Filter takes time according to length of ground motion record and number of updated parameter. Therefore, Simulated Annealing algorithms was utilized in order to update nonlinear parameters of springs by minimizing difference between simulated and measured responses at assumed instrumented floors. It is a fact that there may be more than one solution of objective function used in Simulated Annealing algorithm. In order to discuss this problem, estimated values of updated nonlinear spring parameters for 11 earthquakes were examined in detail. Simulated Annealing algorithm estimated parameters of nonlinear shear and flexural springs in certain range for more than half earthquake records used in this study. However, there were deviations in parameters of nonlinear shear springs because shear springs generally remained in elastic range under nonlinear analysis of the structure.

Changes in modal frequencies and inter-story drift ratios were used as damage indicators because they can be predicted by analyzing vibration data recorded by SHM systems. Threshold values were determined for different performance levels according to relationship between changes in modal frequencies, inter-story drift ratios and structural deformations after nonlinear analysis of representative tall building model.

The proposed mathematical models and condition assessment procedure were used for two different structures to analyze vibration data recorded during seismic events. STBM and DTBM approaches were utilized to estimate inter-story drift ratios along the structure remained in elastic limits during the earthquake. Simulated and measured responses of instrumented floors showed good agreement. Afterwards, inter-story drift ratios along entire building were estimated to assess damage level of structure after the earthquake. The proposed threshold values for different damage levels confirmed that the structure was not damaged under Marmara Sea Earthquake. Since there is no publicly available vibration record of tall building damaged under an earthquake, NLSM approach was validated by using vibration response of 7-story building damaged under Northridge Earthquake. Firstly, linear properties of shear and flexural springs were determined. Afterwards, nonlinear relations of springs were estimated by Simulated Annealing method. In updating process, response of one floor with accelerometer was not included in updating algorithm to evaluate efficiency of the algorithm by comparing simulated and measured response of this floor. After analysis, simulated and measured responses of instrumented floors presented good agreement. Finally, inter-story drift ratios throughout entire building were estimated by analyzing additional two different earthquake records causing low damage on the structure. It was determined that defined limit ranges were reliable to assess different performance levels.

Structural condition assessment can be done by tracking changes in modal frequencies. However, different mechanism may also change modal frequencies. In addition, changes in modal frequencies during small earthquakes may be within the fluctuation range observed under operational conditions. Therefore, estimation of damage level using both maximum drift ratio and frequency changes provides more reliable assessment and enables more clear connection between ratio of change in these parameters and performance of structures.

The following points should be considered in future studies to be carried out according to significant findings in this study:

- In this study, soil-structure interaction was not considered. Therefore, there is no comment about changes in dynamic properties of structures due to soil-structure interaction. It can be useful to take into account soil-structure interaction in future studies especially for condition assessment of piles.

- Since Simulated Annealing updates nonlinear properties of shear and flexural springs by minimizing difference between simulated and measured responses of instrumented floors based on defined boundary conditions, there may be more than one solution of objective function. Therefore, parameters that control local responses can be added to parameters that control global responses inside objective function to get more accurate results. In addition, updating boundary conditions after each iteration based on results of previous iteration may provide more reliable optimization with faster convergence.
- All approaches are insufficient to estimate responses of structure at floors where stiffness changes abruptly. Therefore, additional parameters to control local and global responses of floors where basement walls end and normal floors begin should be included in objective function.
- In this study, it was proposed that damage level of structures after a possible earthquake can be determined by relationship between changes in fundamental frequencies and maximum inter-story drift ratios. It is a fact that, fluctuations can be observed in frequencies of structures during long-term monitoring. Frequency change can remain within this fluctuation during an earthquake caused minor damage. Therefore, DI may not be properly calculated for minor damages.

REFERENCES

1. Mazzoni, S., F. McKenna, M. H. Scott, and G. L. Fenves, "OpenSees Command Language Manual", Pacific Earthquake Engineering Research Center, Los Angeles, 2006.

2. McKenna, F., M. H. Scott, and G. L. Fenves, "Nonlinear Finite-element Analysis Software Architecture Using Object Composition", *Journal of Computing in Civil Engineering*, Vol. 24, No. 1, pp. 95-107, 2009.

3. The MathWorks Inc. (2022). MATLAB version: 9.13.0 (R2022b), Natick, Massachusetts: The MathWorks Inc. https://www.mathworks.com.

4. Brownjohn, J. M. W., F. Magalhaes, E. Caetano, and A. Cunha, "Ambient Vibration Re-testing and Operational Modal Analysis of the Humber Bridge", *Engineering Structures*, Vol. 32, pp. 2003-2018, 2010.

5. Cross, E. J., K. Y. Yoo, J. M. W. Brownjohn, and K. Worden, "Long-term Monitoring and data Analysis of the Tamar Bridge", *Mechanical Systems and Signal Processing*, Vol. 35, pp. 16-34, 2012.

6. Soyoz, S., and M. Q. Feng, "Instantaneous Damage Detection of Bridge Structures and Experimental Verification", *Structural Control and Health Monitoring*, Vol. 15, No. 7, pp. 958-973, 2008.

7. Soyoz, S., and M. Q. Feng, "Long-term Monitoring and Identification of bridge Structural Parameters", *Computer-Aided Civil and Infrastructure Engineering*, Vol. 24, No. 2, pp. 82-92, 2009.

8. Oliveira, G., F. Magalhaes, A. Cunha, and E. Caetano, "Vibration-based Damage Detection in a Wind Turbine Using 1 Year of Data", *Structural Control Health Monitoring*, Vol. 25, No. 11, pp. 1-22, 2018.

9. Oliveira, G., F. Magalhaes, A. Cunha, and E. Caetano, "Continuous Dynamic Monitoring of an Onshore Wind Turbine", *Engineering Structures*, Vol. 164, pp. 22-39, 2018.

10. Pereira, S., F. Magalhaes, J. P. Gomes, A. Cunha, and J. V. Lemos, "Dynamic Monitoring of a Concrete Arch Dam During the First Filling of the Reservoir", *Engineering Structures*, Vol. 174, pp. 548-560, 2018.

11. Brownjohn, J. M. W., "Ambient Vibration Studies for System Identification of Tall Buildings", *Earthquake Engineering and Structural Dynamics*, Vol. 32, No.1, pp. 71-95, 2003.

12. Celebi, M., "Recorded Earthquake Responses from the Integrated Seismic Monitoring Network of the Atwood Building, Anchorage, Alaska", *Earthquake Spectra*, Vol. 22, No. 4, pp. 847-864, 2006.

13. Nayeri, R. D., S. F. Masri, and N .R. L Ghanem, "A Novel Approach for the Structural Identification and Monitoring of a Full-scale 17-story Building Based on Ambient Vibration Measurements", *Smart Materials and Structures*, Vol. 17, No. 2, 2008.

14. Yuen, K. V., and S. C. Kuok, "Ambient Interference in Long-term Monitoring of Buildings", *Engineering Structures*, Vol. 32, pp. 2379-2386, 2010.

15. Celebi, M., M. Huang, and A. Shakal, "Ambient Response of a Unique Performance-based Design Tall Building with Dynamic Response Modification Features", *Structural Design of Tall and Special Buildings*. Vol. 22, No. 10, pp. 816-829, 2013.

16. Celebi, M., N. Toksoz, and O. Buyukozturk, "Rocking Behavior of an Instrumented Unique Building on the MIT Campus Identified from Ambient Shaking Data", *Earthquake Spectra*, Vol. 30, No. 2, pp. 705-720, 2014.

17. Zhang, F. L., H. B. Xiong, W. X. Shi, and X. Ou, "Structural Health Monitoring of Shanghai Tower During Different Stages Using a Bayesian Approach", *Structural Control and Health Monitoring*, Vol. 23, No. 11, pp.1366-1384, 2016.

18. Mordret, A., H. Sun, G. A. Prieto, M. N. Toksoz, and O. Buyukozturk, "Continuous Monitoring of High-Rise Buildings Using Seismic Interferometry", *Bulletin of the Seismological Society of America*, Vol. 107, No. 6, pp. 2759-2773, 2017.

19. Celebi, M., and E. Safak, "Seismic Response of Transamerica", *Journal of Structural Engineering*, Vol. 117, No. 8, pp. 2389-2425, 1991.

20. Celebi, M., and E. Safak, "Seismic Response of Pacific Park Plaza", *Journal of Structural Engineering*, Vol. 118, No. 6, pp. 1547-1589, 1992.

21. Kohler, M. D., P. M. Davis, and E. Safak, "Earthquake and Ambient Vibration Monitoring of the Steel-frame UCLA Factor Building", *Earthquake Spectra*, Vol. 21, No. 3, pp. 715-736, 2005.

22. Snieder, R., and E. Safak, "Extracting the Building Response Using Seismic Interferometry: Theory and Application to the Millikan Library in Pasadena, California", *Bulletin of the Seismological Society of America*, Vol. 96, No. 2, pp. 586–598, 2006.

23. Rodgers, J. E., and M. Celebi, "Seismic Response and Damage Detection Analyses of an Instrumented Steel Moment-framed Building", *Journal of Structural Engineering*, Vol. 13, No. 10, pp. 1543-1552, 2006.

24. Todorovska, M. I., and M. D. Trifunac, "Earthquake Damage Detection in Imperial County Services Building I: The Data and Time-frequency Analysis", *Soil Dynamics and Earthquake Engineering*, Vol. 27, pp. 564-576, 2007.

25. Todorovska, M. I., and M. D. Trifunac, "Earthquake Damage Detection in Imperial County Services Building III: Analysis of Wave Travel Times via Impulse Response Function", *Soil Dynamics and Earthquake Engineering*, Vol. 28, pp. 387-404, 2008.

26. Todorovska, M. I., and M. D. Trifunac, "Impulse Response Analysis of the Van Nuys 7-story Hotel During 11 Earthquakes and Earthquake Damage Detection", *Structural Control and Health Monitoring*, Vol. 15, No. 1, pp. 90-116, 2008.

27. Todorovska, M. I., and M. D. Trifunac, "Earthquake Damage Detection in Imperial County Services Building II: Analysis of Novelties via Wavelets", *Structural Control and Health Monitoring*, Vol. 17, pp. 895-917, 2010.

28. Moaveni, B., J. P. Conte, and F. M. Hemez, "Uncertainty and Sensitivity Analysis of Damage Identification Results Obtained Using Finite Element Model Updating", *Computer-Aided Civil and Infrastructure Engineering*, Vol. 24, No. 5, pp. 320-334, 2009.

29. Bodin, P., J. Vidale, T. Walsh, R. Cakir, and M. Celebi, "Transient and Long-term Changes in Seismic Response of the Natural Resources Building Olympia, Washington, due to Earthquake Shaking", *Journal of Earthquake Engineering*, Vol. 16, No. 5, pp. 607-622, 2012.

30. Saito, T., K. Morita, T. Kashima, and T. Hasegawa, "Performance of High-rise Buildings During the 2011 Great East Japan Earthquake", *15th World Conference on Earthquake Engineering*, Lisboa, Portugal, p. 10, 2012.

31. Ebrahimian, M., M. Rahmani, and M. I. Todorovska, "Nonparametric Estimation of Wave Dispersion in High-rise Buildings by Seismic Interferometry', *Earthquake Engineering and Structural Dynamics*, Vol. 43, No. 15, pp. 2361-2375, 2014.

32. Celebi, M., Y. Hisada, and R. Omrani, "Responses of Two Tall Buildings in Tokyo, Japan, Before, During, and After the M9.0 Tohoku Earthquake of 11 March 2011", *Earthquake Spectra*, Vol. 32, No. 1, pp.463-495, 2016.

33. Abazarsa, F., F. Nateghi, S .F. Ghahari, and E. Taciroglu, "Extended Blind Modal Identification Technique for Non-stationary Excitations and Its Verification and Val-

idation", *Journal of Engineering Mechanics*, Vol. 142, No. 2, pp. 1-19, 2016.

34. Astorga, A., P. Guegen, and T. Kashima, "Nonlinear Elasticity in Buildings: A Prospective Way to Monitor Structural Health", *X International Conference on Structural Dynamics*, Rome, Italy, p. 7, 2017.

35. Ghahari, S. F., F. Abazarsa, and E. Taciroglu, "Blind Modal Identification of Non-classically Damped Structures under Non-stationary Excitations", *Structural Control and Health Monitoring*, Vol. 24, No. 6, pp. 1-21, 2017.

36. Kashima, T., "Study on Changes in Dynamic Characteristics of High-rise Steel-framed Buildings Based on Strong Motion Data", *X International Conference on Structural Dynamics*, Rome, Italy, p. 6,2017.

37. Taciroglu, E., S. F. Ghahari, and F. Abazarsa, "Efficient Model Updating of a Multi-story Frame and Its Foundation Stiffness from Earthquake Records Using a Timoshenko Beam Model", *Soil Dynamics and Earthquake Engineering*, Vol. 92, pp. 25-35, 2017.

38. Shirzad, N., M. Mahsuli, S. F. Ghahari, and E. Taciroglu, "Bayesian Identification of Soil-foundation Stiffness of Building Structures", *Structural Control and Health Monitoring*, Vol. 25, No. 3, pp. 1-19, 2018.

39. Miranda, E., and S. Taghavi, "Approximate Floor Acceleration Demands in Multistory Buildings. I: Formulation", *Journal of Structural Engineering*, Vol. 131, No. 2, pp. 203-211, 2005.

40. Taghavi, S., and E. Miranda, "Approximate Floor Acceleration Demands in Multistory Buildings. I: Applications", *Journal of Structural Engineering*, Vol. 131, No. 2, pp. 212-220, 2005.

41. Goel, R. K., "Mode-based Procedure to Interpolate Strong Motion Records of Instrumented Buildings", *Journal of Earthquake Technology*, Vol. 45, No. 3-4, pp.

97–113, 2008.

42. Kaya, Y., S. Kocakaplan, and E. Safak, "System Identification and Model Calibration of Multi-story Buildings Through Estimation of Vibration Time Histories at Non-instrumented Floor", *Bulletin of Earthquake Engineering*, Vol. 13, pp. 3301-3323, 2015.

43. Limongelli, M. P., "Optimal Location of Sensors for Reconstruction of Seismic Responses Through Spline Function Interpolation", *Earthquake Engineering and Structural Dynamics*, Vol. 32, No. 7, pp. 1055-1074, 2003.

44. Limongelli, M. P., "The Interpolation Damage Detection Method for Frames under Seismic Excitation", *Journal of Sound and Vibration*, Vol. 330, No. 22, pp. 5474-5489, 2011.

45. Limongelli, M. P., "Seismic Health Monitoring of an Instrumented Multistory Building Using the Interpolation Method", *Earthquake Engineering and Structural Dynamics*, Vol. 43, No. 11, pp. 1581-1602, 2014.

46. Acunzo, G., N. Fiorini, D. Spina, and M. Dolce, "Application of Genetic Algorithms for a New Approach for Seismic Building Monitoring: Integrated Measurement Systems with Physical and Virtual Sensors", *Bulletin of Earthquake Engineering*, Vol. 20 No. 9, pp. 4293-4317, 2022.

47. Hoult, R., "A Computationally-Effective Method for Rapidly Determining the Seismic Structural Response of High-Rise Buildings with a Limited Number of Sensors", *Bulletin of Earthquake Engineering*, Vol. 20, pp. 4395-4417, 2022.

48. Turkish Building Seismic Code, Disaster and Emergency Management Presidency, Ankara, 2019.

49. Deierlein, G. G., A. M. Reinhorn, and M. R. Willford, "Nonlinear Structural Analysis for Seismic Design, NEHRP Seismic Design Technical Brief No. 4, produced by

the NEHRP Consultants Joint Venture, A Partnership of the Applied Technology Council and the Consortium of Universities for Research in Earthquake Engineering, for the National Institute of Standards and Technology", Gaithersburg, MD, NIST GCR 10-917-5, 2010.

50. Correia, A. A., J. P. Almeida, and R. Pinho, "Force-based Versus Displacement-based Formulations in the Cyclic Nonlinear Analysis of RC Frames", *The 14th World Conference on Earthquake Engineering*, Beijing, China, p. 8, 2008.

51. Neuenhofer, A., and F. C. Filippou, "Evaluation of Nonlinear Frame Finite-element Models", *Journal of Structural Engineering*, Vol. 123, No. 7, pp. 958-966, 1997.

52. Zendaoui, A., A. Kadid, and D. Yahiaoui, "Comparison of Different Numerical Models of RC Elements for Predicting the Seismic Performance of Structures", *International Journal of Concrete Structures and Materials*, Vol. 10, No. 4, pp. 461-478, 2016.

53. Carreno, R., K. H. Lotfizdeh, J. P. Conte, and J. I. Restrepo, "Material model Parameters for Giuffre-Menegotto-Pinto Uniaxial Steel Stress-strain Model", *Journal of Structural Engineering*, Vol. 146, No. 2, pp. 1-21, 2020.

54. Mazzoni, S., F. McKenna, M. H. Scott, and G. L. Fenves, "OpenSees Command Language Manual, Steel02 Material", Pacific Earthquake Engineering Research Center, University of California, Berkeley, 2006.

55. Mazzoni, S., F. McKenna, M. H. Scott, and G. L. Fenves, "OpenSees Command Language Manual, Two Node Link Element", Pacific Earthquake Engineering Research Center, University of California, Berkeley, 2006.

56. Cheng, B., C. Yang,and K. L. R. Su, "Seismic Retrofit Analysis of Concrete Coupled Shear Wall Structures with Laterally Restrained Steel Plate Coupling Beams", *Advances in Structural Engineering*, Vol. 27, No. 7, pp. 962-974, 2018.

57. Ji, X., D. Liu, Y. Sun, and C. M. Hutt, "Seismic Performance Assessment of a Hybrid Coupled Wall System with Replaceable Steel Coupling Beams Versus Traditional RC Coupling Beams", *Earthquake Engineering Structural Dynamics*, Vol. 46, No. 4, pp. 517-535, 2017.

58. Han, S. W., H. Koh, and C. S. Lee, "Accurate and Efficient Simulation of Cyclic Behavior of Diagonally Reinforced Concrete Coupling Beams", *Earthquake Spectra*, Vol. 35, No. 1, pp. 361-381, 2019.

59. Yang, C., S. C. Chen, C. H. Yen, and C. C. Hung, "Behavior and Detailing of Coupling Beams with High-strength Materials", *Journal of Building Engineering*, Vol. 47, 2022.

60. Arabzadeh, H., and K. Galal, "Seismic-response Analysis of RC C-shaped Core Walls Subjected to Combined Flexure, Shear, and Torsion", *Journal of Structural Engineering*, Vol. 144, No. 10, pp. 1-17, 2018.

61. Pan, C., and D. Weng, "Study on Seismic Performance of Coupled Shear Walls with Vertical Dampers", *Advanced Materials Research*, Vol. 163-167, pp. 4185-4193, 2011

62. Pelletier, K., and P. Leger, "Nonlinear Seismic Modelling of Reinforced Concrete Cores Including Torsion", *Engineering Structures* Vol. 136, pp. 380-392, 2017.

63. Orakcal, K., and J. W. Wallace, "Flexural Modeling of Reinforced Concrete Structural Walls – Experimental Verification", *American Concrete Institute Structural Journal*, Vol. 103, No. 2, pp. 196-206, 2006.

64. Orakcal K., J.W. Wallace and J.P. Conte, "Flexural Modeling of Reinforced Concrete Structural Walls - Model Attributes", *American Concrete Institute Structural Journal*, Vol. 101, No. 5, pp. 688-698, 2004.

65. Kolozvari, K., K. Orakcal, and J. W. Wallace, "Modeling of Cyclic Shear-Flexure

Interaction in Reinforced Concrete Structural Walls. I: Theory", *Journal of Structural Engineering*, Vol. 141, No. 5, 2015.

66. Kolozvari, K., T. Tran, K. Orakcal, and J. W. Wallace, "Modeling of Cyclic Shear-Flexure Interaction in Reinforced Concrete Structural Walls. II: Experimental Validation", *Journal of Structural Engineering*, Vol. 141, No. 5, 2015.

67. Kolozvari, K., K. Kalbasi, K. Orakcal, L. M. Massone, and J. W. Wallace, "Shear-flexure-interaction Models for Planar and Flanged Reinforced Concrete Walls", *Bulletin of Earthquake Engineering*, Vol. 17, pp. 6391-6417, 2019.

68. Tian, Y., L. Xie, Z. Xu, and X. Lu, "GPU-Powered High-performance Computing for the Analysis of Large-scale Structures based on OpenSees", *Computing in Civil Engineering*, pp. 411-418, 2015.

69. Lu, X., L. Xie, H. Guan, Y. Huang, and X. Lu, "A Shear Wall Element for Nonlinear Seismic Analysis of Super-tall Buildings Using OpenSees", *Finite Elements in Analysis and Design*, Vol. 98, pp. 14-25, 2015.

70. Lu, X., X. Xie, H. Guan, and L. Ye, "Collapse Simulation of Reinforced Concrete High-rise Building Induced by Extreme Earthquakes", *Earthquake Engineering and Structural Dynamics*, Vol. 42, No. 5, pp. 705-723, 2013.

71. Xie, L., X. Lu, Y. Huang, and L. Ye, "Multi-layer Shell Element for Shear Walls in OpenSees", *Computing in Civil and Building Engineering*, pp. 1190-1197, 2014.

72. Chopra, A. K., *Dynamics of Structures: Theory and Applications to Earthquake Engineering*, Forth Edition, Prentice-Hall, Upper Saddle River, USA, 2007.

73. Finley, A. C., "Unintended Consequences of Modeling Damping in Structures", *Journal of Structural Engineering*, Vol. 134, No. 4, pp. 581-592, 2008.

74. Hall, J. F., "Problems Encountered from the Use (or misuse) of Rayleigh Damp-

ing", *Earthquake Engineering and Structural Dynamic*. Vol. 35, No. 5, pp. 525–545, 2006.

75. Petrini, L., C. Maggi, M. J. N Priestley, and G. M. Calvi, "Experimental Verification of Viscous Damping Modeling for Inelastic Time History Analyzes", *Journal of Earthquake Engineering*, Vol. 12, pp. 125-145, 2008.

76. Naeim, F., "Performance of 20 Extensively Instrumented Buildings During the 1994 Northridge Earthquake", *Structural Design of Tall and Special Buildings*, Vol. 7, No. 3, pp. 179-194, 1998.

77. Naeim, F., H. Lee, S. Hagie, H. Bhatia, A. Alimoradi, and E. Miranda, "Three-dimensional Analysis, Real-time Visualization and Automated Post-earthquake Damage Assessment of Buildings", *Structural Design of Tall and Special Buildings*, Vol. 15, No. 1, pp. 105-138, 2006.

78. Timoshenko, S. P., "On the Transverse Vibrations of Bars of Uniform Cross-section", *Philosophical Magazine*, Vol. 43, No. 253, pp. 125–131, 1992.

79. Cao, M. S., W. Xu, Z. Su, W. Ostachowicz, and N. Xia, "Local Coordinate Systems-based Method to Analyse High-order Modes of N-step Timoshenko Beam", *Journal of Vibration and Control*, Vol. 23, No. 1, pp. 89-102, 2015.

80. Khaji, N., M. Shafiei, and M. Jalalpour, "Closed-form Solutions for Crack Detection Problem of Timoshenko Beams with Various Boundary Conditions", *International Journal of Mechanical Sciences*, Vol. 51, No. 9-10, pp. 667–681, 2009.

81. Boutin, C., S. Hans, E. Ibraim, and P. Roussilllon, "In Situ Experiments and Seismic Analysis of Existing Buildings. Part 2: Seismic Integrity Threshold", *Earthquake Engineering and Structural Dynamics*, Vol. 34, No.12, pp. 1531-1546, 2005.

82. Cheng, M. H., and T. H. Heaton, "Simulating Building Motions Using Ratios of the Building's Natural Frequencies and a Timoshenko Beam Model", *Earthquake*

Spectra, Vol. 31, No. 1, pp. 403-420, 2015.

83. Kaya, Y., and J. Dowling, "Application of Timoshenko Beam Theory to the Estimation of Structural Response", *Engineering Structures*, Vol. 123, pp. 71-76, 2016.

84. Kaya, Y., and E. Safak, "Real-time Analysis and Interpretation of Continuous Data from Structural Health Monitoring (SHM) Systems", *Bulletin of Earthquake Engineering*, Vol. 13, pp. 917-934, 2015.

85. Wu, J. S., *Analytical and Numerical Methods for Vibration Analyses*, John Wiley and Sons, Singapore, 2013.

86. Huergo, I. F., and H. Hernande, "Coupled Shear-flexural Model for Dynamic Analysis of Fixed-base Tall buildings with Tuned Mass Dampers", *The Structural Design of Tall and Special Buildings*, Vol. 29, No. 17, pp. 1-20, 2019.

87. Khaloo, A. R., and H. Khosravi, "Multi-mode Response of Shear and Flexural Buildings to Pulse-type Fround Motions in Near-field Earthquakes", *Journal of Earthquake Engineering*, Vol. 12, No. 4, pp. 616-630, 2008.

88. Kuang, J. S., and K. Huang, "Simplified Multi-degree-of-freedom Model for Estimation of Seismic Response of Regular Wall-frame Structures", *The Structural Design of Tall and Special Buildings*, Vol. 20, No. 3, pp. 418-432, 2011.

89. Xiong, C., X. Lu, H. Guan, and Z. Xu, "A Nonlinear Computational Model for Regional Seismic Simulation of Tall buildings", *Bulletin of Earthquake Engineering*, Vol. 14, pp. 1047-1069, 2016.

90. Kalman, R. E., "A New Approach to Linear Fltering and Prediction Problems", *Journal of Basic Engineering*, Vol. 82, No. 1, pp. 35-45, 1960.

91. Khodarahmi, M., and V. Maihami, "A Review on Kalman Filter Models", *Archives of Computational Methods in Engineering*, Vol. 30, pp. 727-747, 2023.

92. Astroza, R., H. Ebrahimian, and J. P. Conte, "Material Parameter Identification in Distributed Plasticity FE Models of Frame-type Structures Using Nonlinear Stochastic Filtering", *Journal of Engineering Mechanics*, Vol. 141, No. 5, 2015.

93. Astroza, R., L. Nguyen, and T. Nestorovic, "Finite Element Model of Updating Simulated Annealing Hybridized with Unscented Kalman Filter", *Computers and Structures*, Vol. 177, pp. 176-191, 2016.

94. Astroza, R., H. Ebrahimian, and J. P. Conte, "Performance Comparison of Kalman-based Filters for Nonlinear Structural Finite Element Model Updating", *Journal of Sound and Vibration*, Vol. 438, pp. 520-542, 2019.

95. Ebrahimian, H., R. Astroza, and J. P. Conte, "Extended Kalman Filter for Material Parameter Estimation in Nonlinear Structural Finite Element Models Using Direct Differentiation Method", *Earthquake Engineering and Structural Dynamics*, Vol. 44, No. 10, pp. 1495-1522, 2015.

96. Erazo, K., and E. M. Hernandez, "Uncertainty Quantification of State Estimation in Nonlinear Structural Systems with Application to Seismic Response in Buildings", *Journal of Risk and Uncertainty in Engineering Systems*, Vol. 2, No. 3, 2015.

97. Mariani, S., and A. Ghisi, "Unscented Kalman Filtering for Nonlinear Structural Dynamics", *Nonlinear Dynamics*, Vol. 49, pp. 131-150, 2007.

98. Song, M., R. Astroza, H. Ebrahimian, B. Moaveniand, and C. Papadimitriou, "Adaptive Kalman Filters for Nonlinear Finite Element Model Updating", *Mechanical Systems and Signal Processing*, Vol. 143, 2020.

99. Yang, J. N., S. Lin, H. Huang, and L. Zhou, "An Adaptive Extended Kalman Filter for Structural Damage Detection", *Structural Control and Health Monitoring*, Vol. 13, No. 4, pp. 849-867, 2006.

100. Asgarieh, E., B. Moaveni, A. Barbosa, and E. Chatzi, "Nonlinear Model Calibra-

tion of a Shear Wall Building Using Time and Frequency Data Features", *Mechanical Systems and Signal Processing*, Vol. 85, pp. 236-251, 2017.

101. Kirkpatrick, S., C. D. Gelatt, and M. P. Vecchi, "Optimization by Simulated Annealing", *Science*, Vol. 220, No. 4598, pp. 671-680, 1983.

102. Teughels, A., G. D. Roeck, and A. K. S. Johan, "Global Optimization by Coupled Local Minimizers and Its Application to FE Model Updating", *Computers and Structures*, Vol. 81, pp. 2337-2351, 2003.

103. Cosenza, E., and G. Manfredi, "Damage Indices and Damage Measures", *Progress in Structural Engineering*, Vol. 2, pp. 50-59, 2000.

104. Elenas, A., "Interrelation Between Seismic Acceleration Parameters of European Earthquakes and the Structural Behavior", *Earthquake Engineering in Europe*, Vol. 12, No. 1, pp. 56–63, 1988.

105. Elenas, A., and K. Meskouris, "Correlation Study Between Seismic Acceleration Parameters and Damage Indices of Structures", *Engineering Structures*, Vol. 23, No. 6, pp. 698-704, 2001.

106. Erduran, E., and A. Yakut, "Drift Based Damage Functions for Reinforced Concrete Columns", *Computers and Structures*, Vol. 82, No. 2-3, pp. 121-130, 2004.

107. Evaluation of earthquake damaged concrete and masonry wall buildings (FEMA 306), Federal Emergency Management Agency, Washington, 1998.

108. Prestandard and commentary for the seismic rehabilitation of buildings (FEMA 306), Federal Emergency Management Agency, Washington, 2000.

109. NEHRP Recommended seismic provisions for new buildings and other structures (FEMA P-750), Federal Emergency Management Agency, Washington, 2009.

110. Mayes, R. L., "Interstory Drift Design and Damage Control Issues", *The Structural Design of Tall Buildings*, Vol. 4, No. 1, pp. 15-25, 1995.

111. Ruiz-Garcia, J., and E. Miranda, "Residual Displacement Ratios for Assessment of Existing Structures", *Earthquake Engineering and Structural Dynamics*, Vol. 35, No. 3, pp. 315-336, 2006.

112. Yazgan, U., and A. Daizo, "Post-earthquake Damage Assessment Using Residual Displacements", *Earthquake Engineering and Structural Dynamics*, Vol.41, No. 8, pp.1257-1276, 2012.

113. Carrilo, J., "Damage Index based on Stiffness Degradation of Low-rise RC walls", *Earthquake Engineering and Structural Dynamics*, Vol. 44, No. 6, pp. 831-848, 2015.

114. Wen, Y. K., and Y. J. Kang, "Minimum Building Life-cycle Cost Design Criteria. II: Applications", *Journal of Structural Engineering*, Vol. 127, No.3, pp. 338-346, 2001.

115. Brincker, R., L. Zhang, and P. Andersen, "Modal Identification of Output – only Systems Using Frequency Domain Decomposition", *Smart Materials and Structures*, Vol. 10, pp. 441-445, 2001.

116. Tamura, Y., "Amplitude Dependency of Damping in Buildings and Critical Tip Drift Ratio", *International Journal of High-Rise Buildings*, Vol. 1, No. 1, pp. 1-13, 2022.

117. Ljung, L. T., *System Identification: Theory for the User*, Second Edition. Prentice Hall PTR, Upper Saddle River, NJ, 1999.

118. Van, O. P., and B. D. Moor, "N4SID: Subspace Algorithms for the Identification of Combined Deterministic-Stochastic Systems", *Automatica*, Vol. 30, No. 1, pp. 75-93, 1994.

119. Skolnik, D., Y. Lei, E. Yu, and J. W. Wallace, "Identification, Model Updating, and Response Prediction of an Instrumented 15-story Steel-frame Building", *Earthquake Spectra*, Vol. 22, No. 3, pp. 781-802, 2006.

120. Ivanovic, S. S., M. D. Trifunac, E. I. Novikova, A. A. Gladkov, and M. I. Todorovska, "Ambient Vibration Tests of a Seven-story Reinforced Concrete Building in Van Nuys, California, Damaged by the 1994 Northridge earthquake", *Soil Dynamics and Earthquake Engineering*, Vol. 19, No.6, pp. 391-411, 2000.

121. Islam, M. S., "Analysis of the Northridge Earthquake Response of a Damaged Non-ductile Concrete Frame Building", *The Structural Design of Tall Buildings*, Vol. 5, No. 3, pp. 151-182, 1996.

122. Trifunac, M. D., S. S. Ivanovic, and M. I. Todorovska, "Apparent Periods of a Building. I: Fourier Analysis", *Journal of Structural Engineering*, Vol. 127, No. 5, pp. 517-526, 2001.

123. Trifunac, M. D., S. S. Ivanovic, and M. I. Todorovska, "Apparent Periods of a Building. II: Time-frequency Analysis.", *Journal of Structural Engineering*, Vol. 127, No. 5, pp. 527-537, 2001.

124. Krawinkler, H., "PEER Report: Van Nuys Hotel Building Testbed Report: Exercising Seismic Performance Assessment", University of California, Berkeley, 2005.

125. Celebi, M., "Real-time Monitoring of Drift for Occupancy Resumption", *14th World Conference on Earthquake Engineering*, Beijing, China, p. 8, 2008.

126. Celebi, M., A. Sanli, and M. Sinclair, "Real-time Seismic Monitoring Needs of a Building Owner and the Solution: A Cooperative Effort", *Earthquake Spectra*, Vol. 20, No. 2, pp. 333-346, 2004.